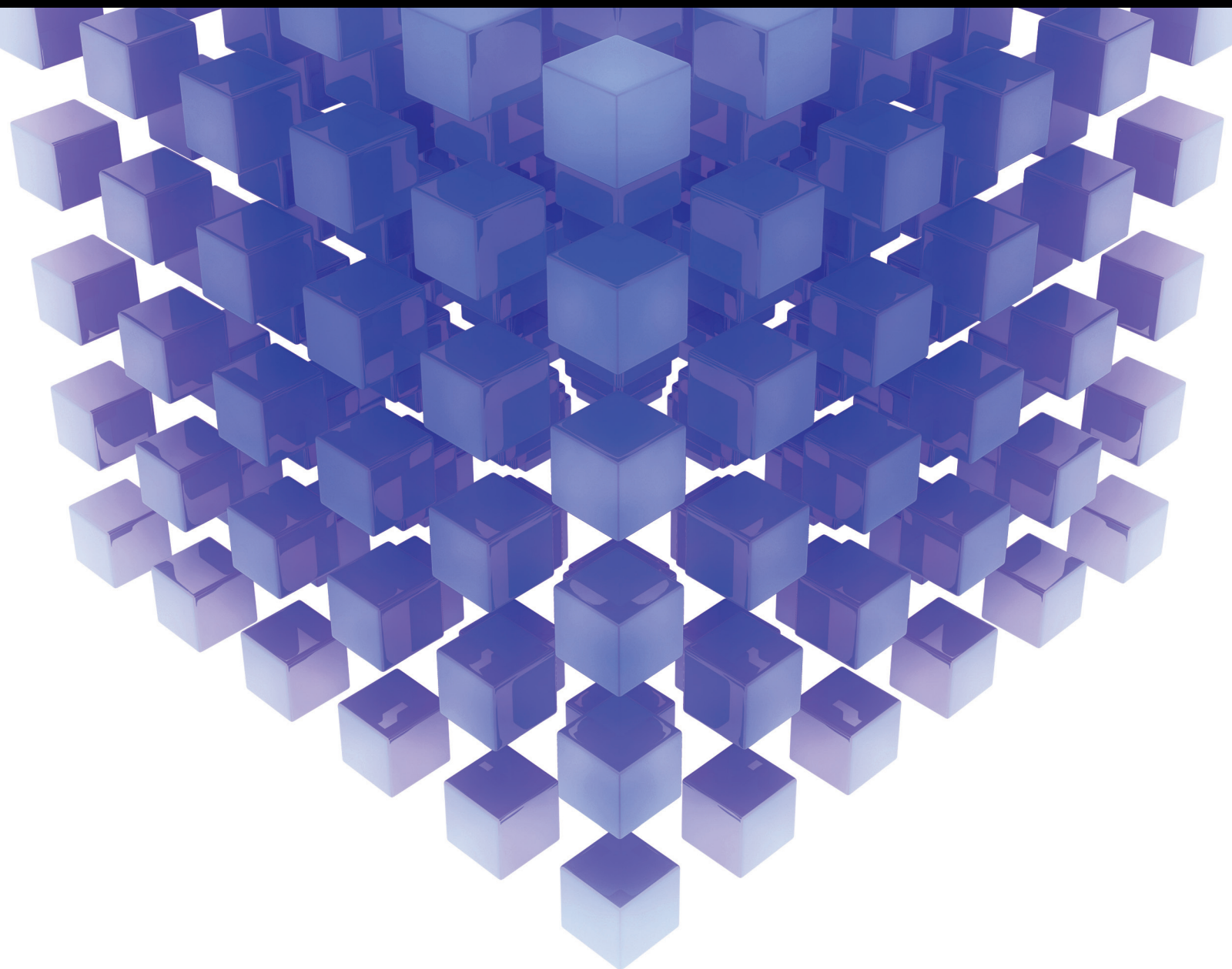


Mathematical Problems in Engineering

# Advanced Mathematical and Numerical Methods in Control and Optimization for Smart Grids

Special Issue Editor in Chief: Zhan Shu

Guest Editors: Michael Z. Q. Chen and Qing Hui





---

# **Advanced Mathematical and Numerical Methods in Control and Optimization for Smart Grids**

Mathematical Problems in Engineering

---

**Advanced Mathematical and Numerical  
Methods in Control and Optimization for  
Smart Grids**

Special Issue Editor in Chief: Zhan Shu

Guest Editors: Michael Z. Q. Chen and Qing Hui



---

Copyright © 2019 Hindawi. All rights reserved.

This is a special issue published in “Mathematical Problems in Engineering.” All articles are open access articles distributed under the Creative Commons Attribution License, which permits unrestricted use, distribution, and reproduction in any medium, provided the original work is properly cited.

## Editorial Board

- Mohamed Abd El Aziz, Egypt  
AITOUCHE Abdelouhab, France  
Leonardo Acho, Spain  
José A. Acosta, Spain  
Daniela Addressi, Italy  
Paolo Addresso, Italy  
Claudia Adduce, Italy  
Ramesh Agarwal, USA  
Francesco Aggogeri, Italy  
Juan C. Agüero, Australia  
Ricardo Aguilar-Lopez, Mexico  
Tarek Ahmed-Ali, France  
Elias Aifantis, USA  
Muhammad N. Akram, Norway  
Guido Ala, Italy  
Andrea Alaimo, Italy  
Reza Alam, USA  
Nicholas Alexander, UK  
Salvatore Alfonzetti, Italy  
Mohammad D. Aliyu, Canada  
Juan A. Almendral, Spain  
José Domingo Álvarez, Spain  
Cláudio Alves, Portugal  
J. P. Amezcua-Sanchez, Mexico  
Lionel Amodeo, France  
Sebastian Anita, Romania  
Renata Archetti, Italy  
Felice Arena, Italy  
Sabri Arik, Turkey  
Francesco Aristodemo, Italy  
Fausto Arpino, Italy  
Alessandro Arsie, USA  
Edoardo Artioli, Italy  
Fumihiko Ashida, Japan  
Farhad Aslani, Australia  
Mohsen Asle Zaeem, USA  
Romain Aubry, USA  
Matteo Aureli, USA  
Richard I. Avery, USA  
Viktor Avrutin, Germany  
Francesco Aymerich, Italy  
Sajad Azizi, Belgium  
Michele Baccocchi, Italy  
Seungik Baek, USA  
Adil Bagirov, Australia  
Khaled Bahlali, France  
Laurent Bako, France  
Pedro Balaguer, Spain  
Stefan Balint, Romania  
Ines Tejado Balsera, Spain  
Alfonso Banos, Spain  
Jerzy Baranowski, Poland  
Roberto Baratti, Italy  
Andrzej Bartoszewicz, Poland  
David Bassir, France  
Mahmoud Bayat, USA  
Chiara Bedon, Italy  
Azeddine Beghdadi, France  
Denis Benasciutti, Italy  
Ivano Benedetti, Italy  
Rosa M. Benito, Spain  
Elena Benvenuti, Italy  
Giovanni Berselli, Italy  
Giorgio Besagni, Italy  
Michele Betti, Italy  
Pietro Bia, Italy  
Carlo Bianca, France  
Simone Bianco, Italy  
Vincenzo Bianco, Italy  
Vittorio Bianco, Italy  
David Bigaud, France  
Antonio Bilotta, Italy  
Paul Bogdan, USA  
Guido Bolognesi, UK  
Rodolfo Bontempo, Italy  
Alberto Borboni, Italy  
Paolo Boscariol, Italy  
Daniela Boso, Italy  
Guillermo Botella-Juan, Spain  
Boulaïd Boulkroune, Belgium  
Fabio Bovenga, Italy  
Francesco Braghin, Italy  
Ricardo Branco, Portugal  
Maurizio Brocchini, Italy  
Julien Bruchon, France  
Matteo Bruggi, Italy  
Michele Brun, Italy  
Vasilis Burganos, Greece  
Tito Busani, USA  
Raquel Caballero-Águila, Spain  
Filippo Cacace, Italy  
Pierfrancesco Cacciola, UK  
Salvatore Caddemi, Italy  
Roberto Caldelli, Italy  
Alberto Campagnolo, Italy  
Eric Campos-Canton, Mexico  
Marko Canadija, Croatia  
Salvatore Cannella, Italy  
Francesco Cannizzaro, Italy  
Javier Cara, Spain  
Ana Carpio, Spain  
Caterina Casavola, Italy  
Sara Casciati, Italy  
Federica Caselli, Italy  
Carmen Castillo, Spain  
Inmaculada T. Castro, Spain  
Miguel Castro, Portugal  
Giuseppe Catalanotti, UK  
Nicola Caterino, Italy  
Alberto Cavallo, Italy  
Gabriele Cazzulani, Italy  
Luis Cea, Spain  
Song Cen, China  
Miguel Cerrolaza, Venezuela  
M. Chadli, France  
Gregory Chagnon, France  
Ludovic Chamoin, France  
Ching-Ter Chang, Taiwan  
Qing Chang, USA  
Michael J. Chappell, UK  
Kacem Chehdi, France  
Peter N. Cheimets, USA  
Xinkai Chen, Japan  
Luca Chiapponi, Italy  
Francisco Chicano, Spain  
Nicholas Chileshe, Australia  
Adrian Chmielewski, Poland  
Ioannis T. Christou, Greece  
Hung-Yuan Chung, Taiwan  
Simone Cinquemani, Italy  
Roberto G. Citarella, Italy  
Joaquim Ciurana, Spain

John D. Clayton, USA  
Francesco Clementi, Italy  
Piero Colajanni, Italy  
Giuseppina Colicchio, Italy  
Vassilios Constantoudis, Greece  
Enrico Conte, Italy  
Francesco Conte, Italy  
Alessandro Contento, USA  
Mario Cools, Belgium  
Jean-Pierre Corriou, France  
J.-C. Cortés, Spain  
Carlo Cosentino, Italy  
Paolo Crippa, Italy  
Andrea Crivellini, Italy  
Erik Cuevas, Mexico  
Maria C. Cunha, Portugal  
Mehmet Cunkas, Turkey  
Peter Dabnichki, Australia  
Luca D'Acerno, Italy  
Weizhong Dai, USA  
Andrea Dall'Asta, Italy  
Purushothaman Damodaran, USA  
Bhabani S. Dandapat, India  
Farhang Daneshmand, Canada  
Giuseppe D'Aniello, Italy  
Sergey Dashkovskiy, Germany  
Fabio De Angelis, Italy  
Samuele De Bartolo, Italy  
Abílio De Jesus, Portugal  
Pietro De Lellis, Italy  
Alessandro De Luca, Italy  
Stefano de Miranda, Italy  
Filippo de Monte, Italy  
Michael Defoort, France  
Alessandro Della Corte, Italy  
Xavier Delorme, France  
Laurent Dewasme, Belgium  
Angelo Di Egidio, Italy  
Roberta Di Pace, Italy  
Ramón I. Diego, Spain  
Yannis Dimakopoulos, Greece  
Zhengtao Ding, UK  
M. Djemai, France  
Alexandre B. Dolgui, France  
Georgios Dounias, Greece  
Florent Duchaine, France  
George S. Dulikravich, USA  
Bogdan Dumitrescu, Romania  
Horst Ecker, Austria  
Saeed Eftekhari Azam, USA  
Ahmed El Hajjaji, France  
Antonio Elipe, Spain  
Fouad Erchiqui, Canada  
Anders Eriksson, Sweden  
R. Emre Erkmen, Canada  
G. Espinosa-Paredes, Mexico  
Leandro F. F. Miguel, Brazil  
Andrea L. Facci, Italy  
Giacomo Falcucci, Italy  
Giovanni Falsone, Italy  
Hua Fan, China  
Nicholas Fantuzzi, Italy  
Yann Favennec, France  
Fiorenzo A. Fazzolari, UK  
Giuseppe Fedele, Italy  
Roberto Fedele, Italy  
Zhongyang Fei, China  
Arturo J. Fernández, Spain  
Jesus M. Fernandez Oro, Spain  
Massimiliano Ferraioli, Italy  
Massimiliano Ferrara, Italy  
Francesco Ferrise, Italy  
Eric Feulvarch, France  
Barak Fishbain, Israel  
S. Douwe Flapper, Netherlands  
Thierry Floquet, France  
Eric Florentin, France  
Alessandro Formisano, Italy  
Francesco Franco, Italy  
Elisa Francomano, Italy  
Tomonari Furukawa, USA  
Juan C. G. Prada, Spain  
Mohamed Gadala, Canada  
Matteo Gaeta, Italy  
Mauro Gaggero, Italy  
Zoran Gajic, USA  
Erez Gal, Israel  
Jaime Gallardo-Alvarado, Mexico  
Mosè Gallo, Italy  
Ugo Galvanetto, Italy  
Akemi Gálvez, Spain  
Rita Gamberini, Italy  
Maria L. Gandarias, Spain  
Zhiwei Gao, UK  
Zhong-Ke Gao, China  
Giovanni Garcea, Italy  
Luis Rodolfo Garcia Carrillo, USA  
Jose M. Garcia-Aznar, Spain  
Akhil Garg, China  
Harish Garg, India  
Alessandro Gasparetto, Italy  
Gianluca Gatti, Italy  
Oleg V. Gendelman, Israel  
Stylianos Georgantzinou, Greece  
Fotios Georgiades, UK  
Parviz Ghadimi, Iran  
Mergen H. Ghayesh, Australia  
Georgios I. Giannopoulos, Greece  
Agathoklis Giaralis, UK  
Pablo Gil, Spain  
Anna M. Gil-Lafuente, Spain  
Ivan Giorgio, Italy  
Gaetano Giunta, Luxembourg  
Alessio Gizzi, Italy  
Jefferson L.M.A. Gomes, UK  
Emilio Gómez-Déniz, Spain  
Antonio M. Gonçalves de Lima, Brazil  
David González, Spain  
Chris Goodrich, USA  
Rama S. R. Gorla, USA  
Kannan Govindan, Denmark  
Antoine Grall, France  
George A. Gravvanis, Greece  
Fabrizio Greco, Italy  
David Greiner, Spain  
Simonetta Grilli, Italy  
Jason Gu, Canada  
Federico Guarracino, Italy  
Michele Guida, Italy  
Zhaoxia Guo, China  
José L. Guzmán, Spain  
Quang Phuc Ha, Australia  
Petr Hájek, Czech Republic  
Weimin Han, USA  
Zhen-Lai Han, China  
Thomas Hanne, Switzerland  
Mohammad A. Hariri-Ardebili, USA  
Xiao-Qiao He, China  
Nicolae Herisanu, Romania  
Alfredo G. Hernández-Díaz, Spain  
M.I. Herreros, Spain

Eckhard Hitzer, Japan  
Paul Honeine, France  
Jaromir Horacek, Czech Republic  
Muneo Hori, Japan  
András Horváth, Italy  
S. Hassan Hosseinnia, Netherlands  
Gordon Huang, Canada  
Sajid Hussain, Canada  
Asier Ibeas, Spain  
Orest V. Iftime, Netherlands  
Przemyslaw Ignaciuk, Poland  
Giacomo Innocenti, Italy  
Emilio Insfran Pelozo, Spain  
Alessio Ishizaka, UK  
Nazrul Islam, USA  
Benoit Jung, France  
Benjamin Ivorra, Spain  
Payman Jalali, Finland  
Mahdi Jalili, Australia  
Łukasz Jankowski, Poland  
Samuel N. Jator, USA  
Juan C. Jauregui-Correa, Mexico  
Reza Jazar, Australia  
Khalide Jbilou, France  
Piotr JÓdrzejowicz, Poland  
Isabel S. Jesus, Portugal  
Linni Jian, China  
Bin Jiang, China  
Zhongping Jiang, USA  
Emilio Jiménez Macías, Spain  
Ningde Jin, China  
Xiaoliang Jin, USA  
Liang Jing, Canada  
Dylan F. Jones, UK  
Palle E. Jorgensen, USA  
Viacheslav Kalashnikov, Mexico  
Tamas Kalmar-Nagy, Hungary  
Tomasz Kapitaniak, Poland  
Julius Kaplunov, UK  
Haranath Kar, India  
Konstantinos Karamanos, Belgium  
Krzysztof Kecik, Poland  
Jean-Pierre Kenne, Canada  
Do Wan Kim, Republic of Korea  
Nam-Il Kim, Republic of Korea  
Jan Koci, Czech Republic  
Ioannis Kostavelis, Greece  
Sotiris B. Kotsiantis, Greece  
Manfred Krafczyk, Germany  
Frederic Kratz, France  
Petr Krysl, USA  
Krzysztof S. Kulpa, Poland  
Shailesh I. Kundalwal, India  
Jurgen Kurths, Germany  
Cedrick A. K. Kwuimy, USA  
Kyandoghere Kyamakya, Austria  
Davide La Torre, Italy  
Risto Lahdelma, Finland  
Hak-Keung Lam, UK  
Giovanni Lancioni, Italy  
Jimmy Lauber, France  
Antonino Laudani, Italy  
Hervé Laurent, France  
Aimé Lay-Ekuakille, Italy  
Nicolas J. Leconte, France  
Dimitri Lefebvre, France  
Eric Lefevre, France  
Marek Lefik, Poland  
Yaguo Lei, China  
Kauko Leiviskä, Finland  
Thibault Lemaire, France  
Roman Lewandowski, Poland  
Chen-Feng Li, China  
Jian Li, USA  
Yang Li, China  
Huchang Liao, China  
En-Qiang Lin, USA  
Zhiyun Lin, China  
Peide Liu, China  
Peter Liu, Taiwan  
Wanquan Liu, Australia  
Bonifacio Llamazares, Spain  
Alessandro Lo Schiavo, Italy  
Jean Jacques Loiseau, France  
Francesco Lolli, Italy  
Paolo Lonetti, Italy  
Sandro Longo, Italy  
António M. Lopes, Portugal  
Sebastian López, Spain  
Pablo Lopez-Crespo, Spain  
Luis M. López-Ochoa, Spain  
Ezequiel López-Rubio, Spain  
Vassilios C. Loukopoulos, Greece  
Jose A. Lozano-Galant, Spain  
haiyan Lu, Australia  
Gabriel Luque, Spain  
Valentin Lychagin, Norway  
Dazhong Ma, China  
Antonio Madeo, Italy  
José María Maestre, Spain  
Alessandro Magnani, Italy  
Fazal M. Mahomed, South Africa  
Noureddine Manamanni, France  
Paolo Manfredi, Italy  
Didier Maquin, France  
Giuseppe Carlo Marano, Italy  
Damijan Markovic, France  
Francesco Marotti de Sciarra, Italy  
Rui Cunha Marques, Portugal  
Rodrigo Martinez-Bejar, Spain  
Guiomar Martín-Herrán, Spain  
Denizar Cruz Martins, Brazil  
Benoit Marx, France  
Elio Masciari, Italy  
Franck Massa, France  
Paolo Massioni, France  
Alessandro Mauro, Italy  
Fabio Mazza, Italy  
Laura Mazzola, Italy  
Driss Mehdi, France  
Roderick Melnik, Canada  
Pasquale Memmolo, Italy  
Xiangyu Meng, USA  
Jose Merodio, Spain  
Alessio Merola, Italy  
Mahmoud Mesbah, Iran  
Luciano Mescia, Italy  
Laurent Mevel, France  
Mariusz Michta, Poland  
Aki Mikkola, Finland  
Giovanni Minafò, Italy  
Hiroyuki Mino, Japan  
Pablo Mira, Spain  
Dimitrios Mitsotakis, New Zealand  
Vito Mocella, Italy  
Sara Montagna, Italy  
Roberto Montanini, Italy  
Francisco J. Montáns, Spain  
Gisele Mophou, France  
Rafael Morales, Spain  
Marco Morandini, Italy

Javier Moreno-Valenzuela, Mexico  
Simone Morganti, Italy  
Caroline Mota, Brazil  
Aziz Moukrim, France  
Dimitris Mourtzis, Greece  
Emiliano Mucchi, Italy  
Josefa Mula, Spain  
Jose J. Muñoz, Spain  
Giuseppe Muscolino, Italy  
Marco Mussetta, Italy  
Hakim Naceur, France  
Alessandro Naddeo, Italy  
Hassane Naji, France  
Mariko Nakano-Miyatake, Mexico  
Keivan Navaie, UK  
AMA Neves, Portugal  
Luís C. Neves, UK  
Dong Ngoduy, New Zealand  
Nhon Nguyen-Thanh, Singapore  
Tatsushi Nishi, Japan  
Xesús Nogueira, Spain  
Ben T. Nohara, Japan  
Mohammed Nouari, France  
Mustapha Nourelfath, Canada  
Włodzimierz Ogryczak, Poland  
Roger Ohayon, France  
Krzysztof Okarma, Poland  
Mitsuhiro Okayasu, Japan  
Alberto Olivares, Spain  
Enrique Onieva, Spain  
Calogero Orlando, Italy  
Alejandro Ortega-Moñux, Spain  
Sergio Ortobelli, Italy  
Naohisa Otsuka, Japan  
Erika Ottaviano, Italy  
Pawel Packo, Poland  
Arturo Pagano, Italy  
Alkis S. Paipetis, Greece  
Roberto Palma, Spain  
Alessandro Palmeri, UK  
Pasquale Palumbo, Italy  
Weifeng Pan, China  
Jürgen Pannek, Germany  
Elena Panteley, France  
Achille Paolone, Italy  
George A. Papakostas, Greece  
Xosé M. Pardo, Spain  
Vicente Parra-Vega, Mexico  
Manuel Pastor, Spain  
Petr Páta, Czech Republic  
Pubudu N. Pathirana, Australia  
Surajit Kumar Paul, India  
Sitek Paweł, Poland  
Luis Payá, Spain  
Alexander Paz, Australia  
Igor Pažanin, Croatia  
Libor Pekař, Czech Republic  
Francesco Pellicano, Italy  
Marcello Pellicciari, Italy  
Haipeng Peng, China  
Mingshu Peng, China  
Zhengbiao Peng, Australia  
Zhi-ke Peng, China  
Marzio Pennisi, Italy  
Maria Patrizia Pera, Italy  
Matjaz Perc, Slovenia  
A. M. Bastos Pereira, Portugal  
Ricardo Perera, Spain  
Francesco Pesavento, Italy  
Ivo Petras, Slovakia  
Francesco Petrini, Italy  
Lukasz Pieczonka, Poland  
Dario Piga, Switzerland  
Paulo M. Pimenta, Brazil  
Antonina Pirrotta, Italy  
Marco Pizzarelli, Italy  
Vicent Pla, Spain  
Javier Plaza, Spain  
Kemal Polat, Turkey  
Dragan Poljak, Croatia  
Jorge Pomares, Spain  
Sébastien Poncet, Canada  
Volodymyr Ponomaryov, Mexico  
Jean-Christophe Ponsart, France  
Mauro Pontani, Italy  
Cornelio Posadas-Castillo, Mexico  
Francesc Pozo, Spain  
Christopher Pretty, New Zealand  
Luca Pugi, Italy  
Krzysztof Puszynski, Poland  
Giuseppe Quaranta, Italy  
Vitomir Racic, Italy  
Jose Ragot, France  
Carlo Rainieri, Italy  
Kumbakonam Ramamani Rajagopal, USA  
Ali Ramazani, USA  
Higinio Ramos, Spain  
Alain Rassinoux, France  
S.S. Ravindran, USA  
Alessandro Reali, Italy  
Jose A. Reinoso, Spain  
Oscar Reinoso, Spain  
Carlo Renno, Italy  
Fabrizio Renno, Italy  
Nidhal Rezg, France  
Ricardo Riaza, Spain  
Francesco Riganti-Fulginei, Italy  
Gerasimos Rigatos, Greece  
Francesco Ripamonti, Italy  
Jorge Rivera, Mexico  
Eugenio Roanes-Lozano, Spain  
Bruno G. M. Robert, France  
Ana Maria A. C. Rocha, Portugal  
José Rodellar, Spain  
Luigi Rodino, Italy  
Rosana Rodríguez López, Spain  
Ignacio Rojas, Spain  
Alessandra Romolo, Italy  
Debasish Roy, India  
Gianluigi Rozza, Italy  
Jose de Jesus Rubio, Mexico  
Rubén Ruiz, Spain  
Antonio Ruiz-Cortes, Spain  
Ivan D. Rukhlenko, Australia  
Mazen Saad, France  
Kishin Sadarangani, Spain  
Andrés Sáez, Spain  
Mehrddad Saif, Canada  
John S. Sakellariou, Greece  
Salvatore Salamone, USA  
Vicente Salas, Spain  
Jose Vicente Salcedo, Spain  
Nunzio Salerno, Italy  
Miguel A. Salido, Spain  
Roque J. Saltarén, Spain  
Alessandro Salvini, Italy  
Sylwester Samborski, Poland  
Ramon Sancibrian, Spain  
Giuseppe Sanfilippo, Italy  
José A. Sanz-Herrera, Spain  
Nickolas S. Sapidis, Greece

Evangelos J. Sapountzakis, Greece  
Luis Saucedo-Mora, Spain  
Marcelo A. Savi, Brazil  
Andrey V. Savkin, Australia  
Roberta Sburlati, Italy  
Gustavo Scaglia, Argentina  
Thomas Schuster, Germany  
Oliver Schütze, Mexico  
Lotfi Senhadji, France  
Junwon Seo, USA  
Joan Serra-Sagrsta, Spain  
Gerardo Severino, Italy  
Ruben Sevilla, UK  
Stefano Sfarra, Italy  
Mohamed Shaat, UAE  
Mostafa S. Shadloo, France  
Leonid Shaikhet, Israel  
Hassan M. Shanechi, USA  
Bo Shen, Germany  
Suzanne M. Shontz, USA  
Babak Shotorban, USA  
Zhan Shu, UK  
Nuno Simões, Portugal  
Christos H. Skiadas, Greece  
Konstantina Skouri, Greece  
Neale R. Smith, Mexico  
Bogdan Smolka, Poland  
Delfim Soares Jr., Brazil  
Alba Sofi, Italy  
Francesco Soldovieri, Italy  
Raffaele Solimene, Italy  
Jussi Sopenan, Finland  
Marco Spadini, Italy  
Bernardo Spagnolo, Italy  
Paolo Spagnolo, Italy  
Ruben Specogna, Italy  
Vasilios Spitas, Greece  
Sri Sridharan, USA  
Ivanka Stamova, USA  
RafaD StanisDawski, Poland  
Florin Stoican, Romania  
Salvatore Strano, Italy  
Yakov Strelniker, Israel  
Ning Sun, China  
Qiuye Sun, China  
Sergey A. Suslov, Australia  
Thomas Svensson, Sweden  
Andrzej Swierniak, Poland  
Andras Szekrenyes, Hungary  
Kumar K. Tamma, USA  
Yang Tang, Germany  
Hafez Tari, USA  
Alessandro Tasora, Italy  
Sergio Teggi, Italy  
Ana C. Teodoro, Portugal  
Alexander Timokha, Norway  
Gisella Tomasini, Italy  
Francesco Tornabene, Italy  
Antonio Tornambe, Italy  
Javier Martinez Torres, Spain  
Mariano Torrisi, Italy  
Sang-Bing Tsai, China  
George Tsiatas, Greece  
Antonios Tsourdos, UK  
Federica Tubino, Italy  
Nerio Tullini, Italy  
Andrea Tundis, Italy  
Emilio Turco, Italy  
Ilhan Tuzcu, USA  
Efstratios Tzirtzilakis, Greece  
Filippo Ubertini, Italy  
Francesco Ubertini, Italy  
Mohammad Uddin, Australia  
Hassan Ugail, UK  
Giuseppe Vairo, Italy  
Eusebio Valero, Spain  
Pandian Vasant, Malaysia  
Marcello Vasta, Italy  
Carlos-Renato Vázquez, Mexico  
Miguel E. Vázquez-Méndez, Spain  
Josep Vehi, Spain  
Martin Velasco Villa, Mexico  
K. C. Veluvolu, Republic of Korea  
Fons J. Verbeek, Netherlands  
Franck J. Vernerey, USA  
Georgios Veronis, USA  
Vincenzo Vespri, Italy  
Renato Vidoni, Italy  
V. Vijayaraghavan, Australia  
Anna Vila, Spain  
Rafael J. Villanueva, Spain  
Francisco R. Villatoro, Spain  
Uchechukwu E. Vincent, UK  
Gareth A. Vio, Australia  
Francesca Vipiana, Italy  
Stanislav Vitek, Czech Republic  
Thuc P. Vo, UK  
Jan Vorel, Czech Republic  
Michael Vynnycky, Sweden  
Hao Wang, USA  
Liliang Wang, UK  
Shuming Wang, China  
Yongqi Wang, Germany  
Roman Wan-Wendner, Austria  
Jaroslaw Wąs, Poland  
P.H. Wen, UK  
Waldemar T. Wójcik, Poland  
Changzhi Wu, China  
Desheng D. Wu, Sweden  
Yuqiang Wu, China  
Michalis Xenos, Greece  
Guangming Xie, China  
Xue-Jun Xie, China  
Gen Q. Xu, China  
Hang Xu, China  
Joseph J. Yame, France  
Xinggang Yan, UK  
Jixiang Yang, China  
Mijia Yang, USA  
Yongheng Yang, Denmark  
Luis J. Yebra, Spain  
Peng-Yeng Yin, Taiwan  
Yuan Yuan, UK  
Qin Yuming, China  
Elena Zaitseva, Slovakia  
Arkadiusz Zak, Poland  
Daniel Zaldivar, Mexico  
Francesco Zammori, Italy  
Vittorio Zampoli, Italy  
Rafal Zdunek, Poland  
Ibrahim Zeid, USA  
Hao Zhang, China  
Haopeng Zhang, USA  
Huaguang Zhang, China  
Kai Zhang, China  
Qingling Zhang, China  
Xianming Zhang, Australia  
Xuping Zhang, Denmark  
Zhao Zhang, China  
Yifan Zhao, UK  
Jian G. Zhou, UK



---

Quanxin Zhu, China  
Mustapha Zidi, France  
Gaetano Zizzo, Italy

Zhixiang Zou, Germany  
J. A. Fonseca de Oliveira Correia, Portugal  
M. do Rosário de Pinho, Portugal

Chaudry M. Khalique, South Africa

# Contents

## **Advanced Mathematical and Numerical Methods in Control and Optimization for Smart Grids**

Zhan Shu , Michael Z. Q. Chen , and Qing Hui

Editorial (2 pages), Article ID 2074019, Volume 2019 (2019)

## **Abnormal Detection of Wind Turbine Based on SCADA Data Mining**

Liang Tao , Qian Siqi, Yingjuan Zhang, and Huan Shi

Research Article (10 pages), Article ID 5976843, Volume 2019 (2019)

## **Emulator Based on Switching Functions for a Dual Interleaved Buck-Boost Converter**

Marco Antonio Sánchez Vázquez , Ismael Araujo-Vargas , and Kevin Cano-Pulido

Research Article (10 pages), Article ID 5930548, Volume 2019 (2019)

## **Operation of Parallel Inverters in Microgrid Using New Adaptive PI Controllers Based on Least Mean Fourth Technique**

A. Elnady  and M. AlShabi

Research Article (19 pages), Article ID 4854803, Volume 2019 (2019)

## **Modeling and Analysis of Progressive Ice Shedding along a Transmission Line during Thermal De-Icing**

Yunyun Xie , Linyan Huang, Da Wang, Huaiping Ding, and Xiaochun Yin

Research Article (12 pages), Article ID 4851235, Volume 2019 (2019)

## **Distributed Learning Algorithms and Lossless Convex Relaxation for Economic Dispatch with Transmission Losses and Capacity Limits**

Kwang-Ki K. Kim 

Research Article (11 pages), Article ID 9159851, Volume 2019 (2019)

## **Noninvasive Vehicle-to-Load Energy Management Strategy to Prevent Li-Ion Batteries Premature Degradation**

Martín-Antonio Rodríguez-Licea , Francisco-J. Perez-Pinal , Allan-Giovanni Soriano-Sánchez , and José-Antonio Vázquez-López

Research Article (9 pages), Article ID 8430685, Volume 2019 (2019)

## **Model Predictive Control of Electric Spring for Voltage Regulation and Harmonics Suppression**

Yun Zou , Yinlong Hu , and Sifan Cao

Research Article (8 pages), Article ID 7973591, Volume 2019 (2019)

## Editorial

# Advanced Mathematical and Numerical Methods in Control and Optimization for Smart Grids

Zhan Shu <sup>1</sup>, Michael Z. Q. Chen <sup>2</sup> and Qing Hui<sup>3</sup>

<sup>1</sup>Engineering and Physical Sciences, University of Southampton, Southampton, UK

<sup>2</sup>School of Automation, Nanjing University of Science and Technology, Nanjing, China

<sup>3</sup>University of Nebraska-Lincoln, Lincoln, USA

Correspondence should be addressed to Zhan Shu; [z.shu@soton.ac.uk](mailto:z.shu@soton.ac.uk)

Received 18 August 2019; Accepted 20 August 2019; Published 15 September 2019

Copyright © 2019 Zhan Shu et al. This is an open access article distributed under the Creative Commons Attribution License, which permits unrestricted use, distribution, and reproduction in any medium, provided the original work is properly cited.

While renewable energy, as a part of smart-grid technologies, brings clean energy, it also brings a series of power quality problems. An increasing number of power electronic devices and new smart-grid technologies are used to ensure a safe, reliable, and high-quality operation of the power grid. However, the effectiveness of these control devices and technologies largely depends on the accuracy of the model, the advancement of control methods, and the numerical optimization of the parameters.

This special issue focuses on recent advances in modeling, numerical analysis, control, and optimization of smart grids with some special emphasis on the mathematical problems encountered at any stage of power grid operation. It contains seven papers, the contents of which are summarized as follows.

In the study of numerical analysis and optimization operation of a smart grid, L. Tao et al. use the genetic algorithm and cross-validation method to optimize the parameters of the support vector regression (SVR) model from the SCADA (Supervisory Control and Data Acquisition) system to realize the wind turbine condition monitoring in “Abnormal Detection of Wind Turbine Based on SCADA Data Mining.” K.-K. K. Kim considers problems of economic dispatch in power networks that contain independent power generation units and loads in “Distributed Learning Algorithms and Lossless Convex Relaxation for Economic Dispatch with Transmission Losses and Capacity Limits.”

In the area of modeling and analysis of smart grids, M. A. S. Vázquez et al. propose the use of switching functions for the modeling of power converters of a hybrid

power system (HPS), allowing the reduction of hardware resources of the FPGA in “Emulator Based on Switching Functions for a Dual Interleaved Buck-Boost Converter.” A mechanical model of progressive ice shedding (PIS) to analyze PIS during thermal de-icing to ensure the security of transmission lines is established by Y. Xie et al. in “Modeling and Analysis of Progressive Ice Shedding along a Transmission Line during Thermal De-Icing.”

Regarding control methods of smart grids, M. A. Rodríguez-Licea et al. propose an energy management strategy (EMS) that operates autonomously and non-invasively as an additional layer to the battery management system (BMS) to increase the life expectancy of the Li-ion battery bank in “Noninvasive Vehicle-to-Load Energy Management Strategy to Prevent Li-Ion Batteries Premature Degradation.” A model predictive control (MPC) strategy is presented by Y. Zou et al. for electric spring (ES) to address the power quality problems, especially the voltage regulation and harmonic suppression in “Model Predictive Control of Electric Spring for Voltage Regulation and Harmonics Suppression.” A. Elnady and M. AlShabi show the operation of a microgrid using a new adaptive PI controller-based operational (control) scheme for voltage amplitude and frequency stability in “Operation of Parallel Inverters in Microgrid Using New Adaptive PI Controllers Based on Least Mean Fourth Technique.”

We would like to thank all the authors for their contributions and acknowledge all the reviewers for their time and effort devoted to assessing the manuscripts. We also thank the Editor-in-Chief and the Editorial Office of the

Mathematical Problems in Engineering, without which the completion of this project would not have been possible.

### **Conflicts of Interest**

The guest editors declare that they do not have conflicts of interest regarding the publication of the special issue entitled “Advanced Mathematical and Numerical Methods in Control and Optimization for Smart Grids.”

*Zhan Shu*  
*Michael Z. Q. Chen*  
*Qing Hui*

## Research Article

# Abnormal Detection of Wind Turbine Based on SCADA Data Mining

Liang Tao , Qian Siqi, Yingjuan Zhang, and Huan Shi

Hebei University of Technology, College of Artificial Intelligence and Data Science, Tianjin, China

Correspondence should be addressed to Liang Tao; 54008214@qq.com

Received 29 March 2019; Revised 20 June 2019; Accepted 25 June 2019; Published 7 August 2019

Guest Editor: Michael Z. Q. Chen

Copyright © 2019 Liang Tao et al. This is an open access article distributed under the Creative Commons Attribution License, which permits unrestricted use, distribution, and reproduction in any medium, provided the original work is properly cited.

In order to reduce the curse of dimensionality of massive data from SCADA (Supervisory Control and Data Acquisition) system and remove data redundancy, the grey correlation algorithm is used to extract the eigenvectors of monitoring data. The eigenvectors are used as input vectors and the monitoring variables related to the unit state as output vectors. The genetic algorithm and cross validation method are used to optimize the parameters of the support vector regression (SVR) model. A high precision prediction is carried out, and a reasonable threshold is set up to alarm the fault. The condition monitoring of the wind turbine is realized. The effectiveness of the method is verified by using the actual fault data of a wind farm.

## 1. Introduction

SCADA system changes the operation mode of wind farm systems with healthy working environment and reduces the costs of operation and maintenance. However, a large set of high dimensions and many types of data are not fully utilized or developed; only stay on real-time data and historical data reporting statistics are typically monitored or gathered. Therefore, it is important to make full use of the data collected by wind power centralized control center to collect the data of the massive wind turbines, conduct state monitoring of the turbines, and predict their condition and life [1, 2]. Several surveys of WT failures have been conducted in the last two decades to identify failure rates and associated downtime for different subassemblies. However, the different taxonomies used by different turbine manufacturers, wind farm operators, and researchers make comparisons between these surveys challenging. The evaluation of 15 years of data from the German “250 MW Wind” programme [3] and >95% of all the turbines operating between 1997 and 2005 in Sweden [4] gave first insights into the reliability of the first onshore WTs. The German turbines had an average availability of about 98%. An average failure rate of 0.4 failures per turbine per year resulted in an average downtime of 130 hours per turbine per year for the Swedish turbines. A distinctive difference between failure

rate and downtime distribution in subassembly groups was identified. The electrical and electronic control systems were identified as the most failure-prone, but gearbox and generator failures caused the longest downtime.

Many scholars have researched large power wind turbine monitoring and fault diagnoses [5], based on statistical learning method to detect abnormal situations through the wind turbine response model of the weighted least squares support vector-based wind power generator and external regression conditions [6]. The results show that the model is better than conventional forecasting methods. Pandit and Infield [7] used an in-depth analysis of commonly used stationary covariance functions in which wind turbine power curve was used, where GP-based power curve was constructed using different stationary covariance functions, and after that, a comparative analysis was carried out in order to identify the most effective covariance function. The commonly used squared exponential covariance function is taken as the benchmark, against which other covariance functions are assessed. The results show that the performance (in terms of model accuracy and uncertainty) of GP fitted power curve models based on rational quadratic covariance functions is almost the same as for the most commonly used squared exponential function. The studies of Astolfi et al. [8, 9] are a catalog of generalizable methods

for studying wind turbine power curve upgrades. In particular, from the study of the selected test cases, it arises that complex wind conditions might affect wind turbine operation such that the production improvement is non-negligibly different from what can be estimated under the hypothesis of ideal wind conditions. Wan et al. [10] proposed wind farm using wavelet based on energy function for asymmetrical fault detection in doubly fed induction generator. The proposed method not only detects the fault within one and half cycle of fundamental wave but also reveals the effectiveness under time-varying conditions. Turbine condition monitoring (TCM) through vibration analysis has pros and cons: basically high diagnostic power against high cost and high complexity for elaborating the information [11] from the data stream into knowledge. Chun-yu et al. [12] put forward a dynamic prediction model of wind turbine blade failure based on the grey theory. The relative error between prediction and field investigation data is less than 5%, meeting the actual needs of engineering and verifying the effectiveness and applicability of the proposed algorithm. The main contribution of Chakkor et al. [13] is designing an intelligent wireless remote monitoring and control system according to features and requirements of wind turbines. This system based on *IP* communication combines *Web* and database client/server technology to copy data measurements received from the different sensors installed in the wind turbine machines. Eggers et al. [14] used *Hotelling T2* control chart and an automatic relevance neural network to analyze the wind turbine power to identify wind turbine detection faults. Zhang [15], combined with *AHP* and variable weight theory, used a wind turbine performance evaluation model based on *Grey Theory* and a variable weight fuzzy comprehensive evaluation. However, these studies did not consider the correlation and coupling between the components of the unit, which makes the model inaccurate. Zhang et al. [16], based on SVR prediction model, helped to establish a prediction model, which takes the amount of SCADA systems as input and the active power of the unit as output. The disadvantage of this model is that the feature extraction of the high-dimensional input vectors is not easy, and the power is used as the only standard to diagnose the state of the unit. BP neural network is used to model and predict gearbox and generator [17], and multiagent method is used to synthetically analyze the diagnosis results of different components, giving the overall operation status of the unit. However, the use of neural network modelling requires time-consuming learning process, and the selection of learning samples lacks basis.

Being based on statistical analysis, it commonly requires vast datasets for providing meaningful indications: the most common opinion therefore is that SCADA can detect incipient faults at a late stage. Astolfi et al. [18] employed artificial neural networks, for their capability in reconstructing nonlinear dependency between inputs and outputs, and formulated simple models for the diagnosis of occurring faults at the level of gearbox. The datasets employed have the 10-minute sampling time of the common SCADA control systems; the gearbox vibrations and the gearbox temperatures are selected as target output to model.

It will be shown that the time resolution of SCADA is too coarse for reliable vibration analysis, which should be rather observed at its proper time scale (several Hz). At present, data mining methods such as clustering and statistical model are widely used in domestic and foreign enterprises, but their cleaning process is complicated and the cleaning conditions are harsh [19]. Therefore, in order to make a reliable analysis of the power generation performance of wind turbines, an efficient and versatile cleaning method is urgently needed.

In view of this, this paper firstly extracts the features from the massive and high-dimensional data collected by the SCADA system, removes the irrelevant and redundant parameters of the operation state of the unit, and improves the monitoring accuracy of the wind turbine by improving the model input. The reasonable threshold is selected to alarm the abnormal state of wind turbine to avoid false alarm and untimely alarm.

The paper is organized in three sections. Section 2 discusses feature selection and sparse learning technology to reduce the dimension of the operation parameters of the SCADA system, remove the independent and redundant parameters of the operating state of the wind turbine, and retain the related characteristic parameters. In Section 3, the multi-input and multi-output SVR model, which takes the active power, the speed of the blade, and the pitch 1 angle as the output vector and the characteristic parameter as the input vector, is established. Cross validation (CV) is combined with a genetic algorithm (GA) for parameter optimization. In Sections 4 and 5, the proposed method is applied to the industrial data. Performance of the proposed model is also discussed. Section 6 concludes the paper.

## 2. Data Mining of Characteristic Parameters for Wind Turbines

The data collected and recorded by the SCADA system of the wind turbine has high-dimensional characteristics. In this paper, 74 digits of the wind turbine components are selected. The method of feature parameter data mining reduces the number of features and dimension disaster so that the generalization ability of the model is stronger and the overfitting phenomenon is reduced. The commonly used methods for selecting characteristic parameters include principal component analysis (*PCA*) [20], the Pearson correlation coefficient [14], and the random forest method [21]. When the data are high-dimensional vectors, the calculation of *PCA* is complicated and it is most suitable for linear data. Pearson correlation coefficient is only sensitive to the disadvantages of the most obvious linear relationship. The random forest method is prone to an overfitting phenomenon. Therefore, in this paper, a data mining algorithm based on the grey correlation degree [22] is proposed to overcome the above shortcomings and to improve the accuracy and effectiveness of wind turbine operation state assessments.

*2.1. Extraction of the Characteristic Parameters Based on Grey Relational Grade.* There are 74 variables in wind turbine information recorded by the SCADA system. The acquisition interval is 10 minutes, as shown in Figure 1. Figure 1

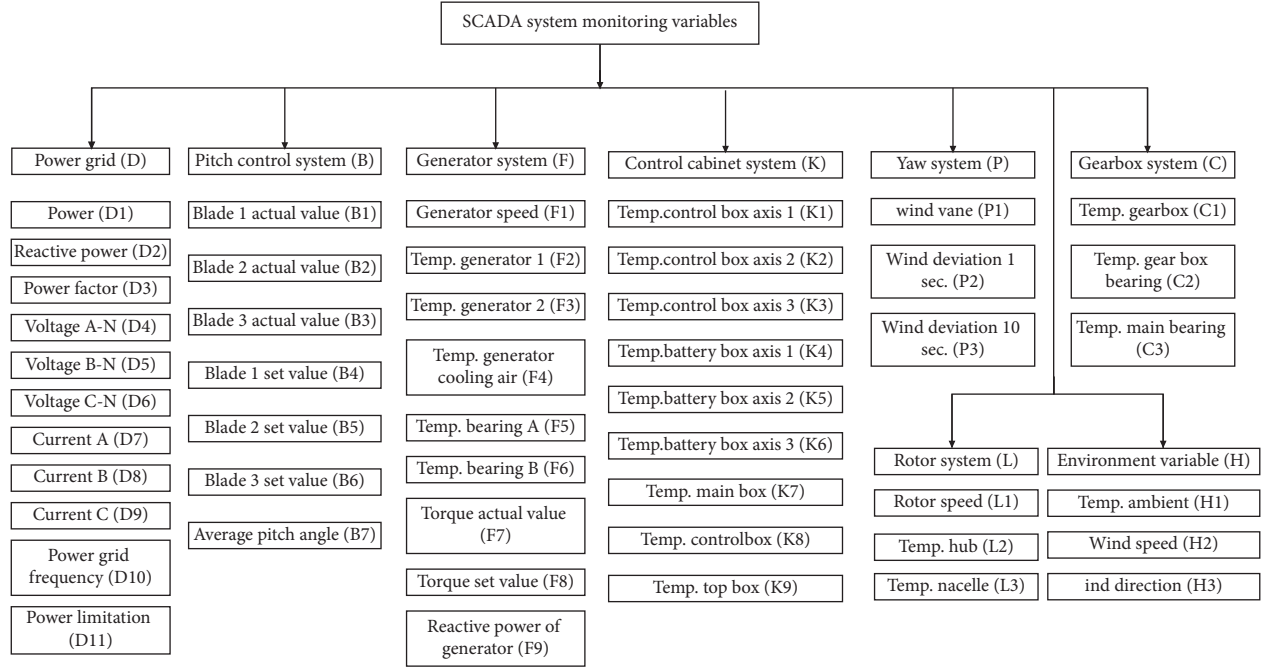


FIGURE 1: Monitoring variables and numbers of SCADA system.

shows the monitoring variables collected by the wind turbine SCADA system and its response code. The object of study in this paper is that the wind turbines are in the condition of unlimited power and healthy operation. They have some monitoring quantities such as the control mode and alarm of some parameters recorded in the SCADA system, speed mode, state of shaft 1, shaft 2, and shaft 3 converters, etc. Variables in an invariant state can be ignored. Table 1 is part of the parameter alarm information of GE wind turbine manufacturer. To preprocess these eigenvectors, we must remove these eigenvectors to avoid the disaster of dimensionality caused by too many features.

Wind turbine operation is mainly reflected in active power, rotor speed, and pitch angle; these three parameters are used as input vectors. We take the pitch angle 1 as an example to monitor the pitch angle. The grey correlation with other variables is calculated to reduce the wind turbine data dimension while ensuring the smallest loss of information. The concrete steps of extracting the operating characteristic parameters using the grey correlation degree are as follows:

- (1) The characteristic set of the wind turbine operating state  $D$  is  $D = [p_1, p_2, \dots, p_m]$ .
- (2) According to the parameters of the primary wind turbine  $D$ , the corresponding parameters are extracted from the SCADA system as the sample set of the grey correlation degree  $\Omega$ :

$$\Omega = \begin{bmatrix} x_{11} & x_{12} & \cdots & x_{1n} \\ \vdots & \vdots & \cdots & \vdots \\ x_{m1} & x_{m2} & \cdots & x_{mn} \end{bmatrix}, \quad (1)$$

where  $x_{mm}$  is the  $n$  parameter of the  $m$  samples. The degree of correlation between the calculated parameters is found as follows.

TABLE 1: Alarm information of some parameters of wind turbine.

| Alarm information                                    |
|--|
| Latest(=n) alarm coming from the frequency converter |
| $n-1$ alarm coming from the frequency converter      |
| $n-2$ alarm coming from the frequency converter      |
| $n-3$ alarm coming from the frequency converter      |

Determine the reference sequence  $X_0$  and the comparison sequence  $X_i (i = 1, 2, \dots, m)$  according to the training sample  $\Omega$ .

The absolute difference  $X_i$  between  $X_0$  and sequences  $\Omega$  is calculated from the sample set as

$$\Delta_i(k) = |x_0(k) - x_i(k)|, \quad i = 1, 2, \dots, n. \quad (2)$$

The absolute difference  $\Delta_i$  is used to calculate the maximum difference and minimum difference of level two, respectively, as

$$M = \max_i \max_k \Delta_i(k),$$

$$N = \min_i \min_k \Delta_i(k). \quad (3)$$

$X_0$  is calculated, and the sequence  $X_i$  in the moment of  $k$  for correlation coefficient  $r_{0i}(k)$  is compared by

$$r_{0i}(k) = \frac{N + \xi M}{\Delta_i(k) + \xi M}, \quad \xi \in (0, 1); k = 1, 2, \dots, n; i = 1, 2, \dots, m,$$

$$r_{0i} = \frac{1}{n} \sum_{k=1}^n r_{0i}(k), \quad i = 1, 2, \dots, m. \quad (4)$$

2.2. Mining of Characteristic Parameter Data of Wind Turbines. The grey correlation analysis mentioned above is

applied to 1.6 MW wind turbines. By preprocessing the eigenvectors, 23 variables related to the operating state of the wind turbine are selected, and the values of these variables are extracted from the SCADA system. Based on operational data from January 1, 2015, to January 1, 2017, the sample set features selected by grey correlation analysis and the characteristic parameters of the grey correlation matrix for color map are as shown in Figure 2. According to Figure 1, the grey correlation degree between each primary parameter of the power, rotor speed, and pitch angle is different, which makes it feasible to excavate the characteristic parameters of the generator set. In this paper, variables with correlation degree greater than 0.5 are selected as input of monitoring variables. The set of characteristic parameters is shown in Tables 2–4.

### 3. Prediction Model Based on Support Vector Regression

After the data effectiveness analysis and dimensionality reduction are conducted, the parameters of the wind turbine are regressed. SVR [23] algorithm of structural risk minimization criterion solves the practical problems of small sample, non-linearity, and high dimension and overcomes the shortcomings of the indetermination of the network structure and local minima, over learning and under learning. Therefore, this paper chooses SVR algorithm to build regression prediction model. The specific algorithm is as follows.

Set a given sample training set for  $(x_i, y_i) i = 1, 2, \dots, l, x \in R^l, y \in R, x_i$  is the  $i$  input vector, and  $y_i$  is the  $i$  output vector. Nonlinear mapping should be used for the nonlinear SVR model  $\varphi(\cdot)$ . The mapping sample sets are used to feature spaces  $\varphi(x_i)$ . The optimal decision function is as follows:

$$f(x) = w^T \cdot \varphi(x) + b, \quad (5)$$

$$\begin{aligned} \min & \frac{1}{2} \sum_{i=1, j=1}^l (\alpha_i - \tilde{\alpha}_i)(\alpha_j - \tilde{\alpha}_j)(\varphi(x_i) \cdot \varphi(x_j)) + \sum_{i=1}^l (\alpha_i - \tilde{\alpha}_i)y_i - \sum_{i=1}^l (\alpha_i + \tilde{\alpha}_i)\varepsilon, \\ \text{s.t.} & \begin{cases} \sum_{i=1, j=1}^l (\alpha_i - \tilde{\alpha}_i) = 0, \\ \alpha_i - \tilde{\alpha}_i \in [0, C]. \end{cases} \end{aligned} \quad (8)$$

Using the positive definite matrix theorem, the  $\varphi(x_i)\varphi(x_j)$  inner product is replaced by a kernel function  $k(x_i, x_j)$ . Therefore, the SVR function can be obtained as follows:

$$f(x) = \sum_{i=1}^l (\alpha_i - \tilde{\alpha}_i)k(x_i, x_j) + b. \quad (9)$$

In the kernel function, the structure of the radial basis function (RBF) kernel is simple, and its generalization ability

where  $w^T$  is the characteristic space weight coefficient vector and  $b$  is the bias. It is assumed that all training samples can be in precision with linear functions at  $\varepsilon$  accuracy. According to the principle of structural risk minimization, the problem can be formulated as

$$\begin{aligned} \min & \frac{1}{2} w^T w + c \sum_{i=1}^l (\xi_i + \tilde{\xi}_i), \\ \text{s.t.} & \begin{cases} y_i - f(x_i) \leq \varepsilon + e_i, \\ f(x_i) - y_i \leq \varepsilon + e_i, \\ \xi_i \geq 0, \\ \tilde{\xi}_i, \quad i = 1, \dots, l, \end{cases} \end{aligned} \quad (6)$$

where  $\tilde{\xi}_i$  is the relaxation factor. Introducing the Lagrange function, the optimization problem in the dual space is used to obtain the following formula:

$$\begin{aligned} L(w, b, e, \alpha) = & \frac{1}{2} w^T w + c \sum_{i=1}^l (\xi_i + \tilde{\xi}_i) - \sum_{i=1}^l \alpha_i [\xi_i + \varepsilon - y_i + f(x_i)] \\ & - \sum_{i=1}^l \tilde{\alpha}_i [\tilde{\xi}_i + \varepsilon - y_i + f(x_i)] - \sum_{i=1}^l (\xi_i \gamma_i + \tilde{\xi}_i \hat{\gamma}_i), \end{aligned} \quad (7)$$

where  $\alpha_i, \tilde{\alpha}_i, \gamma_i$ , and  $\hat{\gamma}_i$  are the Lagrange multipliers and  $c$  is the penalty factor respective to  $w, b, \xi$ , and  $\alpha$ . Find the partial derivative and make it equal to 0 and bring the derivative into the Lagrange function:

is better. Based on this, the kernel function of the model is selected as the radial basis function.  $k(x_i, x_j) = \exp(-\|x_i - x_j\|^2/2\sigma^2)$ , where  $\sigma$  is the kernel width.

**3.1. Genetic Algorithm (GA).** In this model, the penalty coefficient and parameter of the kernel function affect the SVR precision. Therefore, GA is used to optimize the parameters of the SVR model, which is based on the natural selection and genetic mechanism of the theory of biological

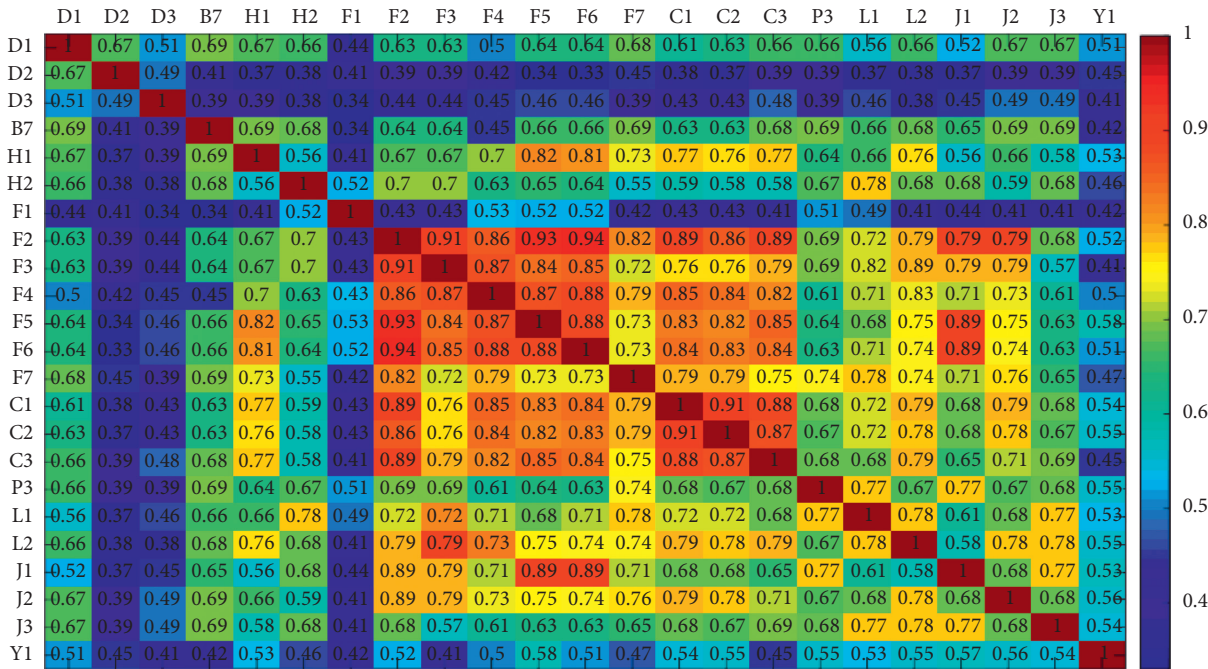


FIGURE 2: Feature parameters of the grey correlation degree color map.

TABLE 2: Feature parameters' code of power prediction.

|                      |   |
|----------------------|---|
| Pitch system         | Average pitch angle   |
| Gearbox              | Temp. gearbox, temp. gearbox bearing, temp. shaft bearing   |
| Power grid           | Reactive power  |
| Generator            | Temp. generator 1, temp. generator 2, generator speed (CCU), generator speed (PLC), temp. generator cooling air |
| Environment variable | Temp. ambient, wind speed   |
| Nacelle              | Temp. nacelle, nacelle revolution   |
| Rotor system         | Rotor speed (PLC), temp. hub  |
| Yaw system           | Wind deviation 10 sec.  |

TABLE 3: Feature parameters' code of rotor speed prediction.

|                      |   |
|----------------------|---|
| Gearbox              | Temp. gearbox, temp. gearbox bearing, temp. shaft bearing   |
| Power grid           | Reactive power  |
| Generator            | Temp. generator 1, temp. generator 2, generator speed (CCU), generator speed (PLC), temp. generator cooling air |
| Environment variable | Temp. ambient, wind speed   |
| Nacelle              | Temp. nacelle, tower acceleration, nacelle position   |
| Rotor system         | Rotor speed (PLC), temp. hub  |
| Wind deviation       | Wind deviation 10 sec.  |

TABLE 4: Feature parameters' code of pitch 1 angle prediction.

|                      |   |
|----------------------|---|
| Pitch system         | Collective actual (measured) pitch angle  |
| Gearbox              | Temp. gearbox, temp. gearbox bearing, temp. shaft bearing   |
| Power grid           | Reactive power  |
| Generator            | Temp. generator 1, temp. generator 2, generator speed (CCU), generator speed (PLC), temp. generator cooling air |
| Environment variable | Temp. ambient, wind speed   |
| Nacelle              | Temp. nacelle, nacelle revolution   |
| Rotor system         | Rotor speed (PLC), temp. hub  |
| Yaw system           | Wind deviation 1 sec., wind deviation 10 sec.   |

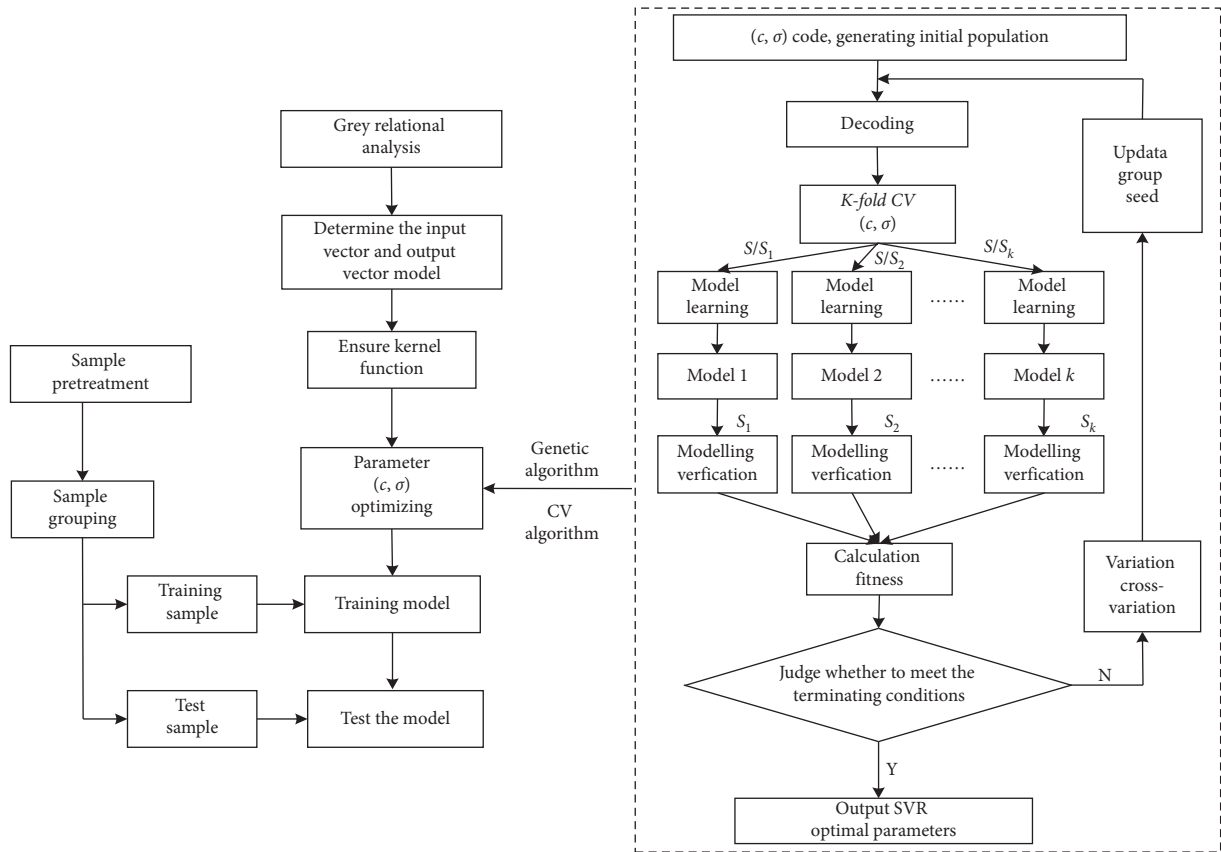


FIGURE 3: Flow chart of the model.

evolution by Darwin [24] to find the optimal solution. The main process is to encode the solution to the problem. There are two ways to code the solution individually, including binary coding and real number coding, which essentially maps the solution space to the chromosome space. Then, a reasonable initial population is generated in these solution spaces, and individuals are selected according to fitness function, genetic selection, crossover, and mutation operation. The individual with high fitness value is kept and vice versa. This new generation of offspring retains the advantages of the previous generation, whereas the last generation did not. This process is iterated many times until the optimal solution is obtained.

**3.2. Cross Validation (CV).** In machine learning, CV is mainly used for model performance evaluation and learning. The basic principle is that the original sample is divided into a training set and a validation set, and then the training set is used to train the model. The model validated by the test set is obtained from the training model. As a performance index evaluation model, CV considers the training error as well as the generalization error. The most common CV method is  $k$ -folding cross validation ( $K$ -fold CV), and the specific algorithms are as follows:

- (1) The sample  $S$  are divided into  $k$  subsets that are not intersected, and the number of samples is  $m/k$ .  $S_1, S_2, \dots, S_k$  are remembered.

- (2) For each model  $M_i (i = 1, \dots, k)$ , do the following. Training set  $S_1 \cup \dots \cup S_{j-1} \cup S_{j+1} \cup \dots \cup S_k$  and model  $M_i$ . Get the corresponding hypothesis function  $h_{ij}$ . Validation set  $S_j$  is used to calculate the generalization error  $\hat{\varepsilon}_{S_j}(h_{ij})$ .
- (3) The average generalization error of each model is calculated, and the model with the least generalization error  $M_i$  is selected.

**3.3. SVR Parameter Selection Based on CV and GA.** The selection of the parameters of the SVR model is essentially the optimization of the model. The algorithm of  $K$ -fold CV and GA is used to optimize the parameters of SVR, and  $k = 3, 5, 8, 10$ . The model as shown in Figure 3 is as follows:

- (1) The SVR parameters  $(c, \sigma)$  are coded to form the initial population.
- (2) For population decoding, we calculate the fitness of individuals based on the  $K$ -fold CV method. In this paper,  $\hat{\varepsilon}_{S_j}(h_{ij})$ , the minimum mean square error  $MSE$  of samples  $(c, \sigma)$ , is chosen as the fitness function value of the GA algorithm.
- (3) Judge whether or not to meet the terminating condition if it is satisfied to turn (5); otherwise, proceed to (4).
- (4) Update the population by selection, cross, and variation; then, return to (2).
- (5) The optimal  $(c, \sigma)$  and optimal model is output.

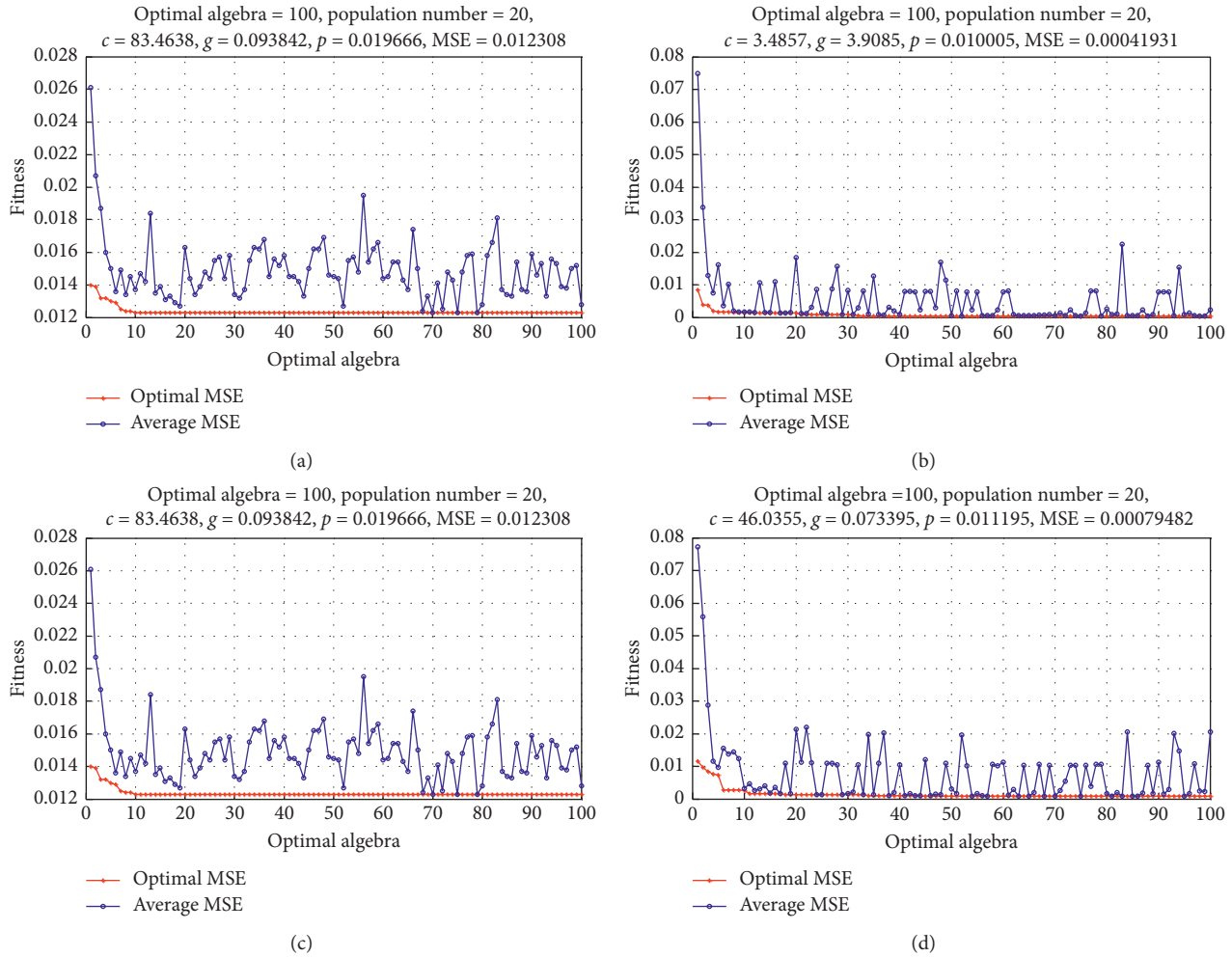


FIGURE 4: (a) 3-CV MSE of SVR model. (b) 5-CV MSE of SVR model. (c) 8-CV MSE of SVR model. (d) 10-CV MSE of SVR model.

#### 4. Condition Monitoring Based on SVR Parameter Optimization

4.1. *Data Processing.* In this paper, power, rotor speed, and pitch angle are taken as the output vectors and other feature parameters are taken as input vectors, and then multiple-input and multiple-output SVR model is established. The accuracy of the proposed model is verified by running data of the wind turbine for four months.

- (1) According to the fault information recorded by the SCADA system, the samples of the maintenance shutdown due to the failure of the wind turbine and the samples of the less power operation are eliminated.
- (2) Consider that the cutting wind speed is 3 m/s, the rated wind speed is 12 m/s, and the cutting wind speed is 25 m/s. According to the actual power curve of wind turbine, the wind speed range selected in this paper is 3 to 25.
- (3) To eliminate the magnitude of interference between the parameters, the parameters are normalized to [0, 1], according to the dimensions.

4.2. *Model Establishment.* In order to prove the validity of the model, this paper selects four months effective data of wind turbine to predict. In this model, the principle of cross validation selection first considers the minimum error MSE. According to the errors of MSE, to avoid the occurrence of the learning state, a group of smaller penalty parameters is selected as the best parameter. From Figure 4, we can see that 5-CV and GA model are the best. The average fitness curve in Figure 4 indicates the average fitness of all the individuals in each generation. The best fitness curve represents the maximum fitness of all individuals in each generation. The convergence of the fitness curve is very fast, and the convergence level of the final fitness curve is relatively consistent, which reflects the optimization of SVR parameters. When the power, rotor speed, and pitch angle are output, the best parameter is applied to the SVR model. The comparison between the actual and predicted values of the SVR model is shown in Figure 5. Table 5 lists the power, rotor speed, and pitch error. The mean relative error values indicating the good prediction accuracy and stability of the SVR model CV-GA algorithm is shown in Table 5.

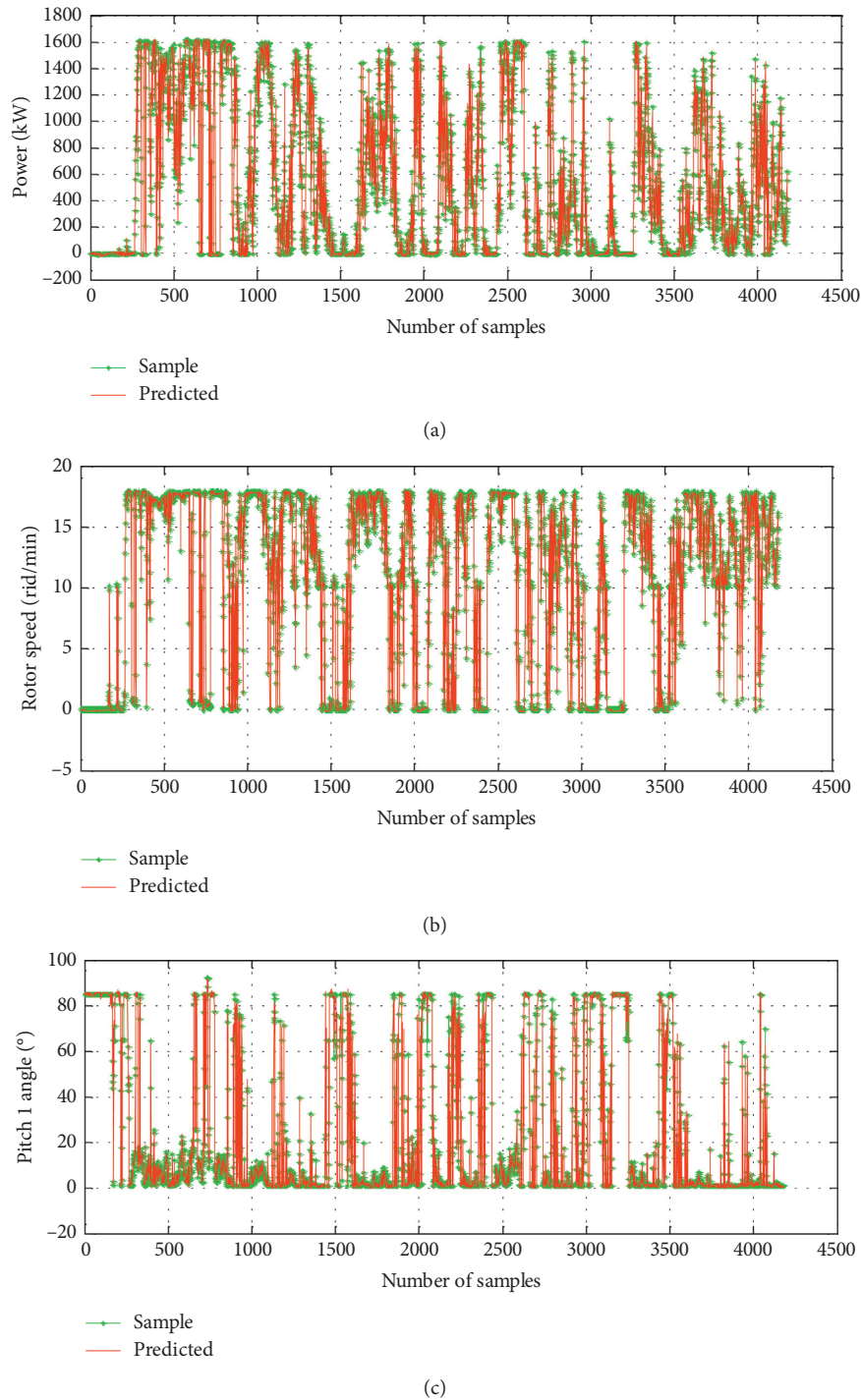


FIGURE 5: (a) Predicted and actual values of power. (b) Predicted and actual values of rotor. (c) Predicted and actual values of pitch 1 angle.

*4.3. Discriminating the Health Status of Wind Turbine Based on Threshold.* According to the trained SVR model, the observed values of power, rotor speed, and pitch angle can be obtained from the current input vector, and the distance between the measured value and the observed value extracted from SCADA system is  $\delta$ . According to the distance between the measured value and the observed value,

TABLE 5: Errors of the SVR model.

| SVR model              | Power (%) | Rotor speed (%) | Pitch angle (%) |
|------------------------|-----------|-----------------|-----------------|
| Maximum relative error | 10.36     | 11.87           | 11.95           |
| Minimum relative error | 0.49      | 0.91            | 0.51            |
| Mean relative error    | 3.01      | 4.95            | 3.73            |

TABLE 6: Operational conditions for the wind turbine with different distance thresholds.

| Threshold $\nu$ | Leakage rate (%) | False positive (%) |
|-----------------|------------------|--------------------|
| 0.04            | 0                | 92                 |
| 0.06            | 3                | 86                 |
| 0.08            | 7                | 72                 |
| 0.1             | 10               | 41                 |
| 0.12            | 12               | 33                 |
| 0.14            | 15               | 24                 |
| 0.16            | 16               | 12                 |
| 0.18            | 28               | 11                 |
| 0.2             | 37               | 8                  |
| 0.22            | 52               | 5                  |

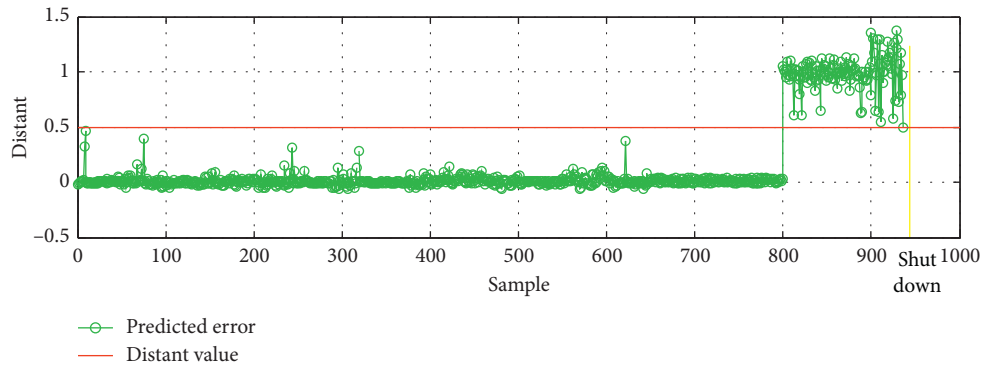


FIGURE 6: Distance between the predicted and actual values.

the threshold  $\nu$  is compared with the set threshold to distinguish the operating state of the wind turbine. The distance from the observed value to the measured value in the SCADA system is defined as

$$\delta = \frac{|\alpha_j - \alpha'_j|}{\alpha_j} \quad (10)$$

If  $\nu$  is selected too low, the algorithm is too sensitive to the change of the operating state of the wind turbine and it is prone to misjudge the results. If  $\nu$  selection is too large, the prediction time will be reduced and the detection rate of the abnormal operating state will be affected. To solve this problem, it is necessary to select the appropriate threshold  $\nu$ . In this paper, two-year SCADA data of the 1.6 MW wind turbine is analyzed, and the appropriate threshold is determined. From Table 5, it can be seen that threshold selection will cause the operating state of the wind turbine to not be normally recognized. To find a lower detection rate and the misjudgment rate, the threshold is selected as  $\nu = 0.16$  (in Table 6).

### 5. Example Analysis

At 5:32 on August 7, 2016, a wind turbine in Hebei Province went into shutdown due to the SCADA system failure alarm. After checking the pitch gear of blade 1 of the wind turbine, the wind turbine went into shutdown due to failure. 950 sets of data were extracted from the SCADA system before the blower alarm stopped. 950 sets of collected data are input

into the model, as shown in Figure 6. As can be seen from the figure, close to 150 data points were detected as abnormal points before the wind turbine shut down. The situation of power restriction indicates that some of the wind turbines have begun to deteriorate at these times, and the unit has issued abnormal alarms. The reduced power generated by the unit indicates that the model can give a hint before the failure occurs. Therefore, the proposed model is effective for the state monitoring and fault prediction of the wind turbine, and it can avoid the continued deterioration of the fault and the influence on the safe operation of the power grid.

### 6. Conclusion

In order to extract relevant state from massive and high-dimensional data of the SCADA system, realizing the monitoring of the state of the wind turbine, a grey correlation degree is proposed based on data mining technology to extract characteristic parameters of the wind turbine's operating state, which reduces the data dimensions and computation. To improve the precision, GA and CV are combined to optimize the parameters of the regression model. To verify the validity of the model, the threshold of the SVR model is analyzed, and the model is applied to wind farm. The results show the following:

- (1) By establishing a data mining model of the characteristic parameters based on the grey correlation analysis, we extract parameters that are more related to the power, rotor speed, and pitch angle, effectively avoiding "dimension disaster."

- (2) By comparing the power, rotor speed, pitch angle regression model, and the measured values, the results showed that the average relative error of the SVR model is low. The regression model has high accuracy and generalization ability; it can be applied to wind turbine anomaly distinguishing analysis.
- (3) Applying the model to practice, the analysis of the model results and the SCADA system can be used to record the measured values. The results show that when using the distance threshold to choose the appropriate conditions, the wind turbine condition monitoring can reflect the operating status of the wind turbine to provide technical references for online monitoring of wind turbines.

### Data Availability

The data used to support the findings of this study are available from the corresponding author upon request.

### Conflicts of Interest

The authors declare that they have no conflicts of interest.

### Authors' Contributions

Liang Tao provided data and ideas as well as optimization algorithm; Qian Siqi mined and analyzed data; Zhang Yingjuan used GA-optimized SVR algorithm to predict monitoring variables; and Shi Huan analyzed and summarized the experimental results.

### References

- [1] T. Liang, Z. Yuan, C. Mei et al., "Wind power remote centralized intelligent monitoring system design and management," *Automation and Instrumentation*, vol. 30, no. 11, pp. 50–53, 2015.
- [2] P. Tchakoua, R. Wamkeue, M. Ouhrouche, F. Slaoui-Hasnaoui, T. Tameghe, and G. Ekemb, "Wind turbine condition monitoring: state-of-the-art review, new trends, and future challenges," *Energies*, vol. 7, no. 4, pp. 2595–2630, 2014.
- [3] B. Hahn, M. Durstewitz, and K. Rohrig, "Reliability of wind turbines experience of 15 year with 1500 WTs," in *Wind Energy*, J. Peinke, P. Schaumann, and S. Barth, Eds., pp. 329–332, Springer, Berlin, Germany, 2007.
- [4] J. Ribrant and L. M. Bertling, "Survey of failures in wind power systems with focus on Swedish wind power plants during 1997–2005," *IEEE Transactions on Energy Conversion*, vol. 22, no. 1, pp. 167–173, 2007.
- [5] Lingwu Energy, H. Naishan, and R. Li, "Short-term wind power prediction based on cloud support vector machine model," *Power Automation Equipment*, vol. 33, no. 7, pp. 34–38, 2013.
- [6] H. H. Yang, M. L. Huang, and P. C. Huang, "Detection of wind turbine faults using a data mining approach," *Journal of Energy Engineering*, vol. 142, no. 3, article 04015021, 2016.
- [7] R. K. Pandit and D. Infield, "Comparative analysis of Gaussian process (GP) power curve models based on different stationary covariance functions for the purpose of improving model accuracy," *Renewable Energy*, vol. 140, pp. 190–202, 2019.
- [8] D. Astolfi, F. Castellani, and L. Terzi, "Wind turbine power curve upgrades," *Energies*, vol. 11, no. 5, p. 1300, 2018.
- [9] D. Astolfi and F. Castellani, "Wind turbine power curve upgrades: part II," *Energies*, vol. 12, no. 8, p. 1503, 2019.
- [10] S. Wan, J. Wan, and C. Zhang, "Comprehensive evaluation of wind power unit performance evaluation based on grey theory and variable weight fuzzy mathematics," *Acta Energetica Sinica*, vol. 36, no. 9, pp. 2285–2291, 2015.
- [11] K. Bassett, R. Cariveau, and D. S.-K. Ting, "Vibration analysis of 2.3 MW wind turbine operation using the discrete wavelet transform," *Wind Engineering*, vol. 34, no. 4, pp. 375–388, 2010.
- [12] Y. Chun-yu, G. Jian-ying, and X. Shi-guang, "Failure mechanism analysis and failure number prediction of wind turbine blades," *TELKOMNIKA (Telecommunication Computing Electronics and Control)*, vol. 12, no. 3, pp. 533–540, 2014.
- [13] S. Chakkor, M. Baghoury, and A. Hajraoui, "Wind turbine fault detection system in real time remote monitoring," *International Journal of Electrical and Computer Engineering (IJECE)*, vol. 4, no. 6, 2014.
- [14] J. J. Eggers, R. Bauml, R. Tzschoppe, and B. Girod, "Scalar costa scheme for information embedding," *IEEE Transactions on Signal Processing*, vol. 51, no. 4, pp. 1003–1019, 2003.
- [15] C. Zhang, "To evaluate the performance of Waanje, wind turbine fuzzy comprehensive evaluation based on Grey theory and variable weight," *Journal of Solar Energy*, vol. 36, no. 9, pp. 2285–2291, 2015.
- [16] X. Zhang, S. Hao, J. Li et al., "Grey correlation based analysis on impacting factors of maximum power point tracking control of wind power generating unit," *Power System Technology*, vol. 39, no. 2, pp. 445–449, 2015.
- [17] A. Zaher, S. D. J. McArthur, D. G. Infield, and Y. Patel, "Online wind turbine fault detection through automated SCADA data analysis," *Wind Energy*, vol. 12, no. 6, pp. 574–593, 2009.
- [18] D. Astolfi, L. Scappaticci, and L. Terzi, "Fault diagnosis of wind turbine gearboxes through temperature and vibration data," *International Journal of Renewable Energy Research (IJRER)*, vol. 7, no. 2, pp. 965–976, 2017.
- [19] Y. Feng, Y. Qiu, C. J. Crabtree, H. Long, and P. J. Tavner, "Monitoring wind turbine gearboxes," *Wind Energy*, vol. 16, no. 5, pp. 728–740, 2013.
- [20] W. Liao, R. Zhang, W. Yu et al., "PV output power forecast based on similar samples and PCA," *Solar Journal*, vol. 37, no. 9, pp. 2377–2385, 2016.
- [21] L. Breiman, "Random forests," *Machine Learning*, vol. 45, no. 1, pp. 5–32, 2001.
- [22] X. Zhang, H. Sipeng, J. Li et al., "Analysis of influence factors of MPPT control based on grey correlation degree," *Power Grid Technology*, vol. 39, no. 2, pp. 445–449, 2015.
- [23] Wind Turbine Ruiming, *Support Vector Machine Analysis Theory and Application*, China Power Press, Beijing, China, 2007.
- [24] Y.-Y. Hong and Y. Y. Chen, "Placement of power quality monitors using enhanced genetic algorithm and wavelet transform," *IET Generation, Transmission & Distribution*, vol. 5, no. 4, pp. 461–466, 2011.

## Research Article

# Emulator Based on Switching Functions for a Dual Interleaved Buck-Boost Converter

Marco Antonio Sánchez Vázquez , Ismael Araujo-Vargas , and Kevin Cano-Pulido

National Polytechnic Institute, Higher School of Mechanical and Electrical Engineering Culhuacan, 04430, Mexico

Correspondence should be addressed to Marco Antonio Sánchez Vázquez; [ingmarcosanchezv80@gmail.com](mailto:ingmarcosanchezv80@gmail.com)

Received 15 March 2019; Revised 14 June 2019; Accepted 3 July 2019; Published 4 August 2019

Academic Editor: Zhan Shu

Copyright © 2019 Marco Antonio Sánchez Vázquez et al. This is an open access article distributed under the Creative Commons Attribution License, which permits unrestricted use, distribution, and reproduction in any medium, provided the original work is properly cited.

Under the unavailability of some components of a complex system, the Hardware In the Loop (*HIL*) tool allows the emulation of other subsystems. When these devices are not available, a customized emulator can be developed based on the Piecewise Linear Model (*PWLM*) and a numerical method for solving the differential equations system. However, these implementations require the use of a Field Programmable Gate Array (*FPGA*) with extensive hardware resources. In this article we propose the use of switching functions for the modeling of power converters of a Hybrid Power System (*HPS*), allowing the reduction of hardware resources of the *FPGA*, and the number of steps per switching cycle is increased. The results are compared with *SABER* simulations and a *PWLM* evaluated with the Euler method.

## 1. Introduction

Frequently during the development of a complex system there are multiple subsystems under study; this represents a challenge for the rapid evolution of large projects. With the help of an emulator, multiple components can be developed quickly and efficiently; these tools are called Rapid Control Prototyping (*RCP*) or *HIL*. The *HIL* simulation is a form of simulation of real time; its initial use was in flight simulators and in missile guides, and nowadays its use has been extended to power electronics [1]. *HILs* are based on two technologies: microprocessors and *FPGA*. The disadvantage of the microprocessor-based emulators is that sequential logic would require clocks of the order of  $10^{12}$  Hz to match the *FPGA* concurrence with clocks of the order of  $10^6$  Hz that would perform the same number of operations [2]. The applications in power electronics are the development of the train power system [3], ships [4], electric vehicles [5, 6], and microgrids [7–9], achieving in the best of cases a step size of the order of 10 ns, if the numerical representation is sufficiently accurate to reduce the error by truncation.

It is observed that the development of a *HIL* requires the mathematical model that describes the behaviour of the system; that in the case of power converters refers to

the equations that solve the electrical network. The hardware resources of the *FPGA* depend on the model to be implemented, the synthesis procedure, and the format of the arithmetic: in Fixed Point (*FXP*) or Floating Point (*FP*). In [10] to model an NPC converter, the network equations were described with the Modified and Augmented Node Analysis (*MANA*), obtaining the state equations. In [11] to model a three-phase inverter, the network equations were described under the Associated Discrete Circuit (*ADC*). In [12] the average value method was used to calculate the output value of a three-phase interleaved converter. In [3, 13–19], equations are used in the state space to describe the behaviour of different topologies of power converters. However, in order to be implemented, an *FPGA* with wide range of resources is required; around 65000 Look Up Tables (*LUT*) to obtain a step size of the order of 5 ns, in some cases multiplex arithmetic operations can reduce the size between 15000 and 6000 *LUT*, with a cost of increasing the step size to 250 ns [18]

In this article, the model based on Switching Functions (*SF*) for a Dual Interleaved Buck-Boost Converter (*DIBBC*) with interphase transformer (*IPT*) was developed, and the hardware implementation was made for an *FPGA* of limited resources. Likewise *SABER* simulations results were compared with a *PWLM* and this proposal. It was observed

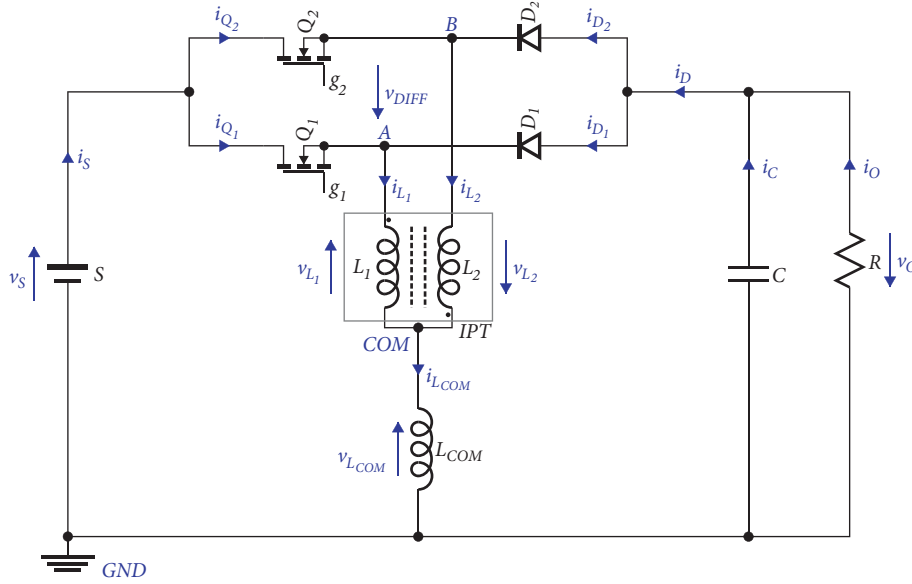


FIGURE 1: Scheme of a Dual Interleaved Buck-Boost Converter (DIBBC).

that the difference between models is minimal; however, in the hardware implementation the difference is drastic. In addition, it was noted that the step size is only restricted to the core speed of the FPGA.

## 2. Switching Functions Model for DIBBC

**2.1. The DIBBC.** Figure 1 shows the diagram of a DIBBC composed of a DC voltage source,  $v_s$ , a switch bridge  $Q_1, Q_2, D_1, D_2$ , an (IPT) that includes  $L_1$  and  $L_2$  where  $L_1 = L_2$ , a common inductor  $L_{COM}$ , an output capacitor  $C$ , and a load  $R$  [20].

**2.2. Operation Principle.** The circuit operates under the state of transistors  $Q_1$  and  $Q_2$ , presenting two possible permanent state operation regions:  $D < 0.5$  and  $D > 0.5$ ; the main waveforms are depicted in Figure 2, in (a) - (k) corresponding to  $D < 0.5$  and in (l) - (v) to  $D > 0.5$ . In (a) and (l) the signals of the states of the transistors  $Q_1$  and  $Q_2$  and  $v_{G1}$  and  $v_{G2}$  are observed for the fixed frequency ( $1/T$ ) and a phase shifted between them of  $T/2$  and a balanced duty cycle,  $D$ . (b) and (m) show the voltages in the nodes  $v_{AG}$  and  $v_{BG}$ . In (c) and (n) is the differential voltage  $v_{AB} = v_{AG} - v_{BG}$ .  $v_{AB}$  produces the current in the differential inductor  $i_{L,DIFF}$  or IPT (d) and (o). (e) and (p) correspond to the voltage in the common inductor  $v_{L,COM}$ . The currents in the common inductor  $i_{L,COM}$  are shown in (f) and (q), the currents in  $L_1$  and  $L_2$  are (g) and (h), and the currents in diodes  $i_{D1}$  and  $i_{D2}$  are shown in (h) and (s). The currents of  $Q_1$  and  $Q_2$  are shown in (i) and (v). The currents  $i_D$  in (j) and (u) are the sum of the currents in diodes  $D_1$  and  $D_2$ , and the current in the capacitor in (k) and (w).

Figure 3 shows the nine possible configurations of the DIBBC. The configurations from I to IV, Figures 3(a)–3(d), correspond to Continuous Current Mode (CCM), the other

five configurations are presented in the DCM, and the Discontinuous Current Mode (DCM) configurations V to IX are shown in Figures 3(e)–3(i); the DCM occurs when  $i_{L1} = 0$  or  $i_{L2} = 0$ ; under these conditions  $i_{D1} = 0$  or  $i_{D2} = 0$ .

**2.3. Switching Functions Model for a DIBBC.** In each configuration of the circuit, the voltages of the nodes  $v_{AB}$  and  $v_{BG}$ , which depend only on  $v_s$  and  $v_o$ , can be established by the product of

$$\mathbf{v}_H = M_V \mathbf{v}_S \quad (1)$$

The vectors  $\mathbf{v}_H$  are the voltages in the  $v_{AG}$  and  $v_{BG}$  nodes:  $[v_{AG} \ v_{BG}]^T$ , and the vector  $\mathbf{v}_S$  is the supply voltage  $v_s$  and the capacitor voltage  $v_o$ :  $[v_s \ v_o]^T$ .  $M_V$  is a transformation matrix for each configuration that is called Voltage Switching Matrix. For the currents of transistors  $Q_1$  and  $Q_2$  there is a current vector  $\mathbf{i}_Q$ :  $[i_{Q1} \ i_{Q2}]^T$ , and for the currents of the diodes,  $\mathbf{i}_D$  is  $[i_{D1} \ i_{D2}]^T$ . The current vector of the inductors  $\mathbf{i}_L$  is  $[i_{L1} \ i_{L2}]^T$ ; after  $\mathbf{i}_L$ ,  $\mathbf{i}_Q$ , and  $\mathbf{i}_D$  it can be obtained through the Current Switching Matrices  $M_{IQ}$  and  $M_{ID}$  shown in (2) and (3), respectively. Equation (1) is called voltage switching function ( $F_{SWV}$ ) and (3) is called current switching function ( $F_{SWI}$ ):

$$\mathbf{i}_Q = M_{IQ} \mathbf{i}_L \quad (2)$$

$$\mathbf{i}_D = M_{ID} \mathbf{i}_L \quad (3)$$

Table 1 shows the  $M_V$  and  $M_{ID}$  matrices for each configuration of the circuit; it indicates that the conditions for each configuration are presented and shade the configurations of the CCM.  $M_Q$  is excluded because at the moment it is not of interest for this work.

The current in  $L_{COM}$  can be divided into two when applying the superposition principle: the current that produces the

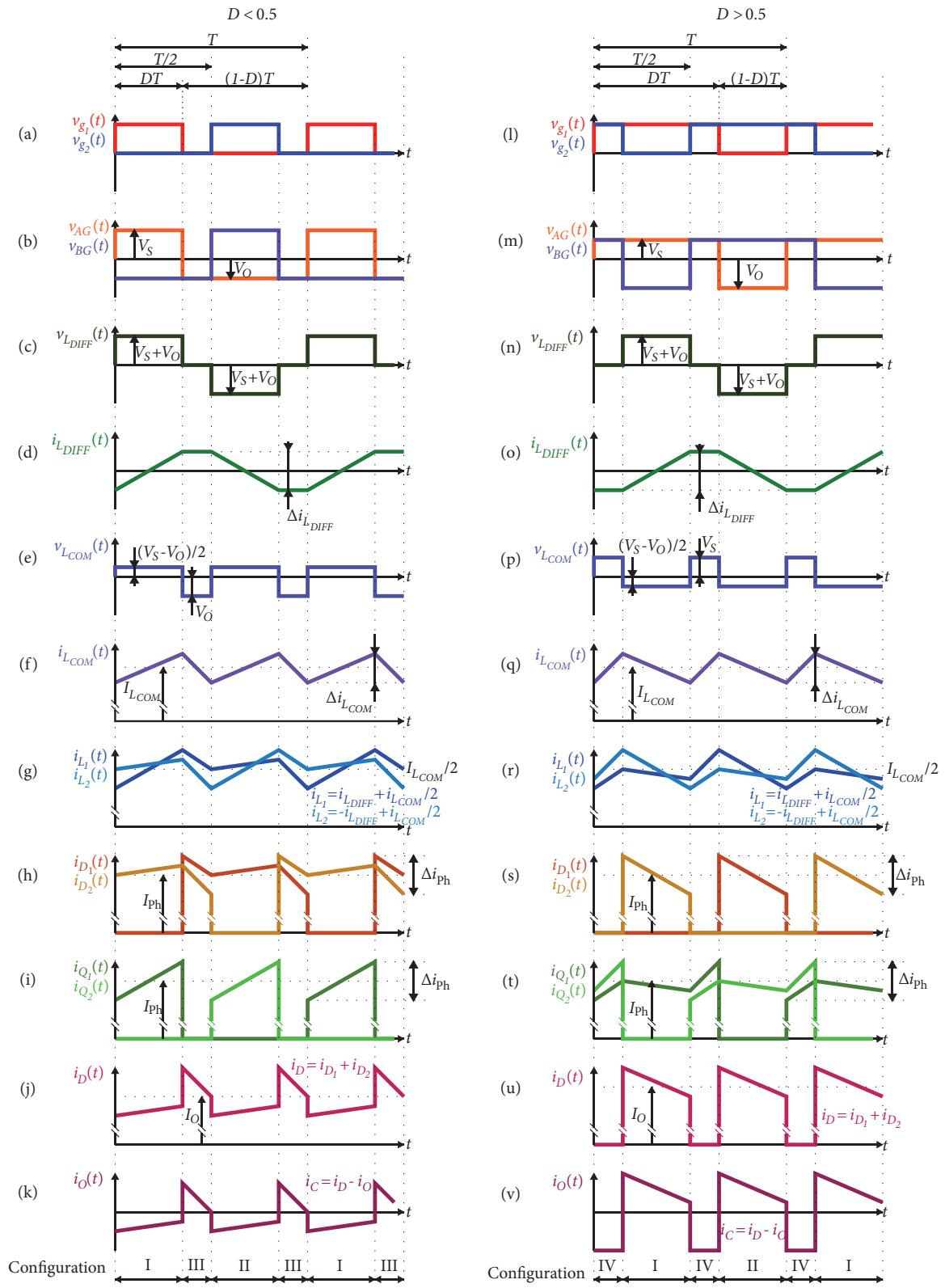


FIGURE 2: Steady-state waveforms of the DIBBC.

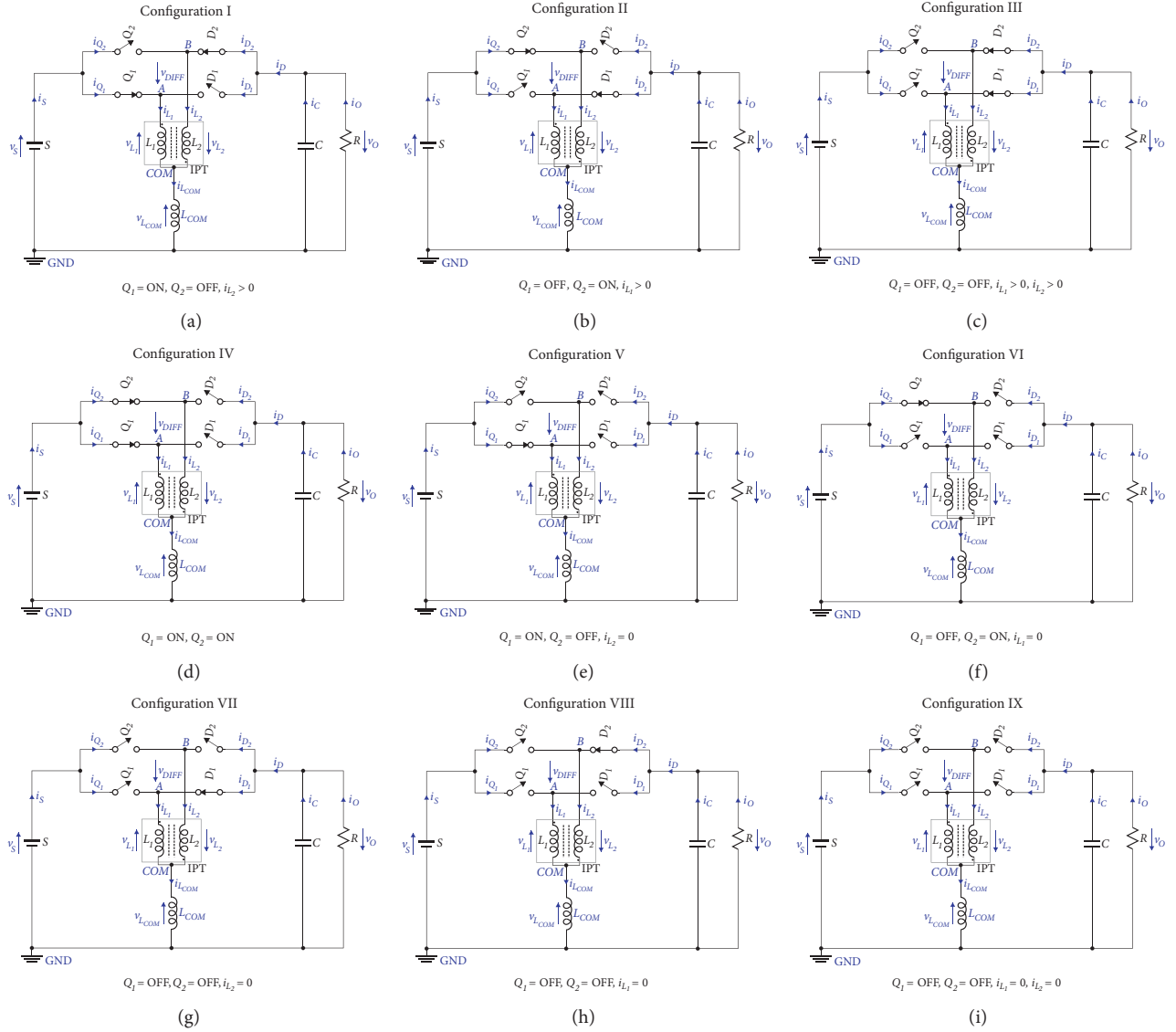


FIGURE 3: DIBBC configurations.

voltage in node A:  $v_{L_{COMA}}$  and the current that produces the voltage in node B:  $v_{L_{COMB}}$ . The voltages in CCM for  $L_{COMA}$ ,  $L_{COMB}$ ,  $L_1$ , and  $L_2$ , are given by (4), (5), (6), and (7), respectively, and are obtained from the node analysis between A, B, COM, and GND of the circuit of Figure 1, for which  $L_1 = L_2$  must be considered.

$$v_{L_{COMA}} = \frac{1}{2} v_{AG} \quad (4)$$

$$v_{L_{COMA}} = \frac{1}{2} v_{BG} \quad (5)$$

$$v_{L_1} = \frac{1}{2} (v_{AG} - v_{BG}) \quad (6)$$

$$v_{L_2} = \frac{1}{2} (v_{BG} - v_{AG}) \quad (7)$$

In DCM the voltages in  $L_{COMA}$ ,  $L_{COMB}$ ,  $L_1$ , and  $L_2$  are given by (8), (9), (10), and (11), respectively:

$$v_{L_{COMA}} = \frac{L_{COM}}{L + L_{COM}} v_{AG} \quad (8)$$

$$v_{L_{COMB}} = \frac{L_{COM}}{L + L_{COM}} v_{BG} \quad (9)$$

$$v_{L_1} = \frac{L}{L + L_{COM}} (v_{AG} - v_{BG}) \quad (10)$$

$$v_{L_2} = \frac{L}{L + L_{COM}} (v_{BG} - v_{AG}) \quad (11)$$

Equations (4) to (11) are the interactions in the voltage in the inductor network between nodes A, B, COM, and GND, and they are called XFRM<sub>v</sub>. The network of inductors is formed by an interphase transformer (IPT) with the branches  $L_1$  and

TABLE 1: Voltage switching function in A and B nodes and current switching function in diodes 1 and 2.

| Configuration | $Q_2$ | $Q_1$ | $v_{AG}$ | $v_{BG}$ | $M_V$  | $i_{Q1}$ | $i_{Q2}$ | $i_{D1}$ | $i_{D2}$ | $M_{ID}$                                       |
|---------------|-------|-------|----------|----------|--|----------|----------|----------|----------|--|
| I             | 0     | 1     | $v_S$    | $-v_O$   | $\begin{bmatrix} 1 & 0 \\ 0 & -1 \end{bmatrix}$  | $i_{L1}$ | 0        | 0        | $i_{L2}$ | $\begin{bmatrix} 0 & 0 \\ 0 & 1 \end{bmatrix}$ |
| II            | 1     | 0     | $-v_O$   | $v_S$    | $\begin{bmatrix} 0 & -1 \\ 1 & 0 \end{bmatrix}$  | 0        | $i_{L2}$ | $i_{L1}$ | 0        | $\begin{bmatrix} 1 & 0 \\ 0 & 0 \end{bmatrix}$ |
| III           | 0     | 0     | $-v_O$   | $-v_O$   | $\begin{bmatrix} 0 & -1 \\ 0 & -1 \end{bmatrix}$ | 0        | 0        | $i_{L1}$ | $i_{L2}$ | $\begin{bmatrix} 1 & 0 \\ 0 & 1 \end{bmatrix}$ |
| IV            | 1     | 1     | $v_S$    | $v_S$    | $\begin{bmatrix} 1 & 0 \\ 1 & 0 \end{bmatrix}$   | $i_{L1}$ | $i_{L2}$ | 0        | 0        | $\begin{bmatrix} 0 & 0 \\ 0 & 0 \end{bmatrix}$ |
| V             | 0     | 1     | $v_S$    | 0        | $\begin{bmatrix} 1 & 0 \\ 0 & 0 \end{bmatrix}$   | $i_{L1}$ | 0        | 0        | 0        | $\begin{bmatrix} 0 & 0 \\ 0 & 0 \end{bmatrix}$ |
| VI            | 1     | 0     | 0        | $v_S$    | $\begin{bmatrix} 0 & 0 \\ 1 & 0 \end{bmatrix}$   | 0        | $i_{L2}$ | 0        | 0        | $\begin{bmatrix} 0 & 0 \\ 0 & 0 \end{bmatrix}$ |
| VII           | 0     | 0     | $-v_O$   | 0        | $\begin{bmatrix} 0 & -1 \\ 0 & 0 \end{bmatrix}$  | 0        | 0        | $i_{L1}$ | 0        | $\begin{bmatrix} 1 & 0 \\ 0 & 0 \end{bmatrix}$ |
| VIII          | 0     | 0     | 0        | $-v_O$   | $\begin{bmatrix} 0 & 0 \\ 0 & -1 \end{bmatrix}$  | 0        | 0        | 0        | $i_{L2}$ | $\begin{bmatrix} 0 & 0 \\ 0 & 1 \end{bmatrix}$ |
| IX            | 0     | 0     | 0        | 0        | $\begin{bmatrix} 0 & 0 \\ 0 & 0 \end{bmatrix}$   | 0        | 0        | 0        | 0        | $\begin{bmatrix} 0 & 0 \\ 0 & 0 \end{bmatrix}$ |

$L_2$  and a common inductor,  $L_{COM}$ , the current proper to the IPT  $i_{LS}$  is obtained by means of (12) where  $\mathbf{v}_L$  is the vector  $[v_{L1} \ v_{L2}]^T$  and  $L^{-1}$  is the inverse matrix of the inductances of the transformer and  $\mathbf{i}_{LS}$  is the vector  $[i_{LS1} \ i_{LS2}]^T$ .

$$\mathbf{i}_{LS} = L^{-1} \int \mathbf{v}_L dt \quad (12)$$

$i_{L_{COMA}}$  and  $i_{L_{COMB}}$  are given by (13) and (14), respectively,

$$i_{L_{COMA}} = \frac{1}{L_{COM}} \int v_{L_{COMA}} dt \quad (13)$$

$$i_{L_{COMB}} = \frac{1}{L_{COM}} \int v_{L_{COMB}} dt \quad (14)$$

The currents  $i_{L1}$  and  $i_{L2}$  are given in (15) and (16), respectively. This set of equations are the interaction of the currents in the inductor network and are called XFRM<sub>i</sub>:

$$i_{L1} = i_{LS1} + i_{L_{COMA}} \quad (15)$$

$$i_{L2} = i_{LS2} + i_{L_{COMB}} \quad (16)$$

In the DCM,  $L_1$  and  $L_2$  stop behaving like a transformer and become an inductor when leaving one of its branches at high impedance, so we can do  $v_{L1} = v_{L2} = 0$ . Observing the sets of (4) and (8), (5) and (9), (6) and (10), and (7) and (10), we have the common factors  $v_{AG}$ ,  $v_{BG}$ ,  $v_{AG}-v_{BG}$ , and  $v_{BG}-v_{AG}$ , respectively, and we can summarize (4) to (11) in Table 2, where we have the common factor for each inductor voltage and  $G_{XFRMV}$  gain factor.

The balance of the current  $i_D$  is described by (17) and (18); (17) corresponds to the current coming from diodes  $D_1$  and  $D_2$  and (18) corresponds to the current injected into the RC output network.

$$i_D = i_{D1} + i_{D2} \quad (17)$$

$$i_D = i_C + i_R \quad (18)$$

 TABLE 2: XFRM<sub>v</sub> factors.

|                | CCM<br>$G_{XFRMV}$<br>(Config. I to IV) | DCM<br>$G_{XFRMV}$<br>(Config. VI to IX) | Common factor     |
|----------------|---|--|-------------------|
| $v_{L_{COMA}}$ | $\frac{1}{2}$                           | $\frac{L_{COM}}{L + L_{COM}}$            | $v_{AG}$          |
| $v_{L_{COMB}}$ | $\frac{1}{2}$                           | $\frac{L_{COM}}{L + L_{COM}}$            | $v_{BG}$          |
| $v_{L1}$       | $\frac{1}{2}$                           | 0  | $v_{AG} - v_{BG}$ |
| $v_{L2}$       | $\frac{1}{2}$                           | 0  | $v_{BG} - v_{AG}$ |

If  $i_R = v_O/R$  and  $i_C = C(dv_O/dt)$  are substituted in (18) and the equation is reordered, then (19) is obtained:

$$\frac{dv_O}{dt} = \frac{i_D}{C} - \frac{v_O}{RC} \quad (19)$$

If (19) is integrated, (20) is obtained, which would be the expression for modeling the output voltage  $v_O$

$$v_O = \frac{1}{C} \int i_D dt - \frac{1}{RC} \int v_O dt \quad (20)$$

Equations (1) to (20) and Tables 1 and 2 describe the system model; if you see each equation as a function of input output you can build a block diagram. This diagram is shown in Figure 4.

**2.4. System Discretization.** The system of Figure 4 is in the time domain; the Laplace transform must be applied to convert it to the domain of the complex variable  $s$ . In this diagram, with the exception of the integrators, all are arithmetic operators or gains, so the discretization consisted of replacing the integrators with discrete integrators of the block diagram. The discrete integrator that was used in this

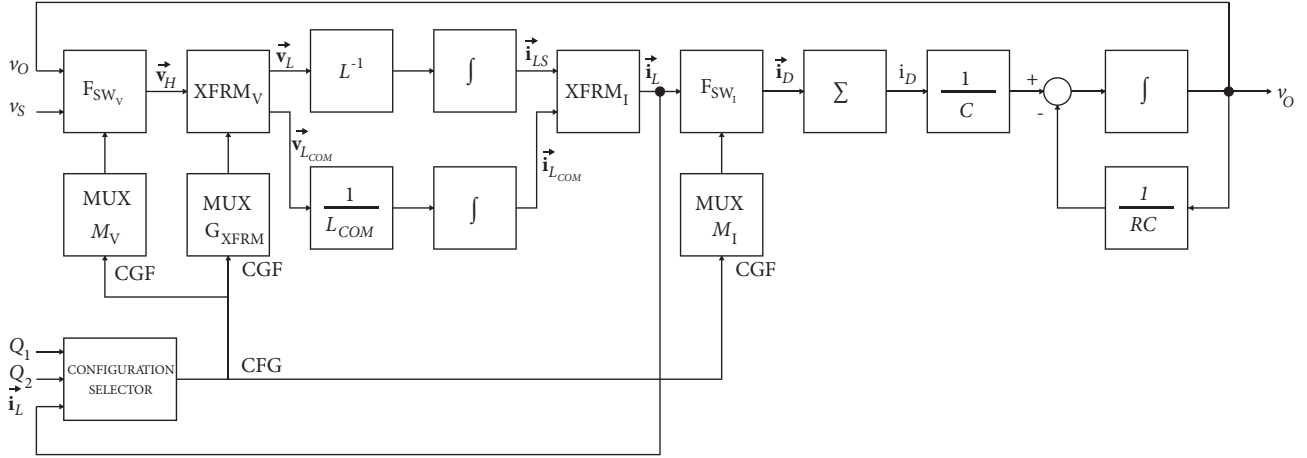


FIGURE 4: Block diagram of the DIBBC described by switching functions.

work has a delay physically feasible, and the transfer function of integration is given in equation (21):

$$H(s) = \frac{1}{s} \quad (21)$$

Equation (21) is discretized by applying the  $z$ -transform, obtaining the transfer function of an integrator shown in (22), where  $T_s$  is the sampling period:

$$z \left[ \frac{1}{s} \right] = \frac{T_s}{1 - z^{-1}} \quad (22)$$

Equation (22) corresponds to an integrator without delay; an integrator with delay according to the delay theorem of the  $z$  transform is shown in

$$H(z) = \frac{T_s z^{-1}}{1 - z^{-1}} \quad (23)$$

In Figure 5 a block diagram of the discrete model of the circuit of Figure 1 is shown.

### 3. Hardware Implementation

For implementation there is a card with a low-end FPGA Altera Cyclone IV E model EP4CE22F17C6N with 22320 LUT. The manufacturer provides the tool to develop systems called Quartus Prime, which allows the implementation of logic and arithmetic, in two languages of hardware description: VHDL and Verilog.

**3.1. Arithmetic.** Using the tool for IP development (Intellectual Property) of Quartus Prime called LPM Mega Wizard, the additions, subtractions, and multiplications of the model of Figure 4 were implemented. It was decided to use fixed point arithmetic with the format Q (64.32), having 32 bits for the integer part and 32 for the fractional part. The advantage of using fixed point is that the implementation in hardware does not require sequential operations and allows all operations to be performed concurrently. The

decision to use the fixed point format was made taking into account the dynamic range of the signals and the error of the representation of the constants of the system. With this format, the truncation error of the representation of the constants is less than 0.0005%. In Results, an error analysis will be shown over time.

**3.2. Switching Functions.** Only in the case that there are two possible states such as that of the switches, in hardware you can replace that switch represented by a product in the switching function by a multiplexer, like the functions of (1) to (3). Figure 6 shows how the switching function was implemented. It is observed that the products are replaced by multiplexers, which are controlled by the configuration multiplexers, which allow the input of the coefficients of the  $m_{x,mn}$  switching matrices. A 64-bit multiplier in hardware for the CYCLONE IV occupies a space of 4352 LUT, while a 64-bit multiplexer occupies only 64 LUT, which represents a reduction of 68 times the hardware space.

### 4. Results

Four simulations were carried out, the first using a simulator for physical systems, which in this case was SABER 2.4, the second simulation using PWLM evaluated by the Euler method in MatLAB 2015a, the third being the switching functions using a SIMULINK 2015a model and evaluated by the Euler method, and the fourth being the embedded model of the switching functions with the RTL simulation tool included in Quartus Prime 18.00. Table 3 shows the values of the simulation parameters. SABER is a very accurate simulator so it will be the reference to calculate the error. The state variables of the PWLM are  $i_{L1}$ ,  $i_{L2}$ , and  $v_O$ , so the graphs for them are displayed. Figures 7, 8, and 9 show the results of the simulations for the time from 0 ms to 10 ms: (a) corresponds to the four simulations, (b) corresponds to the error of the PWLM, the SF evaluated in SIMULINK, and SF evaluated by the FPGA all with respect to SABER, (c) is a zoom between 9.50 ms to 9.55 ms, and (d) is a zoom of the

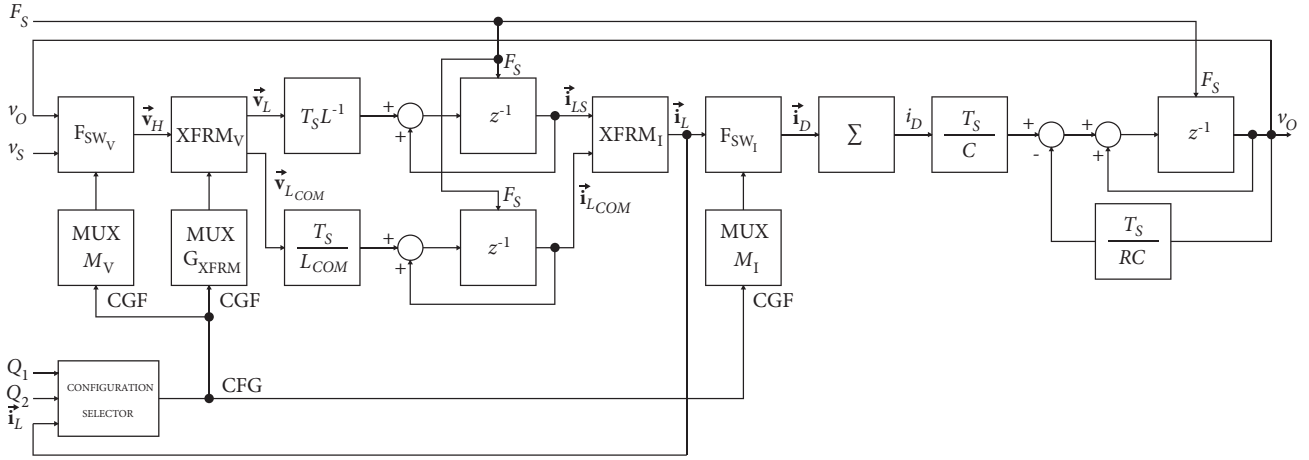


FIGURE 5: Discrete model of a DIBBC.

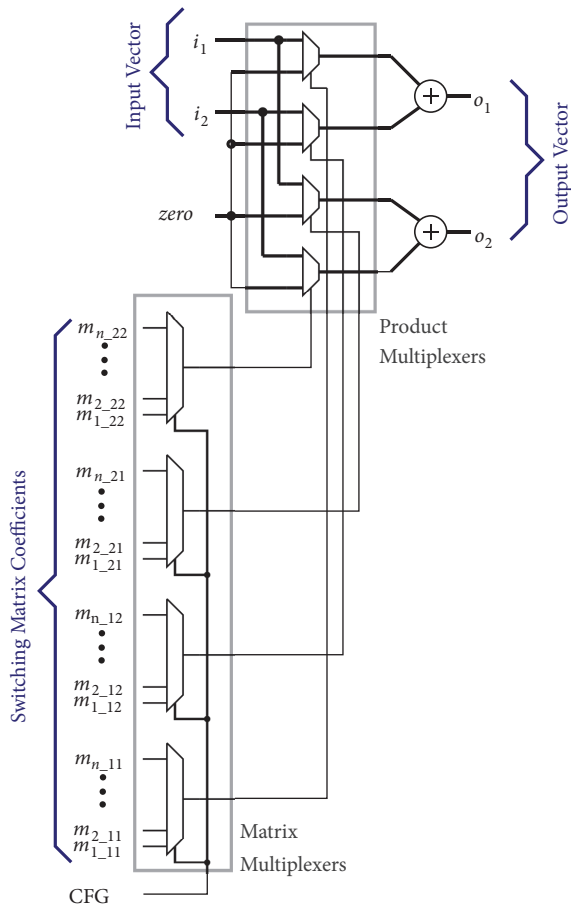


FIGURE 6: Hardware implementation for a switching function.

error for the interval of (c). When the system is in steady state it is observed that the errors between the SFs overlap without diverging. The error for  $i_{L1}$  at  $t = 9.526$  ms for the PWLM is under 1.09%, for both SFs it is 1.22%, the error for  $i_{L2}$  at  $t = 9.526$  ms for PWLM is 0.83%, and for SFs it is 0.63%; the error for  $v_O$  at  $t = 9.526$  ms for PWLM is 0.45% and for SFs it is

TABLE 3: Simulation parameters.

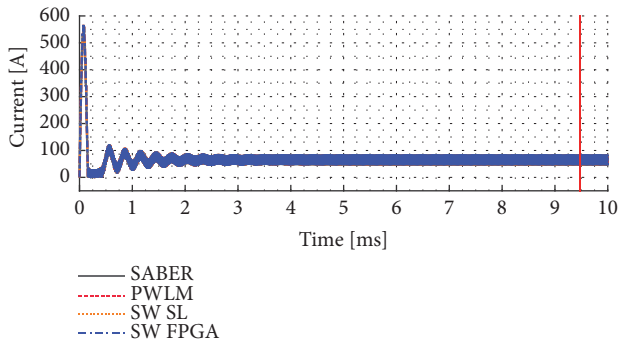
| Parameter | Value      |
|-----------|------------|
| $V_s$     | 350 V      |
| $F_{sw}$  | 75 kHz     |
| $F_{st}$  | 150 MHz    |
| $D$       | 45%        |
| $R$       | 4 $\Omega$ |
| $L$       | 38 $\mu$ H |
| $L_{com}$ | 7 $\mu$ H  |
| $C$       | 95 $\mu$ F |

0.44%. It should be noted that the circuit enters the DCM in two regions: when the circuit is turned on at  $t = 0$ s and during the transient in the interval  $t = 159\mu$ s to  $t = 413\mu$ s. The system reaches the steady state at  $t = 3.5$  ms.

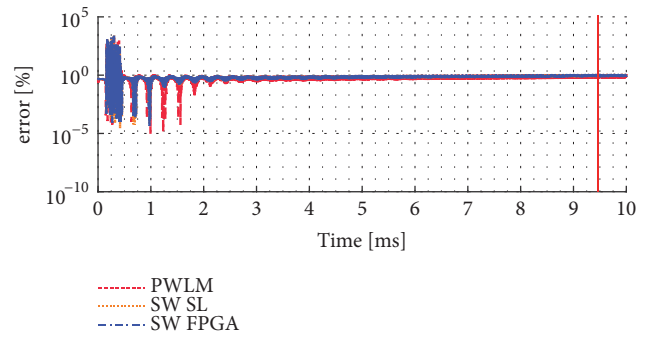
In terms of hardware implementation, a PWLM for the DIBBC would occupy a space of 79552 LUT in a Cyclone IV. In the case of the switching function model it deals with 9738 LUT (43.63% of the resources of the available card), depending on the Quartus Prime synthesis reports. Other embodiments were made for the PWLM by multiplexing the multipliers: one was multiplexing one row of equation and another was multiplexing rows of matrix. The results are shown in Table 4.

## 5. Discussion

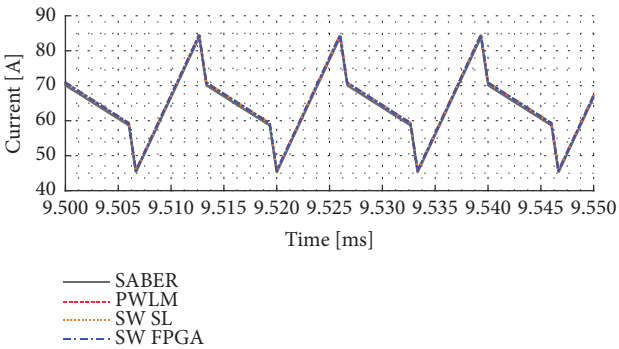
In order to implement a HIL based on a PWLM whose step size is less than 10 ns in an FPGA, extensive hardware resources are required. It is observed that when using a model based on switching functions and fixed point arithmetic with a high resolution, the space in hardware for its implementation is drastically reduced, allowing the use of a FPGA with few resources and with accuracy similar to that of other implementations and the step size is restricted to the core speed of the FPGA. This implementation is intended to be used for the development of a hybrid power system, since it



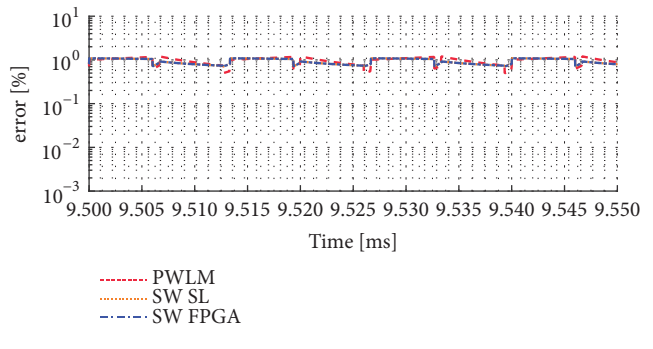
(a)



(b)

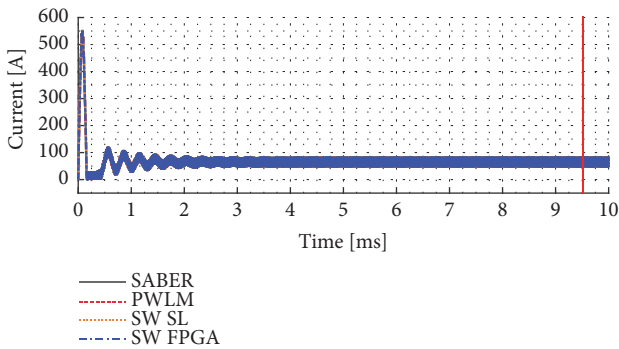


(c)

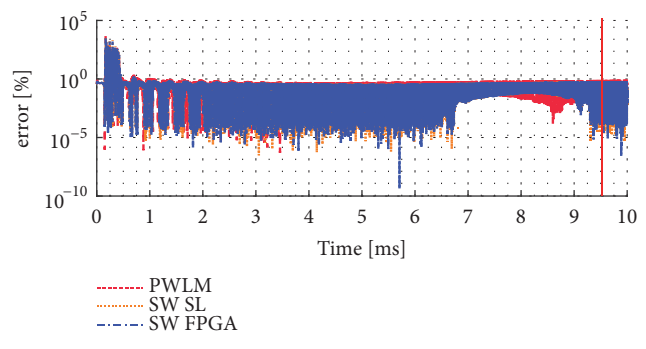


(d)

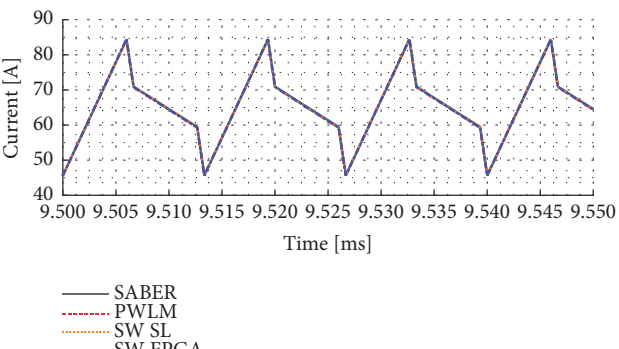
FIGURE 7: Analysis of the error of  $i_{L1}$  between SABER and PWLM, SF Simulink and SF FPGA.



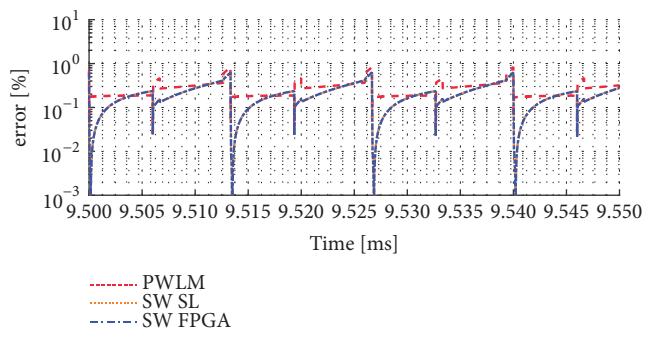
(a)



(b)



(c)



(d)

FIGURE 8: Analysis of the error of  $i_{L2}$  between SABER and PWLM, SF Simulink and SF FPGA.

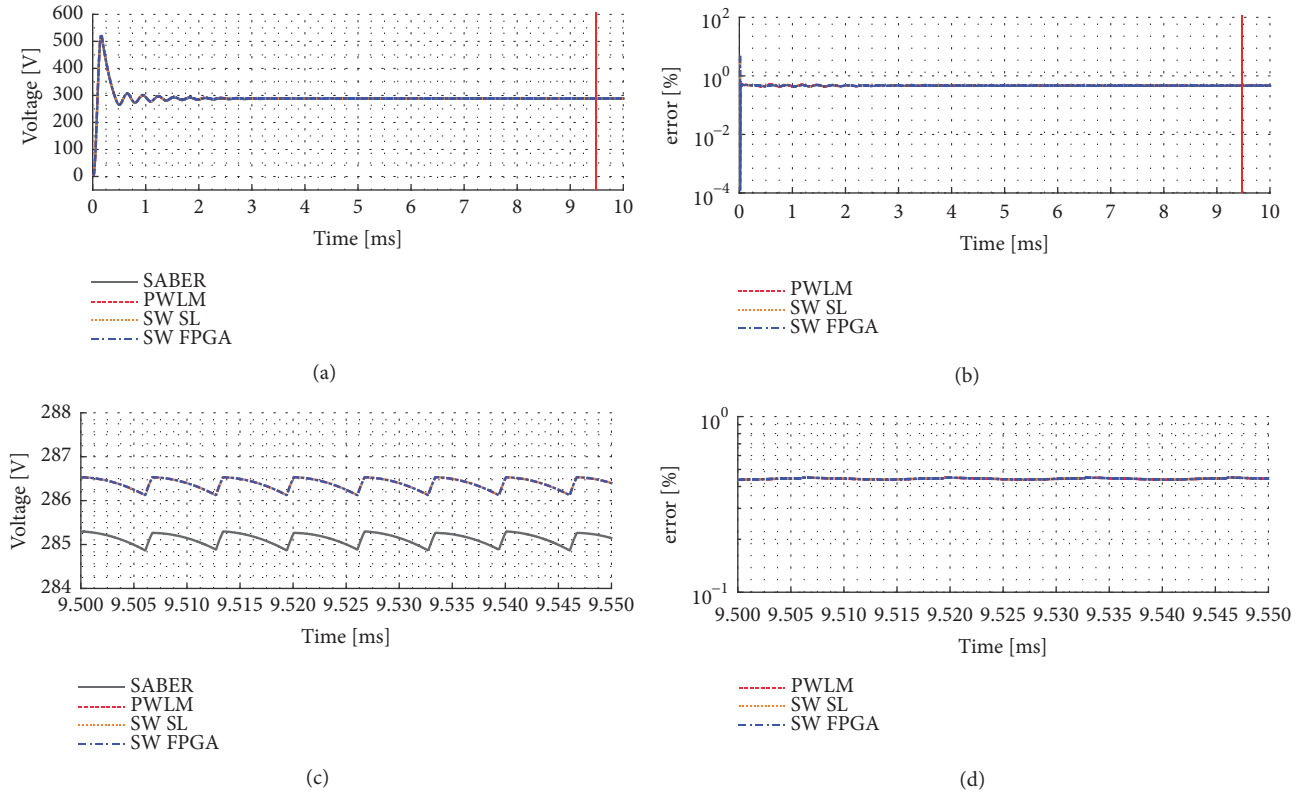


FIGURE 9: Analysis of the error of  $v_O$  between SABER and PWLM, SF Simulink and SF FPGA.

TABLE 4: Comparison between different implementation strategies.

| Implementation                              | Sampling Frequency | Number of steps per switching cycle $F_{sa}/F_{sw}$ | Multipliers | Resources FPGA (CYCLONE 4 22K) |
|---|--------------------|---|-------------|--------------------------------|
| PWLM multiplier multiplexed in equation row | 52.5 MHz           | 700   | 3           | 14.67%                         |
| PWLM multiplexer multiplexed in matrix row  | 105 MHz            | 1400  | 9           | 89.60%                         |
| SFM   | 150 MHz            | 2000  | 5           | 43.63%                         |

is required to embed in a FPGA the models of several power converters, sources, and loads. This implementation can be extended for use in microgrids. The switching functions allow seeing in the systems how the flow of the power is in a natural way so that the power balance does not require a very complex mathematical description that increases the hardware resources of a HIL.

### Data Availability

The simulation data used to support the findings of this study are available from the corresponding author upon request.

### Conflicts of Interest

The authors declare that they have no conflicts of interest.

### Acknowledgments

The authors acknowledge to the Instituto Politécnico Nacional (IPN) Mexico, for its facilities where it has been possible to carry out this work, Comisión de Operación y Fomento de Actividades Académicas of the IPN (COFAA), for its financial support for the publication of this research article, and the Universidad Autonoma de Chihuahua (UACH) Mexico, for academic support granted for the realization of this research.

### References

- [1] C. Buccella, C. Cecati, and H. Latafat, “Digital control of power converters—a survey,” *IEEE Transactions on Industrial Informatics*, vol. 8, no. 3, pp. 437–447, 2012.
- [2] F. Ji, H. Fan, and Y. Sun, “Modelling a FPGA-based LLC converter for real-time hardware-in-the-loop (HIL) simulation,” in

- Proceedings of the 8th IEEE International Power Electronics and Motion Control Conference (IPEMC-ECCE Asia '16)*, pp. 1016–1019, IEEE, China, May 2016.
- [3] C. Liu, R. Ma, H. Bai, Z. Li, F. Gechter, and F. Gao, "Hybrid modeling of power electronic system for hardware-in-the-loop application," *Electric Power Systems Research*, vol. 163, pp. 502–512, 2018.
  - [4] M. Milton, A. Benigni, and J. Bakos, "System-level, FPGA-based, real-time simulation of ship power systems," *IEEE Transactions on Energy Conversion*, vol. 32, no. 2, pp. 737–747, 2017.
  - [5] L. Herrera, C. Li, X. Yao, and J. Wang, "FPGA-based detailed real-time simulation of power converters and electric machines for EV HIL applications," *IEEE Transactions on Industry Applications*, vol. 51, no. 2, pp. 1702–1712, 2015.
  - [6] J.-M. Timmermans, J. Van Mierlo, P. Lataire, F. Van Mulders, and Z. McCaffree, "Test platform for hybrid electric power systems: development of a HIL test platform," in *Proceedings of the European Conference on Power Electronics and Applications (EPE '07)*, Denmark, September 2007.
  - [7] Z. Jiang, R. A. Dougal, R. Leonard, H. Figueroa, and A. Monti, "Hardware-in-the-loop testing of digital power controllers," in *Proceedings of the 21st Annual IEEE Applied Power Electronics Conference and Exposition (APEC '06)*, pp. 901–906, IEEE, USA, March 2006.
  - [8] H. Li, M. Steurer, K. Shi, S. Woodruff, and D. Zhang, "Development of a unified design, test, and research platform for wind energy systems based on hardware-in-the-loop real-time simulation," *IEEE Transactions on Industrial Electronics*, vol. 53, no. 4, pp. 1144–1151, 2006.
  - [9] P. Vlado, A. Evgenije, G. Stevan, V. Marko, and R. Milan, "Precise PV active power - converter control rapid prototyping framework," in *Proceedings of the 19th International Symposium on Power Electronics (Ee '17)*, pp. 1–6, Serbia, October 2017.
  - [10] F. Montano, T. Ould-Bachir, and J. P. David, "An evaluation of a high-level synthesis approach to the FPGA-based sub-microsecond real-time simulation of power converters," *IEEE Transactions on Industrial Electronics*, vol. 65, no. 1, pp. 636–644, 2018.
  - [11] M. Dagbagi, A. Hemdani, L. Idkhajine, M. W. Naouar, E. Monmasson, and I. Slama-Belkhdja, "ADC-based embedded real-time simulator of a power converter implemented in a low-cost FPGA: application to a fault-tolerant control of a grid-connected voltage-source rectifier," *IEEE Transactions on Industrial Electronics*, vol. 63, no. 2, pp. 1179–1190, 2016.
  - [12] R. Kang, S. Kim, I. Yang, K. Jeong, C. Kang, and G. Kim, "The use of FPGA in HIL simulation of three phase interleaved DC-DC converter," in *Proceedings of the IEEE Vehicle Power and Propulsion Conference (VPPC '12)*, pp. 772–776, IEEE, Republic of Korea, October 2012.
  - [13] H. Kidokoro and M. Nakahara, "FPGA-based hardware-in-the-loop simulator of high switching frequency power converters," in *Proceedings of the IEEE International Telecommunications Energy Conference (INTELEC '15)*, IEEE, Japan, October 2015.
  - [14] C. Dufour, H. Blanchette, and J. Bélanger, "Very-high speed control of an FPGA-based finite-element-analysis permanent magnet synchronous virtual motor drive system," in *Proceedings of the 34th Annual Conference of IEEE Industrial Electronics*, pp. 2411–2416, IEEE, Orlando, Fla, USA, November 2008.
  - [15] P. Le-Huy, S. Guerette, L. A. Dessaint, and H. Le-Huy, "Real-time simulation of power electronics in power systems using an FPGA," in *Proceedings of the 2006 Canadian Conference on Electrical and Computer Engineering*, pp. 873–877, IEEE, Ottawa, Canada, May 2006.
  - [16] C. Liu, R. Ma, H. Bai, F. Gechter, and F. Gao, "A new approach for FPGA-based real-time simulation of power electronic system with no simulation latency in subsystem partitioning," *International Journal of Electrical Power & Energy Systems*, vol. 99, pp. 650–658, 2018.
  - [17] S. Ben Said, K. Ben Saad, and M. Benrejeb, "HIL simulation approach for a multicellular converter controlled by sliding mode," *International Journal of Hydrogen Energy*, vol. 42, no. 17, pp. 12790–12796, 2017.
  - [18] T. Ould Bachir, C. Dufour, J. Bélanger, J. Mahseredjian, and J. David, "A fully automated reconfigurable calculation engine dedicated to the real-time simulation of high switching frequency power electronic circuits," *Mathematics and Computers in Simulation*, vol. 91, pp. 167–177, 2013.
  - [19] R. Razzaghi, M. Mitjans, F. Rachidi, and M. Paolone, "An automated FPGA real-time simulator for power electronics and power systems electromagnetic transient applications," *Electric Power Systems Research*, vol. 141, pp. 147–156, 2016.
  - [20] F. Gomez-Olguin, I. Araujo-Vargas, T. Granados-Luna, P. Velazquez-Elizondo, K. Cano-Pulido, and A. Villarruel-Parra, "Design and assessment of a 30 kW/75 kHz DC-DC, two-phase dual interleaved buck-Boost converter," in *Proceedings of the 2nd IEEE Texas Power and Energy Conference (TPEC '18)*, pp. 1–6, IEEE, USA, February 2018.

## Research Article

# Operation of Parallel Inverters in Microgrid Using New Adaptive PI Controllers Based on Least Mean Fourth Technique

A. Elnady<sup>1,2</sup> and M. AlShabi<sup>3</sup>

<sup>1</sup>Electrical and Computer Engineering Department, College of Engineering, University of Sharjah, Sharjah, P.O. Box 27272, UAE

<sup>2</sup>Royal Military College of Canada, P.O. Box 17000, Station Forces, Kingston, Ontario, Canada K7K 7B4

<sup>3</sup>Mechanical and Nuclear Engineering Department, College of Engineering, University of Sharjah, Sharjah, P.O. Box 27272, UAE

Correspondence should be addressed to A. Elnady; [ayelnady71@gmail.com](mailto:ayelnady71@gmail.com)

Received 3 March 2019; Accepted 7 May 2019; Published 19 June 2019

Guest Editor: Michael Z. Q. Chen

Copyright © 2019 A. Elnady and M. AlShabi. This is an open access article distributed under the Creative Commons Attribution License, which permits unrestricted use, distribution, and reproduction in any medium, provided the original work is properly cited.

This paper shows the operation of the microgrid using a new adaptive PI controller based operational (control) scheme. The core of the proposed control scheme is the suggested adaptive PI controller. The parameters of the PI controller are adaptively tuned using a variable step-size least mean fourth algorithm with no need for any system model to operate this adaptive controller. The main merit of the proposed scheme is that it stabilizes the magnitude and frequency of the voltage at any loading condition such as variable balanced loads, variable unbalanced loads, and nonlinear loads. The proposed scheme has a simple structure and accurate performance. In addition, the structure of proposed scheme provides a seamless transition toward any loss or reconnection of any inverter in the microgrid. Furthermore, the suggested operational scheme is flexible enough to enable the microgrid to be operative in a grid-connected mode and to transfer from the voltage control mode to power control mode with a smooth transitional procedure. To validate the meritorious performance of the suggested scheme, its performance is compared to similar schemes based on a linear controller (regular PI controller), single-neuron PI controller (adaptive PI controller), recursive least square-support vector machine based PI controller (another adaptive PI controller), and nonlinear controller (sliding mode controller) for different operations of the microgrid.

## 1. Introduction

The microgrid is a new effective trend in the power system. It gains much popularity nowadays because it solves many problems in the power system [1–3]. The microgrid can accommodate diverse renewable energy resources with power electronics interface. In the microgrid, the carbon emission is minimum compared to the central grid. The microgrid is a perfect solution for the isolated or far-sited loads. The microgrid has a capability to work in an autonomous mode (microgrid mode) and in a grid-connected mode [4]. The microgrid can be considered as backup generation in case a small portion of the central grid experiences some outages.

The operation of the microgrid is mainly dictated by its operational (control) scheme, which is adopted to operate this microgrid. The control scheme of the microgrid is mainly divided into two main categories. The first category is the

droop control schemes (communication-less based schemes) and the second category is the distributed control schemes (communication based schemes). Each category has its own merits and demerits [5–10]. The droop control scheme has the advantage of its independence since it is not required to have any communication among the generation units. Yet, it suffers from some drawbacks, which can be briefly summarized as follows:

- (1) Accurate sharing for power necessitates a steep slope of its droop characteristics, which makes a considerable variation in voltage and frequency.
- (2) The variable impedance of the feeders greatly influences the operation of the droop control and it creates a circulating current.
- (3) The X/R ratio impacts the performance of the droop. If this ratio is high, the performance is good and vice

versa. In the distribution system, this X/R ratio is low, which inflicts the performance of the droop control.

- (4) The low X/R ratio of the distribution feeder increases the coupling between active power and reactive power, which entails substantial modifications to the conventional droop control.
- (5) Existence of the injected harmonics deteriorates the droop performance because the droop is mainly designated for the fundamental voltage and current.

All aforementioned problems motivate the researchers to utilize the second category. The main problem of the distributed control is its essential communication among its generation units (inverters). The main focus of this paper is directed toward the second category. Therefore, the literature survey of this paper focuses on the distributed current control schemes.

The distributed current control scheme has a typical structure of two cascaded control loops [6, 8, 11], which are named in the literature as the primary current control loop (inner loop) and secondary voltage control loop (outer loop). The primary control loop is accountable for adjusting the injected current of the inverter. The secondary control loop is responsible for controlling the voltage at the loads' side. The publications related to the distributed current control give more attention to the different schemes used in this category along with the utilized controller of the primary control loop.

Several schemes are used in the distributed current control. The average and instantaneous current sharing scheme is employed to equalize the current injected by inverters [12], which requires a sort of communication among these inverters to get the power and current share of each inverter. Another scheme is called the master-slave scheme [13], where one inverter is responsible for adjusting the voltage and the other inverters share the load current and power. This scheme suffers from robustness due to the loss of the master inverter. Some modifications have been suggested to this scheme to increase its robustness and modularity. The circular chain control (3C) is another scheme, which is introduced to operate the distributed generation system [14]. This scheme has a typical structure of two cascaded control loops (inner for current and outer for voltage). This scheme requires communications among the inverters such that the inner current loop tracks the current of the previous inverter. A current limiting control is introduced in [15], where its control scheme consists of two loops: one for voltage and the other one for current. The current command of each module (inverter) is generated by the previous module based on the module capacity. By limiting the output current command of these modules in [15], each module has to share the load current with a different factor not similar to the factors provided by all previous modules.

The core of the primary control loop (current control) is the controller that is adopted to govern the primary control loop in terms of adjusting the injected current of the inverter. The most widely used controllers in the current control are the PI or PID controller in the  $d - q$  rotating frame and

the proportional-resonant (PR) or proportional-complex-integral (PCI) controllers in the  $\alpha - \beta$  stationary frame [16]. The main shortcoming of the PI and PR controllers is that they do not give their optimum performance at all operating conditions. The predictive current control is proposed in [17], where the current error is corrected by an adaptive strategy. It has the disadvantage of susceptibility to the system uncertainty. The deadbeat controller is commonly used for current control [18], in which the current error is predicted and corrected from an adaptive self-tuning load model. The sliding mode control is also utilized for the current control in the distributed generation system [19]; it proves that it is a robust controller for any uncertainty in the system, but its main problem is the chattering that appears due to the existence of the discrete input in its control law. The 2<sup>nd</sup> order sliding mode current control [20] is also utilized in the distributed generation system so as to precisely govern the injected current with the minimum chattering level. The H $\infty$  current controller allows maintaining balanced currents for the three-phase four-wire inverter [21].

This paper presents an innovative operational (control) scheme to stabilize the voltage along with its frequency in the microgrid under different loading conditions such as variable balanced loads, variable unbalanced loads, and nonlinear loads. This operational scheme is based on the self-adaptive PI controller, which has not been used before for microgrid operations. The suggested controller innovatively adapts its own parameters such that the error cost function is minimized at any operating condition; therefore, the proposed controller gives its best performance at any operation condition. This paper is composed of seven sections. The second section shows the microgrid under study. The third section explains the mathematical formulation of the proposed controller along with other controllers used to validate the performance of the proposed controller. The proposed control scheme is compared to other common controllers in the fourth section. The simulation results of the microgrid operation are illustrated in the fifth section. The results of the microgrid in a grid-connected mode are displayed in the sixth section. The findings are concluded in the last section.

## 2. Microgrid Under Study

This section shows the configuration of the microgrid with its simple mathematical model. To ease understanding this section, the microgrid under study with several inverters is already depicted in Figure 1

The load voltage of Figure 1 is expressed as follows.

$$E_{abc} = V_{abc-load} + I_{abc-load} * Z_{feeder} \quad (1)$$

Equation (1) is transformed from the  $a - b - c$  natural frame to the  $d - q$  rotating frame, which yields a state space form written as

$$\begin{bmatrix} pI_{d-load} \\ pI_{q-load} \end{bmatrix} = \begin{bmatrix} -\frac{R}{L} & \omega \\ \omega & -\frac{R}{L} \end{bmatrix} \begin{bmatrix} I_{d-load} \\ I_{q-load} \end{bmatrix} + \begin{bmatrix} \frac{1}{L} & 0 \\ 0 & \frac{1}{L} \end{bmatrix} \begin{bmatrix} E_d \\ E_q \end{bmatrix}$$

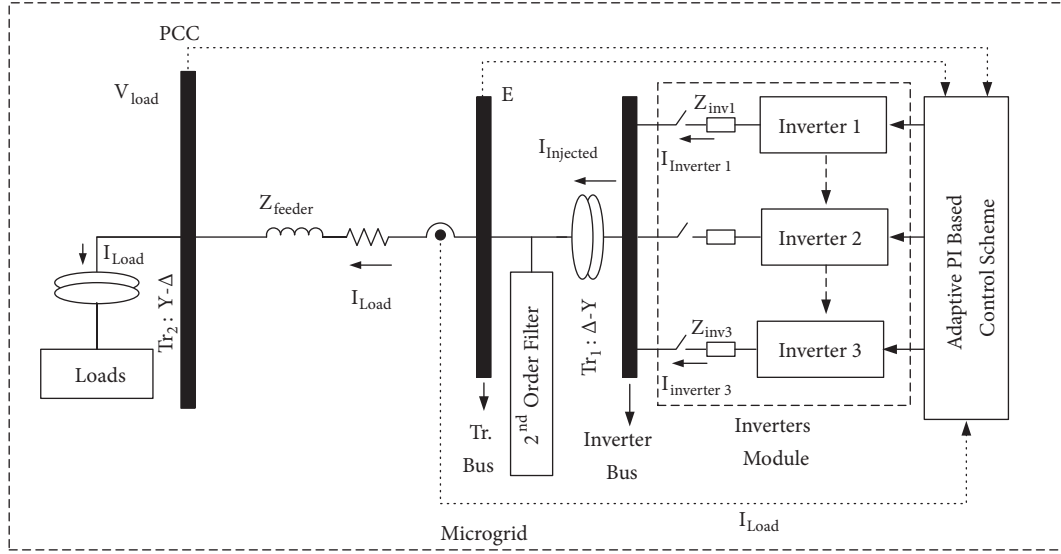


FIGURE 1: Microgrid under study.

TABLE 1: Microgrid parameters.

| Parameter/Description                     | Values                               |
|---|--------------------------------------|
| Voltage level                             | = 6.6 kV                             |
| Microgrid rating/base                     | = 2.5 MVA                            |
| Power Rating/inverter                     | = 0.75MVA                            |
| Feeder impedance $Z_f$                    | = $1.2\Omega + 1.5j \Omega$          |
| Transformer $Tr_1, Tr_2$ rating           | = 2.5 MVA                            |
| Transformer $Tr_1$ voltage ratio          | = $1.32 \text{ kV} : 6.6 \text{ kV}$ |
| Transformer $Tr_1, Tr_2$ resistance       | = $0.0101 \text{ pu}$                |
| Transformers $Tr_1, Tr_2$ inductance      | = $0.1 \text{ pu}$                   |
| Transformer $Tr_1, Tr_2$ rating           | = 2.5 MVA                            |
| Transformer $Tr_2$ voltage ratio          | = $6.6 \text{ kV} : 0.4 \text{ kV}$  |
| Inverter Type                             | 5-level Diode Clamped Inverter       |
| Number of Parallel Inverters in Microgrid | Three                                |

$$\dot{x} = Ax + Bu + Fd + \begin{bmatrix} -\frac{1}{L} & 0 \\ 0 & -\frac{1}{L} \end{bmatrix} \begin{bmatrix} V_{d-load} \\ V_{q-load} \end{bmatrix} \quad (2)$$

where  $p = d/dt$ ; the microgrid is a group of generation units with groups of different loads. The microgrid parameters are listed in Table 1. The utilized inverter is the 5-level diode-clamped inverter, which gives small total harmonic distortion compared to the traditional 2-level and 3-level inverter. The operation and control of the 5-level diode-clamped inverter are well documented in [22]. The switching modulation of the 5-level diode-clamped inverter is the multicarrier pulse width modulation (PWM). The phase-disposition pulse width modulation (PD-PWM) [22] is the modulation technique considered to operate the three-phase 5-level diode-clamped inverters. All given load impedances in this paper are referred to the primary side of the transformer  $tr_2$ .

### 3. Proposed Operational Scheme

This section explains the proposed operational scheme, and how it works to stabilize the magnitude and frequency of the voltage at load side (point of common coupling). The subsequent sections clarify the formulation of the other controllers for comparison with the proposed controller.

#### 3.1. Structure of Proposed Control Scheme for Microgrid Mode.

This section explains the proposed control scheme used to operate the microgrid in an autonomous mode (microgrid mode). The control scheme for positive-sequence components is illustrated in Figure 2. The control scheme of Figure 2 shows that the primary and secondary control loops stabilize the voltage at the load side. The primary current control loop (inner loop) is the main loop in the proposed scheme of Figure 2. The input of this primary control loop is the current reference (current command), which is received from the secondary control loop (voltage control), while the output of this primary current control (inner loop) is the required

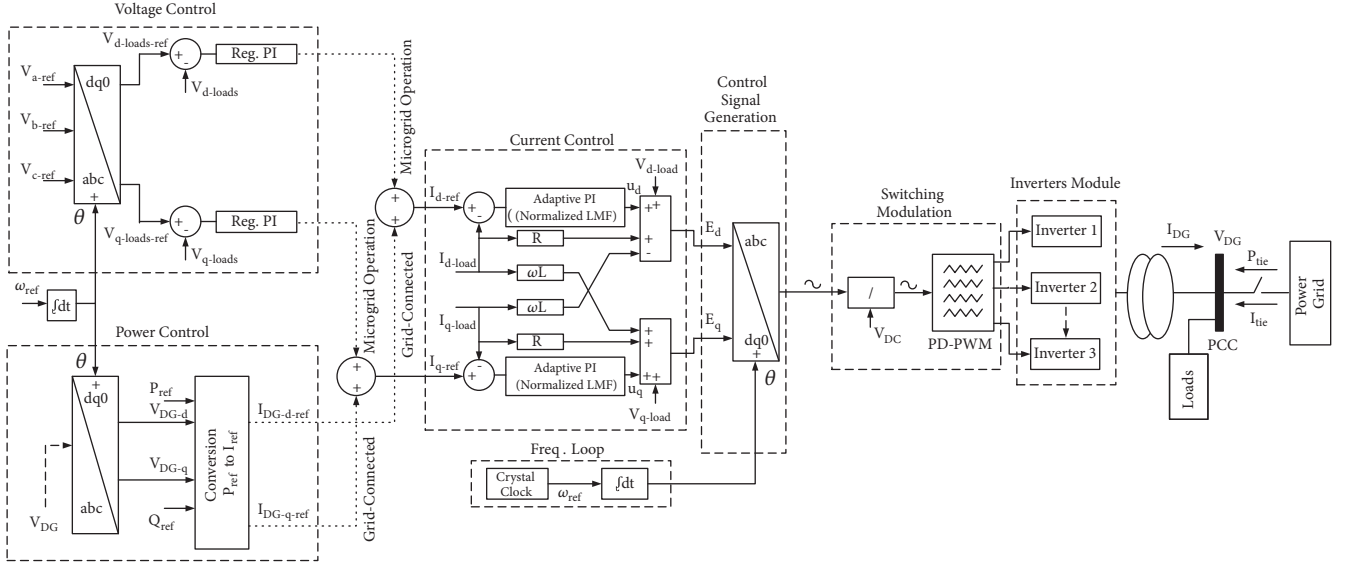


FIGURE 2: Proposed scheme for microgrid operation.

injected voltage by inverters. This required voltage is used to generate a control signal utilized to operate the switching modulation (PD-PWM). The secondary control loop (voltage control) receives the voltage reference in the  $a - b - c$  frame and generates the current references for the primary control loop. Its function is to stabilize the magnitude of the voltage at the load bus.

In the voltage control, its loop commonly employs a linear controller like a regular PI controller because the relation between the load voltage and fundamental load current is almost linear. Thus, a regular PI controller in this loop is enough to get a fast and suitable dynamic performance, whereas the current control governs another part of the microgrid along with the inverter circuits. Therefore, it is strongly recommended that this loop encompasses an efficient (self-adaptive) controller like what is proposed in this paper. The frequency of the generated voltage is always stable and constant because it is driven by an internal crystal clock with a constant frequency  $\omega_{ref}$  as shown in Figure 2. This frequency loop is operated as an open loop control because the switching modulation (PD-PWM) does not change the frequency of the injected voltage and it is always constant regardless of any variation in loading conditions.

The effectiveness of this control scheme is exemplified in the operation of the inverters' module. This inverters' module contains three three-phase inverters. Each three-phase inverter receives the same switching signals generated by the PD-PWM, meaning that each inverter independently injects a certain voltage to stabilize the voltage along with its frequency at the load side. Another advantage of this proposed structure for the operational scheme is that the total load current/power is equally divided among all working inverters. In case one inverter is disconnected/reconnected, the total load current is seamlessly redistributed among

all working inverters with the minimum voltage transition (similar to plug-and-play capability) as will be illustrated in later sections. More importantly, this proposed scheme does not need any sort of communication among the inverters because each inverter is working independently of the others.

**3.1.1. Mathematical Formulation of Proposed Scheme/Controller for Balanced Loads.** The proposed adaptive PI controller is based on adaptation of the controller parameters ( $K_p, K_I$ ) using an improved version of the least mean fourth algorithm. In the primary control loop (current control), the error is defined as

$$e(k) = I_{ref}(k) - I_{feedback}(k) = r(k) - y(k) \quad (3)$$

where  $r = I_{ref}$ ,  $y = I_{feedback}$ . The recursive form of the adaptive PI controller is expressed using the Dahlin formula as in [23]

$$u(k) = u(k-1) + K_p(e(k) - e(k-1)) + K_I(e(k)) \quad (4)$$

where  $K_p, K_I$  are the parameters that should be recursively changed such that the error of (3) is minimized using the least mean fourth algorithm whose cost function is defined as follows.

$$J = \min(e^4) \quad (5)$$

The controller is redefined in terms of some weights as

$$u(k) = u(k-1) + K_1 W_1(k) X_1(k) + K_1 W_2(k) X_2(k) \quad (6)$$

where  $X_1 = (e(k) - e(k-1))$ ,  $X_2 = e(k)$ ,  $K_p = K_1 W_1$ ,  $K_I = K_2 W_2$ . The optimization of the cost function in (5) is obtained from its gradient descent with respect to the

variables ( $W_1, W_2$ ) [24], and the result of the differentiation of the cost function is given as follows.

$$\begin{aligned} \frac{\partial J}{\partial W_1} &= \Delta W_1 = -\frac{\partial}{\partial W_1} (e^4) = -4\eta e^3 \\ \frac{\partial u}{\partial W_1} \frac{\partial e}{\partial u} &= 4\eta e^3 K_1 X_1 \frac{\partial (r-y)}{\partial u} \\ \frac{\partial J}{\partial W_2} &= \Delta W_2 = -\frac{\partial}{\partial W_2} (e^4) = -4\eta e^3 \\ \frac{\partial u}{\partial W_2} \frac{\partial e}{\partial u} &= 4\eta e^3 K_1 X_2 \frac{\partial (r-y)}{\partial u} \end{aligned} \quad (7)$$

The term  $\partial y/\partial u$  is calculated based on the model of the system of Figure 2. The output of each control loop  $y$  is equal to the injected voltage  $E$  in each loop as shown in Figure 2. From the formula of (2) and the block diagram of Figure 2, it can be deduced that  $\partial y/\partial u$  is equal to 1 in both loops. Some modifications have been introduced to improve the overall adaptation mechanism for the controller parameters. These modifications are listed as follows.

- (1) In order to improve the stability of the adaptation mechanism. The normalized LMF is considered for adapting the controller parameters [25]. Its stability is improved because the input power does not depend on the adaptation mechanism as proved in [25]. The formula of (7) is modified such that the normalized least mean fourth algorithm is defined as

$$\begin{aligned} \Delta W_i(k) &= 4\eta e^3(k) K_1 \frac{X_i(k)}{\|X_i(k)\|^2} \\ &= \eta' e^3(k) K_1 \frac{X_i(k)}{\|X_i(k)\|^2} \end{aligned} \quad (8)$$

where the subscript  $i$  shown in (8) indicates either 1 or 2 as shown in (7).

- (2) The adaptation mechanism is again modified to fasten its convergence. The suggested modification is to make the step-size  $\eta'$  variable not fixed. A large step-size makes faster convergence and more fluctuation and vice versa. The effective variable step-size algorithm is defined in [26]

$$\begin{aligned} \eta'(k) &= \frac{\alpha p(k)}{X'(k) * X(k)} \\ X'(k) &= [X_1 \quad X_2] \\ X_1 &= e(k) - e(k-1) \\ X_2 &= e(k) \\ p(k) &= \lambda p(k-1) + (1-\lambda) X(k) e(k) \\ \eta'(k) &= \begin{cases} \eta'(k) & \eta'(k) < \eta_{max} \\ \eta_{max} & \eta'(k) > \eta_{max} \end{cases} \end{aligned} \quad (9)$$

TABLE 2: Parameters of proposed adaptive and regular PI controllers for positive loop.

| Parameters   | Value      |
|--|------------|
| Adaptive PI controller of d-axis in current loop   |            |
| $K_1$  | = 2e-4     |
| $\alpha$   | = 0.0125   |
| $\lambda$  | = 0.75     |
| $\eta_{max}$                                       | = 7.5e-3   |
| $p(0)$   | = 0        |
| $W_1(0)$   | = 5.25     |
| $W_2(0)$   | = 5        |
| Adaptive PI controller of q-axis in current loop   |            |
| $K_1$  | = 1.05e-4  |
| $\alpha$   | = 0.7      |
| $\lambda$  | = 0.000125 |
| $\eta_{max}$                                       | = 7.5e-5   |
| $p(0)$   | = 0        |
| $W_1(0)$   | = 5.25     |
| $W_2(0)$   | = 5        |
| Regular PI controller of d-axis in voltage control |            |
| $K_p$  | = 0.282    |
| $K_I$  | = 1.333    |
| Regular PI controller of q-axis in voltage control |            |
| $K_p$  | = 0.423    |
| $K_I$  | = 0.111    |

where  $\alpha$  is a factor selected by trial and error to balance between the convergence rate and stability of adaptation mechanism,  $\lambda$  is a forgetting factor used in the calculation of correlation process, and  $p(k)$  is an estimate of the correlation between the input and the error.

The final adaptation mechanism, including all proposed modifications, is defined as

$$\Delta W_1(k) = \eta'(k) e^3(k) K_1 \frac{X_1(k)}{\|X_1(k)\|^2} \quad (10)$$

$$W_1(k) = W(k-1) + \Delta W_1(k)$$

$$\Delta W_2(k) = \eta'(k) e^3(k) K_1 \frac{X_2(k)}{\|X_2(k)\|^2} \quad (11)$$

$$W_2(k) = W(k-1) + \Delta W_2(k)$$

where  $\eta'(k)$  is defined in (9). The final equations of the normalized least mean fourth algorithm (NLMF) are combined to form the self-adaptive PI controller of (6) along with (9), (10), and (11). The parameters of the suggested adaptation algorithm are tabulated in Table 2.

*3.1.2. Mathematical Formulation of Proposed Scheme for Unbalanced Loads.* The objective of the proposed scheme to

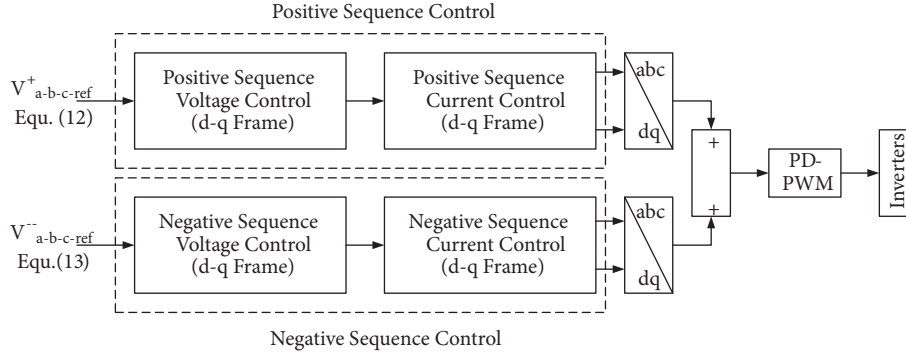


FIGURE 3: Complete operational block diagram for proposed scheme for positive and negative components.

deal with the unbalanced loads is to stabilize the positive-sequence voltages at 1 pu (100 %) and mitigate all negative-sequence voltages to the smallest possible level. The control diagram of Figure 2 is used for the positive-sequence voltages with the voltages references for the system under study of Figure 1 as follows.

$$V^+_{a-ref} = \frac{6.6}{\sqrt{3}} |0^0| \text{ kV}$$

$$V^+_{b-ref} = \frac{6.6}{\sqrt{3}} |-120^0| \text{ kV}, \quad (12)$$

$$\text{and } V^+_{c-ref} = \frac{6.6}{\sqrt{3}} |120^0| \text{ kV}$$

To deal with the negative-sequence components, another scheme similar to the control scheme of Figure 2 (current and voltage control loops) is paralleled with the original one to mitigate the negative-sequence voltages with the voltage references given as follows.

$$V^-_{a-ref} = 0 \text{ kV},$$

$$V^-_{b-ref} = 0 \text{ kV}, \quad (13)$$

$$\text{and } V^-_{c-ref} = 0 \text{ kV}$$

Even the mathematical formulation for the negative-sequence component is similar to (2) with changing the sign of  $\omega$ . The whole control block diagram for operating the microgrid at any load is clarified in Figure 3. Eventually, the output control signals of the positive-sequence and negative-sequence components are aggregated to operate the PD-PWM. The parameters of both adaptive and regular PI controllers of the negative-sequence components are tabulated in Table 3.

**3.1.3. Mathematical Formulation of Single-Neuron Adaptive PI Controller.** To prove the advantageous performance of the suggested controller, the proposed adaptive controller is compared to another commonly used adaptive PI controller, which is the single-neuron (single-perceptron) based PI controller. The single-neuron is the smallest unit in the neural

TABLE 3: Parameters of the proposed adaptive and regular PI controllers for negative loop.

| Parameters   | Value      |
|--|------------|
| Adaptive PI controller of d-axis in current loop   |            |
| $K_1$  | = 2e-4     |
| $\alpha$   | = 0.00125  |
| $\lambda$  | = 0.75     |
| $\eta_{max}$                                       | = 7.5e-3   |
| $p(0)$   | = 0        |
| $W_1(0)$   | = 5.25     |
| $W_2(0)$   | = 5        |
| Adaptive PI controller of q-axis in current loop   |            |
| $K_1$  | = 1.05e-4  |
| $\alpha$   | = 0.7      |
| $\lambda$  | = 0.000125 |
| $\eta_{max}$                                       | = 7.5e-5   |
| $p(0)$   | = 0        |
| $W_1(0)$   | = 5.25     |
| $W_2(0)$   | = 5        |
| Regular PI controller of d-axis in voltage control |            |
| $K_p$  | = 0.0625   |
| $K_i$  | = 0.5      |
| Regular PI controller of q-axis in voltage control |            |
| $K_p$  | = 0.0625   |
| $K_i$  | = 0.5      |

network; it is operated based on the Hebbian rule [27] where the updated weights are given as

$$\Delta W_i(k) = \zeta e(k) X_i(k) u(k)$$

$$W_i(k) = W_i(k-1) + \Delta W_i(k)$$

$$W'_i(k) = \frac{W_i(k)}{\sum_{i=1}^2 \|W_i(k)\|} \quad (14)$$

$$u(k) = u(k-1) + K_1 \sum_{i=1}^2 W'_i X_i(k)$$

TABLE 4: Parameters of single-neuron adaptive and regular PI controllers for positive loop.

| Parameters   | Value      |
|--|------------|
| Adaptive PI controller of d-axis in current loop   |            |
| $K_1$  | $= 1.5e-3$ |
| $\eta_{\rightarrow w_1}$                           | $= 6e-5$   |
| $\eta_{\rightarrow w_2}$                           | $= 3e-5$   |
| $W_1(0)$   | $= 1$      |
| $W_2(0)$   | $= 1$      |
| Adaptive PI controller of q-axis in current loop   |            |
| $K_1$  | $= 5e-5$   |
| $\eta_{\rightarrow w_1}$                           | $= 0.15$   |
| $\eta_{\rightarrow w_2}$                           | $= 0.015$  |
| $W_1(0)$   | $= 1$      |
| $W_2(0)$   | $= 1$      |
| Regular PI controller of d-axis in voltage control |            |
| $K_p$  | $= 0.0625$ |
| $K_I$  | $= 0.5$    |
| Regular PI controller of q-axis in voltage control |            |
| $K_p$  | $= 0.0625$ |
| $K_I$  | $= 0.5$    |

where  $\zeta$  is a positive fixed step less than one. The formulation of (14) is employed to adapt the parameters of the PI controller. The single-neuron PI controller replaces the proposed controller (normalized LMF based PI controller) in the control scheme of Figure 2 and operational block diagram of Figure 3. The parameters of the single-neuron adaptive PI controller for positive control loops that give the best performance are written in Table 4.

**3.1.4. Mathematical Formulation of Recursive Least Square Adaptive PI Controller.** For the sake of tough comparison, the proposed adaptive controller is compared to the recursive least square based PI controller (RLS-PI) presented in [27]. This PI controller parameters are recursively adapted using the same algorithm given in [27], which is newly formulated here as follows.

$$K_p(k+1) = K_p(k) + \eta X_2(k) \frac{dy(k)}{dx} X_1(k) \quad (15)$$

$$K_I(k+1) = K_I(k) + \eta X_2(k) \frac{dy(k)}{dx} X_2(k)$$

The adaptation mechanism of (15) is similar to those described before as  $X_1 = (e(k) - e(k-1))$ ,  $X_2 = e(k)$ , and  $\eta$  is a fixed learning rate. However, the adaptation of (15) differs in how to calculate the derivative term ( $dy(k)/dx$ ) with no need for the system model of Figure 2 or system equation of (2). The derivative term is calculated from the estimated function  $y(k)$  with respect to the input ( $x$ ), which is estimated using the least square-support vector machine (LS-SVM) defined in [28] as

$$y(k) = \sum_{i=1}^L (\alpha_i W_{k,i}(x_b)) + b \quad (16)$$

where  $W_{k,i}(x_{bo})$  (defined in (17)) is a Kernel function of the support vector machine (SVM), and it is a function of batch of  $n$  output data and  $m$  input data, represented in  $x_{bo}$  as  $x_{bo}(k) = [y(k) \dots y(k-n+1) \dots u(k) \dots u(k-m+1)]^T$ .

$$W_{k,i}(x_{bo}) = \exp\left(\frac{-1}{\sigma^2} (x_{bo}(k) - x_{bo}(j))^T (x_{bo}(k) - x_{bo}(j))\right) \quad (17)$$

$n$  and  $m$  are related to the system order. On the other hand,  $\alpha_i$  is a constant and it represents the  $i^{\text{th}}$  item in  $\alpha(k)$ , which is defined as

$$\alpha(k) = W_b(k) (Y_b(k) - 1_{L \times 1} b(k)) \quad (18)$$

where  $Y_b(k)$  is a batch of the output data points in the sliding window of length  $L$  sorted as  $Y_b(k) = [y(k) \dots y(k-L+1)]^T$ ,  $W_b(k)$  is the batch of the Kernel functions in the sliding window and it is defined in (19), and  $b(k)$  is the average constant of  $b$  in the sliding window and it is defined in (20).

$$W_b(k) = \begin{bmatrix} W_{k-1,k-1}(x_{bo}) + C & \dots & W_{k-L,k-1}(x_{bo}) \\ \vdots & \ddots & \vdots \\ W_{k-1,k-L}(x_{bo}) & \dots & W_{k-L,k-L}(x_{bo}) + C \end{bmatrix} \quad (19)$$

$$b(k) = \frac{W_b(k) Y_b(k)}{1_{L \times 1}^T W_b(k) 1_{L \times 1}} \quad (20)$$

where  $C$  is a constant. The derivative of (16) yields the following.

$$\frac{dy(k)}{dx} = \frac{1}{\sigma^2} \sum_{i=k-L}^{k-1} [\alpha_{i-k+L+1}(k) (u(k) - u(i)) W_{k,i}(x_{bo})] \quad (21)$$

The derivative formula in (21) is then plugged in (15). The RL-SVM based PI controller replaces the proposed controller (normalized LMF based PI controller) in the control scheme of Figure 2 and its operational block diagram of Figure 3. The parameters of the RL-SVM based PI controller for the positive control loop that give the best performance are written in Table 5.

**3.1.5. Mathematical Formulation of Sliding Mode Controller.** Another robust controller is added in this paper to compare its performance to the proposed controller of Figure 2. This candidate is very efficient since it is a robust nonlinear controller, which is the sliding mode controller. The adopted sliding mode controller is formulated for the current control loop. The mathematical formulation of this sliding mode control is already detailed in [19]. The utilized control law in this paper is an aggregated form of two terms, which are written as

$$n = n_c + n_{eq} \quad (22)$$

TABLE 5: Parameters of RL-SVM based PI and regular PI controllers for positive loop.

| Parameters   | Value    |
|--|----------|
| RL-SVM-PI controller of d-axis in current loop     |          |
| $K_p$  | = 1.5    |
| $K_I$  | = 1e-17  |
| $\eta_1$   | = 1e-6   |
| $\eta_2$   | = 1e-12  |
| $\sigma^2$   | = 100    |
| $C$  | = 10     |
| RL-SVM-PI controller of q-axis in current loop     |          |
| $K_p$  | = 1.5    |
| $K_I$  | = 1e-17  |
| $\eta_1$   | = 1e-6   |
| $\eta_2$   | = 1e-12  |
| $\sigma^2$   | = 100    |
| $C$  | = 10     |
| Regular PI controller of d-axis in voltage control |          |
| $K_p$  | = 0.0625 |
| $K_I$  | = 0.5    |
| Regular PI controller of q-axis in voltage control |          |
| $K_p$  | = 0.0625 |
| $K_I$  | = 0.5    |

where  $n_c$  is the corrective input, which pushes the system trajectory from its initial location to the sliding manifold, while  $n_{eq}$  is the equivalent input that keeps the system trajectory on the sliding manifold. The definition of the sliding manifold follows the integral sliding mode control and it is given as

$$s = e + \lambda \int edt \quad (23)$$

The corrective input is associated with a boundary layer to minimize the chattering and it is defined as

$$n_c = \begin{cases} -k_1 |s|^\alpha & \rightarrow s > \beta \\ -\frac{s}{\beta} & \rightarrow -\beta < s < \beta \\ +k_2 |s|^\alpha & \rightarrow s < -\beta \end{cases} \quad (24)$$

where  $k_1, k_2, \beta$  are positive constants.

The  $n_{eq}$  is designed such that the system with the sliding mode controller becomes stable; the system stability is derived by Lyapunov stability criterion such that the adopted Lyapunov function is selected to express the distance between the system's state and sliding manifold, and its definition is written as

$$V(s) = \frac{1}{2} s^T s \quad (25)$$

TABLE 6: Parameters of sliding mode and regular PI controllers for positive loop.

| Parameters   | Value    |
|--|----------|
| Sliding mode controller of d-axis in current loop  |          |
| $\lambda$  | = 100    |
| $k_1$  | = 0.8    |
| $k_2$  | = 0.8    |
| $\beta$  | = 20     |
| Sliding mode controller of q-axis in current loop  |          |
| $\lambda$  | = 81     |
| $k_1$  | = 0.8    |
| $k_2$  | = 0.8    |
| $\beta$  | = 20     |
| Regular PI controller of d-axis in voltage control |          |
| $K_p$  | = 0.0625 |
| $K_I$  | = 0.5    |
| Regular PI controller of q-axis in voltage control |          |
| $K_p$  | = 0.0625 |
| $K_I$  | = 0.5    |

The derivative of this function should be less than or equal to zero as

$$\dot{V}(s) = \frac{dV(s)}{ds} \frac{ds}{dt} = s^T \dot{s} \leq 0 \quad (26)$$

For tracking problem like the case of this paper,  $\dot{V}(s) = 0 \rightarrow \dot{s} = 0$ , which leads to the following.

$$\begin{aligned} \dot{s} &= \dot{e} + \lambda e = 0 \\ \dot{s} &= (\dot{r} - \dot{y}) + \lambda e \end{aligned} \quad (27)$$

The state space form of the system model is given as

$$\dot{y} = Ax + Bu + Fd \quad (28)$$

Substitution of (28) in (27) leads to the following.

$$\dot{s} = -(Ax + Bn_{eq} + Fd) + \lambda e = 0 \quad (29)$$

The Lyapunov function requires that its derivative is equal to zero for the stable system. This condition yields the following.

$$\dot{s} = -(Ax + Bn_{eq} + Fd) + \lambda e = 0 \quad (30)$$

Eventually, the equivalent input is given as

$$n_{eq} = -(B)^{-1} (Ax + Fd - \lambda e) \quad (31)$$

The control law of (22) and (23) with its two terms in (24) and (31) is used to control the injected current of the primary control loop. Eventually, this current controller replaces the proposed adaptive PI controller in the control scheme of Figure 2 and its operational block diagram of Figure 3. The parameters of the sliding mode controllers for positive control loops are written in Table 6.

**3.2. Structure of Proposed Control Scheme for Grid-Connected Mode.** Sometimes the microgrid is required to be connected to the main power grid (distribution system) in order to acquire some benefits [4, 5]. The main challenge that faces the suggested control scheme in the grid-connected mode is how to transfer the control concept from the constant voltage/frequency operation to constant current/power operation because both the grid voltage and its frequency are governed by the power grid in a grid-connected mode. Therefore, an additional power control loop is integrated with the utilized operational scheme as depicted in Figure 2. In this additional control loop, any power reference is converted into a current reference, which is consequently applied (as input) to the primary current control loop of the scheme illustrated in Figure 2. The power formula in the  $d-q$  frame is expressed as

$$\begin{bmatrix} P \\ Q \end{bmatrix} = \frac{3}{2} \begin{bmatrix} V_{DG-d} & V_{DG-q} \\ V_{DG-q} & -V_{DG-d} \end{bmatrix} \begin{bmatrix} I_{DG-d} \\ I_{DG-q} \end{bmatrix} \quad (32)$$

Then, the current reference of power control can be deduced using the inverse of (32) as

$$\begin{bmatrix} I_{DG-d-ref} \\ I_{DG-q-ref} \end{bmatrix} = \frac{2}{3} \begin{bmatrix} V_{DG-d} & V_{DG-q} \\ V_{DG-q} & -V_{DG-d} \end{bmatrix}^{-1} \begin{bmatrix} P_{ref} \\ Q_{ref} \end{bmatrix} \quad (33)$$

#### 4. Comparing Proposed Adaptive PI to Other Controllers

The objective of this section is to validate the meritorious characteristics of the proposed controller along with the suggested scheme for the microgrid operation. This section includes comparisons between the proposed controller and the regular PI controller, single-neuron adaptive PI controller, recursive least square adaptive PI controller, and sliding mode controller for the same control scheme including its block diagram given in Figures 2 and 3. For all subsequent sections, the comparison encompasses the performance of each controller during the starting of the microgrid whose loads are the parallel combination of two balanced loads of  $Z_{load1-phase} = 55 + 18.84j$  and  $Z_{load2-phase} = 65 + 31.4j$  (all impedances in this section are referred to the primary side of transformer  $tr_2$  in Figure 1). At time  $t = 2.5$  s, the second load is disconnected and the first load remains connected to the microgrid.

**4.1. Comparing Regular PI Controller to Proposed Controller.** In order to justify the praiseworthy performance of the proposed scheme, its performance is compared to the regular PI controller. This regular PI controller replaces the proposed controller in the control scheme of Figure 2 and in the whole operational diagram in Figure 3. The parameters of PI controllers that give the optimized performance are listed in Table 7. The rms voltage profile in percent of the load side at the point of common coupling (PCC) is given in Figure 4(a) with the voltage profile of the proposed controller to compare both profiles, and the zoom-in view for both voltages is given in Figure 4(b). It is worth mentioning that

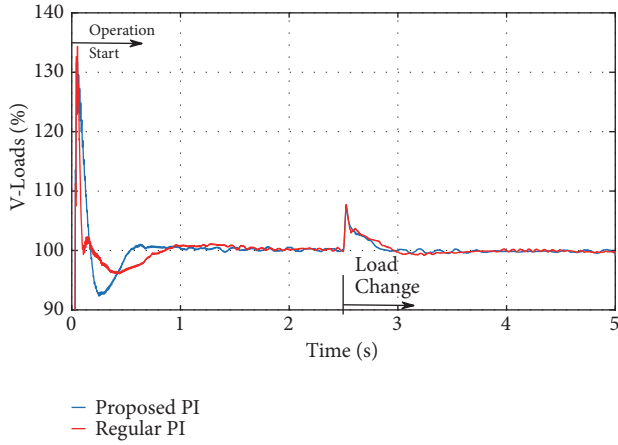
TABLE 7: Parameters of regular PI controllers for positive control loop.

| Parameters   | Value    |
|--|----------|
| Regular PI controller of d-axis in current control |          |
| $K_p$  | = 1      |
| $K_I$  | = 18.75  |
| Regular PI controller of q-axis in current control |          |
| $K_p$  | = 1.5    |
| $K_I$  | = 18.75  |
| Regular PI controller of d-axis in voltage control |          |
| $K_p$  | = 0.0625 |
| $K_I$  | = 0.5    |
| Regular PI controller of q-axis in voltage control |          |
| $K_p$  | = 0.0625 |
| $K_I$  | = 0.5    |

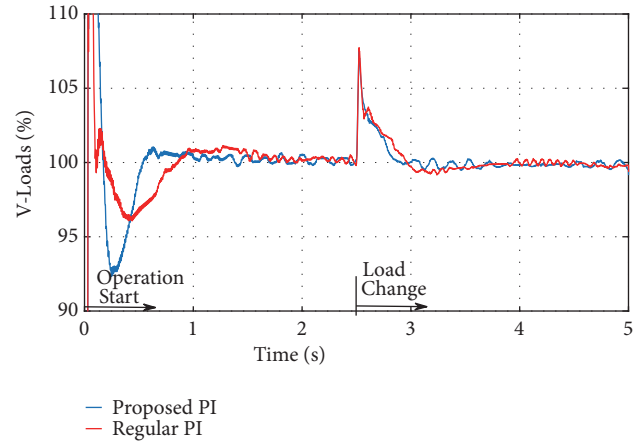
the proposed controller has a better performance than the regular PI controller for all operating conditions. Figure 4(a) affirms that the transient performance of the regular PI is not guaranteed at all operating conditions. The oscillation around 100% does not exceed  $\pm 1\%$ . The adaptation of the proposed controller weights ( $W_1, W_2$ ) in the d-axis current control loop is illustrated in Figure 4(c). Also, the current performance (current reference vs feedback current) of the d-axis current control is elucidated in Figure 4(d), which shows good transient and steady-state performance. In addition, the formula shown in (9) is used to change the step-size ( $\eta'(n)$ ) such that at the beginning of the adaptation process it becomes very small to stabilize the adaptation mechanism; afterward it gets bigger when the adaptation reaches its steady state to fasten its convergence. This variable step-size  $\eta'(n)$  is shown in Figure 4(e).

**4.2. Comparing Single-Neuron Adaptive PI Controller to Proposed Controller.** The single-neuron adaptive PI controller is another strong candidate for comparison. This controller is already explained before, where the parameters of the controller,  $K_p, K_I$ , are recursively tuned such that the mean square error becomes minimum as explained earlier. The parameters of the controllers are already written in Table 4. The rms voltage in percent is portrayed in Figure 5(a) with the performance of the proposed controller, and its zoom-in view is also depicted in Figure 5(b). Figure 5 reveals that the proposed controller is faster than the single-neuron PI controller at the starting of the microgrid operation and at the load change after time  $t > 2.5$  s.

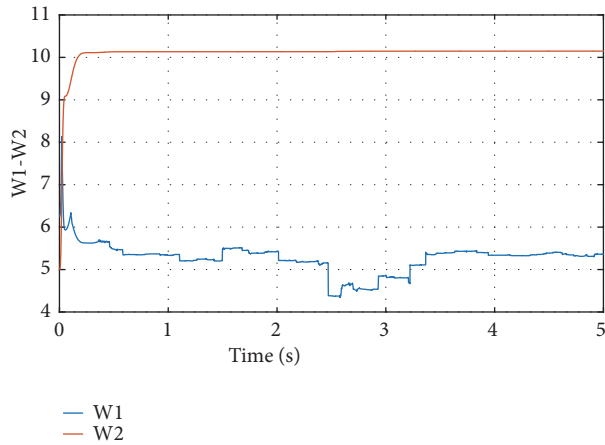
**4.3. Comparing Recursive Least Square Adaptive PI Controller to Proposed Controller.** This section shows the performance of the recursive least square-support vector machine based adaptive PI controller. The mathematical formulation is already explained in a previous section. The recursive least square PI controller replaces the proposed controller in Figure 2 and in its overall operational block diagram of



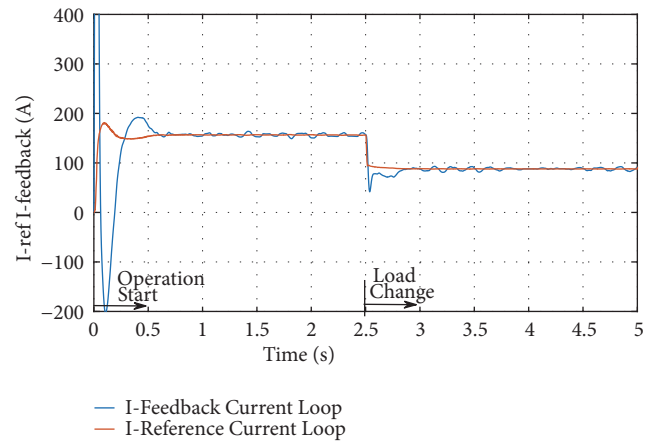
(a) Voltage profile at PCC for regular PI controller and proposed controller



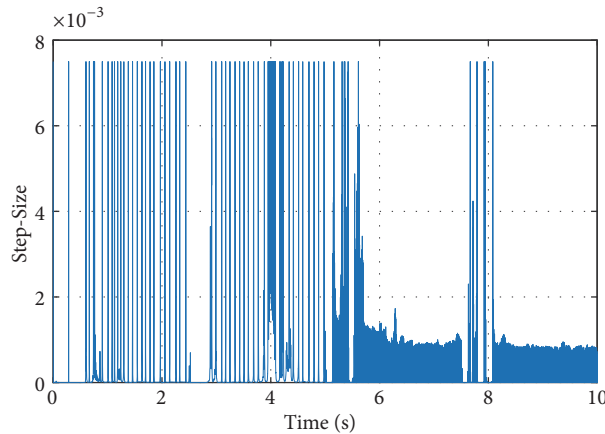
(b) Zoom-in view for voltage curves in Figure 4(a)



(c) Adaption of controller weights (W1, W2) for d-axis current control loop



(d) Performance of current reference and feedback current for d-axis current control loop

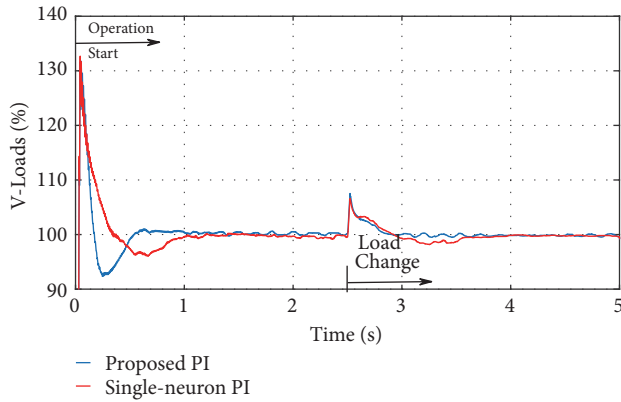


(e) Performance of variable step size for d-axis current control loop

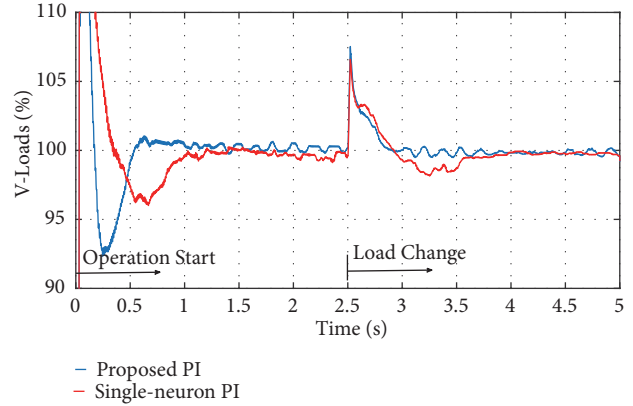
FIGURE 4: Performance of regular PI controller compared to proposed controller along with parameters adaptation.

Figure 3. Its performance is depicted in Figure 6(a) with the performance of the proposed controller, and its zoom-in view is displayed in Figure 6(b). From Figure 6, it is clear that the proposed controller is faster with more oscillation at the start of the microgrid operation and at the load change.

4.4. Comparing Sliding Mode Controller to Proposed Controller. The sliding mode is a robust nonlinear controller used for nonlinear and linear systems. This controller, explained in a previous section, is adopted in the control scheme of Figure 2 instead of the proposed controller. The controller

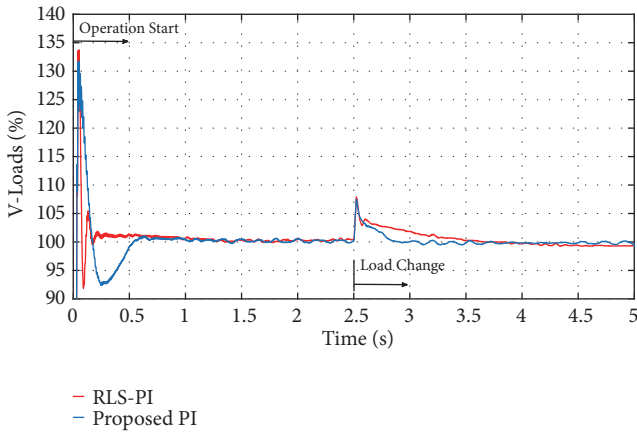


(a) Voltage profile at PCC for single-neuron adaptive PI controller and proposed controller

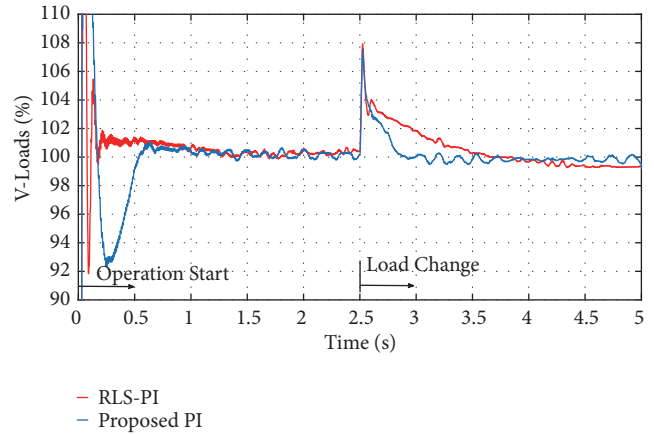


(b) Zoom-in view for voltage curves in Figure 5(a)

FIGURE 5: Performance of single-neuron PI controller compared to proposed controller.



(a) Voltage profile at PCC for recursive least square PI controller and proposed controller



(b) Zoom-in view for voltage curves in Figure 6(a)

FIGURE 6: Performance of recursive least square PI controller compared to proposed controller.

parameters, which give the best performance for this microgrid, are written in Table 6. The performance of the SMC is displayed in Figure 7(a) compared to the proposed controller, and its zoom-in view is portrayed in Figure 7(b). This figure indicates that the sliding mode controller has less overshoot/undershoot and the proposed controller converges faster to minimize its error. The major difference between the proposed controller and the sliding mode controller is that the later controller needs the full model of the system and the proposed controller works without utilizing any model for the microgrid.

**4.5. Quantitative Comparisons between Proposed Controller and Other Controllers.** In previous subsections, the proposed controller is compared to some linear/adaptive/nonlinear controllers to affirm its good characteristics for the operation of the microgrid at different operating conditions. The summary of this comparisons is tabulated in Table 8.

## 5. Simulation Results of Proposed Operational Scheme in Microgrid Mode

This section is divided into some subsections to show the performance of the proposed scheme, which stabilizes the voltage at the load side for different loading conditions.

**5.1. Variable Balanced Loads.** This section exhibits the simulation results for the proposed scheme and controller documented in a previous section and depicted in Figures 2 and 3 for the microgrid of Figure 1. The loads in the microgrid are the parallel combination of two balanced loads of  $Z_{load1-phase} = 55 + 18.84j$  and  $Z_{load2-phase} = 65 + 31.4j$ . At time  $t = 2.5$  s, the second load is disconnected and the first load remains connected to the grid. The voltages at the inverters' bus and after transformer bus (before and after the used filter) are given in Figure 8(a). The rms voltage in percent at the point of common coupling (PCC) is displayed in Figure 8(b). In the control scheme of Figure 2, the output

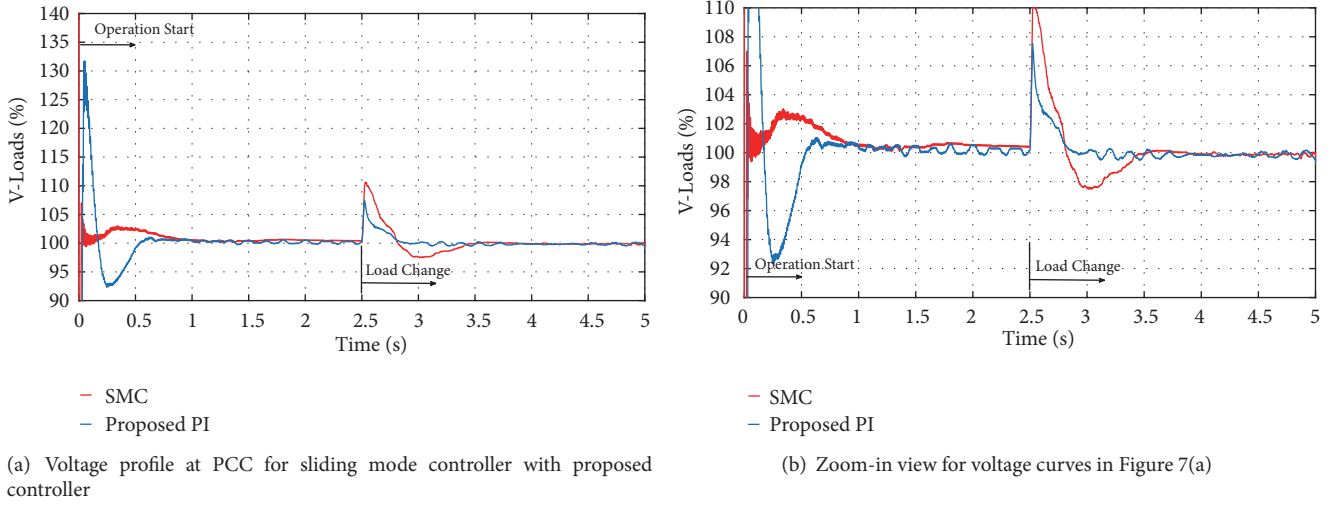


FIGURE 7: Performance of sliding mode controller compared to proposed controller.

TABLE 8: Comparative analysis of proposed controller with other linear/adaptive/nonlinear controllers.

| Parameters  | Proposed Adaptive Controller            | Regular PI Controller                         | Single-Neuron Adaptive PI                | Recursive Least Square Adaptive PI              | SMC                             |                      |
|---|---|---|--|---|---------------------------------|----------------------|
| Average steady-state error (%)  | < 0.5 %                                 | < 1 %   | < 0.5 %                                  | 2 %   | 1 %                             |                      |
| Average settling time (s)   | 0.5 s                                   | 1 s   | 1 s                                      | 1.5 s   | 1 s                             |                      |
| 1 <sup>st</sup> overshoot (%)   | at the start of microgrid operation     | 32 %  | 34 %                                     | 32 %  | 34 %                            | Large for short time |
| 1 <sup>st</sup> undershoot (%)  |   | 7 %   | 4 %                                      | 4 %   | 8 %                             | 0 %                  |
| Variation of controller performance with operating conditions (at time= 0 s and time = 2.5 s) | Small - almost same optimum performance | Large - optimum performance is not guaranteed | Medium - almost same optimum performance | Medium - performance differ from one to another | Small - almost same performance |                      |

of the switching modulation (PD-PWM) is applied on each inverter separately. Therefore, the load power (active and reactive) is equally shared among the working inverters. The load active power and the injected active power by three inverters are given in Figures 8(c), 8(d), 8(e), and 8(f), respectively. The reactive power has a similar performance to the active power sharing of Figure 8. Another advantage of using the 5-level diode-clamped inverter is exemplified in Figure 8(g), where the voltage THD of the injected voltage is less than 2% at any operating condition.

**5.2. Variable Unbalanced Loads.** This section depicts the simulation results for the suggested scheme in a previous section, which is depicted in Figure 3 for the positive- and negative-sequence control loops. Before time  $t < 5$  s, the existing balanced load in the system is  $Z_{load1} = 55 + 18.84j$ . At time  $t = 5$  s, the first unbalanced loads are connected to the system; these loads are  $Z_{load-a} = 25 + 6.28j$ ,  $Z_{load-b} = 50 + 31.4j$ , and  $Z_{load-c} = 35 + 15.7j$ , which are attached in parallel to the original balanced loads. At time  $t = 7.5$  s, the second unbalanced loads of  $Z_{load-a} = 30 + 9.42j$ ,  $Z_{load-b} = 35 + 11j$ , and  $Z_{load-c} = 45 + 14.13j$  are connected

to the loads mentioned above. The rms voltage in percent is given in Figure 9(a) for the connection of two groups of unbalanced loads. The effectiveness of the mitigation for the negative-sequence voltage by its control loop is manifested by the negative-sequence factor as defined in IEEE Standard 1159-1995, which should not be greater than 2%. Figures 9(b) and 9(c) show the negative-sequence factor without and with using its control loop (lower blocks) in Figure 3. The reflection of the small negative-sequence factor is shown in the instantaneous voltage and current waveforms at the loads, shown in Figures 10(a) and 10(b), respectively.

**5.3. Nonlinear Loads.** The nonlinear load is a drastically problematic issue for the droop control schemes because the conventional droop is designed to let all generators share the fundamental components only. The existence of harmonics adds more complexity to the droop control [29]. On the contrary, the proposed scheme handles the harmonics without any modification or adding more complexity since each inverter is given the same control signals (output of the PD-PWM) to stabilize the voltage at the loads. Therefore, the load harmonics are evenly shared among the inverters. This

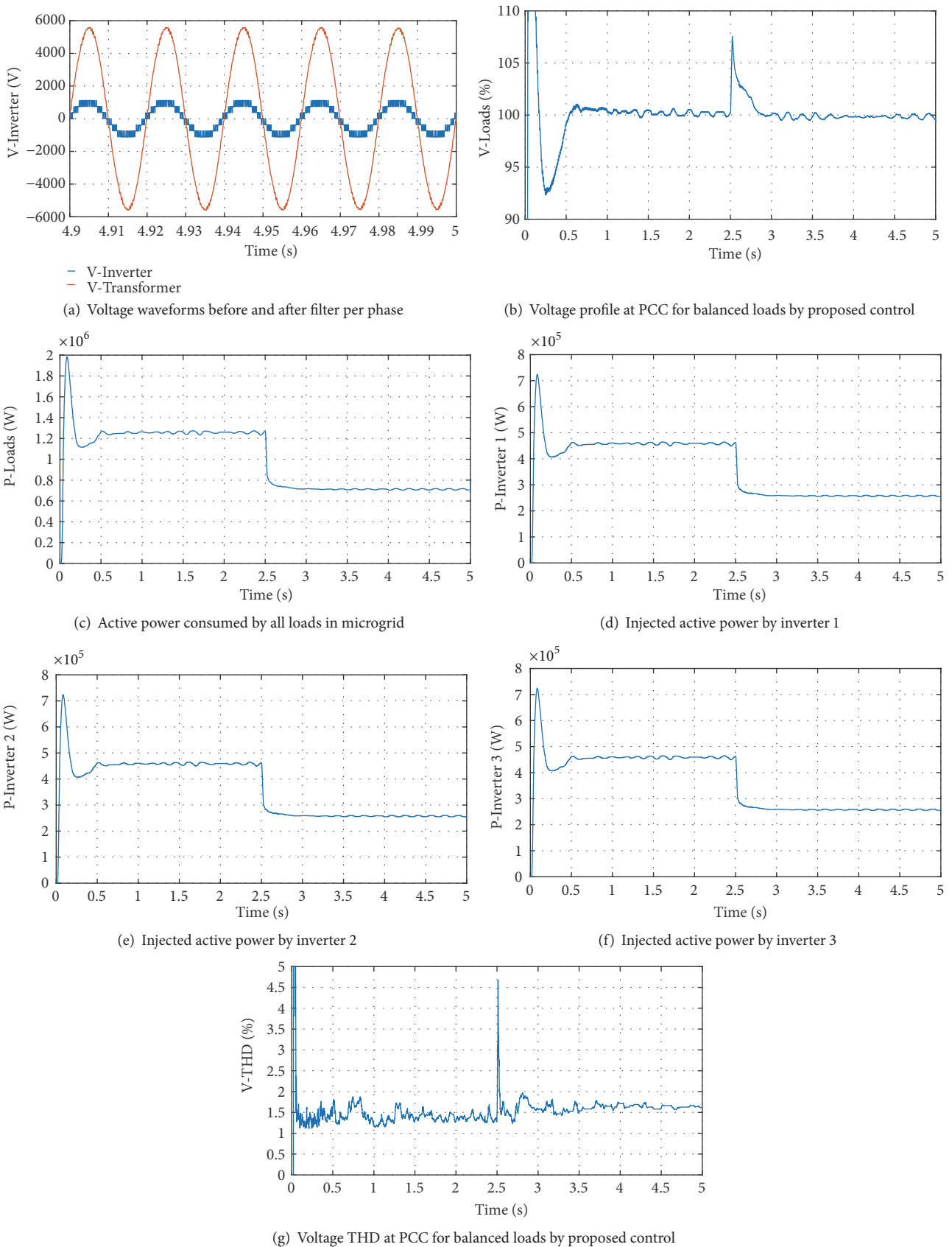


FIGURE 8: Voltage profile, power sharing, and THD at PCC for balanced loads by proposed control.

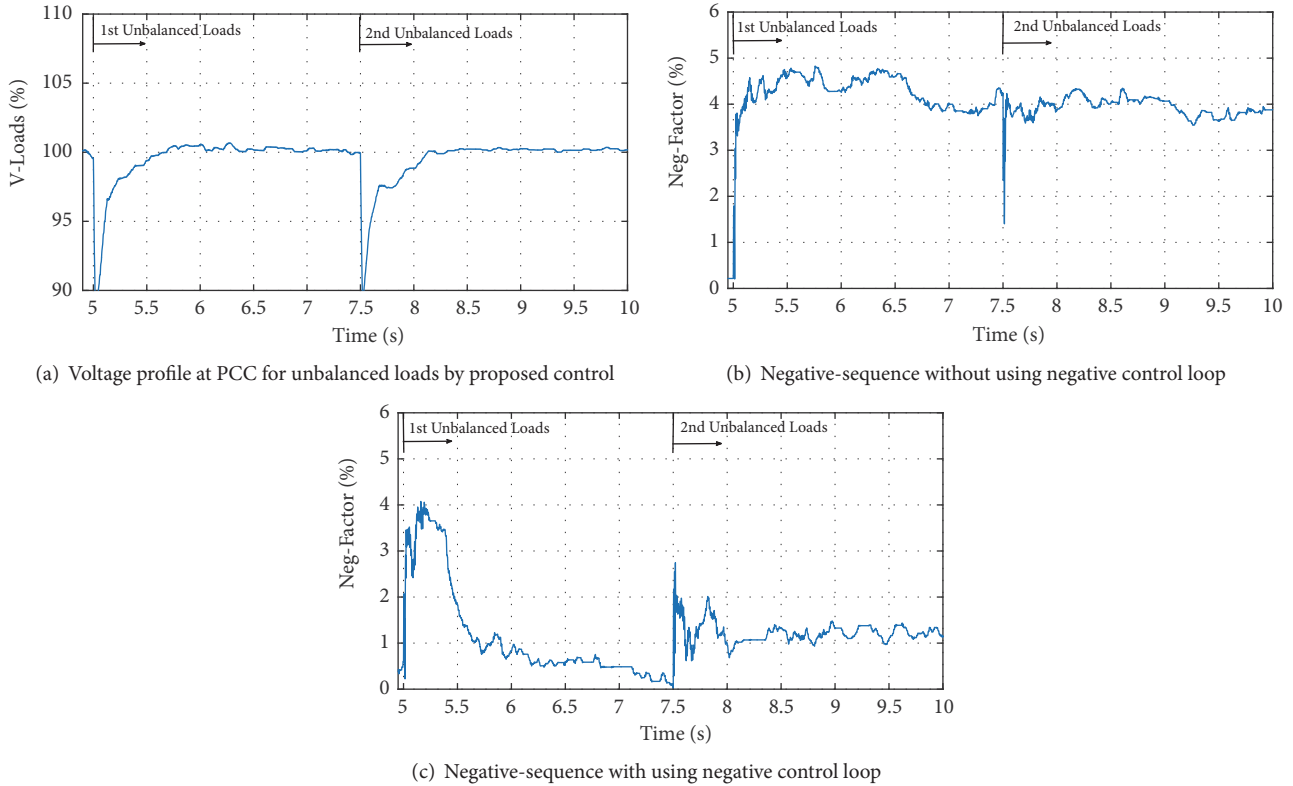
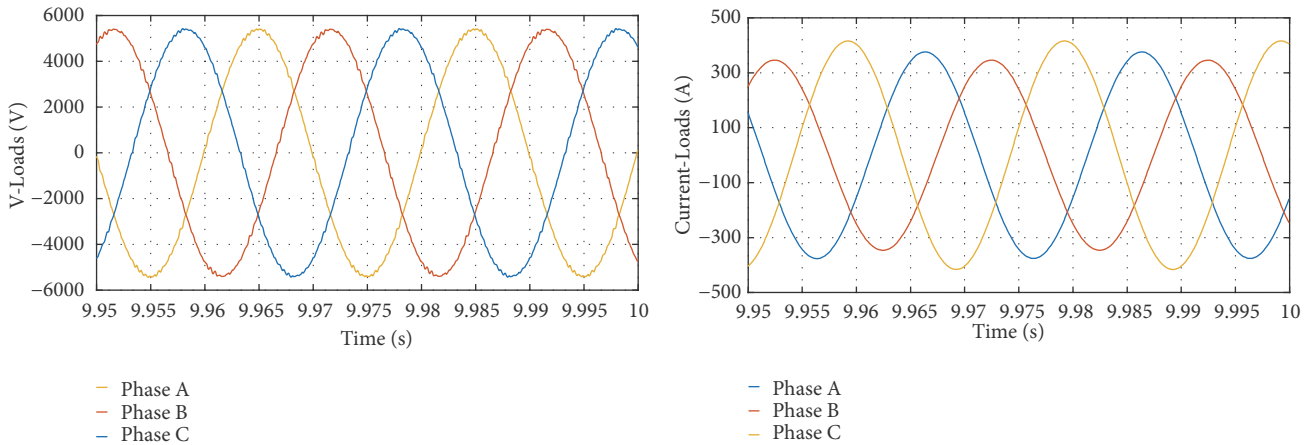


FIGURE 9: Voltage profile and negative-sequence factor with and without using negative control loop.



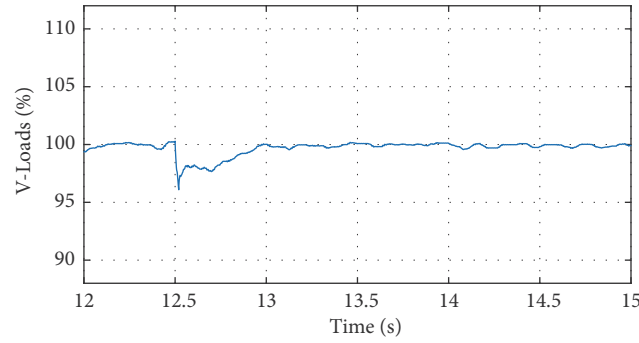
(a) Instantaneous voltage waveforms at load side (PCC) with unbalanced loads

(b) Instantaneous current waveforms with unbalanced loads

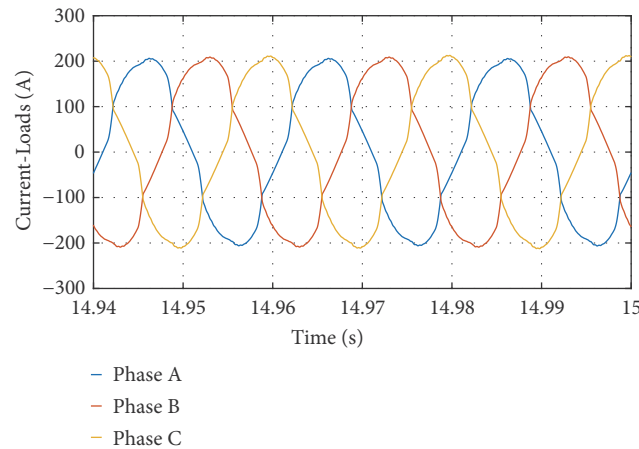
FIGURE 10: Instantaneous voltage and current waveforms with unbalanced loads.

equal distribution of harmonics among the inverters comes naturally (plug-and-play capability) due to the structure of the proposed operational (control) scheme depicted in Figure 2. The nonlinear load is presented by diode bridges with a highly inductive load. This nonlinear load is added to the system at time  $t = 12.5$  s with the balanced original load of  $Z_{load1} = 55 + 18.84j$ . The rms voltage in percent is given in Figure 11(a). The total three-phase load currents are given in Figure 11(b).

**5.4. Loss/Reconnection of Any Inverter (Generation Unit) to Microgrid.** In the droop control scheme, the loss of any inverter greatly influences the transient performance at the instant of the inverter loss [29]. This transition requires the droop control to have a high bandwidth in order to recover the voltage fast. Another advantage of the proposed scheme is its seamless transitional profile during the loss or reconnection of any inverter circuit. The smooth transient performance emanates from the propounded structure of



(a) Voltage profile at PCC for nonlinear loads by proposed controller



(b) Instantaneous three-phase load current for all loads

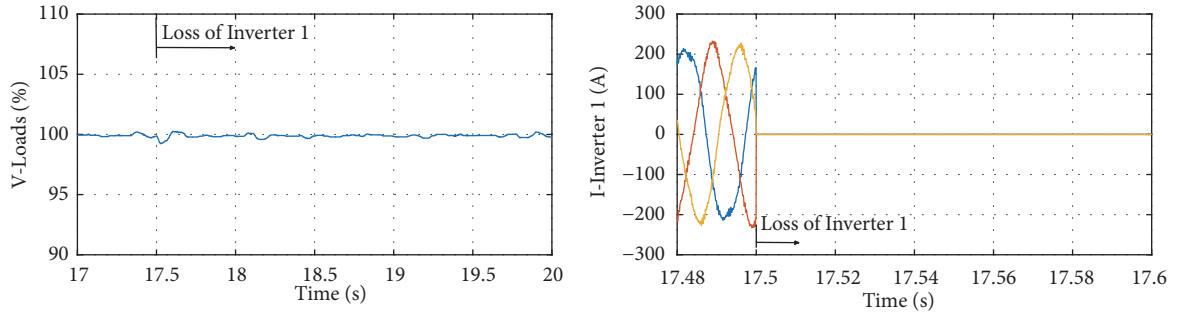
FIGURE 11: Voltage and current performance during nonlinear loads.

the control scheme because the output of the modulation technique (PD-PWM) is applied on all inverters at the same time, meaning that each inverter works independently of the other inverters to stabilize the voltage at the loads during any transition. As a result, the load current is equally divided among the existing (working) inverters. At time  $t = 17.5$  s, the inverter-1 is disconnected, and both inverter-2 and inverter-3 are adaptively sharing the loads' currents; that is why there is an increase in the injected current generated by inverter-2 and inverter-3. Consequently, the injected voltage of each existing inverter also changes (slightly increases) to accommodate the change in the injected current. The rms voltage profile in percent during the loss of the inverter-1 is illustrated in Figure 12(a). The three-phase currents of all three inverters are portrayed in Figures 12(b), 12(c), and 12(d). The instantaneous voltage waveforms per phase (before the transformer) of inverter-2 (or inverter-3) before and after the instant of inverter-1 loss are depicted in Figures 12(e) and 12(f), respectively. These two figures (Figures 12(e) and 12(f)) show a difference in the pattern of the voltage pulses, where the pulses of the voltage waveform (after the loss of inverter-1) are wider; this indicates more injected voltage at inverters' bus to push more currents as shown in Figures 12(c) and 12(d). Almost an adverse performance can be obtained when a new inverter is connected to the microgrid.

## 6. Simulation Results of Proposed Operational Scheme in Grid-Connected Mode

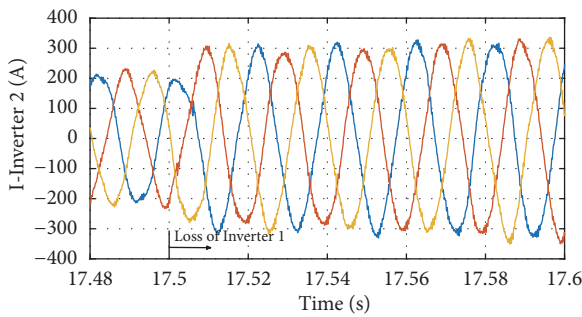
The microgrid has an advantage of autonomous working, or working connected to the power grid. The connection between both grids fetches some merits to the microgrid and power grid as well [30]. The current references of (33) are plugged to the current control loop as shown in Figure 2 so as to operate the power control. In order to have a smooth transition from the microgrid operation (microgrid mode) to the grid-connected mode, the following procedure is suggested.

- (1) The current control is adjusted such that its input current references are transferred from the microgrid operation (upper block-voltage control of Figure 2) to the grid-connected mode (lower block-power control of Figure 2). Meaning that the outputs of the voltage control (upper block) in Figure 2 become zero.
- (2) The power references are adjusted to barely cover the loads' power inside the microgrid only. Therefore, the exchanged power and tie-feeder current between both grids are zero. At this operating condition, the connection between both grids can be established.
- (3) After step-2 is successfully realized, the power references are adjusted such that the power can be injected or absorbed in the tie feeder between both grids.

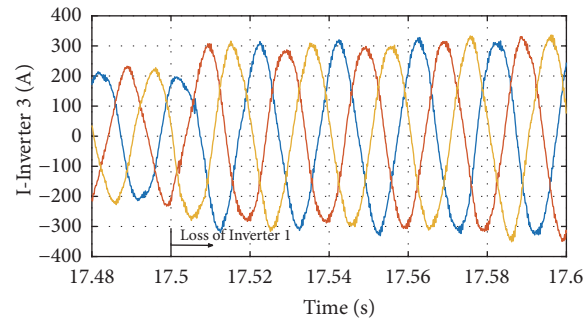


(a) Voltage profile at PCC during loss of inverter 2 by proposed controller

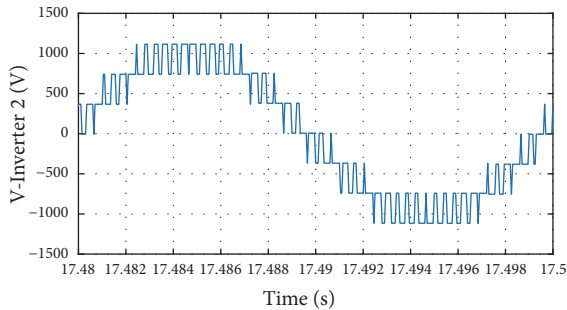
(b) Three-phase currents of inverter-1 during loss of inverter-1



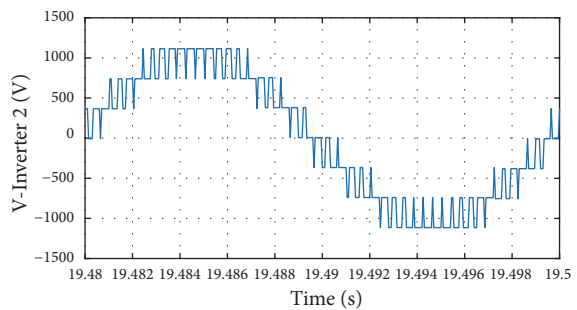
(c) Three-phase currents of inverter-2 during loss of inverter-1



(d) Three-phase currents of inverter-3 during loss of inverter-1



(e) Voltage waveform Inverter-2 (or inverter-3) of one phase (phase A) before loss of inverter-1



(f) Voltage waveform Inverter-2 (or inverter-3) of one phase (phase A) after loss of inverter-1

FIGURE 12: Root mean square (rms) and instantaneous voltage and instantaneous current waveforms during loss of inverter 1.

This aforementioned transition from the microgrid operation (microgrid mode) to the grid-connected mode is depicted in Figure 13(a), which shows the three steps mentioned above and the active power tracking performance to arbitrary power references. Also, the reactive power performance is depicted in Figure 13(b). In Figure 13 at time  $t = 20$  s, the operation is intentionally transferred from the microgrid operation (microgrid mode) to the grid-connected mode. The transient time is almost 1 s for any transition in power and the performance tends to be of 1st order due

to the suggested adaptation mechanism of the PI controller parameters.

Figure 14 gives more clarification to Figure 13, and it proves the advantages of connecting the microgrid to the main power grid for the same power curves of Figure 13. As shown in Figure 14 from time  $t = 20$  s till  $t = 22.5$  s, the power references are adjusted to cover the loads inside the microgrid only. Therefore, the exchanged power between both grids is zero ( $P_{tie}=0$ ). If the power reference is greater than what the loads inside the microgrid need, then the

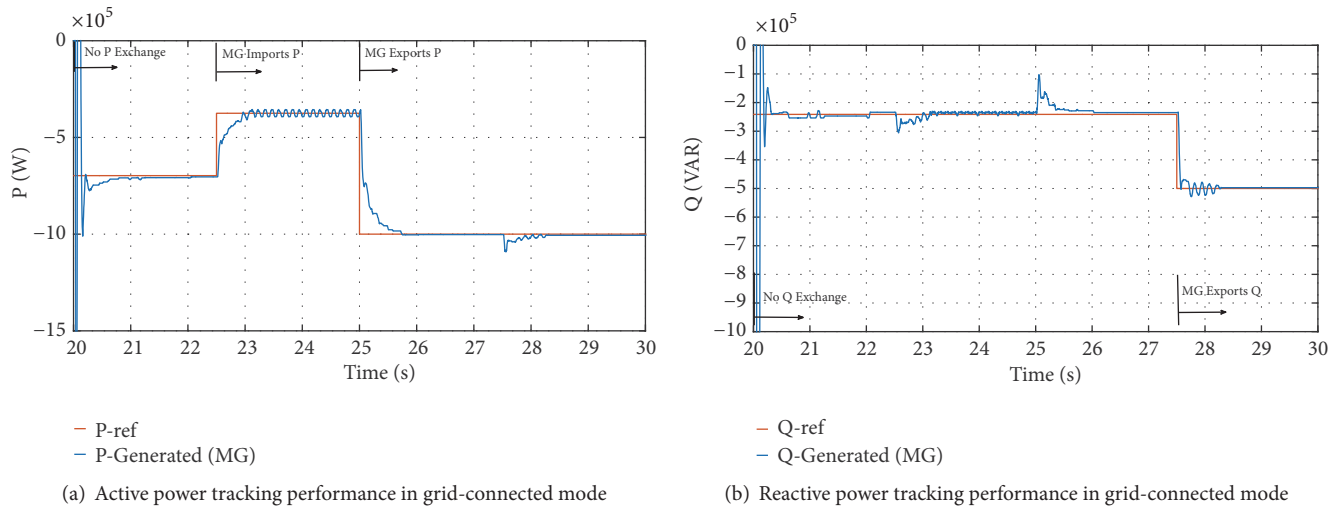


FIGURE 13: Power tracking performance in grid-connected mode of control scheme.

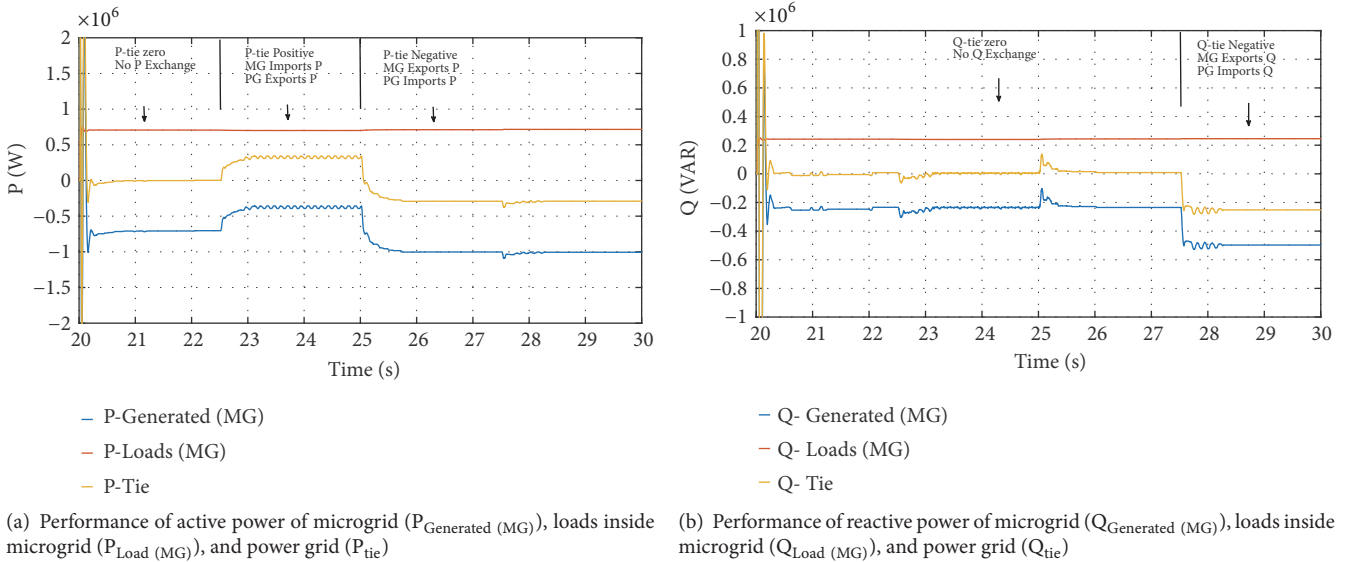


FIGURE 14: Active and reactive Powers of microgrid, loads inside microgrid, and power grid in grid-connected mode.

rest of the generated power ( $P_{Generated(MG)}$ ) is exported from the microgrid (MG) to the power grid (PG) and vice versa. The exchanged active power between the microgrid and power grid ( $P_{Tie}$ ), microgrid load power ( $P_{Load(MG)}$ ), and generated power of the microgrid ( $P_{Generated(MG)}$ ) is depicted in Figure 14(a), and in Figure 14(b) the reactive power is depicted.

## 7. Conclusion

This paper presents an innovative operational scheme for the microgrid. This scheme has a new adaptive PI controller, which is based on an improved normalized least mean fourth algorithm. This adaptation mechanism is developed with a variable step-size technique in order to fasten its convergence and enhance its stability. The proposed operational scheme

along with the developed controller is used to stabilize the magnitude and frequency of the voltage across the loads. This voltage is maintained around 1 pu (100% percent) at different loading conditions such as balanced, unbalanced, and nonlinear loads. The proposed scheme outperforms other linear, adaptive, and nonlinear controllers based similar schemes for the same microgrid operating conditions. Also, the propounded scheme has an advantage of enabling the microgrid to operate in a grid-connected mode and to seamlessly transfer from the microgrid mode (voltage control mode) to grid-connected mode (power control mode).

## Data Availability

The data used to support the findings of this study are available from the corresponding author upon request.

## Disclosure

A. Elnady serves as an Adjunct Associate Professor at Royal Military College of Canada.

## Conflicts of Interest

The authors declare that they have no conflicts of interest.

## Funding

This research work is sponsored by the University of Sharjah under the grant no 1802040393-P.

## References

- [1] R. H. Lasseter, "Smart distribution: Coupled microgrids," *Proceedings of the IEEE*, vol. 99, no. 6, pp. 1074–1082, 2011.
- [2] A. Hirsch, Y. Parag, and J. Guerrero, "Microgrids: A review of technologies, key drivers, and outstanding issues," *Renewable & Sustainable Energy Reviews*, vol. 90, pp. 402–411, 2018.
- [3] K. S. Rajesh, S. S. Dash, R. Rajagopal, and R. Sridhar, "A review on control of ac microgrid," *Renewable & Sustainable Energy Reviews*, vol. 71, pp. 814–819, 2017.
- [4] Q. Jiang, M. Xue, and G. Geng, "Energy management of microgrid in grid-connected and stand-alone modes," *IEEE Transactions on Power Systems*, vol. 28, no. 3, pp. 3380–3389, 2013.
- [5] S. Parhizi, H. Lotfi, A. Khodaei, and S. Bahramirad, "State of the art in research on microgrids: A review," *IEEE Access*, vol. 3, pp. 890–925, 2015.
- [6] H. Han, X. Hou, J. Yang, J. Wu, M. Su, and J. M. Guerrero, "Review of power sharing control strategies for islanding operation of AC microgrids," *IEEE Transactions on Smart Grid*, vol. 7, no. 1, pp. 200–215, 2016.
- [7] S. K. Khadem, M. Basu, and M. F. Conlon, "Parallel operation of inverters and active power filters in distributed generation system - A review," *Renewable & Sustainable Energy Reviews*, vol. 15, no. 9, pp. 5155–5168, 2011.
- [8] P. Monica and M. Kowsalya, "Control strategies of parallel operated inverters in renewable energy application: A review," *Renewable & Sustainable Energy Reviews*, vol. 65, pp. 885–901, 2016.
- [9] J. Rocabert, A. Luna, F. Blaabjerg, and P. Rodríguez, "Control of power converters in AC microgrids," *IEEE Transactions on Power Electronics*, vol. 27, no. 11, pp. 4734–4749, 2012.
- [10] C. A. Canizares and R. Palma-Behnke, "Trends in microgrids control," *IEEE Transactions on Smart Grid*, vol. 5, no. 4, pp. 1905–1919, 2014.
- [11] A. M. Bouzid, J. M. Guerrero, A. Cheriti, M. Bouhamida, P. Sicard, and M. Benghanem, "A survey on control of electric power distributed generation systems for microgrid applications," *Renewable & Sustainable Energy Reviews*, vol. 44, pp. 751–766, 2015.
- [12] N. Hur and K. Nam, "A robust load-sharing control scheme for parallel-connected multisystems," *IEEE Transactions on Industrial Electronics*, vol. 47, no. 4, pp. 871–879, 2000.
- [13] M. Borrega, L. Marroyo, R. González, J. Balda, and J. L. Agorreta, "Modeling and control of a master-slave PV inverter with n-paralleled inverters and three-phase three-limb inductors," *IEEE Transactions on Power Electronics*, vol. 28, no. 6, pp. 2842–2855, 2013.
- [14] W. Tsai-Fu, Y.-K. Chen, and H. Yong-Heh, "3C strategy for inverters in parallel operation achieving an equal current distribution," *IEEE Transactions on Industrial Electronics*, vol. 47, no. 2, pp. 273–281, 2000.
- [15] S. J. Chiang, C. H. Lin, and C. Y. Yen, "Current limitation control technique for parallel operation of UPS inverters," in *Proceedings of the 35th Annual Power Electronics Specialists Conference*, vol. 3, pp. 1922–1926, Aachen, Germany, 2004.
- [16] X. Q. Guo and W. Y. Wu, "Improved current regulation of three-phase grid-connected voltage-source inverters for distributed generation systems," *IET Renewable Power Generation*, vol. 4, no. 2, pp. 101–115, 2010.
- [17] J. M. Espí, J. Castelló, R. García-Gil, G. Garcerá, and E. Figueres, "An adaptive robust predictive current control for three-phase grid-connected inverters," *IEEE Transactions on Industrial Electronics*, vol. 58, no. 8, pp. 3537–3546, 2011.
- [18] Y. A.-R. Ibrahim Mohamed and E. F. El-Saadany, "An improved deadbeat current control scheme with a novel adaptive self-tuning load model for a three-phase PWM voltage-source inverter," *IEEE Transactions on Industrial Electronics*, vol. 54, no. 2, pp. 747–759, 2007.
- [19] A. Elnady, "Newly developed 1st order sliding mode of power and voltage control of multilevel inverter based distributed generator," *International Journal of Power and Energy Systems*, vol. 37, no. 4, pp. 23–30, 2018.
- [20] A. Elnady and S. Sinan, "An improved second-order sliding mode control for the distributed generation system in stand-alone and grid-connected modes," *International Transactions on Electrical Energy Systems*, vol. 27, no. 11, pp. 45–55, 2017.
- [21] T. Hornik and Z. H. Qing-Chang, "Current control strategy for the neutral point of a three-phase inverter," in *Proceedings of the 5th IEEE conference on decision and control and European control conference (CDC-ECC '11)*, pp. 2994–2999, 2011.
- [22] J. Rodríguez, J.-S. Lai, and F. Z. Peng, "Multilevel inverters: a survey of topologies, controls, and applications," *IEEE Transactions on Industrial Electronics*, vol. 49, no. 4, pp. 724–738, 2002.
- [23] V. Kucera, *Analysis and Design of Discrete Linear Control Systems*, Prentice-Hall, Inc, Upper Saddle River, NJ, USA, 1991.
- [24] E. Walach and B. Widrow, "The least mean fourth (LMF) adaptive algorithm and its family," *IEEE Transactions on Information Theory*, vol. 30, no. 2, pp. 275–283, 1984.
- [25] A. Zerguine, "Convergence and steady-state analysis of the normalized least mean fourth algorithm," *Digital Signal Processing*, vol. 17, no. 1, pp. 17–31, 2007.
- [26] D. Bismor, K. Czyz, and Z. Ogonowski, "Review and comparison of variable step-size LMS algorithms," *International Journal of Acoustics and Vibration*, vol. 21, no. 1, pp. 24–39, 2016.
- [27] L. Osorio, J. Mendes, R. Araujo, and T. Matias, "A comparison of adaptive PID methodologies controlling a DC motor with a varying load," in *Proceedings of the 18th IEEE Conference on Emerging Technologies Factory Automation (ETFA '13)*, pp. 1–7, 2013.
- [28] X. Wang and M. Ye, "Nonlinear dynamic system identification using least squares support vector machine regression," in *Proceedings of the 3rd International Conference on Machine Learning and Cybernetics*, pp. 26–29, Shanghai, China, 2004.

- [29] U. B. Tayab, M. A. B. Roslan, L. J. Hwai, and M. Kashif, "A review of droop control techniques for microgrid," *Renewable & Sustainable Energy Reviews*, vol. 76, pp. 717-727, 2017.
- [30] IEEE 2030-2011 - IEEE Guide for Smart Grid Interoperability of Energy Technology and Information Technology Operation with the Electric Power System (EPS), End-Use Applications, and Loads.

## Research Article

# Modeling and Analysis of Progressive Ice Shedding along a Transmission Line during Thermal De-Icing

Yunyun Xie <sup>1</sup>, Linyan Huang,<sup>2</sup> Da Wang,<sup>3</sup> Huaiping Ding,<sup>4</sup> and Xiaochun Yin<sup>4</sup>

<sup>1</sup>School of Automation, Nanjing University of Science and Technology, Nanjing, Jiangsu Province 210094, China

<sup>2</sup>State Grid Nantong Power Supply Company, Nantong 226006, China

<sup>3</sup>Delft University of Technology, Delft 2628cd, Netherlands

<sup>4</sup>School of Science, Nanjing University of Science and Technology, Nanjing, Jiangsu Province 210094, China

Correspondence should be addressed to Yunyun Xie; xyy\_njust@163.com

Received 3 March 2019; Revised 2 May 2019; Accepted 19 May 2019; Published 17 June 2019

Academic Editor: Zhan Shu

Copyright © 2019 Yunyun Xie et al. This is an open access article distributed under the Creative Commons Attribution License, which permits unrestricted use, distribution, and reproduction in any medium, provided the original work is properly cited.

Progressive ice shedding (PIS) along transmission lines is a common type of ice shedding during thermal de-icing that requires investigation to ensure the security of transmission lines. In current research, PIS is commonly analyzed using a constant speed for ice detaching from the conductor, which is not accurate for PIS simulation. Therefore, a mechanical model of PIS is established in this study to analyze PIS during thermal de-icing. First, an ice detachment model during thermal de-icing is built to determine the detachment times of the initial ice and remaining ice. Then, a two-node isoparametric truss element is employed to derive the static and dynamic equilibrium equations of an iced conductor to simulate the dynamic response of PIS. Relative to commercial software, these equations can easily accommodate the changing mass of ice with the flow of melted water. The dynamic equilibrium equations are then solved using the ice detachment model to obtain the dynamic response of PIS. Finally, small-scale and full-scale experimental results are employed to verify the proposed method. The simulation results show that the results of the proposed method are more consistent with the experimental results than are the results of existing methods that assume a constant propagation speed. The proposed method can be further applied to optimize transmission line designs and evaluate the application of thermal de-icing devices.

## 1. Introduction

Ice shedding is one of the major sources of iced transmission line faults in cold regions. The statistics of historical ice disasters, such as the ice storm in North America in 1998 and the ice disaster in southern China in 2008, show that conductor vibration caused by ice shedding can result in flashover, fire burn, burnout and other electrical accidents, insulator rupture, cable breakage and tower deformation, and collapse [1]. The electrical and mechanical faults of transmission lines threaten the reliability of power system operation and the security of transmission lines. To enhance the design of transmission lines and ensure the security of power systems, analysis of the dynamic response of ice shedding is necessary.

Current research on the dynamic response of ice shedding from transmission lines generally focuses on ice shedding

scenarios with a fixed amount of ice shedding. Various ice shedding scenarios have been analyzed, including ice shedding from a single-span transmission line [2, 3], a continuous-span line [4], an overhead ground wire [5], a tower-line system [6], a transmission line with bundled conductors and spacers [3, 7], and a high-voltage overhead transmission line [8, 9].

This research assumes that, after the initial ice shedding, the remaining ice does not detach from the vibrating conductor. However, the remaining ice may fracture into small fragments from conductor vibration due to its plastic strain [10] and result in progressive ice shedding (PIS) along the transmission line [5]. When transmission lines are exposed to thermal de-icing [11], the maximum allowed plastic strain of the ice decreases as the inner ice melts during thermal de-icing, and the ice detaches from the conductor due to the propagation of transverse waves along the transmission

line. This phenomenon was confirmed through experiments on thermal de-icing [12]. Consequently, PIS is a common type of ice shedding during thermal de-icing. Therefore, it is significant to analyze the dynamic response of PIS during thermal de-icing for the security of transmission lines and the application of thermal de-icing.

Analyzing PIS during thermal de-icing involves two challenges: the criterion of ice detachment from the conductor and the dynamic model for analyzing the PIS dynamic response during thermal de-icing. For the ice detachment criterion (IDC), in current research, the time of ice detachment from the conductor is determined by a constant propagation speed of the transverse wave along the transmission line [13]. Nevertheless, the constant propagation speed is variable for various ice and conductor parameters, and the ice may not break apart with the propagation of transverse waves. Consequently, the IDC for a constant ice shedding speed is inaccurate for analyzing PIS. The ice detaches from the conductor due to interaction between the inner and external forces in the ice [5, 14, 15]. The maximum bending stress and maximum effective plastic strain of ice were employed as the IDC in [5, 14], and the adhesive force and cohesive force on the ice were adopted to calculate the IDC in [15]. These IDCs are effective for solid ice, but the ice in thermal de-icing is hollow ice with an air gap that involves a different IDC than that of solid ice. Although the model to calculate the air gap by thermal de-icing was proposed in [16], the IDC in thermal de-icing must be further researched.

The current research considers relatively simple ice shedding scenarios, such as a fixed amount of ice shedding from conductor. It is not easy for existing methods to simulate progressive ice melting and the resultant complex dynamics, such as the mass variation and dynamic force variation on the remaining ice caused by conductor fluctuation [2–9]. Moreover, the ability to simultaneously analyze many ice shedding scenarios with various transmission line parameters, ice thicknesses, and ice shedding positions also needs to be improved.

To consider the complicated PIS during thermal de-icing, this paper proposes a new modeling method, which is able to deal with the progressive dynamics of PIS. This method is based on the finite element mathematical model which is widely used in the research of suspended cable structures in mechanics [17]. The finite element method can consider the mass variation of ice and simulate the dynamic force variation in the ice for PIS. The proposed method first analyzes the characteristics of PIS during thermal de-icing. Compared with existing work, the detachment time of the initial ice shedding and the dynamic detaching model of the remaining ice are described in detail. Then, these characteristics are integrated into a finite element model to develop a more practical and exact PIS model. The proposed method has four advantages: (1) the mass variation of ice with thermal de-icing and the fluctuating conductor is considered; (2) the dynamic force on the ice is calculated dynamically; (3) the time of ice detachment from the conductor is more accurate because the IDC is obtained from the dynamic force of the ice; and (4) various PIS scenarios can be built flexibly because of the transparent modeling and solution process.

The paper is organized as follows. Section 2 presents the ice detachment model for thermal de-icing. Section 3 describes the static and dynamic equilibrium equations of a conductor based on a finite-element mathematical model. Section 4 explains the solution of the dynamic equilibrium equations considering the integration of ice detachment and conductor vibration. Case studies are presented and discussed in Section 5, followed by conclusions.

## 2. Characteristic Analysis of PIS during Thermal De-Icing

In this section, two types of ice detachment are introduced by analyzing the dynamic process of PIS. Then, two ice detachment models for the initial ice and remaining ice are proposed based on the ice melting model and the mechanical model of ice.

*2.1. Ice Detachment Process in Thermal De-Icing.* Due to the torque of the conductor and the gravity of the ice and wind, accreted ice usually has an irregular shape, which complicates the analysis of ice shedding. To analyze the PIS, we assume that the cross section of the ice is eccentric and round and that the conductor is farther from the center of the round from the middle of the conductor to the suspension point [12, 15].

When the de-icing current flows through the conductor, the ice at different positions on the conductor melts simultaneously. However, because the conductor near the suspension point is closest to the upper surface of the ice, the ice near the suspension point detaches from the conductor first and produces the initial ice shedding and conductor vibration. At this time, the ice remaining on the conductor vibrates with the conductor. When the external force on the remaining ice is greater than the inner force of the ice, the ice detaches from the conductor, resulting in PIS. Therefore, the detachment models of the ice near the suspension point and the ice remaining on the conductor are the foundation for modeling PIS.

*2.2. Classic Thermal De-Icing Model.* Although the sun and wind can melt ice, thermal de-icing is the preferred solution in severe weather. Additionally, the duration of thermal de-icing is between 0.5 and 3 hours [18]. Relative to the energy produced by thermal de-icing, ice melting by severe weather can be ignored. Therefore, the following assumptions are adopted in the study: (1) external conditions will not result in ice melting or ice accumulation and (2) the conductor resistance is constant, and the ice melting current evenly heats the conductor.

Based on the above assumptions, the heat conduction process of thermal de-icing can be described as follows. An electric current flowing through the transmission conductor produces Joule heat. Part of the heat warms the ice layer, conductor, and air gap, and part of the heat (namely, the latent heat) melts the ice, and the remaining heat reaches the outer surface of the ice layer and is dissipated through convection and radiation [11, 18]. This heat conductor process can be formulated as

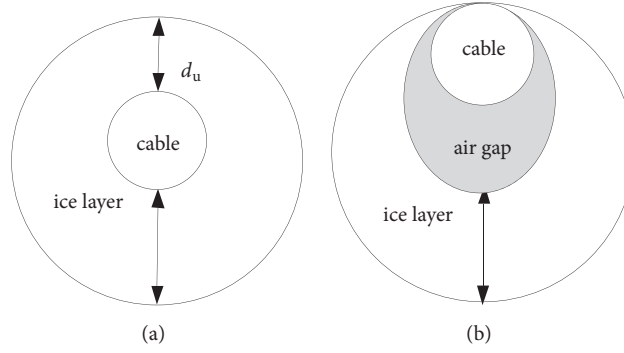


FIGURE 1: Cross section of an eccentric iced conductor. (a) Before ice melting. (b) After ice melting.

$$Q_j = R_0 I^2 t = Q_1 + Q_2 + Q_3 \quad (1)$$

where  $Q_j$  is to the Joule heat produced by the ice melting current per unit length, J/m;  $R_0$  is the conductor resistance per unit length,  $\Omega/m$ ;  $I$  is the ice melting current, A;  $t$  is the duration of thermal de-icing, s;  $Q_1$  is the heat dissipated through convection and radiation;  $Q_2$  is the latent heat for melting ice; and  $Q_3$  is the heat that warms the ice layer (the heat to warm the conductor and air gap is ignored) [11].

$$Q_1 = 2\pi r_{ice} h (T_{oi} - T_{air}) t \quad (2)$$

$$Q_2 = \rho_{ice} L_f V_m \quad (3)$$

$$Q_3 = \rho_{ice} V_{ice} C_{ice} T_{ice} \quad (4)$$

Here,  $r_{ice}$  is the radius of the iced conductor, m;  $h$  is the heat-exchange coefficient [18],  $W/(m^2 \cdot K)$ ;  $T_{oi}$  is the outer surface temperature of the ice layer [18],  $^{\circ}C$ ;  $T_{air}$  is the ambient temperature,  $^{\circ}C$ ;  $\rho_{ice}$  is the density of ice,  $kg/m^3$ ;  $L_f$  is the latent heat for melting ice ( $L_f = 335,000$  J/kg);  $V_m$  is the volume of melted ice per unit length,  $m^2$ ;  $V_{ice}$  is the volume of the ice layer per unit length,  $m^2$ ;  $C_{ice}$  is the specific heat of ice,  $J/(kg \cdot ^{\circ}C)$ ; and  $T_{ice}$  is the temperature of the ice layer, which can be simplified as  $(T_{oi}/2 - T_{air})$  [18],  $^{\circ}C$ .

The entire equation can be expressed as

$$\begin{aligned} & [R_0 I^2 - 2\pi r_{ice} h (T_i - T_a)] t \\ & = \rho_{ice} L_f V_m + \rho_{ice} V_{ice} C_{ice} \left( \frac{T_{oi}}{2} - T_{air} \right) \end{aligned} \quad (5)$$

where  $R_0$  and  $r_{ice}$  are the conductor parameters;  $d_{ice}$ ,  $L_f$ ,  $C_{ice}$ ,  $T_{oi}$ , and  $V_{ice}$  are the ice parameters;  $h$  and  $T_{air}$  are environmental parameters; and  $I$ ,  $t$ , and  $V_m$  are the parameters associated with thermal de-icing. In the process of thermal de-icing,  $I$  and  $V_m$  are determined through an initial calculation. In addition, the duration  $t$  of thermal de-icing is determined to calculate the mechanical parameters of the ice remaining on the conductor. Therefore, based on formula (5), we can build the detachment models of the initial ice shedding and the ice remaining on the conductor.

**2.3. The Detaching Time of Initial Ice Shedding.** The cross section of the eccentric iced conductor before and after ice

melting is illustrated in Figure 1, in which the shadow area denotes melted ice (the air gap).

When the elliptical air gap is tangent to the outer surface of both the conductor and the ice layer, the ice hangs from the conductor [18], which is the detachment criterion of the initial ice shedding in the static state. Therefore, at the moment of detachment, the volume of the air gap per length [18] can be expressed as

$$V_m = 0.5\pi \left( r_c + \frac{d_u}{2} \right)^{3/2} (r_c^{1/2} + r_{ice}^{1/2}) - \pi r_c^2 \quad (6)$$

where  $r_c$  is the radius of the conductor, m, and  $d_u$  denotes the minimum distance between the upper surface of the conductor and the ice layer, m. For eccentric iced conductor, this distance can be calculated as

$$d_u = r_{ice} - r_c - d_e \quad (7)$$

where  $d_e$  is the distance between the center of the iced conductor and the center of the cable before thermal de-icing, m.

By substituting formula (6) into formula (5), the duration of thermal de-icing of the iced layer is obtained.

$$\begin{aligned} t_d &= \frac{[\rho_{ice} L_f V_m + \rho_{ice} V_{ice} C_{ice} (T_{oi}/2 - T_{air})]}{R_0 I^2 - 2\pi r_{ice} h (T_{oi} - T_{air})} \\ V_m &= 0.5\pi \left( r_c + \frac{d_u}{2} \right)^{3/2} (r_c^{1/2} + r_{ice}^{1/2}) - \pi r_c^2 \quad (8) \\ V_i &= \pi r_{ice}^2 - \pi r_c^2 \end{aligned}$$

**2.4. Dynamic Detachments of Remaining Ice.** When the initial ice detaches from the conductor, the remaining ice hangs from the conductor. Because the remaining ice melts simultaneously along with the initially detached ice, the remaining ice will move down with the cross section shown in Figure 2, in which  $O_1$  is the center of the circle ice layer,  $O_2$  and  $O_3$  are the center of the conductor before and after ice melting, separately,  $d_m$  is the rising distance of the conductor after ice melting, and the shadowed area is the air gap. Due to the flowing melted water, the air gap of the ice near the middle point is filled with water, which increases the entire mass of

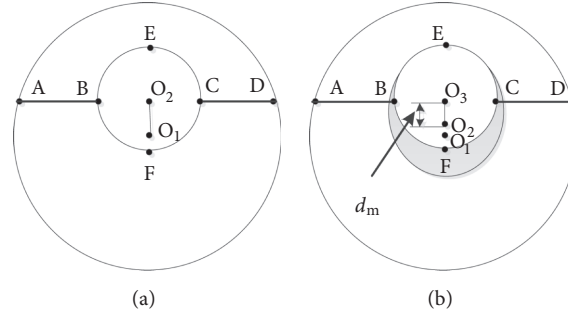


FIGURE 2: Cross section of the remaining ice. (a) Before ice melting. (b) After ice melting.

the remaining ice. The air gap of the remaining ice can be expressed as

$$V_{\text{melt}} = \frac{[R_0 I^2 - 2\pi r_{\text{ice}} h (T_{\text{oi}} - T_{\text{air}})] t_d - \rho_{\text{ice}} V_{\text{ice}} C_{\text{ice}} (T_{\text{oi}}/2 - T_{\text{air}})}{\rho_{\text{ice}} L_f} \quad (9)$$

The mass of the remaining ice is

$$m_r = \rho_{\text{ice}} \pi [(r_c + d_{\text{ice}})^2 - r_c^2] - \rho_{\text{ice}} V_{\text{melt}} \quad (10)$$

The rising distance of the conductor after ice melting [10, 15] is

$$d_m = 2 \left[ \frac{(r_c^2 + V_{\text{melt}}/\pi)^2}{r_c} \right]^{1/3} - 2r_c \quad (11)$$

The initial ice detachment from the conductor creates conductor vibration that may break the remaining ice. According to the detachment criterion of solid ice under instantaneous ice shedding in [15], the ice breaks when the inertia force of the ice is greater than the composition of the adhesive force on the ice and the cohesive force in the ice, and the ice is assumed to be split into two parts along line A-B-C-D as shown in Figure 2.

The detachment of solid ice in [15] differs in two ways from the detachment of the remaining ice in this study. First, the adhesive force between the ice and conductor is small and can be ignored in this study [19]. Second, the mass of the remaining ice changes with the flow of melted water. Therefore, when the resultant force of the inertia force and gravity on the ice layer is greater than the cohesive force in the ice, the remaining ice detaches from the conductor. A force analysis of the remaining ice is shown in Figure 3. The detachment criterion can be written as

$$F_{\text{vi}} + G_r \geq F_{\text{co}} \quad (12)$$

where  $F_{\text{vi}}$  is the inertia force,  $G_r$  is gravity, and  $F_{\text{ad}}$  is the cohesive force of the ice.

The forces in (12) can be expressed as

$$\begin{aligned} F_{\text{vi}} &= m_{\text{r1}} a_r \\ G_r &= m_{\text{r1}} g \\ F_{\text{co}} &= 2 \left( \sqrt{r_{\text{ice}}^2 - d_m^2} - r_c \right) \tau_{\text{co}} \end{aligned} \quad (13)$$

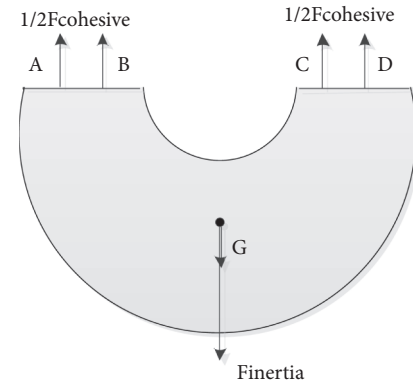


FIGURE 3: Force analysis of the lower part of the ice after ice melting.

where  $m_{\text{r1}}$  is the mass of the ice under line A-B-C-D;  $a_r$  is the vertical acceleration of the remaining ice;  $g$  is the acceleration of gravity; and  $\tau_{\text{co}}$  is the cohesive strength of the ice [15].

Due to the flowing of melted water, there is no water in the air gap of the remaining ice near the suspension point, and the air gap of the remaining ice near the middle point is filled with water. With melted water in the air gap, the mass of the remaining ice under line A-B-C-D can be expressed as

$$\begin{aligned} m_{\text{r1}} &= \rho_{\text{ice}} \left[ \pi r_{\text{ice}}^2 - r_{\text{ice}}^2 \arccos \frac{2d_m}{r_c + d_{\text{ice}}} \right. \\ &\quad \left. + d_m \sqrt{\frac{r_{\text{ice}}^2}{4} - d_m^2} - \frac{\pi r_c^2}{2} + \frac{(\rho_{\text{water}} - \rho_{\text{ice}}) V_{\text{melt}}}{\rho_{\text{ice}}} \right] \end{aligned} \quad (14)$$

From formulas (12)-(14), the critical detachment acceleration of the remaining ice with melted water can be calculated as follows:

$$a_{\text{c1}} = \frac{2 \left( \sqrt{r_{\text{ice}}^2 - 4d_m^2} - r_c \right) * \tau_{\text{co}}}{m_{\text{r1}}} - g \quad (15)$$

Without melted water in the air gap, the mass of the remaining ice under line A-B-C-D and the critical detachment acceleration of the remaining ice can be expressed as

$$m_{r1,2} = \rho_{ice} \left[ \pi r_{ice}^2 - r_{ice}^2 \arccos \frac{2d_m}{r_c + d_{ice}} + d_m \sqrt{\frac{r_{ice}^2}{4} - d_m^2} - \frac{\pi r_c^2}{2} - V_{melt} \right] \quad (16)$$

$$a_{c,2} = \frac{2 \left( \sqrt{r_{ice}^2 - 4d_m^2} - r_c \right) * \tau_c}{m_{r1,2}} - g \quad (17)$$

### 3. Dynamic PIS Model Based on Finite Element Mathematical Model

Since the volume of the air gap, the mass of the remaining ice, and the cohesive force of the ice all vary with conductor vibration, it is challenging to use commercial software to model the dynamic process of PIS during thermal de-icing. In this section, a finite element mathematical model is built to model the dynamic process of PIS.

*3.1. Static Model of an Iced Transmission Line.* Building a finite element mathematical model of a complex scenario is a common method by which to characterize the dynamic processes of complex scenarios in mechanics research. First, the conductor can be uniformly divided into multiple segments. Then, the mathematical model of each segment, including static and dynamic equilibrium equations, is built using element models. The equations of every segment can be combined into the conductor model, which can be solved to obtain the dynamic response of the conductor.

For a suspended cable structure, the most common element models are the two-node isoparametric truss element (TNITE) [20], two-node parabolic element (TNPE) [21], two-node catenary element (TNCE) [22], and multinode isoparametric curve element (MNICE) [23]. The TNPE model and TNCE model are suitable for static analysis but are inaccurate for dynamic analysis of conductor vibration because of the deformation in the vibration. The MNICE models require more calculation resources. The TNITE model has similar accuracy but requires less calculation resources, which is more suitable for the dynamic analysis of PIS.

According to Hooke's law, the relation between stress and strain in the element is [22]

$$\{\sigma\} = E \{\varepsilon\} + \{\sigma_0\} = \frac{4E}{L^2} \left( \{X_e\}^T [C] \{u_e\} + \frac{1}{2} \{\delta\}^T [C] \{u_e\} \right) + \sigma_0 \quad (18)$$

where  $\sigma$ ,  $\varepsilon$ , and  $\sigma_0$  are the axis stress, axis strain, and initial axis stress of the element, respectively; the axial direction means the direction perpendicular to the cross section of the conductor;  $E$  is the elastic modulus of the cable;  $X_e$  is the integral coordinate matrix of two nodes in an element before cable deformation; and  $H$  is the correlation matrix of the shape function, which can be expressed as

$$[H] = \frac{d[N]^T}{d\xi} \frac{d[N]}{d\xi} \quad (19)$$

where  $N$  is a shape function matrix defined as

$$N = \begin{bmatrix} N_1 & 0 & 0 & N_2 & 0 & 0 \\ 0 & N_1 & 0 & 0 & N_2 & 0 \\ 0 & 0 & N_1 & 0 & 0 & N_2 \end{bmatrix} \quad (20)$$

where  $N_1 = 1/2 - (1/2)\xi$ ,  $N_2 = 1/2 + (1/2)\xi$ , and  $\xi = 2s/L$ ;  $\xi$  is a relative coordinate;  $s$  is the length from a point to the midpoint of the element; and  $L$  is the element length of the power line.

According to the virtual work principle ( $\delta U - \delta W = 0$ ), the virtual work by external forces equals that by internal forces, which can be written as

$$\delta \{\varepsilon\}^T \{\sigma\} dV - \delta \{u_e\}^T \{R_e\} = 0 \quad (21)$$

where  $\{R_e\}$  is the matrix of the equivalent nodal load, which can be defined as

$$\{R_e\} = \frac{L}{2} \int_{-1}^1 [N]^T \{q(s)\} d\xi \quad (22)$$

where  $q(s)$  is the uniformly distributed load on the element, which is the integration of the self-weight load and the ice load before ice shedding and of only the self-weight load after ice shedding. The equivalent form of formula (22) is  $R_e = K\delta$ , which is the static equilibrium equation of the element.

By integrating formulas (18)-(22), the element equilibrium equation can be written as

$$\frac{2A}{L} \int_{-1}^1 [C]^T (\{X_e\} + \{\delta\}) \left( \frac{4E}{L^2} (\{X_e\}^T [C] \{\delta\} + \frac{1}{2} \{\delta\}^T [C] \{\delta\}) + \sigma_0 \right) d\xi - \{R_e\} = 0 \quad (23)$$

*3.2. Dynamic Model of PIS.* In the vibration process of the conductor, the equivalent nodal load  $R_e$  consists of the self-weight load and the ice load, in addition to the inertial force and damping force. The dynamic equilibrium equation can be expressed as

$$R_e = M \ddot{\delta} + C \dot{\delta} + K\delta$$

$$M = \frac{L}{2} * \int_{-1}^1 \rho [N]^T N d\xi \quad (24)$$

$$C = \frac{L}{2} * \int_{-1}^1 u [N]^T N d\xi$$

where  $M$ ,  $C$ , and  $K$  are the mass, damping, and stiffness matrices, respectively, and  $\ddot{\delta}$ ,  $\dot{\delta}$ , and  $\delta$  are the nodal acceleration, velocity, and displacement, respectively.

The damping matrix  $C$  is defined in terms of Rayleigh damping:

$$C = \alpha M + \beta K \quad (25)$$

$$\alpha = \frac{2(\xi_i \omega_j - \xi_j \omega_i)}{\omega_j^2 - \omega_i^2} \omega_i \omega_j \quad (26)$$

$$\beta = \frac{2(\xi_j \omega_j - \xi_i \omega_i)}{\omega_j^2 - \omega_i^2} \quad (27)$$

where  $\alpha$  and  $\beta$  are the mass and stiffness ratio coefficients,  $\omega_i$  and  $\omega_j$  are the cut-off frequencies of the lower and upper bounds in the frequency domain of interest, and  $\xi_i$  and  $\xi_j$  are the corresponding damping ratios.

#### 4. Dynamic Model Solution

In the PIS during thermal de-icing, the flow of melted water and the detachment of ice affect the dynamic response of PIS and result in perturbation of the mass matrix, which must be corrected with the conductor vibration. In this section, the correction method of the mass matrix is presented, and the solution method for the dynamic equilibrium equations is described.

**4.1. Mass Correction for the Analysis of PIS.** From formulas (12)~(13), we can observe that the mass of the ice can impact the force in the ice and further impact the time of ice detachment and the accuracy of the dynamic response solution. Therefore, it is necessary to calculate the mass mutation in every element during solving of the dynamic model of PIS. The mechanism of mass mutation for an element is different before and after the initial ice detachment. Before the initial ice detachment, the iced conductor is in a static state, and the mass mutation is caused by the melted water, which flows along the air gap to the bottom of the ice layer. Nevertheless, after the initial ice detachment, the mass mutation results from the PIS and the melted water that spills from the element when the original low point of the two end nodes is higher than the original high point. Therefore, the following two mass mutation methods are discussed.

**4.1.1. Mass Correction before the Initial Ice Shedding.** The melted ice results in an air gap in the ice layer, as shown in Figure 1. For one element, the gap volume, which is the volume of melted ice, is greater than the volume of melted water because the density of ice is less than the density of water. The melted water flows from the element near the suspension point to the element near the lowest point.

The number of elements with water can be obtained from the volume of the melted water. Taking a conductor with an equal altitude at two end nodes for example, the volume of melted ice in the ice layer can be expressed as

$$V_{\text{ice}} = \sum_{j=1}^k V_{m,j} L_{m,j} \quad (28)$$

where  $V_{m,j}$  refers to the volume of melted ice of element  $j$ ;  $L_{m,j}$  refers to the length of element  $j$ ; and  $k$  refers to the number of elements.

The volume of the melted water in the ice layer can be expressed as

$$V_{\text{water}} = \frac{V_{\text{ice}} \rho_{\text{ice}}}{\rho_w} \quad (29)$$

where  $\rho_{\text{ice}}$  and  $\rho_w$  refer to the densities of ice and water, respectively.

The elements without water can be written as follows:

$$\sum_{j=1}^n V_{m,j} L_{m,j} \geq \frac{(V_{\text{ice}} - V_{\text{water}})}{2} \quad (30)$$

where  $n$  refers to the number of elements without water counted from the suspension point.

After the number of elements without water is obtained, the mass of the elements without water can be calculated using formula (14), and the mass of the other elements can be computed using formula (15).

**4.1.2. Mass Correction after Initial Ice Shedding.** After the initial ice shedding, the element mass can mutate with conductor vibration and the melted flowing water. For the dropped ice, the element mass shifts to the self-weight by modifying the parameters in formula (24). While the ice does not fall, the element mass is determined by the flow of melted water. When the altitude of the original low point  $P_{m1}$  at the two end nodes is greater than the altitude of the original high point  $P_{m2}$ , the element mass can be expressed as formula (14); otherwise, the mass can be expressed as formula (16). Therefore, the element mass with conductor vibration can be obtained as follows:

$$m_{r1} = \begin{cases} m_{r1,1} & \text{if } P_{m1} \geq P_{m2} \\ m_{r1,2} & \text{if } P_{m1} < P_{m2} \end{cases} \quad (31)$$

The altitude of the two end nodes must be updated in each iteration.

**4.2. Solution of the Dynamic Equilibrium Equations.** The dynamic equilibrium equations for analyzing the PIS are higher-order differential-algebra equations, which makes obtaining an analytic solution challenging. The method integrating the Newmark- $\beta$  and Newton-Raphson methods is applied to the dynamic equilibrium equations in this study.

The dynamic equilibrium equation (24) at time  $t + \Delta t$  can be written as

$$M \ddot{\delta}_{t+\Delta t} + C \dot{\delta}_{t+\Delta t} + K \delta_{t+\Delta t} = R(e) \quad (32)$$

The solution procedure for PIS induced by thermal de-icing is shown in Figure 4 and consists of the following steps:

- (1) Initialize. Set the transmission line parameters (such as the span length and conductor type), icing parameters (such as the shape, density, and thickness), and ice melting parameters (such as the ice melting current and ambient temperature).

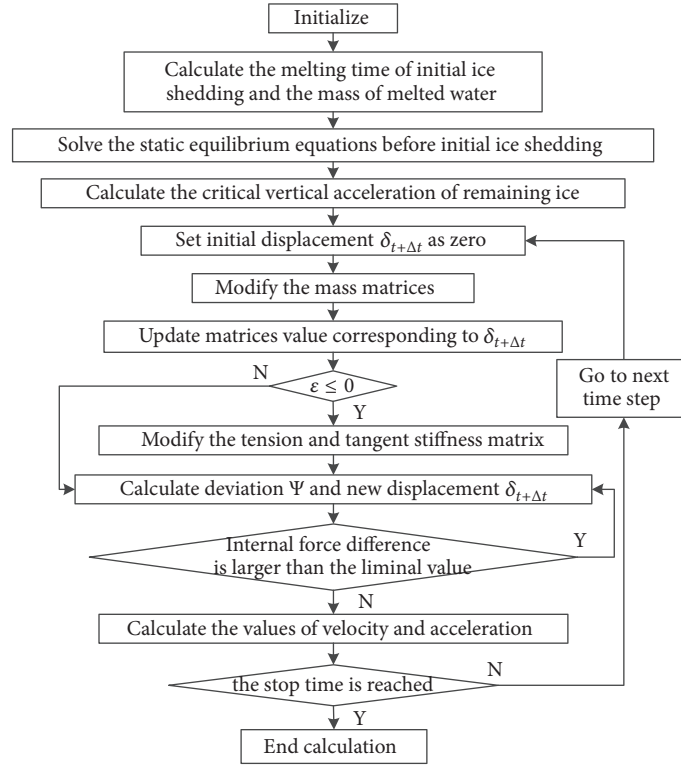


FIGURE 4: Solution flow chart of the dynamic analysis.

- (2) Calculate the melting time of the initial ice shedding from the ice detachment model of initial ice shedding in Section 2 and the mass of melted water by the mass correction before initial ice shedding in Section 4.
- (3) Employ the above parameters to solve the static equilibrium equations before the initial ice shedding.
- (4) Calculate the critical vertical acceleration of the remaining ice on each element according to the ice detachment model of the remaining ice in Section 2.
- (5) Set the initial displacement  $\delta_{t+\Delta t}$  equal to zero.
- (6) Modify the mass matrices in Section 4.
- (7) Update the matrix values corresponding to  $\delta_{t+\Delta t}$ , including the value of the equivalent nodal load matrix, internal force matrix, tangent stiffness matrix, and strain matrix at  $t + \Delta t$ .
- (8) Modify the tension and tangent stiffness matrix while  $\varepsilon \leq 0$ .
- (9) The values of the displacement, velocity, and accelerated speed at  $t$  clock and the values of the displacement, internal force matrix, and mass matrix at  $t + \Delta t$  are substituted into (32) to calculate the value of deviation  $\Psi$ . By substituting  $\Psi$  and the tangent stiffness matrix at time  $t + \Delta t$  into formula (33), the new displacement  $\delta_{t+\Delta t}$  can be obtained.

$$\delta_{t+\Delta t} = \delta_t - \left( K_T^{t+\Delta t} + \frac{1}{\alpha \Delta t^2} M + \frac{\delta}{\alpha \Delta t} C \right)^{-1} \psi \quad (33)$$

- (10) Go back to step (9) if the difference in internal force between two continuous iterations is greater than the liminal value. Otherwise, continue.
- (11) Calculate the values of velocity and acceleration. If the stop time is not reached, go back to step (6) to compute the parameters in the next time step. Otherwise, end the calculation.

## 5. Validation of the Proposed Method

In this section, the results of the proposed method are compared with the results of a small-scale experiment to confirm the effectiveness of the TITNE method. Then, the results of a full-scale experiment are employed to verify the effectiveness of the proposed ice detachment model by comparison with the results of PIS with constant speed.

### 5.1. Effectiveness of the Proposed TNITE Model

**5.1.1. Experimental Configuration.** Because the uniform accreted ice along the conductor is challenging to simulate in the warm regions and warm seasons, it is common to simulate the icing on conductors as lumped loads [8, 24]. The experimental results of a single span in [8] are employed to validate the effectiveness of the proposed TNITE model.

The accreted ice in the experiment is simulated as 10 lumped loads that are fixed along the 235 m-long conductor with remote-controlled cutters. The cutters can release the lumped loads partially or simultaneously. In this paper, the scenario in which the lumped loads are released

TABLE 1: Mechanical parameters of LGJ 630/45.

| Parameter                 | Unit              | LGJ 630/45 |
|---------------------------|-------------------|------------|
| Wind span                 | m                 | 235        |
| Cross-sectional area      | mm <sup>2</sup>   | 666.55     |
| Young's modulus           | MPa               | 63,000     |
| Weight per unit length    | kg/m              | 2.06       |
| Diameter                  | mm                | 33.6       |
| Rated tensile strength    | N                 | 148,700    |
| Initial horizontal stress | N/mm <sup>2</sup> | 39.6069    |

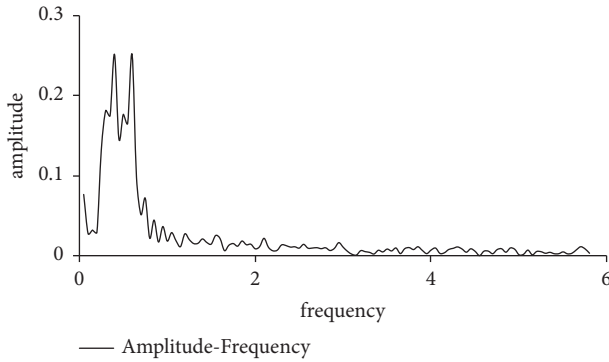


FIGURE 5: Diagram of the spectrum analysis of the conductor fluctuation.

simultaneously is employed to verify the effectiveness of proposed method. The parameters of the conductor (LGJ 630/45) are shown in Table 1. The equivalent ice thickness simulated by the loads is 15 mm. The lumped loads are released simultaneously in the experiment.

To obtain the modal damping ratios, a spectral analysis of experimental data is conducted, and the results are shown in Figure 5. Two significant frequencies,  $\omega_1 = 0.398$  Hz and  $\omega_2 = 0.596$  Hz, are observed. Meanwhile, the damping ratios calculated by Half power bandwidth method are about  $\xi_1 = 0.1055$  and  $\xi_2 = 0.0713$ . Consequently, the mass and stiffness ratio coefficients are calculated by (25)~(27) as  $\alpha = 0.0832$  and  $\beta = 0.0051$ .

**5.1.2. Results Comparison.** The vertical displacement of the experiment, ANSYS, and the proposed method are shown in Figure 6. In the simulation using ANSYS, Link10 is used to simulate the transmission conductor. The transmission conductor is divided into 100 elements. The simulation time is 10 s, and the simulation step size is 0.05 s for both ANSYS and the method developed in this study. The amplitude and fluctuation trends of the displacement are similar for the three methods, and the amplitude decreases under the action of damping with increasing vibration time. The amplitude and fluctuation trends of tension are very similar for the three methods. Some displacement errors appear between the proposed method and the experiment, possibly due to the damping coefficients in the simulation not accurately representing the experimental value and the fact that certain devices used in the experiment, such as the tension sensor and insulators, were not modeled in the simulation. However,

TABLE 2: Mechanical parameters of the full scale experiment.

| Parameter    | Unit                  | Value                    |
|--------------|-----------------------|--------------------------|
| $\rho_{ice}$ | kg/m <sup>3</sup>     | 670                      |
| $T_{oi}$     | °C                    | -1.093                   |
| $T_{air}$    | °C                    | -4                       |
| $R_0$        | $\Omega$              | $0.09614 \times 10^{-3}$ |
| $I$          | A                     | 600                      |
| $h$          | W/(m <sup>2</sup> ·K) | 4.7835                   |
| $r_{ice}$    | M                     | $12.1 \times 10^{-3}$    |
| $d_u$        | m                     | $19.26 \times 10^{-3}$   |
| $r_c$        | m                     | $36.2 \times 10^{-3}$    |

we can conclude that the conductor model TNITE has a similar precision to that of the experiment and commercial software and has sufficient precision to simulate PIS by thermal de-icing.

Because the tension curve is very smooth, we need to confirm whether the FE model properly captures the shock wave induced in the conductor by the weight loads dropping. The effectiveness is confirmed in terms of mesh size and time steps. The vertical displacement and tension results of the proposed method with different mesh sizes and time steps are illustrated in Figure 7. When the mesh sizes are 200 and 300 and the time steps are 0.01 s and 0.005 s, the vertical displacement and tension result are almost the same as the result with 100 elements and a 0.05 s time step. This result means that the model in this paper can capture the shock wave properly.

**5.2. Effectiveness of the Proposed PIS Model.** PIS is the cracking process of ice on a conductor. Its cracking speed is difficult to determine. Therefore, PIS is a discrete dynamic process of some small segments. When the segments are small enough, the dynamic response of the small segments is equivalent to the PIS. In this subsection, this idea is verified by comparing the result of proposed method with the result of thermal de-icing, as well as by comparison with other PIS models.

**5.2.1. Experimental Configuration.** A full-scale experiment of thermal de-icing was conducted in the Xuefeng Mountain Natural Icing Station established by Chongqing University [18]. There are two towers in the station. The distance between the towers is 80 m, between which various types of conductors are installed [25]. The transmission conductors, type LGJ-300, are powered by DC current for thermal de-icing. The parameters of the ice shedding scenario are illustrated in Table 2. The PIS during thermal ice shedding is recorded and described in [12], which is employed to validate the proposed method.

**5.2.2. Simulation Configuration.** The experiment in [12] was simulated using uniform loads fixed along the 80 m-long conductor. The shape of the ice coating and the conductor in the experiment is equivalent to the eccentric circle illustrated in Figure 8. The eccentricity of the ice coating gradually increases from the middle to the suspension point,

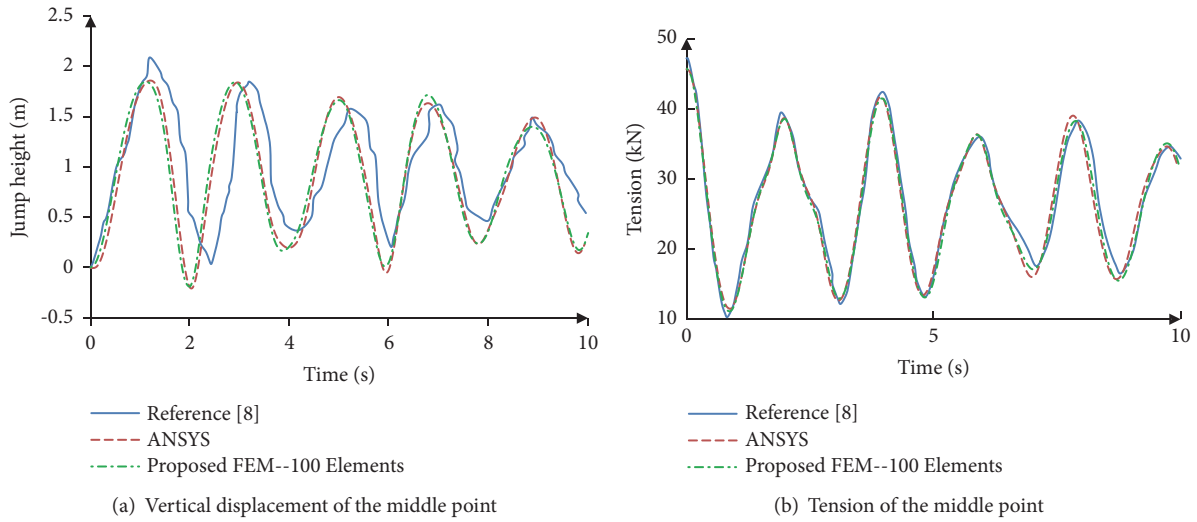


FIGURE 6: Vertical displacement of the middle point obtained using various methods.

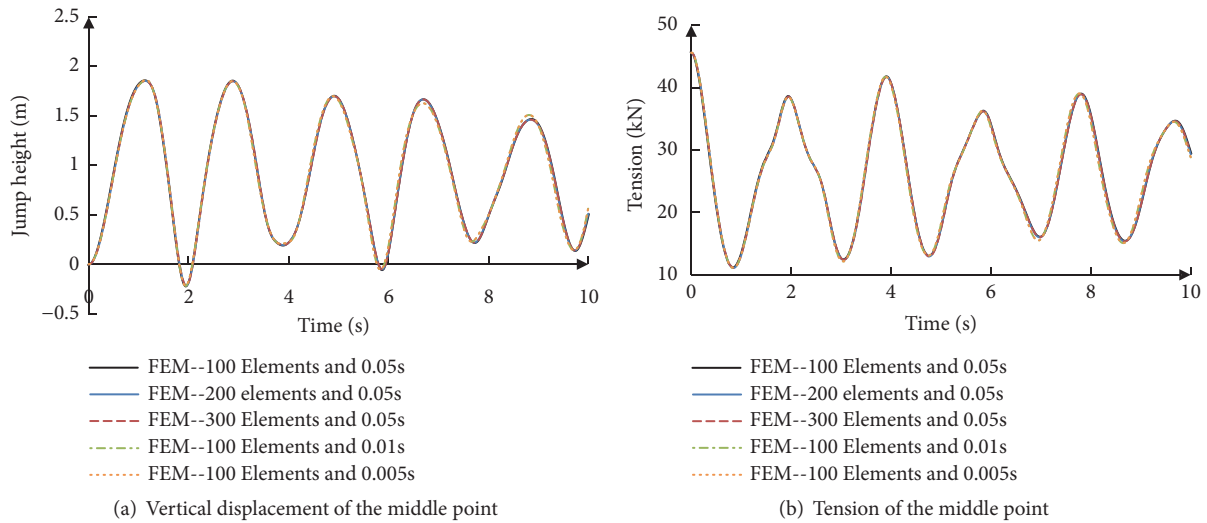


FIGURE 7: Vertical displacement and tension of the middle point with different mesh sizes and time steps.

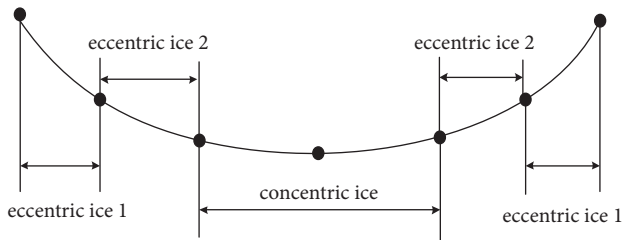


FIGURE 8: Ice coating before ice melting.

which can be measured by the distance between the center of the iced conductor and the center of the cable before thermal de-icing. The ice coating diameter is 24.1 mm, and the distance between the center of the conductor and the center of the ice coating is 12.0 mm and 7.2 cm for ices

1 and 2, respectively. The influence of the insulator string and vibration coupling effect of the transmission line and tower is ignored in this isolated-span power line model. The damping coefficients cannot be obtained by the method in section A, because the ice is shed with the fluctuation of the conductor. The value selection of damping coefficients needs to depend on experience. The damping of cable is modeled as equivalent viscous damping based on a lumped parameter model in many papers [4–6]. In this paper, the method used to select damping refers to the method in [8], which compares the results of numerical computations and physical tests. A series of damping parameters is set, and the damping coefficients which have the best fit for the results of numerical computation and physical tests are adopted to be the damping coefficients for the numerical computations. The simulation results of different mass ratio coefficients are shown in Figure 9. When the mass ratio coefficient is 0.17 and

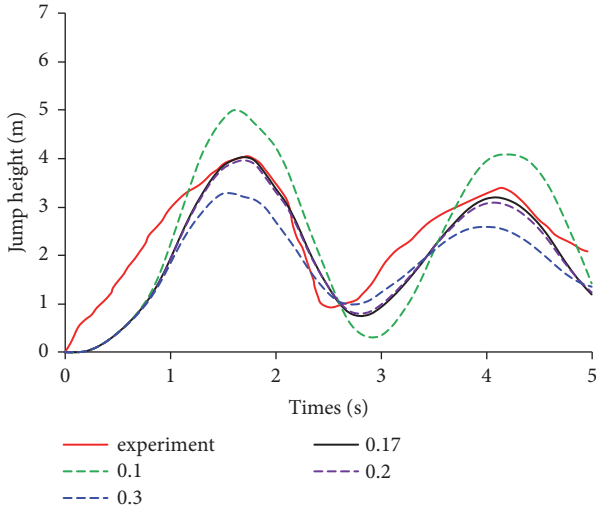


FIGURE 9: Simulation results of the proposed method and different dampings.

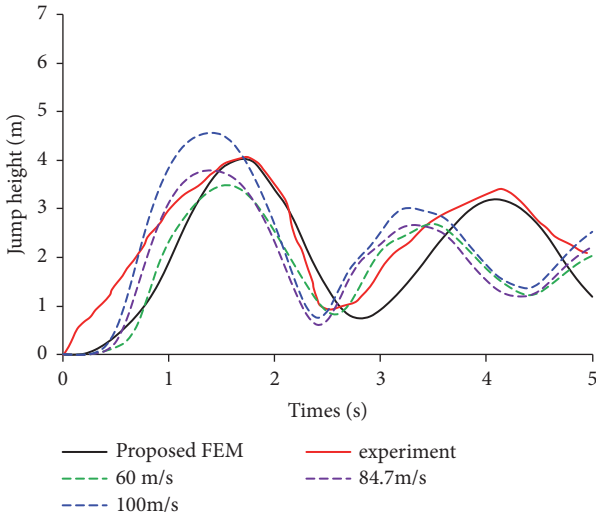


FIGURE 10: Simulation results of the proposed method and PIS with constant speed.

the stiffness ratio coefficient is 0, the simulation result best fits the experimental result. The temperature is  $-5^{\circ}\text{C}$ , and the ice melting current is 1000 A.

**5.2.3. Results Comparison.** Based on the experimental results, the results of the proposed method are compared with the results of PIS with a constant ice shedding speed. The vertical displacement of the middle point was illustrated in [18] with details and is employed as a benchmark to compare the different methods. The results of the proposed method and the PIS with a constant ice shedding speed are demonstrated in Figure 10.

*(1) Accuracy of the Proposed Method.* Before PIS, the conductor is in a static state, and the sag of the iced conductor is 2.39 m. When the initial ice sheds from the conductor, the

middle point jumps with the fluctuation of the conductor. The jump height of the middle point in the first peak is 4.05 m as determined by the proposed method, while it is 4.06 m in the experiment. The time to reach the peak is 1.8 s for the proposed method and the experiment. The vertical displacement and peak times of the proposed method and the experiment are similar. The jump height of the middle point in the first valley is 0.93 m in the experiment and 0.75 m as determined by the proposed method. The time to reach the valley is 2.55 s and 2.8 s for the experiment and the proposed method, respectively. The peak time, the maximum vertical displacement, and the vibration period of the experiment and proposed method are similar. The vertical displacements of the proposed method and the experiment contain some error because the ice was not completely shed in the experiment. Therefore, the proposed method is accurate for simulating PIS.

*(2) Accuracy of PIS with Constant Speed.* PIS with constant speed is simulated using the same simulation scenario as in the proposed method. For PIS with a constant ice shedding speed, the dynamic response is related to the ice shedding speed. When the ice shedding speed is 60 m/s, the vertical displacement of the middle point in the first peak is 3.52 m, the time to reach the peak is 1.5 s, the position of the middle point in the valley is  $-1.52$  m, and the time to reach the valley is 2.6 s. When the ice shedding speed is 84.7 m/s, the vertical displacement of the middle point in the first peak is 3.84 m, the time to reach the peak is 1.4 s, the position of the middle point in the valley is  $-1.74$  m, and the time to reach the valley is 2.4 s. When the ice shedding speed is 100 m/s, the vertical displacement of the middle point in the first peak is 4.59 m, the time to reach the peak is 1.4 s, the position of the middle point in the valley is  $-1.60$  m, and the time to reach the valley is 2.4 s. All the simulation results for various ice shedding speeds have some errors relative to the experimental results. The times to reach the first peak for all ice shedding speeds are less than those in the experiment. For the PIS with a speed of 60 m/s, the vibration period is similar to that in the experiment, but the vertical displacement in the peak and valley is less than that in the experiment. For the PIS with a speed of 84.7 m/s, the vertical displacement in the first peak is similar to that in the experiment, but the position of the valley and the time to reach the peak and valley are less than those in the experiment. For the PIS with a speed of 100 m/s, the vertical displacement in the peak is larger than that in the experiment, while the position of the valley and the time to reach the peak and valley are less than those in the experiment. Therefore, PIS with a constant ice shedding speed is less accurate than the proposed method.

In [8], the PIS speed is set to be less than 50 m/s. The results of this study are inaccurate for analyzing PIS from the results of constant speed in this study.

Ice shedding can result in a transversal wave along the span. The transversal wave was assumed to generate ice shedding in [15]. The theoretical wave speed can be obtained using the following equation:

$$v_{\text{wave}} = \sqrt{\frac{T}{m}} \quad (34)$$

where  $T$  is the conductor tension and  $m$  is the mass per unit length of the string.

The transverse wave speed of the experiment is 84.7 m/s according to the theoretical model (34). The speed is consistent with the observation in the experiment [12]. However, the dynamic response of PIS with a speed of 84.7 m/s is inconsistent with the results of the experiment illustrated in Figure 10, indicating that the simulation results of ice shedding with a constant ice shedding speed are inaccurate, even though the ice shedding speed is accurate.

(3) *Reason for Inaccuracies in PIS with a Constant Speed.* The mechanism of the dynamic response difference with different shedding speeds is that the ice shedding speed can impact the mass and vertical speed of the segments. The theoretical transverse wave speed caused by initial ice shedding can be employed as a reference. If the ice shedding speed is faster than the transverse wave speed, the ice is detached from the segment when the wave arrives at the segment. On one hand, the mass of the segment is smaller than that of the iced segment, which results in a larger vertical displacement of the conductor by the energy of the transverse wave. On the other hand, the detachment of ice will generate vertical movement of the conductor. The vertical movement with the addition of the theoretical wave will result in a higher vertical displacement. If the ice shedding speed is slower than the transverse wave speed, the energy of the transverse wave needs to afford the movement of the iced conductor, which will result in a smaller vertical displacement of the segment. Because the actual ice shedding time is different from the theoretical transverse wave speed, the dynamic response of PIS with the theoretical transverse wave speed is inconsistent with the results of the experiment.

The difference between the PIS with theoretical transverse wave and the proposed method is the IDC. The IDC of the proposed method is that the inertia force of ice is greater than the composition of the adhesive force on the ice and the cohesive force in the ice, while the IDC of PIS with theoretical transverse wave is that the detachment time and the time the wave arrives are according to the speed. The ice shedding time of the proposed method is longer than the arriving time of the transversal wave because the inertia force for the ice shedding is calculated from the vertical acceleration. The vertical acceleration of the middle point is shown in Figure 11. The time at which the transverse wave arrives is 0.47 s, and the acceleration begins to increase with the wave propagation. The time of maximum acceleration is approximately 0.6 s, which is approximately 0.13 s later than when the transverse wave arrives. The delay time of the ice detachment from the conductor is the main reason for the inaccuracy of PIS with constant speed.

## 6. Conclusion

To study the dynamic response of PIS, a mechanical model of PIS during thermal de-icing is established in this study.

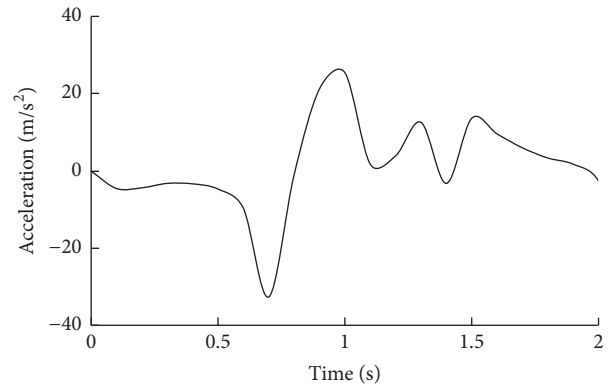


FIGURE 11: Vertical acceleration of the middle point.

An ice detachment model for the initial ice and the remaining ice is built based on an ice melting model and an ice mechanical model. Then, a finite-element mathematical model is proposed to simulate the dynamic process of PIS. Finally, the proposed model is verified with experimental results. Comparison with a small-scale experiment shows that the dynamic simulation result is as accurate as that of the commercial finite element software ANSYS. Based on the results of a full-scale experiment, a comparison of the proposed method and PIS with a constant ice shedding speed shows that the proposed method is more accurate for simulating PIS. Because of the transparent modeling and solving process, the proposed method can be used to analyze complex ice shedding scenarios and can serve as a reference tool for system operators to optimize transmission line designs and evaluate the application of thermal de-icing devices.

Because the TNITE model cannot bend, mechanical ice fracturing cannot be considered in this model. Neglecting mechanical ice fracturing will result in errors in the ice detachment time. This may be one of the reasons that the vertical displacement of the proposed method has some error relative to the experiment. In future work, an element model which can consider the bend and compression should be employed to simulate the dynamic process of PIS.

## Data Availability

The data used to support the findings of this study are included within the article.

## Conflicts of Interest

The authors declare that they have no conflicts of interest.

## Acknowledgments

This work is supported by the National Natural Science Foundation of China (51507080, 61673213) and the Fundamental Research Funds for the Central Universities (30918011330).

## References

- [1] X. Xu, D. Niu, P. Wang, Y. Lu, and H. Xia, "The weighted support vector machine based on hybrid swarm intelligence optimization for icing prediction of transmission line," *Mathematical Problems in Engineering*, vol. 2015, Article ID 798325, 9 pages, 2015.
- [2] L. E. Kollár and M. Farzaneh, "Vibration of bundled conductors following ice shedding," *IEEE Transactions on Power Delivery*, vol. 23, no. 2, pp. 1097–1104, 2008.
- [3] L. E. Kollar and M. Farzaneh, "Modeling sudden ice shedding from conductor bundles," *IEEE Transactions on Power Delivery*, vol. 28, no. 2, pp. 604–611, 2013.
- [4] M. R. Fekr and G. McClure, "Numerical modelling of the dynamic response of ice-shedding on electrical transmission lines," *Atmospheric Research*, vol. 46, no. 1-2, pp. 1–11, 1998.
- [5] T. Kálmán, M. Farzaneh, and G. McClure, "Numerical analysis of the dynamic effects of shock-load-induced ice shedding on overhead ground wires," *Computers & Structures*, vol. 85, no. 7, pp. 375–384, 2007.
- [6] G. McClure and M. Lapointe, "Modeling the structural dynamic response of overhead transmission lines," *Computers & Structures*, vol. 81, no. 8, pp. 825–834, 2003.
- [7] L. E. Kollár and M. Farzaneh, "Modeling the dynamic effects of ice shedding on spacer dampers," *Cold Regions Science and Technology*, vol. 57, no. 2, pp. 91–98, 2009.
- [8] X. Meng, L. Wang, L. Hou et al., "Dynamic characteristic of ice-shedding on UHV overhead transmission lines," *Cold Regions Science and Technology*, vol. 66, no. 1, pp. 44–52, 2011.
- [9] F. Yang, J. Yang, and Z. Zhang, "Unbalanced tension analysis for UHV transmission towers in heavy icing areas," *Cold Regions Science and Technology*, vol. 70, pp. 132–140, 2012.
- [10] K. Ji, X. Rui, L. Li, A. Leblond, and G. McClure, "A novel ice-shedding model for overhead power line conductors with the consideration of adhesive/cohesive forces," *Computers & Structures*, vol. 157, pp. 153–164, 2015.
- [11] X. L. Jiang and S. H. Fan, "Simulation and experimental investigation of dc ice-melting process on an iced conductor," *IEEE Transactions on Power Delivery*, vol. 25, no. 2, pp. 919–929, 2010.
- [12] X. Jiang, M. Bi, Z. Li, Z. Xiang, B. Dong, and S. Zhao, "Study on DC ice melting and ice shedding process under natural condition," *Dianwang Jishu/Power System Technology*, vol. 37, no. 9, pp. 2626–2631, 2013.
- [13] X. Meng, L. Hou, L. Wang et al., "Oscillation of conductors following ice-shedding on UHV transmission lines," *Mechanical Systems and Signal Processing*, vol. 30, pp. 393–406, 2012.
- [14] F. Mirshafiei, G. McClure, and M. Farzaneh, "Modelling the dynamic response of iced transmission lines subjected to cable rupture and ice shedding," *IEEE Transactions on Power Delivery*, vol. 28, no. 2, pp. 948–954, 2013.
- [15] K. P. Ji, X. M. Rui, and L. Li, "Dynamic response of overhead transmission lines with eccentric ice deposits following shock loads," *IEEE Transactions on Power Delivery*, vol. 32, no. 3, pp. 1287–1294, 2017.
- [16] W. Yaoxuan, J. Xingliang, F. Songhai, and M. Zhigao, "Asynchronism of ice shedding from the de-iced conductor based on heat transfer," *IET Science, Measurement & Technology*, vol. 10, no. 4, pp. 389–395, 2016.
- [17] H.-T. Thai and S.-E. Kim, "Nonlinear static and dynamic analysis of cable structures," *Finite Elements in Analysis and Design*, vol. 47, no. 3, pp. 237–246, 2011.
- [18] X. Jiang, Y. Wang, L. Shu, Z. Zhang, Q. Hu, and Q. Wang, "Control scheme of the de-icing method by the transferred current of bundled conductors and its key parameters," *IET Generation, Transmission & Distribution*, vol. 9, no. 15, pp. 2198–2205, 2015.
- [19] S. Y. Sadov, P. N. Shivakumar, D. Firsov, S. H. Lui, and R. Thulasiram, "Mathematical model of ice melting on transmission lines," *Journal of Mathematical Modelling and Algorithms*, vol. 6, no. 2, pp. 273–286, 2007.
- [20] A. Tiar, W. Zouari, H. Kebir, and R. Ayad, "A nonlinear finite element formulation for large deflection analysis of 2D composite structures," *Composite Structures*, vol. 153, pp. 262–270, 2016.
- [21] W.-X. Ren, M.-G. Huang, and W.-H. Hu, "A parabolic cable element for static analysis of cable structures," *Engineering Computations (Swansea, Wales)*, vol. 25, no. 4, pp. 366–384, 2008.
- [22] M.-G. Yang, Z.-Q. Chen, and X.-G. Hua, "A new two-node catenary cable element for the geometrically non-linear analysis of cable-supported structures," *Proceedings of the Institution of Mechanical Engineers, Part C: Journal of Mechanical Engineering Science*, vol. 224, no. 6, pp. 1173–1183, 2010.
- [23] Y. Wang, S. R. Zuo, and C. Wu, "A finite element method with six-node isoparametric element for nonlinear analysis of cable structures," *Applied Mechanics and Materials*, vol. 275, pp. 1132–1135, 2013.
- [24] L. E. Kollár, M. Farzaneh, and P. van Dyke, "Modeling ice shedding propagation on transmission lines with or without interphase spacers," *IEEE Transactions on Power Delivery*, vol. 28, no. 1, pp. 261–267, 2013.
- [25] S. H. Fan and X. L. Jiang, "DC ice-melting model for elliptic glaze iced conductor," *IEEE Transactions on Power Delivery*, vol. 26, no. 4, pp. 2697–2704, 2011.

## Research Article

# Distributed Learning Algorithms and Lossless Convex Relaxation for Economic Dispatch with Transmission Losses and Capacity Limits

Kwang-Ki K. Kim 

*Department of Electrical Engineering, Inha University, Incheon 22212, Republic of Korea*

Correspondence should be addressed to Kwang-Ki K. Kim; [kwangki.kim@inha.ac.kr](mailto:kwangki.kim@inha.ac.kr)

Received 14 March 2019; Accepted 27 May 2019; Published 13 June 2019

Guest Editor: Michael Z. Q. Chen

Copyright © 2019 Kwang-Ki K. Kim. This is an open access article distributed under the Creative Commons Attribution License, which permits unrestricted use, distribution, and reproduction in any medium, provided the original work is properly cited.

This paper considers problems of economic dispatch in power networks that contain independent power generation units and loads. For efficient distributed economic dispatch, we present a mechanism of multiagent learning in which each agent corresponding to a generation unit updates the power generation based on the received information from the neighborhood. The convergence of the proposed distributed learning algorithm to the global optimal solution is analyzed. Another method of distributed economic dispatch we propose is a decentralized iterative linear projection method in which the necessary optimality conditions are solved without considering the generation capacities and the obtained solutions are iteratively projected onto the convex set corresponding to the generation capacities. A centralized method based on semidefinite programming for economic dispatch with a loss coefficient matrix is also presented for comparisons. For demonstration, the proposed methods of distributed economic dispatch are applied to a 6-generator test case and the three different methods of economic dispatch give the same solutions. We also analyze parametric dependence of the optimal power generation profiles on varying power demands in economic dispatch.

## 1. Introduction

The smart grid infrastructure including smart sensors and meters and communication technology has triggered revisiting fundamental problems of power systems research. In such energy system infrastructures with communication networks, different independent units take the control and operational responsibility in different areas of the system [1, 2].

In particular, economic dispatch with integration of distributed generators and energy storage systems in a smart grid infrastructure is one of the major challenges for large-scale complex power networks to meet the total power demand by allocating demand among many independently operated distributed generators in an efficient way with guaranteed quality of service and safety [3]. Because of distributed and hierarchical structures of power supplies and demands, and their connections through information and communication infrastructures, it requires distributed mechanisms of dispatching electrical power demands among available generation units in efficient ways. Several distributed algorithms for economic dispatch have been presented in the literature,

whereas many of existing approaches to economic dispatch are centrally performed. In [4, 5], the authors propose the distributed incremental cost consensus algorithm in which the dual variable corresponding to the marginal price and the power generation mismatches are updated by a weighted-sum consensus rule. But such algorithms do not consider any transmission constraints.

Other consensus-based distributed algorithms for economic dispatch are presented by different research groups. For the method presented in [6], each generator learns the mismatch between demand and total power generation by communication over a strongly connected graph and corrects its own power generation to achieve the consensus. In [7, 8], the authors present a consensus-based distributed bisection method in which the dual variable corresponding to the marginal price is explicitly computed by a bisection method with power generation updates of distributed generators. In addition, the authors of [9] propose a distributed method of lambda-iteration in which the conventional lambda-iteration method [10] is modified to take the presence of prohibited

operating zones and to avoid an oscillatory phenomenon. In [11], a game-theoretic learning distributed algorithm based on population dynamics without considering transmission losses is presented. Another game-theoretic approach is presented by the authors of [12] in which a cooperative game is formulated for optimal power aggregation to minimize the total generation cost while meeting the generation capacity constraints. Evolutionary algorithms are also applied to the problem of economic dispatch: genetic algorithm [13], particle swarm optimization [14], and evolutionary programming techniques [15].

Our contribution is threefold. First, we present a method of primal-dual iteration for computing optimal power generation profiles in economic dispatch with transmission losses and generation limits. The proposed algorithm is based on distributed computations of the independent decision-making processes with information exchange. The convergence of the proposed algorithm to the global optimum is analyzed. Secondly, semidefinite programming relaxation of the associated quadratic constrained quadratic program formulated from a constrained economic dispatch problem. This convex relaxation is shown to be exact; i.e., strong duality holds. Thirdly, we present a decentralized method of iterative linear projection for the same class of economic dispatch. This algorithm is based on iterative projections of linear system solution corresponding to the reduced KKT conditions and its convergence is guaranteed with relatively small size of iteration numbers. In addition, the explicit dependence of the optimal power generation profiles on varying power demand is investigated in terms of multiparametric programming. This paper is organized as follows.

Section 2 presents a distributed iteration method for economic dispatch in the presence of generation capacity limits and quadratic transmission losses. In Section 3, a semidefinite programming relaxation of the associated quadratic constrained quadratic program is studied and its strong duality is analyzed. In addition, the explicit parametric dependence of the optimal generation profiles on varying power demand is investigated. To demonstrate the effectiveness of the proposed distributed and convex relaxation algorithms, the methods are applied to the IEEE 26-bus 6-generator test case in Section 4. Section 5 concludes this paper.

## 2. Distributed Economic Dispatch in Smart Grids

*2.1. A Brief Introduction to Economic Dispatch.* Economic dispatch is an optimization problem in which the objective is to minimize the total power generation cost under physical limitations of distributed generators and demand-supply balance that are represented as inequality and equality constraints:

$$\text{ED} \begin{cases} \text{minimize} & \sum_{i=1}^N f_i(p_i) \\ \text{subject to} & p_i^{\min} \leq p_i \leq p_i^{\max}; \quad i = 1, 2, \dots, N \\ & \sum_{i=1}^N p_i - \sum_{i=1}^N \sum_{j=1}^N p_i B_{ij} p_j = P_d \end{cases} \quad (1)$$

where  $p_i$  refers to the power generation output of the generator  $i$ , and  $p_i^{\min}$  and  $p_i^{\max}$  are the minimum and maximum generation output limits of the generator  $i$ , respectively. The power loss in transmission is given as a quadratic form parameterized by the loss-coefficient matrix  $B$  [10]. The power generation cost functions  $f_i : \mathbb{R}_+ \rightarrow \mathbb{R}_+$  for  $i = 1, 2, \dots, N$  are usually modeled as quadratic forms:

$$f_i(p_i) = \frac{1}{2} a_i p_i^2 + b_i p_i + c_i \quad (2)$$

where  $a_i$  ([\$/MW<sup>2</sup>]),  $b_i$  ([\$/MW]), and  $c_i$  (\$) denote the cost coefficients of generator  $i$ .

*2.2. Optimality Conditions for Economic Dispatch.* Consider a Lagrange function (or Lagrangian) defined by

$$L(p_1, p_2, \dots, p_N, \mu) := \sum_{i=1}^N f_i(p_i) + \mu \left( P_d + \sum_{i=1}^N \sum_{j=1}^N p_i B_{ij} p_j - \sum_{i=1}^N p_i \right) \quad (3)$$

for which the equality constraint corresponding to the power balance is relaxed and integrated into the objective function by introducing a Lagrange multiplier  $\mu \in \mathbb{R}$ . With this definition of Lagrangian, the necessary conditions for optimality are given as follows:

(1) Stationarity:

$$\nabla_{p_i} L(p_1^*, p_2^*, \dots, p_N^*, \mu^*) = 0 \quad \text{for } i = 1, 2, \dots, N \quad (4)$$

(2) Primal feasibility:

$$P_d + \sum_{i=1}^N \sum_{j=1}^N p_i^* B_{ij} p_j^* - \sum_{i=1}^N p_i^* = 0 \quad (5)$$

$$p_i^{\min} \leq p_i^* \leq p_i^{\max} \quad \text{for } i = 1, 2, \dots, N \quad (6)$$

To find an optimal demand allocation in economic dispatch (1), we need to solve  $N + 1$  equations while satisfying  $2N$  inequalities for  $N + 1$  variables  $(p_1^*, p_2^*, \dots, p_N^*, \mu^*)$  in (4)~(6).

*2.3. Multiagent Learning for Distributed Economic Dispatch.*

To find a solution profile  $(p_1^*, p_2^*, \dots, p_N^*, \mu^*)$  that satisfies the optimality conditions (4)~(6), we develop an iterative method of distributed optimization that is based on multiagent learning. Figure 1 shows a schematic diagram for message exchanges and updates among the aggregator (denoted by Node 0) and the agents (indexed by  $1, 2, \dots, N$ ). Best response dynamics of power generation updates for agents and gradient descent dynamics of price updates for the aggregator are depicted in Figure 2 as block diagrams with arrows denoting message exchanges.

*2.3.1. Primal Updates (Distributed Learning).* Define sets  $\mathcal{N}_i \triangleq \{j : B_{ij} \neq 0\}$  for  $i = 1, 2, \dots, N$  and the associated vector

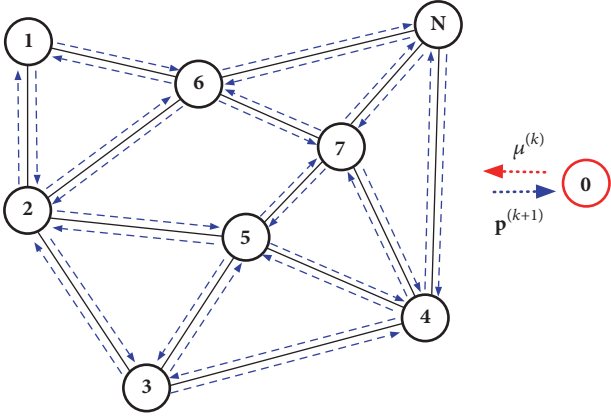


FIGURE 1: A schematic diagram for physical connections and communication in power-generation grid. The solid black lines denote the electrical connections between generators, the blue dashed arrows denote communication links between generators, the red dotted arrow denotes the broadcasting of the Lagrange multiplier, and the blue dotted arrows denote the generators' willing-to-supply powers for given Lagrange multiplier.

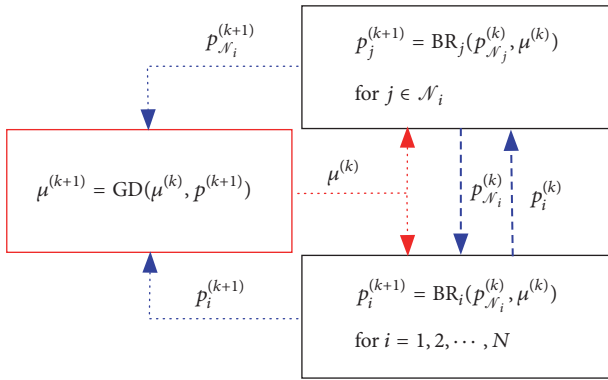


FIGURE 2: Block diagram of distributed iterative computations of primal-dual variables in economic dispatch with coupled power loss. The update rules  $BR_i$  and  $GD_i$  are defined in (10) and (11), respectively.

$p_{\mathcal{N}_i} = (p_j)_{j \in \mathcal{N}_i} \in \mathbb{R}^{|\mathcal{N}_i|}$ , where  $|\mathcal{N}_i|$  denotes the cardinality of the set  $\mathcal{N}_i$ . Each unit of the  $i$ th generator receives the current computation of  $p_{\mathcal{N}_i}$  from its neighbour hood  $\mathcal{N}_i$  and the current computation of Lagrangian multiplier  $\mu$  and updates its computation of  $p_i$  by solving a local optimization

$$p_i^{(k+1)} := \arg \min_{p_i^{\min} \leq p_i \leq p_i^{\max}} L_i(p_i, p_{\mathcal{N}_i}^{(k)}, \mu^{(k)}) \quad (7)$$

where

$$L_i(p_i, p_{\mathcal{N}_i}^{(k)}, \mu^{(k)}) \triangleq f_i(p_i) + \mu^{(k)} \left( 2p_i \sum_{j \in \mathcal{N}_i} B_{ij} p_j^{(k)} - p_i \right) \quad (8)$$

for  $k = 0, 1, \dots$  and for each  $i = 1, 2, \dots, N$ . More succinctly, we write

$$p_i^{(k+1)} := BR_i(p_{\mathcal{N}_i}^{(k)}, \mu^{(k)}) \quad \text{for } i = 1, 2, \dots, N \quad (9)$$

where the  $i$ th local optimization (7) has a unique solution for every  $k = 0, 1, \dots$ , provided that  $a_i \neq 0$  due to its strict convexity. We note that the  $i$ th local optimization (7) has the following closed-form solution:

$$p_i^{(k+1)} = \begin{cases} p_i^{\min} & \text{for } \tilde{p}_i^{(k)} < p_i^{\min} \\ p_i^{\max} & \text{for } \tilde{p}_i^{(k)} > p_i^{\max} \\ \tilde{p}_i^{(k)} & \text{for } p_i^{\min} \leq \tilde{p}_i^{(k)} \leq p_i^{\max} \end{cases} \quad (10)$$

where  $\tilde{p}_i^{(k)} \triangleq (1/a_i)(\mu^{(k)}(1 - \sum_{j \in \mathcal{N}_i} B_{ij} p_j^{(k)}) - b_i)$ .

**2.3.2. Dual Update.** The Lagrangian multiplier is updated to enforce the demand-supply balance to be satisfied. The aggregator receives the current computations of  $p_i$  for  $i = 1, \dots, N$  and revises its previous computation of  $\mu$  by

$$\mu^{(k+1)} := \mu^{(k)} + \alpha^{(k+1)} \left( P_d + P_L^{(k+1)} - \sum_{i=1}^N p_i^{(k+1)} \right) \quad (11)$$

where  $P_L^{(k+1)} \triangleq \sum_{i=1}^N \sum_{j \in \mathcal{N}_i} p_i^{(k+1)} B_{ij} p_j^{(k+1)}$  denotes the power loss computed for iteration steps  $k = 0, 1, \dots$ , and  $\alpha^{(k+1)} > 0$  is a user-defined step size.

Figure 2 shows how such primal and dual updates are performed with exchange of information among neighboring agents (or generators) and the aggregator.

**2.4. Decentralized Relaxed Convex QP.** Consider a simpler case of ED in (1) for which the power loss coefficients  $B_{ij}$  ( $i, j = 1, 2, \dots, N$ ) are neglected:

$$ED' \begin{cases} \text{minimize} & \sum_{i=1}^N f_i(p_i) \\ \text{subject to} & p_i^{\min} \leq p_i \leq p_i^{\max}; \quad i = 1, 2, \dots, N \\ & \sum_{i=1}^N p_i = P_d \end{cases} \quad (12)$$

For this case with quadratic cost functions in (2), necessary conditions for optimality are given as the following linear system:

$$\begin{bmatrix} a_1 & 0 & \cdots & 0 & -1 \\ 0 & a_2 & \cdots & \vdots & -1 \\ \vdots & \vdots & \ddots & \vdots & \vdots \\ 0 & \cdots & 0 & a_N & -1 \\ 1 & 1 & \cdots & 1 & 0 \end{bmatrix} \begin{bmatrix} p_1^* \\ p_2^* \\ \vdots \\ p_N^* \\ \mu^* \end{bmatrix} = \begin{bmatrix} -b_1 \\ -b_2 \\ \vdots \\ -b_N \\ P_d \end{bmatrix} \quad (13)$$

and

$$p_i^{\min} \leq p_i \leq p_i^{\max} \quad \text{for } i = 1, 2, \dots, N. \quad (14)$$

Note that if  $a_i \neq 0$  for all  $i$  so that system (13) is linearly independent, then we have a unique closed-form solution for (13):

$$p_i^* = \frac{1}{a_i} (\delta\beta + \delta P_d - b_i) \quad \text{for } i = 1, 2, \dots, N \quad (15)$$

$$\mu^* = \delta (\beta + P_d)$$

where  $\delta = (\sum_{i=1}^N 1/a_i)^{-1}$  and  $\beta = \sum_{i=1}^N b_i/a_i$ . The vector  $\mathbf{p} = [p_1^* \ p_2^* \ \dots \ p_N^*]^T \in \mathbb{R}^N$  obtained in the closed-form (15) does not necessarily satisfy the capacity constraints (14).

Define the following sets of indices:

$$\begin{aligned} \mathcal{J}_{\min}(\mathbf{p}) &\triangleq \{i : p_i < p_i^{\min}\} \\ \mathcal{J}_{\max}(\mathbf{p}) &\triangleq \{i : p_i > p_i^{\max}\} \end{aligned} \quad (16)$$

Let  $\mathcal{S}(\mathbf{p}) \triangleq \mathcal{J}_{\min}(\mathbf{p}) \cup \mathcal{J}_{\max}(\mathbf{p})$  define its union and a complementary set  $\tilde{\mathcal{S}}(\mathbf{p}) \triangleq \{1, 2, \dots, N\} - \mathcal{S}(\mathbf{p})$ . For the given solution vector  $\mathbf{p}$  obtained in (15), consider the following reduced economic dispatch

$$\text{ED}'(\mathbf{p}) \begin{cases} \text{minimize} & \sum_{i \in \tilde{\mathcal{S}}(\mathbf{p})} f_i(p_i) \\ \text{subject to} & p_i^{\min} \leq p_i \leq p_i^{\max}, \quad i \in \tilde{\mathcal{S}}(\mathbf{p}) \\ & \sum_{i \in \tilde{\mathcal{S}}(\mathbf{p})} p_i = P_d - \sum_{i \in \mathcal{J}_{\max}(\mathbf{p})} p_i^{\max} \end{cases} \quad (17)$$

where the generators corresponding to the set  $\mathcal{J}_{\max}(\mathbf{p})$  are assigned to produce their upper limits in capacity and the remaining generators are further considered as design variables for optimization. Similar to (15), a closed-form solution satisfying necessary conditions for optimality is obtained as follows:

$$p_i^* = \begin{cases} p_i^{\max} & \text{for } i \in \mathcal{J}_{\max}(\mathbf{p}) \\ \frac{1}{a_i} (\tilde{\delta}\tilde{\beta} + \tilde{\delta}\tilde{P}_d - b_i) & \text{for } i \in \tilde{\mathcal{S}}(\mathbf{p}) \end{cases} \quad (18)$$

$$\mu^* = \tilde{\delta} (\tilde{\beta} + \tilde{P}_d)$$

where  $\tilde{\delta} = (\sum_{i \in \tilde{\mathcal{S}}(\mathbf{p})} 1/a_i)^{-1}$ ,  $\tilde{\beta} = \sum_{i \in \tilde{\mathcal{S}}(\mathbf{p})} b_i/a_i$ , and  $\tilde{P}_d = P_d - \sum_{i \in \mathcal{J}_{\max}(\mathbf{p})} p_i^{\max}$ . Note that this update again does not guarantee satisfaction of the capacity constraints and this process must be iteratively performed. This iteration method stops when the set of saturated generators are the same in subsequent computations, i.e.,  $\tilde{\mathcal{S}}(\mathbf{p}^{(k)}) \equiv \tilde{\mathcal{S}}(\mathbf{p}^{(k-1)})$ , and the resultant optimal solution is given by

$$p_i^* = \begin{cases} p_i^{\min} & \text{for } i \in \mathcal{J}_{\min}(\mathbf{p}^{(k)}) \\ p_i^{\max} & \text{for } i \in \mathcal{J}_{\max}(\mathbf{p}^{(k)}) \\ \frac{1}{a_i} (\tilde{\delta}\tilde{\beta} + \tilde{\delta}\tilde{P}_d - b_i) & \text{for } i \in \tilde{\mathcal{S}}(\mathbf{p}^{(k)}) \end{cases} \quad (19)$$

where

$$\begin{aligned} \tilde{\delta} &= \left( \sum_{i \in \tilde{\mathcal{S}}(\mathbf{p}^{(k)}) - \mathcal{J}_{\min}(\mathbf{p}^{(k)})} \frac{1}{a_i} \right)^{-1}, \\ \tilde{\beta} &= \sum_{i \in \tilde{\mathcal{S}}(\mathbf{p}^{(k)}) - \mathcal{J}_{\min}(\mathbf{p}^{(k)})} \frac{b_i}{a_i}, \\ \tilde{P}_d &= P_d - \sum_{i \in \mathcal{J}_{\max}(\mathbf{p}^{(k)})} p_i^{\max} - \sum_{i \in \mathcal{J}_{\min}(\mathbf{p}^{(k)})} p_i^{\min}. \end{aligned} \quad (20)$$

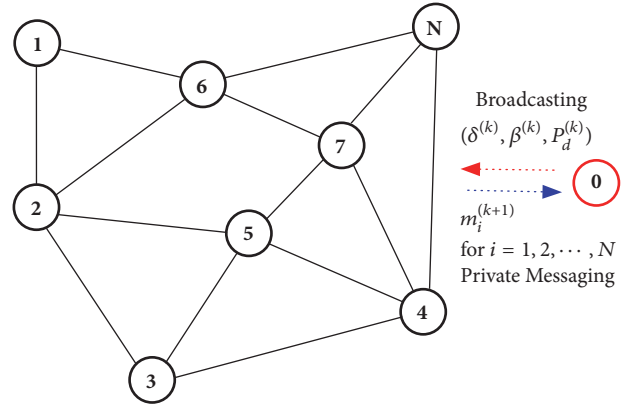


FIGURE 3: A schematic diagram for decentralized iterative computations and message passing. The aggregator (Node 0) broadcasts the values of  $(\delta [\$/\text{MW}^2], \beta [\text{MW}], P_d [\text{MW}])$  and each generator  $i$  (Node  $i$ ) sends a private message  $m_i = (a_i [\$/\text{MW}^2], b_i [\$/\text{MW}], s_i \in \{-1, 0, 1\})$  to the aggregator, where  $s_i = -1$  implies the  $i$ th generator decides to produce its lower limit, i.e.,  $p_i^{\min}$ ,  $s_i = 1$  implies the  $i$ th generator decides to produce its upper limit, i.e.,  $p_i^{\max}$ , and  $s_i = 0$  implies the  $i$ th generator wants to continue negotiation by receiving new values of  $\delta$ ,  $\beta$ , and  $P_d$  from the aggregator.

**Proposition 1.** Let  $\mathbf{p}^{(0)}$  be given by (15) and define a recursive equation  $\mathbf{p}^{(k)} := F(\mathbf{p}^{(k-1)})$ , where  $F : \mathbb{R}^N \rightarrow \mathbb{R}^N$  is defined by (18). If there exists  $p \in \Delta \triangleq \{p \in \mathbb{R}^N : p_i^{\min} \leq p_i \leq p_i^{\max}; i = 1, 2, \dots, N\}$  such that  $\sum_{i=1}^N p_i = P_d$ , then this recursive equation with the initial condition  $\mathbf{p}^{(0)}$  given in (15) converges.

*Proof.* Let the optimal value of  $\text{ED}'(\mathbf{p})$  in (17) be  $J(\mathbf{p})$ . Starting from the initial condition  $\mathbf{p}^{(0)}$ , we define a sequence of real numbers  $\eta_k := J(\mathbf{p}^{(k-1)})$  for  $k \geq 1$ . From the update rule in (18), this sequence is monotonically nondecreasing, i.e.,  $\eta_k \leq \eta_{k+1}$  for  $k \geq 1$ , and it has an upper bound since there exists  $p \in \Delta \triangleq \{p \in \mathbb{R}^N : p_i^{\min} \leq p_i \leq p_i^{\max}; i = 1, 2, \dots, N\}$  such that  $\sum_{i=1}^N p_i = P_d$ . From the monotone convergence theorem [16], this sequence converges. Due to strict convexity of  $f_i$  for all  $i$ ,  $\mathbf{p}^{(k)}$  is uniquely defined for each  $\eta_k$  for all  $k \geq 1$  and the convergence of  $\eta_k$  implies the convergence of  $\mathbf{p}^{(k)}$ .  $\square$

It is also not hard to see that any initial condition  $\mathbf{p}^{(0)} \in \Delta$  guarantees convergence of  $F : \mathbb{R}^N \rightarrow \mathbb{R}^N$  defined by (18) to a unique solution of the economic dispatch (12). That is because  $\mathcal{S}(\mathbf{p}^{(0)}) = \{1, 2, \dots, N\}$  and  $\mathbf{p}^{(1)}$  is given as (15). Figure 3 shows the iterative message-passing between the aggregator (Node 0) and distributed generators (Nodes 1, 2, ..., N). Notice that the broadcasting message announced by the aggregator at time step  $k$  is a tuple  $(\delta^{(k)}, \beta^{(k)}, P_d^{(k)})$  that is computed from the collected private messages  $\{m_i^{(k)} = (a_i^{(k)}, b_i^{(k)}, s_i^{(k)}) : i = 1, 2, \dots, N\}$  by following (18).

*Remark 2.* In our iterative message-passing framework for distributed economic dispatch that is depicted in Figure 3, it is assumed that all generators report their *true* cost (function)

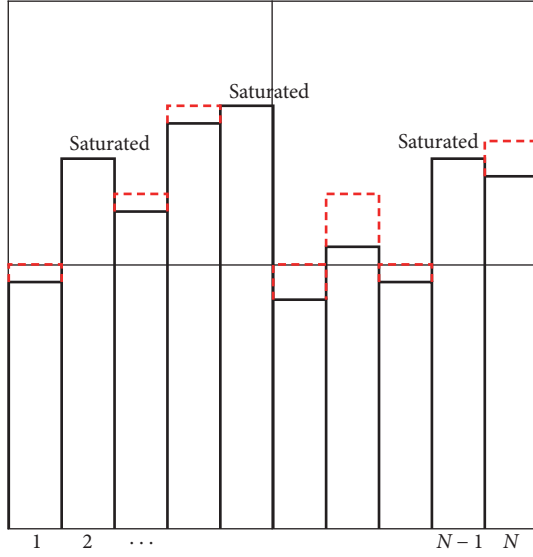


FIGURE 4: A schematic diagram of water-filling in decentralized multiagent learning. When power demand increases as  $P'_d$ , each unsaturated generator  $j$  that does not meet its capacity limit is required to produce additional power  $(P'_d - P_d)((1/a_j)/\sum_{i \in \mathcal{F}} 1/a_i)$ , where  $\mathcal{F}$  refers to the set of unsaturated generators.

parameters  $(a_i, b_i)$ ,  $i = 1, 2, \dots, N$ . It is, of course, possible that a generator can take advantage of lying to the cost parameters. It is our future work to design a pricing mechanism computing  $\mu$  based on the reported cost parameters so that none of generators can benefit from lying. Such a problem is related to the problem of parameterized supply function equilibrium [17–19].

In the presence of nontrivial transmission loss coefficients  $B_{ij}$ , the proposed linear iterative projection method has to be modified. A heuristic method can be applied to take the loss coefficients into account. At each iteration step  $k$ , the power demand  $P_d^{(k)}$  is replaced by  $P_d^{(k)} + \sum_{i=1}^N \sum_{j=1}^N p_i^{(k-1)} B_{ij} p_j^{(k-1)}$  that is computed and broadcasted by the aggregator as depicted in Figure 3. Upon a new residual power demand  $P_d^{(k)} + \sum_{i=1}^N \sum_{j=1}^N p_i^{(k-1)} B_{ij} p_j^{(k-1)}$  is computed, saturated generators are excluded in planning and allocation is performed among generators not yet reached the limits (see Figure 4).

### 3. Further Characteristics of Economic Dispatch

3.1. *Convex Relaxation of QCQP.* Consider the following optimization problem:

$$\begin{aligned} & \text{minimize} && \sum_{i=1}^N f_i(p_i) \\ & \text{subject to} && p_i^{\min} \leq p_i \leq p_i^{\max}; \quad i = 1, 2, \dots, N \quad (21) \\ & && \sum_{i=1}^N p_i - \sum_{i=1}^N \sum_{j=1}^N p_i B_{ij} p_j \geq P_d \end{aligned}$$

in which the equality constraint corresponding to demand-supply balance of ED in (1) is relaxed to be inequality. This can be rewritten as the following quadratically constrained quadratic programming (QCQP):

$$\begin{aligned} & \text{minimize} && \frac{1}{2} \mathbf{p}^\top \mathbf{A} \mathbf{p} + \mathbf{b}^\top \mathbf{p} + c \\ & \text{subject to} && p^{\min} \leq \mathbf{p} \leq p^{\max} \quad (22) \\ & && \mathbf{p}^\top \mathbf{B} \mathbf{p} - \mathbf{1}_N^\top \mathbf{p} + P_d \leq 0 \end{aligned}$$

where  $B$  is symmetric, but not necessarily positive semidefinite, so that this QCQP might be nonconvex. A method of convex relaxation can be applied to obtain the following semidefinite program (SDP):

$$\begin{aligned} & \text{minimize} && \frac{1}{2} \text{tr}(\mathbf{A} \mathbf{P}) + \mathbf{b}^\top \mathbf{p} + c \\ & \text{subject to} && p^{\min} \leq \mathbf{p} \leq p^{\max} \quad (23) \\ & && \text{tr}(\mathbf{B} \mathbf{P}) - \mathbf{1}_N^\top \mathbf{p} + P_d \leq 0 \\ & && \begin{bmatrix} \mathbf{P} & \mathbf{p} \\ \mathbf{p}^\top & 1 \end{bmatrix} \geq 0 \end{aligned}$$

where the linear matrix inequality is obtained from the Schur complement lemma for  $\mathbf{P} - \mathbf{p} \mathbf{p}^\top \geq 0$ . This inequality corresponds to convexification of the equality  $\mathbf{P} = \mathbf{p} \mathbf{p}^\top$ .

**Lemma 3** (lossless relaxation). *The optimal values and the associated solutions of (22) and (23) are the same.*

*Proof.* Let a solution of the optimization (22) be  $\bar{\mathbf{p}}$ . Substituting  $\mathbf{P} = \bar{\mathbf{p}} \bar{\mathbf{p}}^\top + \mathbf{Q}$  with  $\mathbf{Q} \geq 0$  into the optimization (23), we have

$$\begin{aligned} & \text{minimize} && \frac{1}{2} \text{tr}(\mathbf{A} \mathbf{Q}) + \frac{1}{2} \bar{\mathbf{p}}^\top \mathbf{A} \bar{\mathbf{p}} + \mathbf{b}^\top \bar{\mathbf{p}} + c \\ & \text{subject to} && \text{tr}(\mathbf{B} \mathbf{Q}) + \bar{\mathbf{p}}^\top \mathbf{B} \bar{\mathbf{p}} - \mathbf{1}_N^\top \bar{\mathbf{p}} + P_d \leq 0 \quad (24) \\ & && \mathbf{Q} \geq 0 \end{aligned}$$

which reduces to

$$\begin{aligned} & \text{minimize} && \text{tr}(\mathbf{A} \mathbf{Q}) \\ & \text{subject to} && \text{tr}(\mathbf{B} \mathbf{Q}) \leq 0 \quad (25) \\ & && \mathbf{Q} \geq 0 \end{aligned}$$

where the constant factor 1/2 in the objective function is removed for notational convenience. By considering a Lagrange function  $L(\mathbf{Q}, \lambda) = \text{tr}((\mathbf{A} + \lambda \mathbf{B}) \mathbf{Q})$  and from the positive definiteness of  $\mathbf{A} > 0$ , the weak duality gives

$$\begin{aligned} & \text{optimal value of (25)} \geq \max_{\lambda \geq 0} \min_{\mathbf{Q} \geq 0} L(\mathbf{Q}, \lambda) \\ & = \begin{cases} 0 & \text{if } \mathbf{A} + \lambda \mathbf{B} \geq 0 \\ -\infty & \text{otherwise} \end{cases} \quad (26) \end{aligned}$$

and this implies that the *unique* optimal solution of (25) is  $Q^* \equiv 0$ . Therefore, we conclude that the optimal solution of (23) is indeed the rank-one matrix  $P^* \equiv \bar{\mathbf{p}} \bar{\mathbf{p}}^\top$  with an optimal solution  $\bar{\mathbf{p}}$  of (22).  $\square$

**3.2. Multiparametric Programming.** Consider the economic dispatch problem in (12). We analyze the dependence of the optimal solutions to the total power demand:

$$p_i^*(P_d) \quad \text{for } i = 1, 2, \dots, N \quad (27)$$

**Proposition 4.** *Suppose that there exists  $p \in \Delta$  such that  $\sum_{i=1}^N p_i = P_d$ . Every  $p_i^*(P_d)$  is monotonically nondecreasing and continuously piecewise affine in  $P_d \geq 0$  for  $i = 1, 2, \dots, N$ .*

*Proof.* For the given  $P_d > 0$  and the corresponding optimal solution  $p^*(P_d)$  of the optimization (12), consider the optimization (17) with  $\mathbf{p} = p^*(P_d)$  and the associated computation (18). Then, there exists a small enough  $\epsilon > 0$  such that

$$p_i^*(P_d + \epsilon) = \begin{cases} p_i^{\min} & \text{for } i \in \mathcal{J}_{\min}(\mathbf{p}^*(P_d)) \\ p_i^{\max} & \text{for } i \in \mathcal{J}_{\max}(\mathbf{p}^*(P_d)) \\ p_i^*(P_d) + \frac{1/a_i}{\sum_{j \in \tilde{\mathcal{F}}} 1/a_j} \epsilon & \text{for } i \in \tilde{\mathcal{F}}(\mathbf{p}^*(P_d)) \end{cases} \quad (28)$$

is the optimal solution of the economic dispatch (12) when the power demand is given by  $P_d + \epsilon$ . In other words, the index sets  $\mathcal{J}_{\min}(\mathbf{p}^*(P_d + \epsilon))$  and  $\mathcal{J}_{\max}(\mathbf{p}^*(P_d))$  remain the same and the optimal solutions  $p_i^*(P_d)$  corresponding to the index set  $\tilde{\mathcal{F}}(\mathbf{p}^*(P_d))$  change as  $p_i^*(P_d) + ((1/a_i)/\sum_{j \in \tilde{\mathcal{F}}} 1/a_j)\epsilon$ . This shows that optimal solution  $p^*(P_d)$  is (elementwise) *monotonically nondecreasing* and *continuously piecewise affine* in  $P_d \geq 0$ .  $\square$

Now we analyze the *explicit* dependence of the optimal power generation profile  $\mathbf{p}^*$  on the power demand  $P_d$  for which the results from multiparametric programming (MPP) [20] are exploited. We can rewrite the problem of economic dispatch in (12) as the following quadratic programming:

$$\begin{aligned} V^*(P_d) := \text{minimize} \quad & \frac{1}{2} \mathbf{p}^\top \mathbf{A} \mathbf{p} + b^\top \mathbf{p} + c \\ \text{subject to} \quad & \mathbf{H} \mathbf{p} \leq r + EP_d \end{aligned} \quad (29)$$

where

$$A = \begin{bmatrix} a_1 & 0 & \cdots & 0 \\ 0 & a_2 & \ddots & \vdots \\ \vdots & \ddots & \ddots & 0 \\ 0 & \cdots & 0 & a_N \end{bmatrix},$$

$$b = \begin{bmatrix} b_1 \\ b_2 \\ \vdots \\ b_N \end{bmatrix},$$

$$c = \sum_{i=1}^N c_i$$

$$H = \begin{bmatrix} \mathbf{1}_{N \times 1}^\top \\ -\mathbf{1}_{N \times 1}^\top \\ I_{N \times N} \\ I_{N \times N} \end{bmatrix},$$

$$r = \begin{bmatrix} 0 \\ 0 \\ \mathbf{p}^{\max} \\ -\mathbf{p}^{\min} \end{bmatrix},$$

$$E = \begin{bmatrix} \mathbf{1} \\ \mathbf{1} \\ \mathbf{0}_{N \times 1} \\ \mathbf{0}_{N \times 1} \end{bmatrix}$$

(30)

with  $\mathbf{1}_{N \times 1}$  all ones vector in  $\mathbb{R}^N$ ,  $\mathbf{0}_{N \times 1}$  all zeros vector in  $\mathbb{R}^N$ ,  $I_{N \times N}$  identity matrix in  $\mathbb{R}^{N \times N}$ , and  $\mathbf{p}^{\max(\min)} = [p_1^{\max(\min)} \ p_2^{\max(\min)} \ \cdots \ p_N^{\max(\min)}]^\top \in \mathbb{R}^N$ . The associated KKT conditions are given by

$$\mathbf{A} \mathbf{p} + H^\top \mathbf{w} = 0 \quad (\text{stationarity}) \quad (31)$$

$$\mathbf{H} \mathbf{p} - r - EP_d \leq 0 \quad (\text{primal feasibility}) \quad (32)$$

$$\mathbf{w} \geq 0 \quad (\text{dual feasibility}) \quad (33)$$

$$\mathbf{w}^\top (\mathbf{H} \mathbf{p} - r - EP_d) = 0 \quad (\text{complementarity}) \quad (34)$$

where  $\mathbf{w} \in \mathbb{R}^{(2N+2)}$  is a (vector) Lagrange multiplier corresponding to the inequality in (29). For given  $P_d$  with which the optimization in (29) can be solved, the corresponding optimizer  $\mathbf{p}$  yields the set of active constraints defined as

$$\mathcal{J}_a(P_d) \triangleq \{i \in \mathcal{J} : H_i \mathbf{p} = r_i + E_i P_d\} \quad (35)$$

where  $\mathcal{J} = \{1, 2, \dots, 2N + 2\}$  and  $(\cdot)_i$  denotes the  $i$ th row of the argument. The rows of the constraints matrices  $H$ ,  $r$ , and  $E$  corresponding to the index set  $\mathcal{J}_a(P_d)$  are extracted to construct the matrices  $H_{\mathcal{J}_a(P_d)}$ ,  $r_{\mathcal{J}_a(P_d)}$ , and  $E_{\mathcal{J}_a(P_d)}$  that would be rewritten in the following compact forms:  $H_{\mathcal{J}_a}$ ,  $r_{\mathcal{J}_a}$ , and  $E_{\mathcal{J}_a}$ , respectively, by hiding its dependence of  $P_d$ . By definition of  $\mathcal{J}_a(P_d)$ , we have the equality conditions of optimality

$$H_{\mathcal{J}_a} \mathbf{p} - r_{\mathcal{J}_a} - E_{\mathcal{J}_a} P_d = 0. \quad (36)$$

Combining the two systems of equations (31) and (36) gives

$$-H_{\mathcal{J}_a} A^{-1} H^{\top} \mathbf{w} - r_{\mathcal{J}_a} - E_{\mathcal{J}_a} P_d = 0 \quad (37)$$

where  $H^{\top} \mathbf{w} = H_{\mathcal{J}_a}^{\top} \mathbf{w}_{\mathcal{J}_a}$  because the complementarity condition (34) implies  $\mathbf{w}_{\mathcal{J}_a^c} = 0$  for  $\mathcal{J}_a^c = \mathcal{J} \setminus \mathcal{J}_a$ . Therefore, we obtain an active (vector) Lagrange multiplier

$$\begin{aligned} \mathbf{w} = & - \left( H_{\mathcal{J}_a} A^{-1} H_{\mathcal{J}_a}^{\top} \right)^{-1} r_{\mathcal{J}_a} \\ & - \left( H_{\mathcal{J}_a} A^{-1} H_{\mathcal{J}_a}^{\top} \right)^{-1} E_{\mathcal{J}_a} P_d \end{aligned} \quad (38)$$

and the corresponding (primal) optimizer

$$\begin{aligned} \mathbf{p} = & -A^{-1} H_{\mathcal{J}_a}^{\top} \mathbf{w}_{\mathcal{J}_a} \\ = & A^{-1} H_{\mathcal{J}_a}^{\top} \left( H_{\mathcal{J}_a} A^{-1} H_{\mathcal{J}_a}^{\top} \right)^{-1} E_{\mathcal{J}_a} P_d \\ & + A^{-1} H_{\mathcal{J}_a}^{\top} \left( H_{\mathcal{J}_a} A^{-1} H_{\mathcal{J}_a}^{\top} \right)^{-1} r_{\mathcal{J}_a} \end{aligned} \quad (39)$$

where the inverse exists provided that the active constraints are linearly independent. Note that the active Lagrange multiplier and optimizer obtained in (38) and (39), respectively, are affine functions in  $P_d$ . The next step is to find or characterize all the points  $P'_d$  in the neighborhood of  $P_d$  in which the optimizer  $\mathbf{p}(P'_d)$  has the same set of active constraints, i.e.,  $\mathcal{J}_a(P'_d) = \mathcal{J}_a(P_d)$  so that  $\mathbf{p}(P'_d)$  is of the same form as (39). Such neighborhood of  $P_d$  can be obtained by substituting (39) and (38) into (32) and (33), respectively. Furthermore, it turns out that the neighborhood is a polyhedron

$$\mathcal{P}_\ell \triangleq \{P'_d \in \mathbb{R}_+ : Q_\ell P'_d \leq q_\ell\} \quad (40)$$

where

$$\begin{aligned} Q_\ell = & \begin{bmatrix} HA^{-1} H_{\mathcal{J}_a}^{\top} \left( H_{\mathcal{J}_a} A^{-1} H_{\mathcal{J}_a}^{\top} \right)^{-1} E_{\mathcal{J}_a} - E \\ \left( H_{\mathcal{J}_a} A^{-1} H_{\mathcal{J}_a}^{\top} \right)^{-1} E_{\mathcal{J}_a} \end{bmatrix}, \\ q_\ell = & \begin{bmatrix} r - HA^{-1} H_{\mathcal{J}_a}^{\top} \left( H_{\mathcal{J}_a} A^{-1} H_{\mathcal{J}_a}^{\top} \right)^{-1} r_{\mathcal{J}_a} \\ - \left( H_{\mathcal{J}_a} A^{-1} H_{\mathcal{J}_a}^{\top} \right)^{-1} r_{\mathcal{J}_a} \end{bmatrix} \end{aligned} \quad (41)$$

are computed from a given  $P_d$  and the associated optimizer  $\mathbf{p}(P_d)$ .

*Remark 5.* We have shown that the affine dependence of the optimal power generation profiles on the power demand can be explicitly analyzed. This parameterization could be useful when the power demands are not known a priori but forecasted with uncertainty. Analyzing the required power generation profiles over the wide range of power demands offline would help the system operator to schedule the power supply in smaller time-scales.

**3.3. Uncertain Transmission Loss and Power Demand.** In Section 3.2, a method of multiparametric programming is suggested for taking care of uncertain power demand  $P_d$ . By

applying MPP, economic generation dispatch is computed as a function of  $P_d$  in (38) and (39). In addition to uncertain power demand  $P_d$ , we also need to consider uncertain or variable power loss  $P_L$  that is parameterized as a quadratic function  $\sum_{i=1}^N \sum_{j=1}^N p_i B_{ij} p_j$ . The loss coefficients  $B_{ij}$  are not certain but can be assumed to be bounded as

$$B_{ij}^{\min} \leq B_{ij} \leq B_{ij}^{\max}, \quad \text{for } i, j = 1, 2, \dots, N \quad (42)$$

where  $B_{ij}^{\min}$  and  $B_{ij}^{\max}$  refer to the lower and upper bounds of  $B_{ij}$ , respectively. For more general representation of uncertain loss coefficient matrix  $B$ , we assume that  $B$  is not fixed but belongs to a convex polytope that has a finite number of vertices:

$$B \in \text{Conv} \{B^{(0)}, B^{(1)}, \dots, B^{(\ell)}\} \quad (43)$$

where  $\text{Conv}\{\cdot\}$  denotes the convex hull of a set. In other words, there exists  $t_0, t_1, \dots, t_\ell \in [0, 1]$  with  $\sum_{\tau=0}^{\ell} t_\tau = 1$  such that  $B = \sum_{\tau=0}^{\ell} t_\tau B^{(\tau)}$ . This implies that the quadratic loss function is parameterized as  $P_L(p) = \sum_{\tau=0}^{\ell} \sum_{i=1}^N \sum_{j=1}^N t_\tau p_i B_{ij}^{(\tau)} p_j$ , where  $t_\tau \in [0, 1]$  are not known but uncertain. To take care of uncertain loss coefficients, the three proposed methods need to be modified.

*Modified SDP Method.* The SDP method presented in (23) is modified to take the uncertain loss coefficient matrix  $B$  in (43) as follows:

$$\begin{aligned} & \text{minimize} \quad \frac{1}{2} \text{tr}(A\mathbf{P}) + b^{\top} \mathbf{p} + c \\ & \text{subject to} \quad p^{\min} \leq \mathbf{p} \leq p^{\max} \\ & \quad \text{tr}(B^{(\tau)} \mathbf{P}) - \mathbf{1}_N^{\top} \mathbf{p} + P_d \leq 0, \\ & \quad \quad \quad \text{for } \tau = 0, 1, \dots, \ell \\ & \quad \quad \quad \begin{bmatrix} \mathbf{P} & \mathbf{p} \\ \mathbf{p}^{\top} & 1 \end{bmatrix} \geq 0 \end{aligned} \quad (44)$$

that is indeed robust optimization counterpart of (23).

*Modified Iterative Primal-Dual Method.* The iterative primal-dual method presented in (7) and (11) is modified to take the uncertain loss coefficient matrix  $B$  in (43) as follows:

$$\begin{aligned} p_i^{(k+1)} & := \text{BR}_i(p_{\mathcal{N}_i}^{(k)}, \mu^{(k)}) \quad \text{for } i = 1, 2, \dots, N \\ \mu^{(k+1)} & := \mu^{(k)} + \alpha^{(k+1)} \left( P_d + P_L^{(k+1)} - \sum_{i=1}^N p_i^{(k+1)} \right) \end{aligned} \quad (45)$$

where

$$P_L^{(k+1)} := \max_{0 \leq \tau \leq \ell} \left\{ \sum_{i=1}^N \sum_{j \in \mathcal{N}_i} p_i^{(k+1)} B_{ij}^{(\tau)} p_j^{(k+1)} \right\} \quad (46)$$

that is the worst-case line loss for given  $p_i^{(k+1)}$ ,  $i = 1, 2, \dots, N$ .

TABLE 1: Problem data for a test case of 6 generators.

| Generator<br>$i$ | $a_i$<br>[\$/MW <sup>2</sup> ] | $b_i$<br>[\$/MW] | $c_i$<br>[\$] | $p_i^{\min}$<br>[MW] | $p_i^{\max}$<br>[MW] |
|------------------|--------------------------------|------------------|---------------|----------------------|----------------------|
| 1                | 0.00375                        | 2.00             | 0             | 50                   | 200                  |
| 2                | 0.01750                        | 1.75             | 0             | 20                   | 80                   |
| 3                | 0.06250                        | 1.00             | 0             | 15                   | 50                   |
| 4                | 0.00834                        | 3.25             | 0             | 10                   | 35                   |
| 5                | 0.02500                        | 3.00             | 0             | 10                   | 30                   |
| 6                | 0.02500                        | 3.00             | 0             | 12                   | 40                   |

*Modified Iterative Linear Projection Method.* The iterative primal-dual method presented in (19) is modified to take the uncertain loss coefficient matrix  $B$  in (43) as follows:

$$p_i^{(k+1)} = \begin{cases} p_i^{\min} & \text{for } i \in \mathcal{J}_{\min}(\mathbf{p}^{(k)}) \\ p_i^{\max} & \text{for } i \in \mathcal{J}_{\max}(\mathbf{p}^{(k)}) \\ \frac{1}{a_i} (\tilde{\delta}\tilde{\beta} + \tilde{\delta}\tilde{P}_d - b_i) & \text{for } i \in \tilde{\mathcal{F}}(\mathbf{p}^{(k)}) \end{cases} \quad (47)$$

where

$$\tilde{P}_d = P_d + \max_{0 \leq \tau \leq \ell} \left\{ \sum_{i=1}^N \sum_{j \in \mathcal{N}_i} p_i^{(k)} B_{ij}^{(\tau)} p_j^{(k)} \right\} - \sum_{i \in \mathcal{J}_{\max}(\mathbf{p}^{(k)})} p_i^{\max} - \sum_{i \in \mathcal{J}_{\min}(\mathbf{p}^{(k)})} p_i^{\min}, \quad (48)$$

and  $\tilde{\delta}$  and  $\tilde{\beta}$  are defined the same as (19).

#### 4. Case Study

To demonstrate our methods of economic dispatch presented in Sections 2 and 3, we consider the 6-generator test case whose generation cost parameters and generation limits are given in Table 1. This system contains six generation units, 26 buses, and 46 transmission lines [10]. The power loss function  $\mathbf{p}^T B \mathbf{p}$  is parameterized with a symmetric matrix of loss coefficients that is given by

$$B = 10^{-3} \begin{bmatrix} 0.218 & 0.103 & 0.009 & -0.010 & 0.002 & 0.027 \\ 0.103 & 0.181 & 0.004 & -0.015 & 0.002 & 0.030 \\ 0.009 & 0.004 & 0.417 & -0.131 & -0.153 & -0.107 \\ -0.010 & -0.015 & -0.131 & 0.221 & 0.094 & 0.050 \\ 0.002 & 0.002 & -0.153 & 0.094 & 0.243 & -0.000 \\ 0.027 & 0.030 & -0.107 & 0.050 & -0.000 & 0.358 \end{bmatrix} \quad (49)$$

Three different methods, (a) SDP method (centralized), (b) iterative primal-dual method (distributed), and (c) iterative

linear projection method (distributed), are applied to find optimal solutions of economic dispatch with varying power demands. All numerical computations are carried out using MATLAB on a 1.6 GHz Intel Core i5 personal laptop with 8GB 1600 MHz DDR3.

*Optimality.* The resultant optimal power generation profiles computed by the proposed three optimization algorithms are presented in Figure 5. For power demands varying from 117 [MW] to 435 [MW], we observe that the three different methods give the exactly same results of economic generation dispatch. Generators 1 and 2 have smaller  $a_i$  with larger upper bounds  $p_i^{\max}$ , so that they become active in the sense that  $p_i^* > p_i^{\min}$  when  $P_d > P_d^{\min}$ . When Generator 1 with the smallest marginal cost is saturated, i.e.,  $p_1^* = p_1^{\max}$ , as  $P_d$  increases, the slopes corresponding to change rates of Generators 2 and 3 become larger. This is because the value of  $\delta = (\sum_{i=1}^N 1/a_i)^{-1}$  changes to the larger value  $(\sum_{i \neq 1}^N 1/a_i)^{-1}$ . Such changes in slopes occur whenever a generator is saturated in its upper limit. As a matter of fact, such changes in activeness and slopes are explicitly exploited in the iterative linear projection method that significantly reduces computational complexity.

*Computational Complexity.* In Figure 6, we compare the computation times of the three proposed methods. It shows the histograms of the three different methods to compute the optimal economic dispatch profiles with varying total power demand ranging from 117 [MW] to 435 [MW]. Since the computation times heavily depend on the choice of the initial guesses of the primal and dual variables and the algorithms for solving semidefinite programs, we do not exploit any warm-start strategies for fair comparisons. We observe that the algorithm of iterative linear projection requires a significantly small size of iterations and tremendously fast speed in computations—it is three orders of magnitude faster than the primal-dual iteration method in average. The distributed algorithm based on primal-dual iteration is approximately three times faster than the centralized semidefinite program in average. The SDP method presented in (23) requires a test for positive semidefiniteness of a symmetric matrix whose size is  $N + 1$  with  $N(N + 1)/2 + N$  variables at each Newton-KKT iteration step of the interior-point method [21]. Such test has computational complexity  $O((N^2 + 3N)/2)(N +$

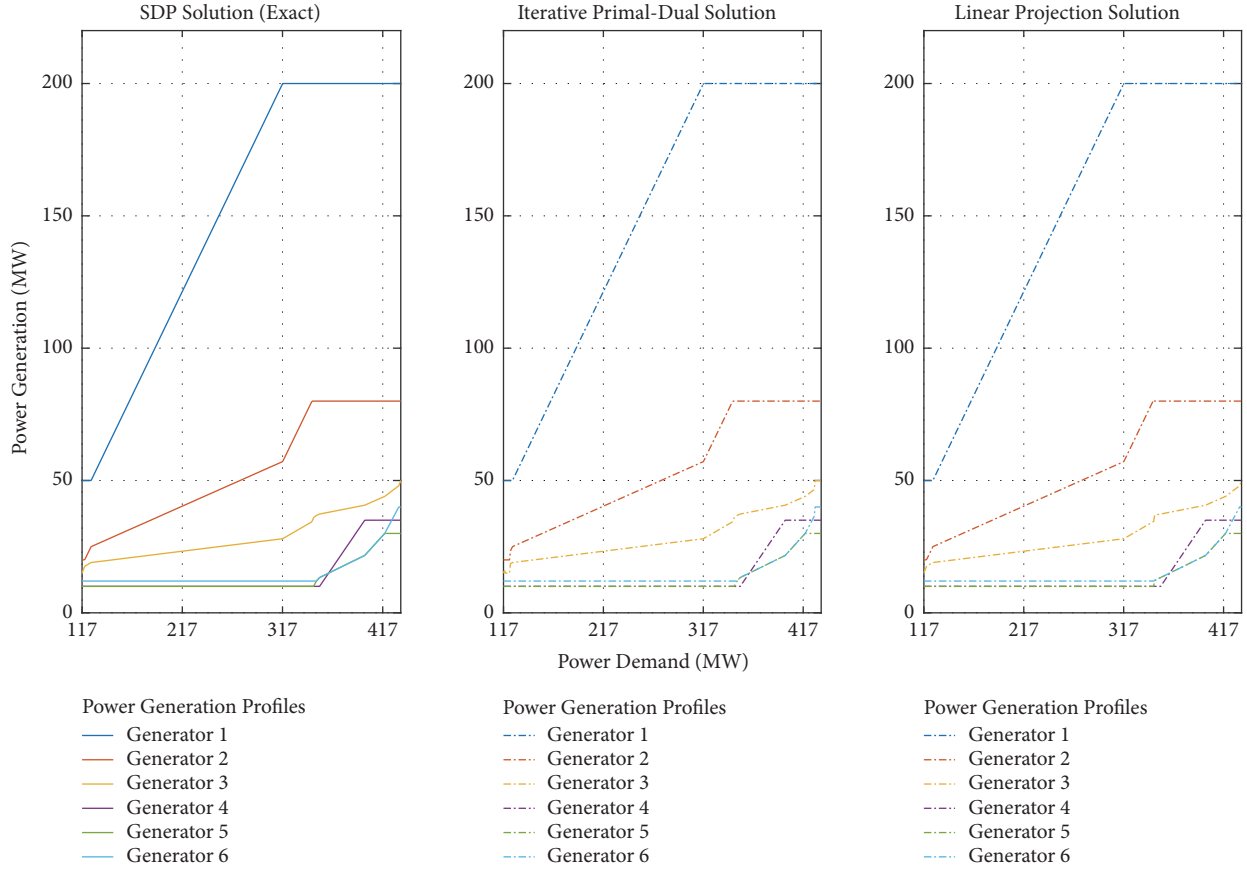


FIGURE 5: Economic dispatch solutions for varying power demands (from 117 [MW] to 435 [MW]) obtained by three different methods: (a) SDP method, (b) iterative primal-dual method, and (c) iterative linear projection method.

$1)^4) + (N + 1)^{O(\min\{(N+1)^2, (N^2+3N)/2\})}$  in terms of floating-point operations [22], without exploiting any sparsity structures in problem. The primal-dual iteration method presented in (7) and (11) requires iterative projections that are decomposed into one-dimensional subspaces in primal updates and linear recursive computations in dual updates. Such procedure has computational complexity  $O(N^2)$ . The convergence rate is heavily dependent on the step-size  $\alpha^{(k)}$  and we choose  $\alpha^{(k)} > 0$  such that  $\sum \alpha^{(k)} = \infty$  and  $\sum (\alpha^{(k)})^2 < \infty$ . The iterative linear projection method presented in (19) requires computations of multiplication and addition. Its computational complexity is  $O(N)$  and more importantly, the projection terminates in less than  $N$  steps. This reduces significant amounts of computation time.

## 5. Conclusion

In this paper, we present three different methods of solving problems of economic dispatch with transmission losses. The iterative primal-dual method is indeed based on indirect approach to optimization in which the KKT conditions are solved in a distributed manner. The iterative linear projection method is based on closed-form solutions for the optimality

conditions of unconstrained counterparts and the closed-form solutions are iteratively projected on the set corresponding to the capacity limits of generation units. The SDP method is based on the convex relaxation of the associated quadratic-constrained quadratic program whose exactness is shown from the strong duality. The parametric dependence of the power generation profiles is also analyzed with varying power demands in economic dispatch.

## Data Availability

No data were used to support this study.

## Conflicts of Interest

The author declares that they have no conflicts of interest regarding the publication of this paper.

## Acknowledgments

This work was supported by Inha University Grant (INHA-57823) and Korea Electric Power Corporation (Grant number: R18XA01).

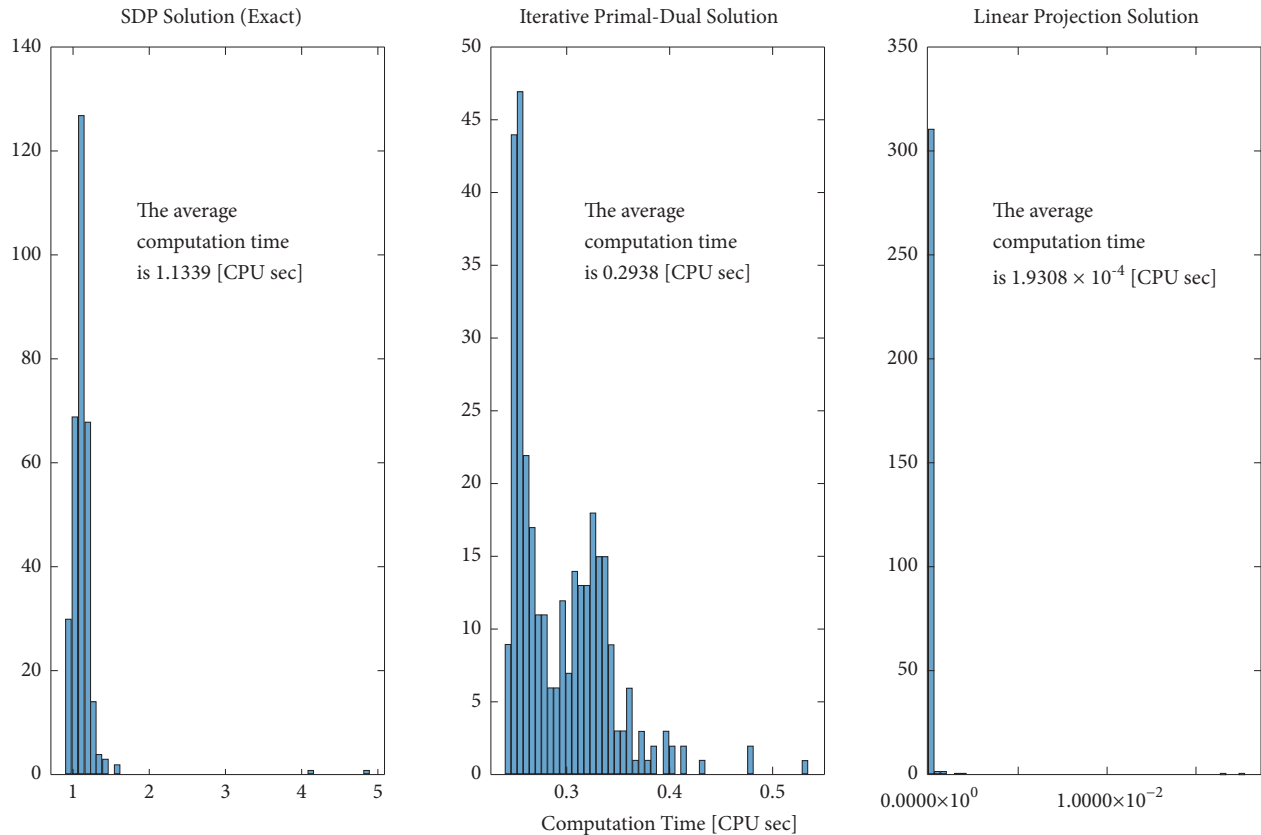


FIGURE 6: Comparison of computation times for three different numerical methods: (a) SDP method, (b) iterative primal-dual method, and (c) iterative linear projection method.

## References

- [1] K. Heussen, A. Saleem, and M. Lind, "Control architecture of power systems: Modeling of purpose and function," in *Proceedings of the 2009 IEEE Power and Energy Society General Meeting, PES '09*, 8, 1 pages, July 2009.
- [2] D. K. Molzahn, F. Dörfler, H. Sandberg et al., "A survey of distributed optimization and control algorithms for electric power systems," *IEEE Transactions on Smart Grid*, vol. 8, no. 6, pp. 2941–2962, 2017.
- [3] B. H. Chowdhury and S. Rahman, "A review of recent advances in economic dispatch," *IEEE Transactions on Power Systems*, vol. 5, no. 4, pp. 1248–1259, 1990.
- [4] Z. Zhang, X. Ying, and M.-Y. Chow, "Decentralizing the economic dispatch problem using a two-level incremental cost consensus algorithm in a smart grid environment," in *Proceedings of the IEEE North American Power Symposium (NAPS)*, pp. 1–7, 2011.
- [5] Z. Zhang and M. Chow, "Convergence analysis of the incremental cost consensus algorithm under different communication network topologies in a smart grid," *IEEE Transactions on Power Systems*, vol. 27, no. 4, pp. 1761–1768, 2012.
- [6] S. Yang, S. Tan, and J.-X. Xu, "Consensus based approach for economic dispatch problem in a smart grid," *IEEE Transactions on Power Systems*, vol. 28, no. 4, pp. 4416–4426, 2013.
- [7] H. Xing, Y. Mou, M. Fu, and Z. Lin, "Consensus based bisection approach for economic power dispatch," in *Proceedings of the 2014 53rd IEEE Annual Conference on Decision and Control, CDC 2014*, pp. 3789–3794, December 2014.
- [8] H. Xing, Y. Mou, M. Fu, and Z. Lin, "Distributed bisection method for economic power dispatch in smart grid," *IEEE Transactions on Power Systems*, vol. 30, no. 6, pp. 3024–3035, 2015.
- [9] H. Xing, Z. Lin, and M. Fu, "Distributed augmented lambda-iteration method for economic dispatch in smart grid," in *Proceedings of the 2017 Chinese Automation Congress, CAC 2017*, pp. 3302–3307, China, October 2017.
- [10] H. Saadat, *Power System Analysis*, McGraw-Hill Book Co., New York, NY, USA, 1999.
- [11] A. Pantoja and N. Quijano, "A population dynamics approach for the dispatch of distributed generators," *IEEE Transactions on Industrial Electronics*, vol. 58, no. 10, pp. 4559–4567, 2011.
- [12] P. Chakraborty, E. Baeyens, P. P. Khargonekar, and K. Poolla, "A cooperative game for the realized profit of an aggregation of renewable energy producers," in *Proceedings of the 55th IEEE Conference on Decision and Control, CDC 2016*, pp. 5805–5812, USA, December 2016.
- [13] C. Chiang, "Improved genetic algorithm for power economic dispatch of units with valve-point effects and multiple fuels," *IEEE Transactions on Power Systems*, vol. 20, no. 4, pp. 1690–1699, 2005.
- [14] Z. Gaing, "Particle swarm optimization to solving the economic dispatch considering the generator constraints," *IEEE Transactions on Power Systems*, vol. 18, no. 3, pp. 1187–1195, 2003.

- [15] N. Sinha, R. Chakrabarti, and P. K. Chattopadhyay, "Evolutionary programming techniques for economic load dispatch," *IEEE Transactions on Evolutionary Computation*, vol. 7, no. 1, pp. 83–94, 2003.
- [16] W. Rudin, *Principles of Mathematical Analysis*, McGraw-Hill Book Co., New York, NY, USA, 1976.
- [17] R. Baldick, "Electricity market equilibrium models: the effect of parametrization," *IEEE Transactions on Power Systems*, vol. 17, no. 4, pp. 1170–1176, 2002.
- [18] R. Johari and J. N. Tsitsiklis, "Parameterized supply function bidding: equilibrium and efficiency," *Operations Research*, vol. 59, no. 5, pp. 1079–1089, 2011.
- [19] W. Lin and E. Bitar, "Parameterized supply function equilibrium in power networks," in *Proceedings of the 55th IEEE Conference on Decision and Control, CDC 2016*, pp. 1542–1548, December 2016.
- [20] E. N. Pistikopoulos, N. A. Diangelakis, and R. Oberdieck, *Multi-parametric Optimization and Control*, Wiley-VCH, New York, NY, USA, 2018.
- [21] L. Vandenberghe and S. Boyd, "Semidefinite programming," *SIAM Review*, vol. 38, no. 1, pp. 49–95, 1996.
- [22] L. Porkolab and L. Khachiyan, "On the complexity of semidefinite programs," *Journal of Global Optimization*, vol. 10, no. 4, pp. 351–365, 1997.

## Research Article

# Noninvasive Vehicle-to-Load Energy Management Strategy to Prevent Li-Ion Batteries Premature Degradation

Martín-Antonio Rodríguez-Licea <sup>1</sup>, Francisco-J. Perez-Pinal <sup>2</sup>,  
Allan-Giovanni Soriano-Sánchez <sup>1</sup> and José-Antonio Vázquez-López<sup>2</sup>

<sup>1</sup>CONACYT-Instituto Tecnológico de Celaya, Mexico

<sup>2</sup>Laboratorio de Innovación en Electrónica Aplicada, Instituto Tecnológico de Celaya, Mexico

Correspondence should be addressed to Martín-Antonio Rodríguez-Licea; [martin.rodriguez@itcelaya.edu.mx](mailto:martin.rodriguez@itcelaya.edu.mx)

Received 7 March 2019; Accepted 28 April 2019; Published 23 May 2019

Guest Editor: Michael Z. Q. Chen

Copyright © 2019 Martín-Antonio Rodríguez-Licea et al. This is an open access article distributed under the Creative Commons Attribution License, which permits unrestricted use, distribution, and reproduction in any medium, provided the original work is properly cited.

Today, electric vehicles available in the market aspire to offer different connections to the end user, for instance, Vehicle to Grid (V2G), Vehicle to Building (V2B), Vehicle to Home (V2H), Vehicle to Vehicle (V2V), and Vehicle to Load (V2L), among others. Notwithstanding these versatility options toward the development of a sustainable society, the additional degradation of the energy storage systems once those operate in extra discharge modes is inevitable. Therefore, in this paper, an energy management strategy (EMS) which operates autonomously and noninvasively as an additional layer to the battery management system (BMS) is proposed. The EMS limits the current flow avoiding high and low temperatures, low state of charge (SoC), high deep of discharge (DoD), noncentered DoD around an optimal SoC point, and high charge and discharge rates. The proposed EMS is evaluated by long-term simulations with a Li-Ion battery degradation model and realistic weather conditions, during standard driving cycles including the V2L operation. The effectiveness and simplicity of tuning of the proposed EMS allow estimating and increasing the life expectancy of the Li-Ion battery bank, by limiting the energy used for V2L operation.

## 1. Introduction

Nowadays, the electric vehicle (EV) is a forced reality more than a futurist conception mostly, due to the high pollution levels and the increasing fossil fuel prices [1–3]. Beyond the difficulties in the generation of green energy that must satisfy an exponentially growing demand [4–8], a future is forecasted in which a vehicle can bring electric power to places or situations wherever it is not available by the usual means. Currently, recognized researchers direct their efforts to the study of technologies and strategies to achieve the smart interaction of an EV with a grid (Vehicle to Grid, V2G, [9]), a building (Vehicle to Building, V2B, [10]), a home (Vehicle to Home, V2H, [11]), another EV (Vehicle to Vehicle, V2V, [12]), and to a lesser extent a load (Vehicle to Load, V2L, [13]) and even improve the power quality ([14–16]). Additionally, some authors consider that V2L is the first approximation to real Vehicle to Everything (V2X) applications, if they act like an independent cluster of generations [17, 18]. V2L

capability will enable the EV to replace the usual electric generator to power an isolated load [17] and there is no coordination with the grid system operator, but there is basic local communication from EVs to the loads [18]; also, several EVs governed by a local coordinator could support a mobile hospital in a Vehicle to Premise (V2P) configuration.

Currently, the science of Li-Ion batteries allows the use of the power bank of the VE to feed point loads (V2L) in addition to extended VE's autonomy. However, it has also been reported that there may be premature degradation ([19–25]) that depends predominantly, to the authors' knowledge, on the temperature, state of charge (SoC), charge and discharge current rate (C-rate), and depth of discharge (DoD) during its usage and in some cases also during its storage. That is, although the State of Health of a battery (SoH) will inevitably decrease due (a) to the number of cycles during its usage (cycling aging) and (b) to its inherent expiration date (calendar aging), the SoH decay rate can be modeled as function of factors such as temperature, SoC, the DoD, and

the C-rate during its regular use as well as the temperature and SoC during storage [18–28].

In other words, preventing model-based battery degradation is not a trivial task, and it usually involves a mechanical/chemical redesign and/or an invasive battery management system (BMS) specific to the device's chemistry and equalization. However, such systems are black-box focused in the charging behavior and very likely not designed to avoid long-term degradation of the battery in a V2L scenario, where extra discharge cycles are introduced. For instance, in [29], a system to collect data from charging sessions has been presented, to correlate with the corresponding EV and some relevant information and evidence of the battery degradation.

An alternative to overcome this difficulty is using an additional layer when the EV operates in V2L. For instance, the authors in [30] introduced a just-in-time strategy from a smart grid perspective (overall cycling) to extend the Li-Ion battery life, benefiting from the storage with low SoC property and a prediction of the EV usage. In such work, the EV energy provided and required in a V2G scenario flows only when possible to avoid premature degradation and such scenario does not include the V2L operation. In other words, unfortunately, this strategy involves a smart grid recharge becoming cluster-dependent, hardly restricts (shutdown) the provided energy, and can leave the vehicle without enough recharging for unusual utilization.

It should be noted at this point that there is very little research into the development of closed-loop control systems to prevent long-term battery degradation in V2L scenarios. For instance, authors in [31] developed a semiempirical Li-Ion battery capacity degradation model and a Battery Energy Storage System to avoid the degradation from the recharge side; in other words, the recharging behavior is optimized to avoid the premature degradation but a V2L discharge scenario is not the aim of such investigation. Additionally, in [32–35] the authors presented devices that can be used in a V2L operation; however, none of them demonstrates the aim to avoid long-term Li-Ion battery degradation.

As can be seen from the previous state of the art review, only some authors have aimed to diminish the degradation of the batteries in V2G scenarios but, for V2L, there is still a lack of energy management systems that allow estimating a priori and regulate the premature degradation of the batteries since the EV acts as a grid-independent generation device. In this paper, a current limiter, energy management strategy (EMS) for a V2L operation layer whose dynamic criteria are based on generic Li-Ion battery degradation mechanisms, is presented. This EMS represents an improvement over V2L and even V2X systems, since it allows establishing a priori the level of additional degradation of the energy storage system based on Li-Ion batteries. This limiter can be easily implemented and tuned for online and on-board operation allowing an independent cluster generation and it is easily tunable. Long-term simulations with accepted degradation models are presented to show the benefit of the proposed controller.

The remainder of this paper is structured as follows. In Section 2 the battery degradation model is presented. In Section 3 the EMS is developed and in Section 4

representative simulations and results are shown, to conclude in Section 5.

## 2. Degradation Model

Many battery degradation models are encountered in literature depending on the chemistry and modeled variables. Most of these models are semiempirical since actual battery life can be extended to tens of years. Three primary semiempirical models are known as the NREL Model [36], the Wang Model [37], and the MOBICUS Model [38]. These models exhibit the nonlinear electromechanical behavior of degradation in form of calendar and cycling aging whose drivers are Temperature, SoC, C-rate, DoD, and the total extracted energy (Ah throughput) with varying sensitivities to the capacity and power fade.

These models almost coincide to avoid both high and low temperatures, high charge and discharge rates, high DoD, DoD noncentered around an optimal SoC point (50%), and low SoC operation (some authors did not mention all these factors but coincide with the rest).

In particular, the NREL is the most complete battery degradation model found, since it describes that the calendar aging cannot be separated from cycling aging effects, allows for reduced calculation time, and is particularly interesting as it demonstrates an understanding for and incorporates nearly all degradation drivers for cost estimation [27].

In this paper, the model presented in [39] is adopted since it includes the characteristics of the NREL model being the most complete for Li-Ion chemistry and the validation includes realistic load profiles in EV. The discharge voltage is

$$v_d = E_0(T) - K(T) \frac{Q(T_a)}{Q(T_a) - i_t} (i + i_t) + Ae^{-Bi_t} - Ci_t \quad (1)$$

$$V_{batt}(T) = v_d - R(T) * i \quad (2)$$

The charge voltage is

$$v_c = E_0(T) - K(T) \frac{Q(T_a)}{i_t + 0.1Q(T_a)} i - K(T) \frac{Q(T_a)}{Q(T_a) - i_t} i_t + Ae^{-Bi_t} - Ci_t \quad (3)$$

$$V_{batt}(T) = v_c - R(T) * i \quad (4)$$

In Table 1 the nomenclature is presented while

$$E_0(T) = E_{0,ref} + \frac{\partial E}{\partial T} (T - T_{ref}) \quad (5)$$

$$K(T) = K_{T_{ref}} e^{\alpha(1/T - 1/T_{ref})} \quad (6)$$

$$Q(T_a) = Q(T_{a,ref}) + \frac{\partial Q}{\partial T} (T_a - T_{ref}) \quad (7)$$

TABLE 1: Nomenclature and nominal values (if applicable).

| Parameter/variable              | Description   | Nominal (LiFeMgPO4) | Units |
|---------------------------------|---|---------------------|-------|
| $E_0$                           | Constant voltage  | 12.6                | V     |
| $E$                             | Exponential zone dynamics                               | 13.1                | V     |
| $S$                             | Battery mode (0 for discharge, 1 for charge)            | -                   | 1     |
| $K$                             | Polarization constant                                   | 0.5                 | V/Ah  |
| $i$                             | Low frequency current dynamics                          | -                   | A     |
| $i_t$                           | Extracted capacity                                      | -                   | Ah    |
| $Q$                             | Maximum battery capacity                                | 40                  | Ah    |
| $T_{ref}$                       | Nominal battery temperature                             | 20                  | C     |
| $T$                             | Cell/internal temperature                               | -                   | C     |
| $T_a$                           | Ambient temperature                                     | -                   | K     |
| $\frac{\partial E}{\partial T}$ | Reversible voltage temperature coefficient              | -                   | V/K   |
| $\alpha$                        | Arrhenius rate constant for the polarization resistance | 0.5                 | 1     |
| $\beta$                         | Arrhenius rate constant for the internal resistance     | 0.5                 | 1     |
| $\frac{\partial Q}{\partial T}$ | Maximum capacity temperature coefficient                | -                   | Ah/K  |
| $C$                             | Nominal discharge curve slope                           | 0.016               | V/Ah  |
| $R_{th}$                        | Thermal resistance, cell to ambient                     | 0.6411              | C/W   |
| $t_c$                           | Thermal time constant, cell to ambient                  | 4880                | s     |
| DoD                             | Depth-of-Discharge of battery                           | -                   | 1     |
| $DoD_{ref}$                     | Maximum DoD recommended for SoC centering               | 50                  | 1     |
| SoC                             | State-of-Charge of battery                              | -                   | 1     |
| $SoC_{ref}$                     | Minimum SoC for V2L operation                           | 50                  | 1     |
| $H$                             | number of cycles  | -                   | 1     |
| $\psi$                          | Exponent factor for the DoD                             | 0.5                 | 1     |
| $\Psi$                          | Arrhenius rate constant for the cycle number            | 0.5                 | 1     |
| $I_d$                           | Average discharge current during a half cycle duration  | 20                  | A     |
| $I_c$                           | Average charge current during a half cycle duration     | 20                  | A     |
| $\gamma_1$                      | Exponent factor for the discharge current               | 0.12                | 1     |
| $\gamma_2$                      | Exponent factor for the charge current                  | 0.14                | 1     |
| $w_1$                           | Weight for allowed temperature                          | 10                  | 1     |
| $w_2$                           | Weight for allowed SoC                                  | 1                   | 1     |
| $w_3$                           | Weight for allowed DoD                                  | 1                   | 1     |
| C-rate                          | Charge and discharge current                            | -                   | Ah    |

$$R(T) = R_{T_{ref}} e^{\beta(1/T - 1/T_{ref})} \quad (8) \quad \text{for } k \text{ cycles,}$$

$$T(t) = \epsilon(n) = \epsilon(n-1) + \frac{0.5}{N(n-1)(2 - (DoD(n-2) + DoD(n))/DoD(n-1))}, \quad (12)$$

$$= \mathcal{L}^{-1} \left( \frac{((E_0(T) - V_b(T))i + (\partial E/\partial T) iT) R_{TH} + T_a}{1 + t_c s} \right) \quad \text{and} \quad (9)$$

$N(n)$

The aging effect due to cycling on the battery capacity is

$$Q(n) = Q_{BoL} - \epsilon(n) (Q_{BoL} - Q_{EoL}) \quad (10)$$

where

$$n = kT_h \quad (11)$$

$$= H \left( \frac{DoD(n)}{100} \right)^{-\psi} e^{-\Psi(1/T_{ref} - 1/T_a(n))} I_d^{-\gamma_1}(n) I_c^{-\gamma_2}(n). \quad (13)$$

### 3. Energy Management Strategy

The EMS of this paper is intended to limit the current flow during V2L operation based on avoiding

- (1) High and low temperatures

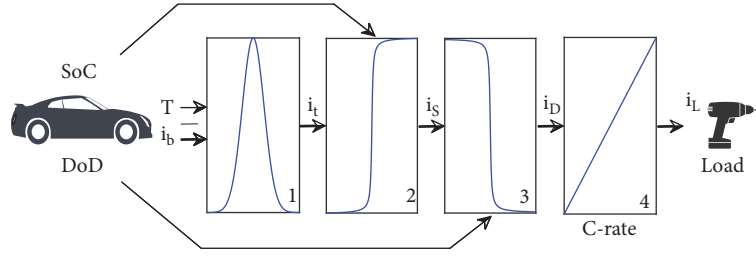


FIGURE 1: EMS block diagram.

- (2) Low SoC
- (3) High DoD
- (4) DoD noncentered around an optimal SoC point
- (5) High charge and discharge rates

These previous generic rules are inferred from previous works and they are semiempirical. In this work continuous semiempirical strategies are designed to comply with the rules as described separately in the following subsections. A continuous behavior is adopted in order to be implemented in either an analog or a digital platform. In Figure 1 a block diagram of the overall EMS of this paper is shown. The sequence of the first three rules of this cascade controller/limiter can be interchanged since they only have a multiplicative (reduction) effect and the last rule must be at the end to smooth high current demand rates that can degrade the battery. However, it is recommended to implement all of the rules in a real application since a single degradation mechanism is enough to deteriorate the battery prematurely.

**3.1. High and Low Temperature.** A Fuzzy-like membership function is proposed to limit the current throughput depending on the temperature; this means it is undesirable to operate in V2L when the temperature is either too low or too high ([22, 27, 28, 36–38]). A Gaussian function is selected to continuously limit the battery current  $i_b$  in function of the battery's temperature:

$$i_t = i_b e^{-(T-T_{ref})^2/w_1^2} \quad (14)$$

In Figure 1 this rule is depicted in block 1; the output current  $i_t$ , fed by the EV's battery ( $i_b$ ), is limited by the temperature  $T$ .

Function (14) can be easily tuned by selecting a weight  $w_1$  which is the width of the Gaussian function and  $T_{ref}$  is the nominal operation temperature. The weight  $w_1 = 10$  means approximately a 60% reduction for  $T_{ref} \pm w_1$  with  $T_{ref} = 30$ . In Figure 2 the temperature membership function with the mentioned values is depicted.

**3.2. Low SoC.** A Fuzzy-like membership function is proposed to limit the current throughput depending on the SoC. While the optimal SoC point is suggested to be 50%, it is recommended to avoid a low SoC operation ([22, 27, 28, 36–38]) and preferably maintain a high SoC level for further usage. A sigmoid function is selected to continuously limit

the current from the temperature limiter (14), as depicted in block 2 of Figure 1:

$$i_s = i_t \left( 0.5 + 0.35 \operatorname{atan} \left( \frac{\operatorname{SoC} - \operatorname{SoC}_{ref}}{w_2} \right) \right) \quad (15)$$

where  $\operatorname{SoC}_{ref} = 50\%$  is the inflection point (obtained from the manufacturer) and  $w_2 = 1$  is the slope of decay to get approximately 0% with  $\operatorname{SoC} = 45$ . This logic/function is illustrated in Figure 2 with the SoC membership function for the mentioned values. The sigmoid percentage, to a lesser extent, overcomes the [0 – 100] % but the energy demand is inherently limited in a real application; if necessary, the constants (0.5, 0.35) with  $w_2$  can be adjusted to avoid such kind of overcoming.

**3.3. High DoD.** A Fuzzy-like membership function is proposed to limit the current throughput depending on the DoD while the centering is obtained by the low SoC rule; it is recommended to avoid a high DoD operation ([22, 27, 28, 36–38]). A reverse sigmoid function is selected to continuously limit the current from the SoC limiter (15), as depicted in block 3 of Figure 1:

$$i_D = i_s \left( 0.45 - 0.35 \operatorname{atan} \left( \frac{\operatorname{DoD} - \operatorname{DoD}_{ref}}{w_3} \right) \right) \quad (16)$$

where  $\operatorname{DoD}_{ref}$  (inflection point) is the maximum recommended DoD for SoC centering that maximizes the number of operation cycles; this data can be obtained from the manufacturer.  $w_3 = 1$  is the slope of decay to get approximately 0% with  $\operatorname{DoD} = 55$ . This logic/function is illustrated in Figure 2 with the DoD membership function for the mentioned values. The sigmoid percentage, to a lesser extent, overcomes the [0 – 100] % but the energy demand is inherently limited in a real application; if necessary, the constants (0.45, 0.35) with  $w_3$  can be adjusted to avoid such kind of overcoming.

**3.4. High Discharge Rate.** A Fuzzy-like membership function is proposed to limit the current rate while on V2L operation. The above is to avoid abrupt changes in the current that degrade the battery ([22, 27, 28, 36–38]). This rule limits the rising first derivative of the current:

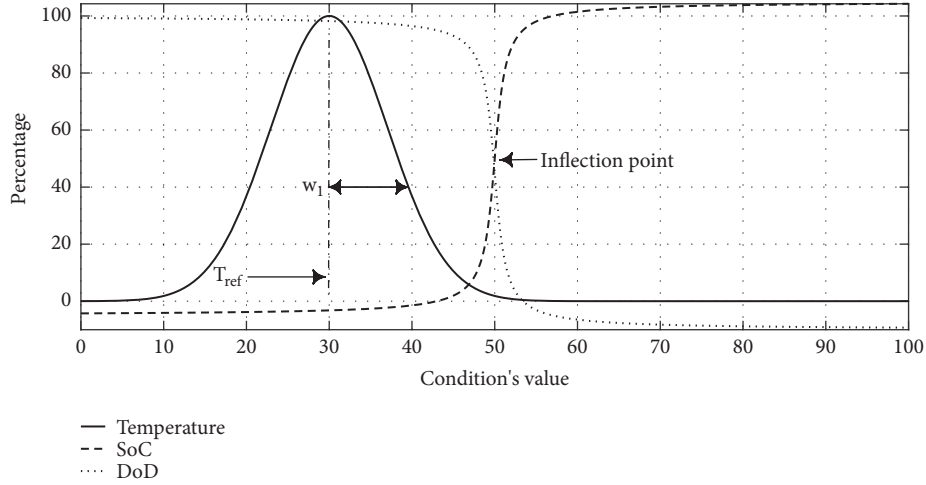


FIGURE 2: Membership functions for the current limiter.

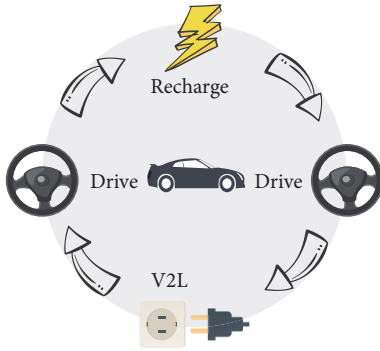


FIGURE 3: Testing routine for V2L battery degradation.

$$i_L(t) = \begin{cases} R[t - \tau] + i_L(t - \tau) & \text{if } C\text{-rate} < \text{discharge rate} < 0 \\ i_L(t - \tau), & \text{elsewise} \end{cases} \quad (17)$$

where the C-rate can be obtained from the manufacturer or tuned to a lesser value and  $\tau$  is the sample rate. This rule is depicted in Figure 2 as block 4.

## 4. Simulations and Results

**4.1. Setup.** In order to show the benefit of the proposed controller, numerical results obtained in Matlab are presented. For the simulations, the workday routine for V2L operation illustrated in Figure 3 is used; such routine consists of driving to a workplace/facility, using V2L, and driving to home using 2 hours for each stage, recharging overnight (slow charge to 1Q), and repeating for 500 days. Standard drive cycle and vehicle are used, namely, the WLTC drive cycle for a Class-3 vehicle ([40]), since they include low, medium, high, and extrahigh speed. The power demand is scaled proportionally to a single cell with the parameters described in Table 1 and it is proposed that the demanded current for the load be  $1/2Q$  on average with peaks of 70% of the maximum

driving cycle peak current. In Figure 4 the current demand for a single day without the recharge period is shown. The environment temperature is emulated from statistical data obtained from a local Davis VANTAGE PRO2 weather station (years 2014-2016 in Celaya, Guanajuato, México) and shown in Figure 5; this dataset is available in a link at the end of this paper.

**4.2. Numerical Results.** In Figure 6 a comparison of the battery capacity in Ah for diverse scenarios is shown. The compared scenarios are V2L without limiter control, V2L with limiter control, and no V2L operation up to 500 workdays. Although the temperature has a direct effect on capacity (oscillatory behavior), an early degradation (the End of Life is premature) can be clearly observed when V2L is used; but also, the behavior with the proposed limiter almost equals the behavior without the use of V2L. In Figure 7 the smoothed version of Figure 6 is shown, in which a premature degradation is clearly observed in approximately 25 workdays in the case of V2L without current limiter with respect to the 290 workdays of life of the proposal in this paper. In Figure 8 is shown the original power profile (assumed) against the limited with the proposal of this paper. Clearly, avoiding premature degradation of the battery has a cost that depends on the amount of energy used in V2L operation and is a highly nonlinear function. In this sense, one can design the current limiting control system to obtain a degradation that is not so premature but allows a V2L operation adequate up to a certain load; such tuning can be obtained by modifying the weights  $w_1 - w_3$  and the inflection points by simulations.

**4.3. About Implementation.** The implementation of the current limiter presented in this paper does not require expensive components. A DSP can be enough to perform the rules and communicate with electronic devices (integrated circuits) designed to estimate the SoC (Texas Instruments, Linear Technologies, and Maxim among other suppliers provide such devices). The current throughput can be regulated by a DC-DC current converter that can later provide AC levels if

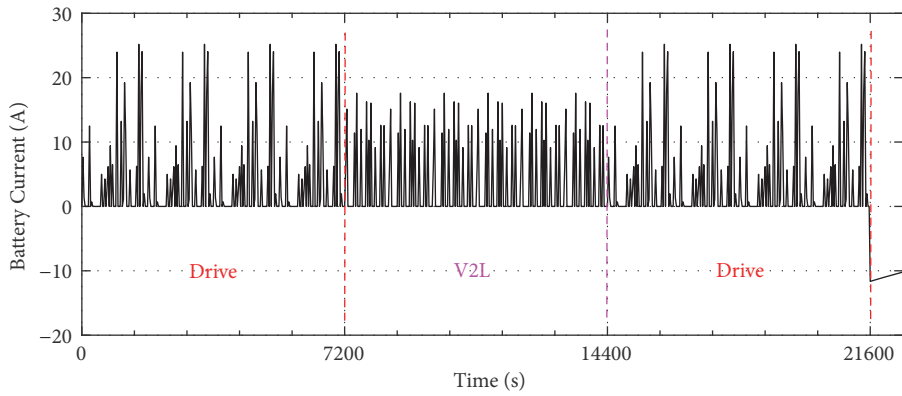


FIGURE 4: Current demand for single testing routine.

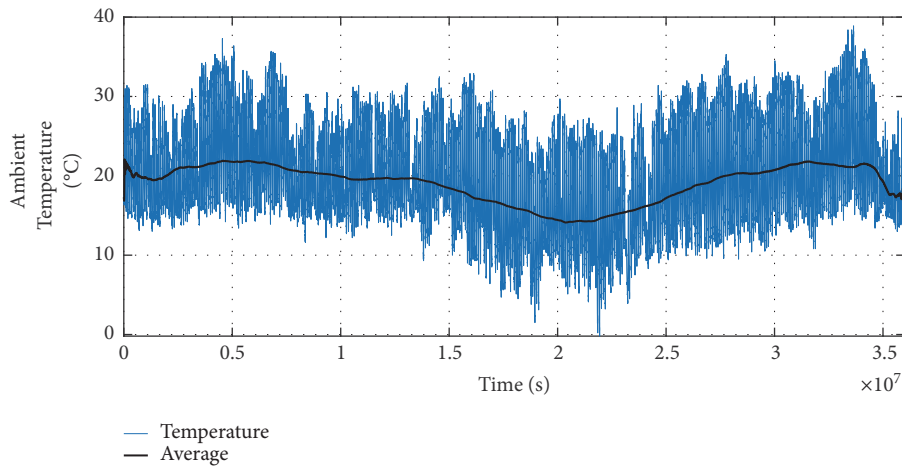


FIGURE 5: 2014-2016 ambient temperature and its average for Guanajuato, México.

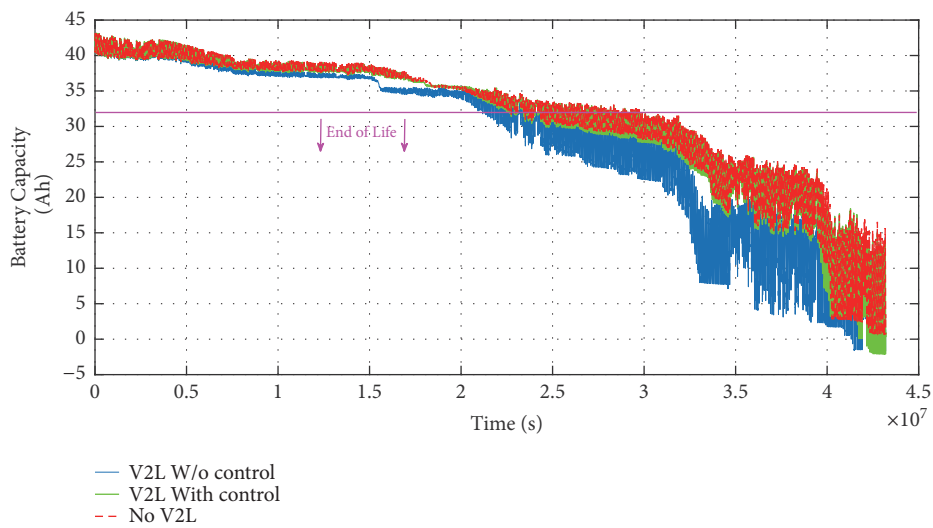


FIGURE 6: Battery capacity comparison for V2L, V2L with limiter, and no V2L.

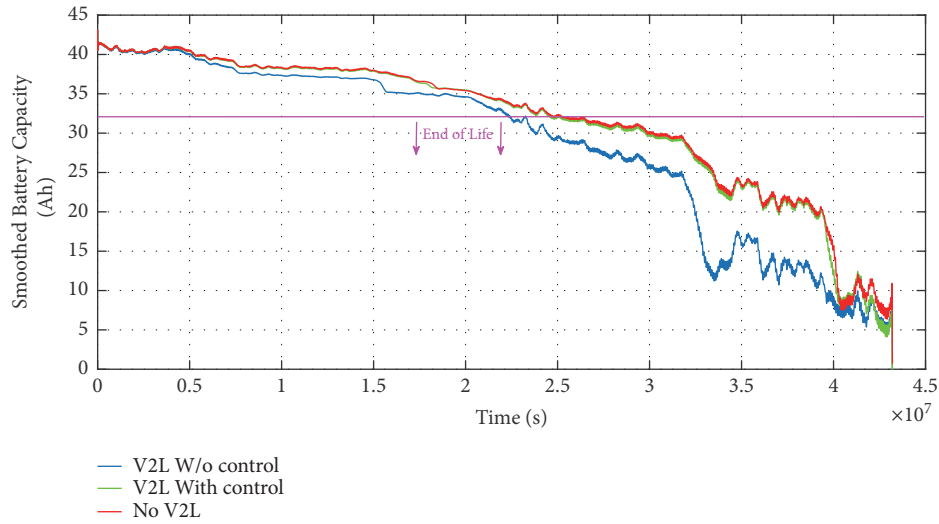


FIGURE 7: Filtered battery capacity comparison for V2L, V2L with limiter, and no V2L.

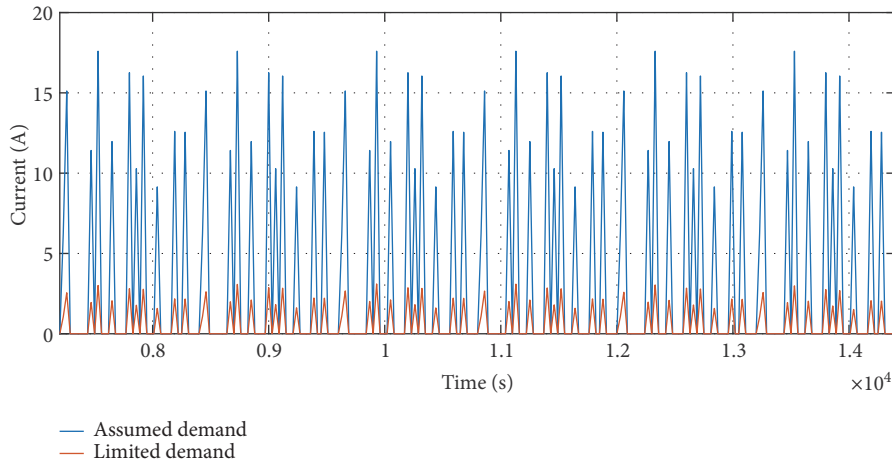


FIGURE 8: Load current profile, assumed vs limited.

necessary, such that the presented scheme does not invade the battery.

### 5. Conclusions

In this paper a new current limiter control for V2L applications is proposed. This limiter control is based on rules extracted from the main degradation mechanisms for Li-Ion batteries. Avoiding premature degradation of the battery in V2L operation depends on the amount of energy used and on the degradation variables as highly nonlinear functions. The main advantage of this controller is that it can be tuned to obtain a degradation that is not so premature but allows a V2L operation.

### Data Availability

The data used to support the findings of this study are available from the corresponding author upon request. A

dataset of weather is available at <https://www.dropbox.com/s/csegzrrthwsnhva/GtoTempLog14-16.rar?dl=0>.

### Additional Points

*Featured Application.* The proposed energy management strategy can be used in Vehicle-to-Load or similar applications with Li-Ion batteries when avoiding battery degradation is imperative.

### Disclosure

Martín-Antonio Rodríguez-Licea, Francisco-J. Perez-Pinal, Allan-Giovanni Soriano-Sánchez, and José-Antonio Vázquez-López current address is Antonio García Cubas, no. 600, Colonia Fovissste, Celaya, Guanajuato, 38010.

### Conflicts of Interest

The authors declare no conflicts of interest for this paper.

## Authors' Contributions

Conceptualization, methodology, software, validation, and formal analysis were performed by Martín-Antonio Rodríguez-Licea. Resources, writing, review, and editing were made by Martín-Antonio Rodríguez-Licea, Allan-Giovanni Soriano-Sánchez, Francisco-J. Perez-Pinal, and José-Antonio Vázquez-López.

## Acknowledgments

The authors would like to express their gratitude to the Tecnológico Nacional de México en Celaya and to the CONACYT for its financial support for the Cátedras ID 4155 and 6782.

## References

- [1] M. Austin and R. Lefevre, "In the new energy revolution, electrical vehicles become reality," *IEEE Transportation Electrification eNewsletter*, vol. 9, 2013.
- [2] A. G. Boulanger, A. C. Chu, S. Maxx, and D. L. Waltz, "Vehicle electrification: Status and issues," *Proceedings of the IEEE*, vol. 99, no. 6, pp. 1116–1138, 2011.
- [3] P. Machura and Q. Li, "A critical review on wireless charging for electric vehicles," *Renewable & Sustainable Energy Reviews*, vol. 104, pp. 209–234, 2019.
- [4] M. A. Rahman and M. R. Islam, "Different control schemes of entire microgrid: A brief overview," in *Proceedings of the 3rd International Conference on Electrical Engineering and Information Communication Technology (ICEEICT)*, pp. 1–6, IEEE, 2016.
- [5] Y. K. Penya, C. E. Borges, J. Haase, and D. Bruckner, "Smart buildings and the smart grid," in *Proceedings of the IECON 2013-39th Annual Conference of the IEEE Industrial Electronics Society*, pp. 113–117, IEEE, 2013.
- [6] M. Mao, Y. Yue, and L. Chang, "Multi-time scale forecast for schedulable capacity of Electric Vehicle fleets using big data analysis," in *Proceedings of the 7th IEEE International Symposium on Power Electronics for Distributed Generation Systems, PEDG 2016*, pp. 1–7, IEEE, 2016.
- [7] M. Andrychowicz and B. Olek, "Energy storing vs. generation curtailment - The measures for controlling renewable generation," in *Proceedings of the 14th International Conference on the European Energy Market, EEM 2017*, pp. 1–5, IEEE, 2017.
- [8] E. Irmak, M. S. Ayaz, S. G. Gok, and A. B. Sahin, "A survey on public awareness towards renewable energy in Turkey," in *Proceedings of the International Conference on Renewable Energy Research and Application (ICRERA)*, pp. 932–937, IEEE, 2014.
- [9] H. Aki, A. Murata, and S. Han, "A survey and analyses on private vehicle use for the development of V2G/V2H management," in *Proceedings of the 12th IEEE Vehicle Power and Propulsion Conference, VPPC 2015*, IEEE, Canada, 2015.
- [10] J. E. Siegel, D. C. Erb, and S. E. Sarma, "A survey of the connected vehicle landscape—architectures, enabling technologies, applications, and development areas," *IEEE Transactions on Intelligent Transportation Systems*, vol. 19, pp. 2391–2406, 2018.
- [11] C. Liu, K. T. Chau, D. Wu, and S. Gao, "Opportunities and challenges of vehicle-to-home, vehicle-to-vehicle, and vehicle-to-grid technologies," *Proceedings of the IEEE*, vol. 101, no. 11, pp. 2409–2427, 2013.
- [12] X. Mou, R. Zhao, and D. T. Gladwin, "Vehicle to vehicle charging (V2V) bases on wireless power transfer technology," in *Proceedings of the IECON 2018 - 44th Annual Conference of the IEEE Industrial Electronics Society*, pp. 4862–4867, IEEE, 2018.
- [13] X. Wang, Y. Liu, W. Qian et al., "A 25kW SiC universal power converter building block for G2V, V2G, and V2L applications," in *IEEE International Power Electronics and Application Conference and Exposition (PEAC)*, pp. 1–6, IEEE, 2018.
- [14] A. Noorul Ameen and S. Suresh, "Design of bi-directional power converter for vehicle-to-grid capability of reactive power compensation," in *Proceedings of the 2nd International Conference on Trends in Electronics and Informatics (ICOEI)*, pp. 1336–1340, IEEE, 2018.
- [15] K. Mahmud, S. Morsalin, Y. R. Kafle, and G. E. Town, "Improved peak shaving in grid-connected domestic power systems combining photovoltaic generation, battery storage, and V2G-capable electric vehicle," in *Proceedings of the IEEE International Conference on Power System Technology (POWERCON)*, pp. 1–4, IEEE, 2016.
- [16] W. Choi, W. Lee, and B. Sarlioglu, "Reactive power compensation of grid-connected inverter in vehicle-to-grid application to mitigate balanced grid voltage sag," in *Proceedings of the 2016 IEEE Power and Energy Society General Meeting, PESGM 2016*, pp. 1–5, IEEE, 2016.
- [17] A. P. Kumar, M. Naresh, and P. Prabhakar, "Smart grid hybrid electric vehicles for road map development based on distributed dynamic pricing policy," *International Journal of Innovative Technology*, vol. 3, pp. 0191–0197, 2015.
- [18] D. P. Tuttle and R. Baldick, "The evolution of plug-in electric vehicle-grid interactions," *IEEE Transactions on Smart Grid*, vol. 3, no. 1, pp. 500–505, 2012.
- [19] Z. Tian, L. Tu, C. Tian, Y. Wang, and F. Zhang, "Understanding battery degradation phenomenon in real-life electric vehicle use based on big data," in *Proceedings of the 3rd International Conference on Big Data Computing and Communications (BIG-COM)*, pp. 334–339, IEEE, 2017.
- [20] D. Ansean, V. M. Garcia, M. Gonzalez et al., "Lithium-ion battery degradation indicators via incremental capacity analysis," *IEEE Transactions on Industry Applications*, 2019.
- [21] D. Wang, J. Coignard, T. Zeng, C. Zhang, and S. Saxena, "Quantifying electric vehicle battery degradation from driving vs. vehicle-to-grid services," *Journal of Power Sources*, vol. 332, pp. 193–203, 2016.
- [22] J. D. K. Bishop, C. J. Axon, D. Bonilla, M. Tran, D. Banister, and M. D. McCulloch, "Evaluating the impact of V2G services on the degradation of batteries in PHEV and EV," *Applied Energy*, vol. 111, pp. 206–218, 2013.
- [23] B. Lunz, Z. Yan, J. B. Gerschler, and D. U. Sauer, "Influence of plug-in hybrid electric vehicle charging strategies on charging and battery degradation costs," *Energy Policy*, vol. 46, pp. 511–519, 2012.
- [24] L. Cai, J. Meng, D. Stroe, G. Luo, and R. Teodorescu, "An evolutionary framework for lithium-ion battery state of health estimation," *Journal of Power Sources*, vol. 412, pp. 615–622, 2019.
- [25] S. K. Rechkemmer, X. Zang, W. Zhang, and O. Sawodny, "Empirical Li-ion aging model derived from single particle model," *Journal of Energy Storage*, vol. 21, pp. 773–786, 2019.
- [26] L. Noel, *Vehicle-to-Grid: A Sociotechnical Transition Beyond Electric Mobility*, Springer, 2019.
- [27] A. W. Thompson, "Economic implications of lithium ion battery degradation for Vehicle-to-Grid (V2X) services," *Journal of Power Sources*, vol. 396, pp. 691–709, 2018.

- [28] S. Shinzaki, H. Sadano, Y. Maruyama, and W. Kempton, "Deployment of vehicle-to-grid technology and related issues [Technical report]," SAE Technical Paper, 2015.
- [29] M. Von Hoffen, "Towards an information system for evidence-based analysis of charging behavior, charging demand, and battery degradation of electric vehicles," in *Proceedings of the 18th IEEE Conference on Business Informatics, CBI 2016*, vol. 1, pp. 182–190, IEEE, 2016.
- [30] K. Uddin, T. Jackson, W. D. Widanage, G. Chouchelamane, P. A. Jennings, and J. Marco, "On the possibility of extending the lifetime of lithium-ion batteries through optimal V2G facilitated by an integrated vehicle and smart-grid system," *Energy*, vol. 133, pp. 710–722, 2017.
- [31] G. Andersson, O. Alexandre, and A. D. A. Ulbig, *Degradation-limiting optimization of battery energy storage systems operation [Ph.D. thesis] [M. Sc. thesis]*, ETH Zurich, 2013.
- [32] K. Ishii and Y. Masuda, "Vehicle power supply device and malfunction diagnosis method thereof," US Patent App. 15/260,022, 2017.
- [33] F. Léonard, D. Champagne, J. Bherer, and D. Pineau, "Protected system for controlling power transactions for an electric vehicle," US Patent App. 14/374,262, 2014.
- [34] Y. Li, X. Zhang, and F. Tang, "Power system switching between charge-discharge function and driving function and electric vehicle comprising the same," US Patent 9,272,629, 2016.
- [35] G. Yang, X. Zhang, Z. Du, X. Zhou, and H. Luo, "Electric vehicle and power system and motor controller for electric vehicle," US Patent 9,260,022, 2016.
- [36] K. Smith, M. Earleywine, E. Wood, and A. Pesaran, "Battery wear from disparate duty-cycles: opportunities for electric-drive vehicle battery health management," Technical report, National Renewable Energy Lab. (NREL), Golden, CO, USA, 2012.
- [37] J. Wang, J. Purewal, P. Liu et al., "Degradation of lithium ion batteries employing graphite negatives and nickel-cobalt-manganese oxide + spinel manganese oxide positives: Part I, aging mechanisms and life estimation," *Journal of Power Sources*, vol. 269, pp. 937–948, 2014.
- [38] P. Gyan, "Calendar ageing modeling of Lithium-Ion batteries," in *Mat4Bat Summer Sch*, pp. 1–49, USAEE, La Rochelle, France, 2015.
- [39] N. Omar, M. A. Monem, Y. Firouz et al., "Lithium iron phosphate based battery - Assessment of the aging parameters and development of cycle life model," *Applied Energy*, vol. 113, pp. 1575–1585, 2014.
- [40] A. Daniel, "Driving Cycle (Simulink Block) @ONLINE," <https://la.mathworks.com/matlabcentral/fileexchange/46777-driving-cycle-simulink-block>, 2018.

## Research Article

# Model Predictive Control of Electric Spring for Voltage Regulation and Harmonics Suppression

Yun Zou <sup>1</sup>, Yinlong Hu <sup>2</sup> and Sifan Cao<sup>3</sup>

<sup>1</sup>*School of Automation, Nanjing University of Science and Technology, Nanjing 210094, China*

<sup>2</sup>*College of Energy and Electrical Engineering, Hohai University, Nanjing 210098, China*

<sup>3</sup>*School of Automation Engineering, University of Electronic Science and Technology of China, Chengdu 611731, China*

Correspondence should be addressed to Yun Zou; z\_ouyun@163.com

Received 21 February 2019; Accepted 14 March 2019; Published 7 April 2019

Guest Editor: Qing Hui

Copyright © 2019 Yun Zou et al. This is an open access article distributed under the Creative Commons Attribution License, which permits unrestricted use, distribution, and reproduction in any medium, provided the original work is properly cited.

This paper presents a model predictive control (MPC) strategy for electric spring (ES) to address the power quality problems, especially voltage regulation and harmonic suppression, which are more acute for a growing proportion of renewable energy generation to the grid. A Kalman filter is used to estimate the random variation of the supply voltage and extract the fundamental and harmonic components of the supply voltage, respectively. In this way, the supply voltage, which is treated as an external disturbance for the plant, can be established in the state-space model form. Such processing brings great convenience to the application of MPC and also lays a foundation for MPC to achieve an ideal control effect. Based on an integrated state-space model of the supply voltage and the ES, an MPC controller is designed for power quality improvement. Simulation studies are carried out and the simulation results are presented to verify the effectiveness and accuracy of the control strategy.

## 1. Introduction

Due to environmental pollution and excessive consumption of fossil energy, more and more attention has been paid to the research, development and utilization of renewable energy sources (RESs) [1]. The increasing proportion of renewable energy generation to the grid means that the inertia of the power system declines, which makes the demand side [2, 3] of the power system sensitive to voltage and frequency fluctuations. Nowadays, solar [4, 5] and wind power [6] are the two most common sources of renewable energy for grid-connected generation. However, their own limitations, mainly randomness and unpredictability [7], cause a variation of active and reactive power at the power generation side, which is expected to cause power system [8, 9] instability. In addition, it should also be considered that the harmonic distortion of line voltage is further aggravated by the additional power electronics used for renewable energy generation. As a consequence, the problems of power quality will be more and more serious with the increase of the proportion of renewable energy power generation, especially

voltage fluctuation and harmonic distortion. These power quality problems will be a great concern for users.

Electric spring (ES) was first introduced in 2012 as a new smart grid technology to balance the power between the power supply and demand automatically [10]. Therefore, power mismatch between the generation side and the demand side can be effectively alleviated. So far, a significant amount of research work has been conducted and rich research results have been achieved, which mainly consist of basic analyses, topological structures, and control strategies of ESs. The most basic function of ESs to keep active and reactive power balance for mitigating voltage and frequency fluctuation is described in [11]. Dynamic modeling for ESs to implement large-scale simulation research and a general analysis on the steady-state behavior of ESs are introduced in [12] and [13, 14], respectively. The actual circuit and algorithm implementation of an ES to regulate the AC mains voltage by reactive power compensation is described in [15]. To reduce the use of energy storage equipment in the future smart grid with substantial renewable energy sources can be realized by ESs [16]. Voltage regulation in a microgrid by multiple

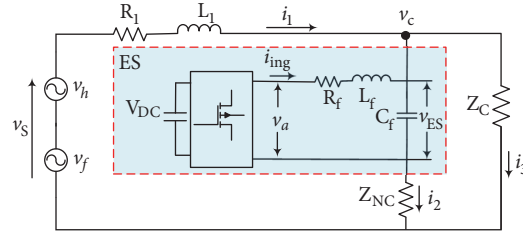


FIGURE 1: Overall simplified schematic diagram of the power system with an ES.

electric springs based on the distributed control is presented in [17], which can reduce the cost of centralized control [18] and compensate the inaccuracy of the traditional droop control effectively. In addition, there are also some research results about the use of ESs to improve power quality [19]. Harmonics suppression for the AC mains voltage by ESs with current-source inverters is introduced in [20]. However, in view of the above results, the research results about control strategies and control methods for ESs are relatively few, which mainly consists of the PI controller and the PR controller. The novel control strategy named  $\delta$  control for ESs to provide different types of power/voltage compensations is presented in [21], which is significantly different from phase-locked control. A fuzzy logic controller designed for ESs to adjust the AC mains voltage is described in [22], which does not take into account the harmonics.

In this paper, model predictive control (MPC) [23–25] is combined with a Kalman filter [26] to be applied to ESs for harmonics suppression and voltage regulation for the first time, where the Kalman filter is used to estimate the random variation of the voltage source and to extract the fundamental and harmonic components, respectively. MPC is an online optimization control method based on a process prediction model, which comprehensively considers system constraints, dynamic responses, and control objectives. It should be noted that the online optimization problem of MPC is usually to solve a quadratic programming problem. The state-space model of ES presented in Section 3 is linear and time-invariant, which is greatly consistent with the requirement of online optimization of MPC. Furthermore, the most prominent advantage of model predictive control is the handling of hard constraints. For ES, the output voltage is realized by a Pulse Width Modulation (PWM) technology and its control signal is limited to  $\pm 1$ . Thus, the active filter is guaranteed to operate in the linear modulation range.

The rest of this paper is organized as follows. In Section 2, the operating principle of ES for the smart grid with high penetration of renewable energy is described. The state-space model of ES is presented in Section 3. Section 4 describes the controller design based on MPC in detail. Numerical simulations are presented in Section 5 to verify the effectiveness of the control strategy. Section 6 draws the conclusions.

## 2. Basic Principles of Electric Spring

A simplified schematic diagram of a power system with an ES is shown in Figure 1. As distributed generation (e.g., such

as wind and solar power generation) requires a large number of power electronic devices, the introduction of power harmonics is inevitable. With more and more distributed power supplies introduced to the power distribution network, the problem of harmonics will be more serious. Therefore, the supply voltage  $v_s$  can be represented by the sum of  $v_f$  (fundamental component) and  $v_h$  (harmonics component) in Figure 1.  $R_1$  and  $L_1$  are the equivalent resistance and inductance of the transmission line, respectively. The voltage at the point of common coupling (PCC) is represented by  $v_c$ , which is also the voltage across the critical load  $Z_c$ . It should be pointed out that  $Z_c$  represents a class of impedance that is sensitive to voltage fluctuation, while noncritical load  $Z_{nc}$  represents a class of impedance that can withstand a wide range of voltage fluctuations. Due to the characteristic of the noncritical load mentioned above, it withstands most of the power fluctuations of the grid.  $i_2$  and  $i_3$  are the currents flowing through the noncritical load  $Z_{nc}$  and critical load  $Z_c$ , respectively.  $i_1$  is the line current. The ES in the red dotted box shown in Figure 1 includes a DC link capacitor, a PWM inverter [27, 28], and an LC filter. The voltage across the capacitor  $C_f$  is the output voltage of the ES, namely,  $V_{ES}$ .  $R_f$  is the equivalent resistance of the inverter transmission line.  $v_a$  is the output equivalent voltage of the PWM inverter. In the case of a half-bridge,

$$v_a = \frac{V_{DC}}{2} * u, \quad (1)$$

where  $V_{DC}$  is the DC link voltage,  $u$  is the modulation index [12] and also the output signal of the controller.

The ES was first proposed as a special reactive power compensator to regulate the line voltage  $v_c$  at its rated value with a standard sine wave at 50Hz in spite of  $v_s$  fluctuations. It injects a voltage, namely,  $v_{ES}$ , leading (or lags) the current flowing through the noncritical load for voltage suppression (or voltage boosting). In simple terms, ES mainly has two compensation modes, namely, inductive mode and capacitive mode to adjust the line voltage. When the voltage  $v_c$  exceeds its reference  $v_{c-ref}$ ,  $v_{ES}$  leads  $i_0$  by 90 degrees in the inductive mode for voltage suppression as shown in Figure 2, where  $v_0$  and  $i_0$  are the voltage and current of the noncritical load, respectively. When the voltage  $v_c$  under its reference  $v_{c-ref}$ , ES operates in the capacitive mode to boost the line voltage. It is noteworthy that the phase angle of  $v_c$  has a significant change before and after ES becomes effective as shown in Figure 2, which corresponds to  $v_s$  [21]. The internal phase relation between  $v_s$  and  $v_c$  is of great importance to the control design

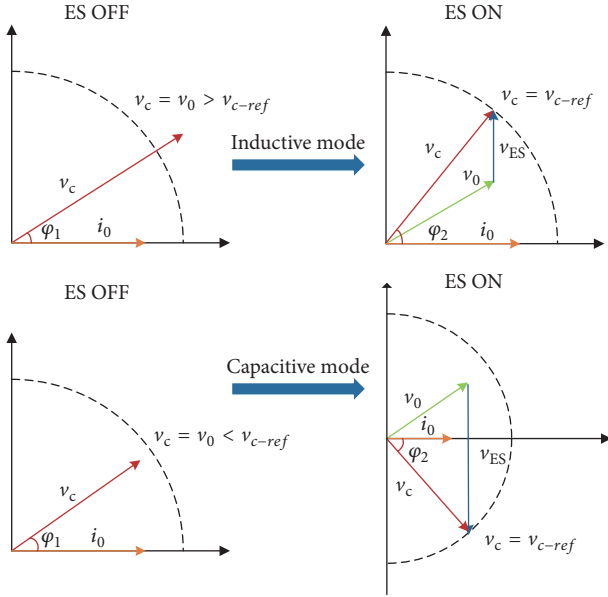


FIGURE 2: Operating modes of ES to adjust line voltage for a resistive-inductive load as a noncritical load (inductive mode for voltage suppression and capacitive mode for voltage boosting).

in Section 4, which determines the compensation mode of the ES. Once the DC link capacitor on the DC side of the inverter is replaced by an energy storage system, ES will not be limited to the above two modes of compensation [13].

### 3. Modelling of Electric Spring

The simplified power circuit of the ES with a supply voltage and transmission lines is shown in Figure 1. Applying Kirchhoff's Voltage and Current Laws, one obtains

$$L_1 \frac{di_1}{dt} = v_s - v_c - R_1 * i_1, \quad (2)$$

$$L_f \frac{di_{ing}}{dt} = v_a - v_{ES} - R_f * i_{ing}, \quad (3)$$

$$C_f \frac{dv_{ES}}{dt} = i_{ing} + i_2, \quad (4)$$

$$i_1 = i_2 + i_3, \quad (5)$$

$$i_2 = \frac{v_c - v_{ES}}{z_{NC}}, \quad (6)$$

$$i_3 = \frac{v_c}{z_C}. \quad (7)$$

Solving (1)–(7), a state-space model for the ES can be derived as

$$\dot{x} = A_e x + B_1 v_s + B_2 u, \quad (8)$$

$$y = C_e x + D_1 v_s + D_2 u, \quad (9)$$

where

$$A_e = \begin{bmatrix} -\frac{z_{NC}z_C + R_1(z_{NC} + z_C)}{L_1(z_{NC} + z_C)} & 0 & -\frac{z_C}{L_1(z_{NC} + z_C)} \\ 0 & -\frac{R_f}{L_f} & -\frac{1}{L_f} \\ \frac{z_{NC}}{C_f(z_{NC} + z_C)} & \frac{1}{C_f} & -\frac{1}{C_f(z_{NC} + z_C)} \end{bmatrix},$$

$$B_1 = \begin{bmatrix} \frac{1}{L_1} \\ 0 \\ 0 \end{bmatrix}, \quad (10)$$

$$B_2 = \begin{bmatrix} 0 \\ \frac{V_{DC}}{2L_f} \\ 0 \end{bmatrix},$$

$$C_e = \begin{bmatrix} \frac{z_{NC}z_C}{z_{NC} + z_C} & 0 & \frac{z_C}{z_{NC} + z_C} \end{bmatrix},$$

$$D_1 = 0,$$

$$D_2 = 0.$$

Denote the state vector as  $x = [i_1 \ i_{ing} \ v_{ES}]^T$ . Ideally, our control aim is to keep the line voltage  $v_c$  at its reference level all the time. Therefore,  $v_c$ , the core of our concern, should be considered as an output of the plant in the above state-space model. In addition, supply voltage  $v_s$  is treated as an external disturbance.  $u$  is the modulation index and also the control signal generated by the MPC controller, which is limited to  $\pm 1$ . It is worth mentioning that the state-space model of ES is a multiple-input-single-output system with only one control input, which means that the complexity of control is greatly reduced. Note that the dynamic of  $V_{DC}$  is not considered for simplicity.

### 4. Control Design for Electric Spring

ES generates the compensation voltage  $v_{ES}$  through the PWM inverter technology based on the control signal  $u$  generated by the MPC controller to correct the harmonic distortion and adjust  $v_c$  to an ideal sine wave with an amplitude of 220 volts and a frequency of 50Hz under the condition that the supply voltage  $v_s$  fluctuates with time. In other words, our aim here is to regulate the line voltage  $v_c$  while suppressing the harmonics of  $v_c$ .

**4.1. Disturbance Modeling.** For the established state-space model of ES, the supply voltage  $v_s$  can be treated as a disturbance signal, which is fortunately a periodic and measurable signal. Thus, an exogenous model for  $v_s$  is employed to access the useful information immediately rather than after one

full period. The exogenous model is designed based on the following observation:

$$\frac{d}{dt} \begin{bmatrix} \cos(\omega_i t) \\ \sin(\omega_i t) \end{bmatrix} = \begin{bmatrix} 0 & -\omega_i \\ \omega_i & 0 \end{bmatrix} \begin{bmatrix} \cos(\omega_i t) \\ \sin(\omega_i t) \end{bmatrix}. \quad (11)$$

In this way, the periodic signal  $v_s$ , which consists of a finite number of harmonics, can be represented as

$$\dot{\xi} = A_\xi \xi, \quad (12)$$

$$v_s = C_\xi \xi, \quad (13)$$

where

$$\xi = [\cos(\omega_1 t), \sin(\omega_1 t), \cos(\omega_3 t), \sin(\omega_3 t), \dots]^T, \quad (14)$$

and  $A_\xi$  is a block-diagonal matrix with the blocks given by

$$\begin{bmatrix} 0 & -\omega_i \\ \omega_i & 0 \end{bmatrix}, \quad (15)$$

$$C_\xi = [1, 0, 1, 0, \dots].$$

In this way, the measured voltage  $v_s$  can be expressed in the form of state-space, which can be combined with the state-space model of ES to form a complete state-space model used for the MPC controller as follows:

$$\dot{\hat{x}} = A\hat{x} + Bu, \quad (16)$$

$$y = C\hat{x}, \quad (17)$$

where

$$A = \begin{bmatrix} A_e & B_1 C_\xi \\ 0 & A_\xi \end{bmatrix},$$

$$B = \begin{bmatrix} B_2 \\ 0 \end{bmatrix}, \quad (18)$$

$$C = [C_e \ 0].$$

Denote the state vector as  $\hat{x} = [x \ \xi]^T$ . Note that 0 in matrix A, matrix B, and matrix C is a vector, not a scalar, whose dimension depends on state  $\xi$ . That is to say, it has to do with the number of harmonics that we predefined. A Kalman filter [29] is used to estimate the state  $\xi$  from the measured voltage signal  $v_s$  by voltage sensors; thus the disturbance to the plant as mentioned in the previous section becomes  $\xi$  instead of  $v_s$ .

**4.2. MPC Controller.** The MPC controller designed for ES is based on the state-space model, while it cannot be applied to ES model (16)–(17) directly for the reason that MPC controller should apply to a discrete-time model. Therefore, model (16)–(17) should be discretized as follows:

$$\hat{x}(k+1) = A_d \hat{x} + B_d u, \quad (19)$$

$$y(k) = C_d \hat{x}(k), \quad (20)$$

where  $A_d, B_d, C_d$  are the discrete forms of  $A, B, C$  in (16)–(17), respectively [29]. The method to construct the optimization problem in MPC is to expand the expression in the model to predict the state  $\hat{x}$  and output  $v_c$  and then formulate a quadratic programming problem according to the control objective as follows:

$$J = \sum_{i=0}^{N_p-1} e(i)^T Q e(i) + \sum_{i=0}^{N_u-1} u(i)^T R u(i), \quad (21)$$

$$e(k) = y(k) - v_{c-ref}(k), \quad (22)$$

where  $Q, R$  are the positive definite gain matrices and  $N_u, N_p$  are the control horizon and the prediction horizon, respectively. In MPC, one should find  $u$  to minimize  $J$  and the first value of the control sequence  $u$  will be applied to the actuator; then the previous steps will be repeated at the next sampling time. It is noteworthy that the prominent feature of the MPC control strategy used in this paper is that the future characteristics of disturbance are fully taken into account in the online optimization based on the disturbance  $v_s$  modeling and the Kalman filter, which is an effective method for state estimation and prediction [26]. In fact, similar methods of Kalman filtering have been used to estimate harmonics in previous studies on power quality problems [30]. Specifically, the system model of the Kalman filter for the state estimation of  $v_s$  is defined as follows:

$$\xi_{i|i-1} = A_{\xi_d} \xi_{i-1|i-1}, \quad (23)$$

$$P_{i|i-1} = A_{\xi_d} P_{i-1|i-1} A_{\xi_d}^T + Q, \quad (24)$$

$$K_{gi} = P_{i|i-1} C_\xi^T (C_\xi P_{i|i-1} C_\xi^T + R)^{-1}, \quad (25)$$

$$\xi_{i|i} = \xi_{i|i-1} + K_{gi} (v_{s-m} - C_\xi \xi_{i|i-1}), \quad (26)$$

$$P_{i|i} = (I - K_{gi} C_\xi) P_{i|i-1}, \quad (27)$$

where  $A_{\xi_d}$  is the discrete form of  $A_\xi$  in (12), which is a block-diagonal matrix with each block taking  $\begin{bmatrix} \cos(n\omega T_s) & -\sin(n\omega T_s) \\ \sin(n\omega T_s) & \cos(n\omega T_s) \end{bmatrix}$ ,  $T_s$  is the sampling time, and  $\omega$  is the angular frequency of the grid.  $Q$  and  $R$  are the covariance matrices of the system noise and the measurement noise, respectively.  $P$  and  $K_g$  are the covariance matrix of the estimation error and the Kalman gain, respectively.  $\xi_{i|i}$  is the estimation of  $\xi_i$ , while  $\xi_{i|i-1}$  is the estimation at time instant  $i-1$ .  $v_{s-m}$  is the measurement of voltage  $v_s$ , which includes measurement noise. In this paper, the voltage  $v_s$  is treated as a measurable disturbance, so the Kalman filter can accurately estimate its state. It should be pointed out that the measurement noise  $R$  in the simulation is far less than the system noise  $Q$  because the random variation of  $v_s$  has a large deviation from the trajectory of the disturbance model. The overall control of the system based on the MPC controller with a Kalman filter [29] is shown in Figure 3. The supply voltage  $v_s$  is measured by the voltage sensors and transmitted to the Kalman filter to obtain the state  $\xi$ , which contains fundamental and harmonic components information. It should be pointed out that the selection of the phase of the reference voltage  $v_{c-ref}$  is closely

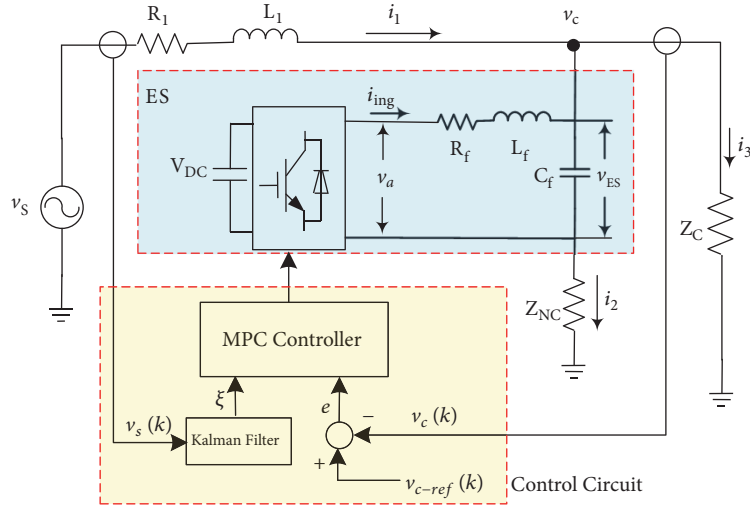


FIGURE 3: Control system block diagram of MPC-controlled ES with a Kalman filter.

TABLE 1: Simulated test system parameters.

| Item                                   | Value              |
|--|--------------------|
| Line resistance $R_1$                  | $0.71 \Omega$      |
| Line inductance $L_1$                  | $19.92 \text{ mH}$ |
| Critical load $z_c$                    | $53 \Omega$        |
| Non-critical load $z_{nc}$             | $50.5 \Omega$      |
| Predefined reference value $V_{c-ref}$ | $220 \text{ V}$    |
| DC voltage source $V_{DC}$             | $1200 \text{ V}$   |
| Control horizon $N_u$                  | $30$               |
| Prediction horizon $N_p$               | $30$               |
| System sampling time $T_s$             | $0.2 \text{ ms}$   |

related to the compensation modes of ES. Choosing different angles of  $v_{c-ref}$  can realize different functions of ES, such as power factor correction, constant reactive power compensation, constant real power compensation, and output voltage minimization of the ES.

## 5. Simulation Studies

To demonstrate the effectiveness of the control scheme proposed in this paper, four case studies are conducted by using MATLAB/SIMULINK. The Simulation parameters are shown in Table 1. Without loss of generality, the RMS of  $v_{c-ref}$  is assumed to be  $220 \text{ V}$ . The number of harmonics is up to the  $15^{th}$ , which is used to simulate supply voltage harmonics.

**5.1. Voltage Support Mode.** In order to verify the voltage support capability of an ES under the MPC control strategy proposed in Section 4, supply voltage  $v_s$  is set below the rated value, which is used to simulate the situation of insufficient power output at the generation side. From Figure 4(a), one can observe a significant variation in the line voltage, namely, the voltage across critical loads, before and after the ES is activated. Before the ES is activated, the line voltage  $v_c$  is about

$203 \text{ V}$ , and it rises to the rated value (i.e.,  $220 \text{ V}$ ) rapidly after the ES is activated at 1 second. Figures 4(b) and 4(c) show the corresponding output voltage of ES and control signal  $u$ , respectively.

**5.2. Voltage Suppression Mode.** To test the voltage suppression capability of an ES under the MPC control strategy, supply voltage  $v_s$  is set over the rated value, which is used to simulate the situation of excess power output on the generation side. From Figure 5(a), one can also observe a significant variation in the line voltage  $v_c$  before and after the ES is activated. Before ES is activated, the line voltage  $v_c$  is about  $228 \text{ V}$ , and it drops to the rated value (i.e.,  $220 \text{ V}$ ) rapidly after the ES is activated at 1 second. Figures 5(b) and 5(c) show the corresponding output voltage of ES and control signal  $u$ , respectively.

**5.3. Harmonic Compensation for Line Voltage.** In order to illustrate the ability of an ES to regulate the voltage while suppressing voltage harmonics at the same time under the proposed MPC control strategy, supply voltage  $v_s$  is set below the rated value, and up to the  $15^{th}$  order of the odd harmonics are added to  $v_s$ , which is closer to the real voltage with an increasing proportion of renewable energy fed into the power grid. As clearly seen from Figure 6(a), the line voltage  $v_c$  is not only smaller than the rated value, but the waveform is non-smooth with a large harmonic distortion before the ES is activated. After the ES is activated at 1 second, the waveform of the line voltage  $v_c$  is effectively improved, whose total harmonics distortion (THD) value is reduced from  $18.79\%$  to  $1.36\%$  as shown in Figures 6(b) and 6(c). Therefore, an ES with the MPC controller can deal with voltage regulation and harmonic correction satisfactorily.

**5.4. Random Variations in Supply Voltage.** To further verify the ability of an ES with the MPC controller for voltage regulation and waveform correction under extreme conditions, the supply voltage is set from step change to rapid

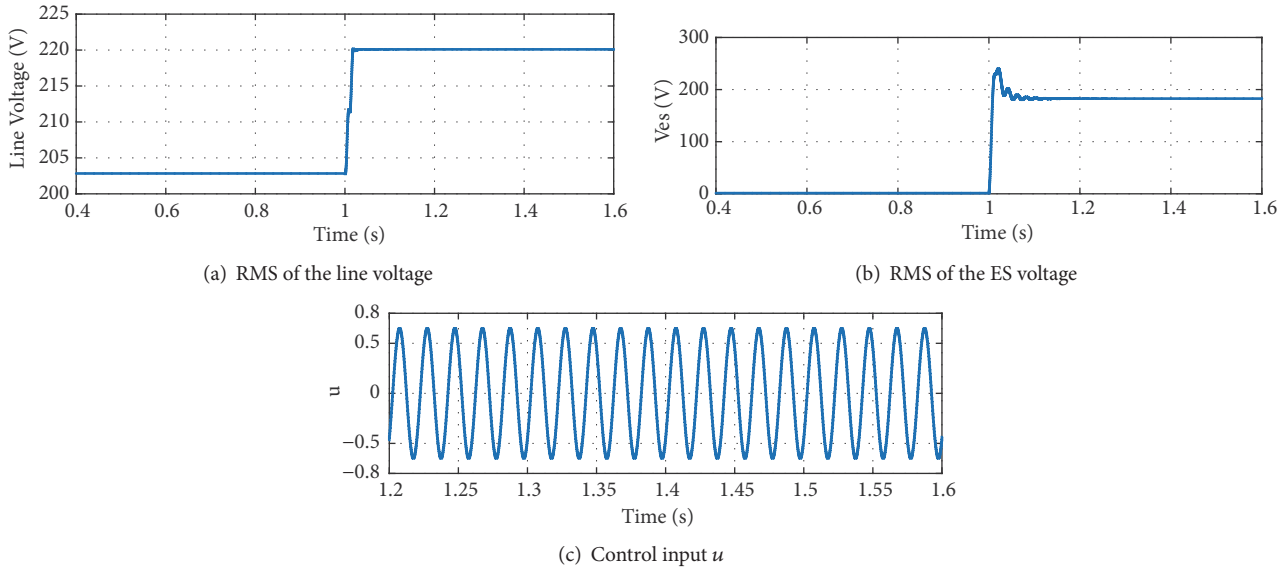


FIGURE 4: Comparison of the changes before and after the ES is activated for voltage boosting. (a) RMS of the line voltage, (b) RMS of the ES voltage, and (c) control input  $u$ .

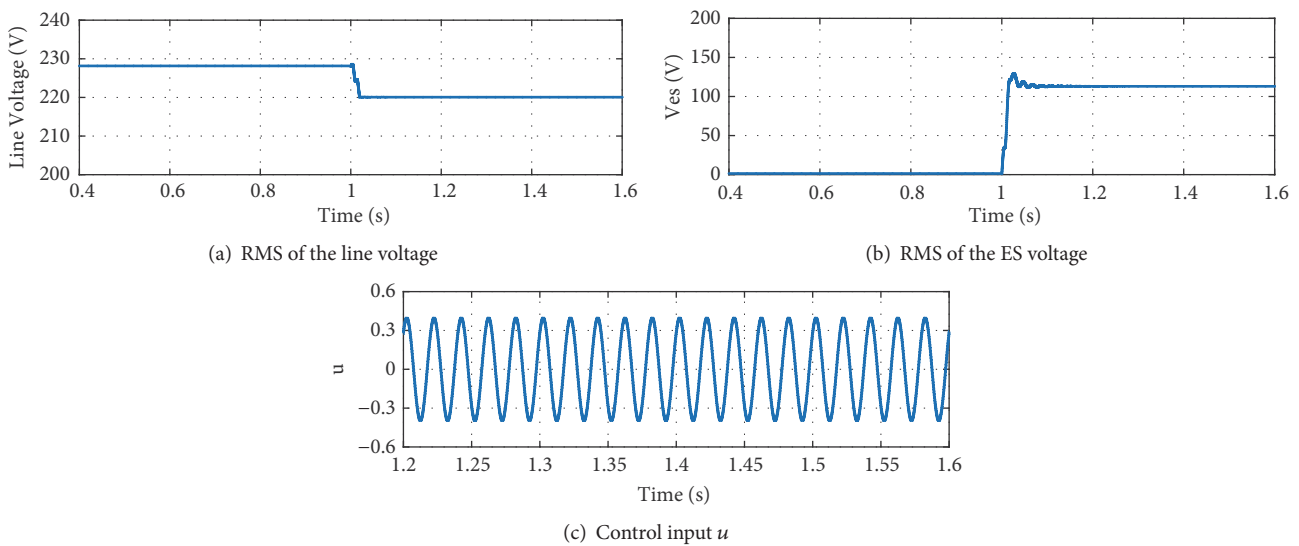


FIGURE 5: Comparison of the changes before and after the ES is activated for voltage suppression. (a) RMS of the line voltage, (b) RMS of the ES voltage, and (c) control input  $u$ .

random change accompanied by relatively large fluctuations. However, the line voltage  $v_c$  is tightly regulated at 220V as shown in Figure 7(a). If one zooms in and looks at the waveform of  $v_c$  as shown in Figure 7(b), one can see that the waveform of  $v_c$  is corrected greatly, which shows that the ES is powerful enough to be used for voltage regulation and harmonics suppression. Figure 7(c) shows the corresponding output voltage of the ES.

## 6. Conclusion

This paper presented a new control strategy based on MPC for ESs to improve the power quality, mainly about voltage

regulation and harmonic suppression. A Kalman filter was used to estimate the random variation of the supply voltage and extract the fundamental and harmonic components of the supply voltage, respectively. In this way, the supply voltage, which was treated as an external disturbance for the plant, could be incorporated in the state-space model form. Then, the supply voltage model was integrated with the ES model into a complete state-space model used for the model predictive controller design. The effectiveness and accuracy of using an ES under the MPC control strategy were verified by the simulation studies, which showed that MPC controller has the capability of realizing voltage regulation and restraining harmonics effectively at the same time.

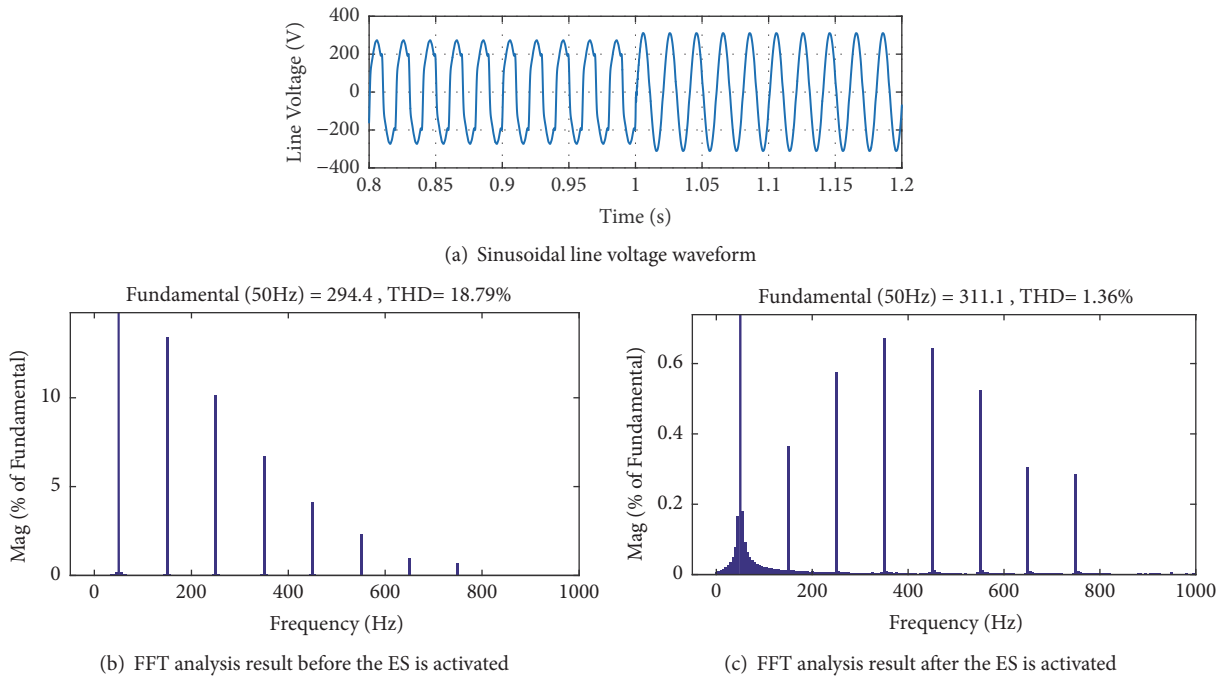


FIGURE 6: Sinusoidal line voltage waveform and results of the FFT analysis before and after the ES is activated. (a) Sinusoidal line voltage waveform, (b) FFT analysis result before the ES is activated, and (c) FFT analysis result after the ES is activated.

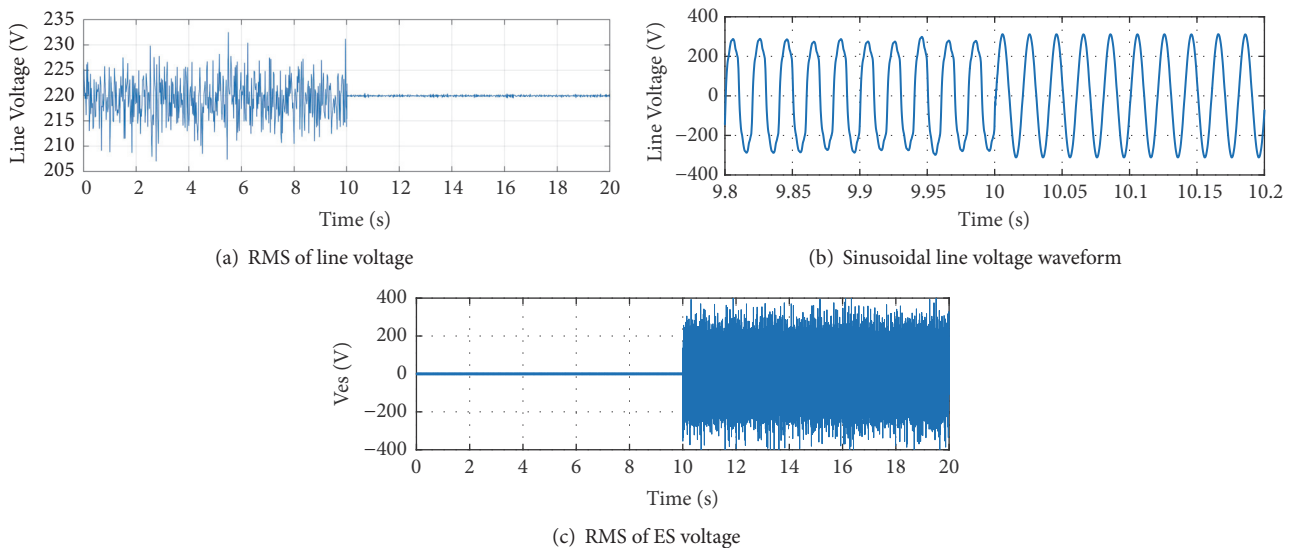


FIGURE 7: ES regulates the line voltage under the condition of the supply voltage varying randomly. (a) RMS of line voltage, (b) sinusoidal line voltage waveform, and (c) RMS of ES voltage.

**Data Availability**

All data can be accessed in the Simulation Studies section of this article.

**Conflicts of Interest**

The authors declare that there are no conflicts of interest regarding the publication of this article.

**Acknowledgments**

This research was supported by the National Natural Science Foundation of China [grant number 61873129].

**References**

[1] J. C. Xiao, J. F. Cai, and X. D. Wang, “A hesitant fuzzy linguistic multicriteria decision-making method with interactive criteria

- and its application to renewable energy projects selection," *Mathematical Problems in Engineering*, vol. 2017, Article ID 9634725, 15 pages, 2017.
- [2] M. Pedrasa, T. Spooner, and I. MacGill, "Scheduling of demand side resources using binary particle swarm optimization," *IEEE Transactions on Power Systems*, vol. 24, no. 3, pp. 1173–1181, 2009.
  - [3] P. Palensky and D. Dietrich, "Demand side management: demand response, intelligent energy systems, and smart loads," *IEEE Transactions on Industrial Informatics*, vol. 7, no. 3, pp. 381–388, 2011.
  - [4] H. Cai, J. Xiang, M. Z. Q. Chen, and W. Wei, "A decentralized control strategy for photovoltaic sources to unify MPPT and DC-bus voltage regulation," in *Proceedings of the American Control Conference (ACC '17)*, pp. 2066–2071, Seattle, Wash, USA, 2017.
  - [5] H. Cai, J. Xiang, W. Wei, and M. Z. Chen, "V-dp/dv droop control for PV sources in DC microgrids," *IEEE Transactions on Power Electronics*, vol. 33, no. 9, pp. 7708–7720, 2018.
  - [6] L. Xu and P. Cartwright, "Direct active and reactive power control of DFIG for wind energy generation," *IEEE Transactions on Energy Conversion*, vol. 21, no. 3, pp. 750–758, 2006.
  - [7] D. F. Teshome, P. F. Correia, and K. L. Lian, "Stochastic optimization for network-constrained power system scheduling problem," *Mathematical Problems in Engineering*, vol. 2015, Article ID 694619, 17 pages, 2015.
  - [8] O. Abedinia and N. Amjadi, "Net demand prediction for power systems by a new neural network-based forecasting engine," *Complexity*, vol. 21, no. S2, pp. 296–308, 2016.
  - [9] L. Xi, Y. Li, Y. Huang, L. Lu, and J. Chen, "A novel automatic generation control method based on the ecological population cooperative control for the islanded smart grid," *Complexity*, vol. 2018, Article ID 2456963, 17 pages, 2018.
  - [10] S. Y. Hui, C. K. Lee, and F. F. Wu, "Electric springs—a new smart grid technology," *IEEE Transactions on Smart Grid*, vol. 3, no. 3, pp. 1552–1561, 2012.
  - [11] X. Chen, Y. Hou, S.-C. Tan, C.-K. Lee, and S. Y. R. Hui, "Mitigating voltage and frequency fluctuation in microgrids using electric springs," *IEEE Transactions on Smart Grid*, vol. 6, no. 2, pp. 508–515, 2015.
  - [12] N. R. Chaudhuri, C. K. Lee, B. Chaudhuri, and S. Y. R. Hui, "Dynamic modeling of electric springs," *IEEE Transactions on Smart Grid*, vol. 5, no. 5, pp. 2450–2458, 2014.
  - [13] S.-C. Tan, C. K. Lee, and S. Y. Hui, "General steady-state analysis and control principle of electric springs with active and reactive power compensations," *IEEE Transactions on Power Electronics*, vol. 28, no. 8, pp. 3958–3969, 2013.
  - [14] X. Wei, Y. Liu, Z. Zhang, and J. Wang, "Steady-state analysis of electric spring for smart grid," in *Proceedings of the 12th World Congress on Intelligent Control and Automation*, pp. 905–909, Guilin, China, 2016.
  - [15] C. K. Lee, B. Chaudhuri, and S. Y. Hui, "Hardware and control implementation of electric springs for stabilizing future smart grid with intermittent renewable energy sources," *IEEE Journal of Emerging and Selected Topics in Power Electronics*, vol. 1, no. 1, pp. 18–27, 2013.
  - [16] C. K. Lee and S. Y. R. Hui, "Reduction of energy storage requirements in future smart grid using electric springs," *IEEE Transactions on Smart Grid*, vol. 4, no. 3, pp. 1282–1288, 2013.
  - [17] X. Chen, Y. Hou, and S. Y. Hui, "Distributed control of multiple electric springs for voltage control in microgrid," *IEEE Transactions on Smart Grid*, vol. 8, no. 3, pp. 1552–1561, 2017.
  - [18] K. T. Tan, X. Y. Peng, P. L. So, Y. C. Chu, and M. Z. Q. Chen, "Centralized control for parallel operation of distributed generation inverters in microgrids," *IEEE Transactions on Smart Grid*, vol. 3, no. 4, pp. 1977–1987, 2012.
  - [19] P. Kanjiya and V. Khadkikar, "Enhancing power quality and stability of future smart grid with intermittent renewable energy sources using electric springs," in *Proceedings of the 2nd International Conference on Renewable Energy Research and Applications, ICRERA '13*, pp. 918–922, Madrid, Spain, 2013.
  - [20] Q. Wang, M. Cheng, and Y. Jiang, "Harmonics suppression for critical loads using electric springs with current-source inverters," *IEEE Journal of Emerging and Selected Topics in Power Electronics*, vol. 4, no. 4, pp. 1362–1369, 2016.
  - [21] Q. Wang, M. Cheng, Z. Chen, and Z. Wang, "Steady-state analysis of electric springs with a novel  $\delta$  control," *IEEE Transactions on Power Electronics*, vol. 30, no. 12, pp. 7159–7169, 2015.
  - [22] M. S. Javaid, U. B. Irshad, A. Hussein, and M. A. Abido, "A novel fuzzy logic controller for smart load voltage regulation," in *Proceedings of the 6th International Conference on Clean Electrical Power (ICCEP '17)*, pp. 620–624, Santa Margherita Ligure, Italy, 2017.
  - [23] H. Zhang and Q. Hui, "Multiagent coordination optimization based model predictive control strategy with application to balanced resource allocation," in *Proceedings of the ASME Dynamic Systems and Control Conference*, San Antonio, Tex, USA, 2014.
  - [24] Y. Xue, D. Meng, S. Yin et al., "Vector-based model predictive hysteresis current control for asynchronous motor," *IEEE Transactions on Industrial Electronics*.
  - [25] K. H. Kwan, Y. S. Png, Y. C. Qui, and P. L. So, "Model predictive control of unified power quality conditioner for power quality improvement," in *Proceedings of the IEEE International Conference on Control Applications*, pp. 916–921, Singapore, 2007.
  - [26] H. Zhang and Q. Hui, "Kalman filter with diffusion strategies for detecting power grid false data injection attacks," in *Proceedings of the IEEE International Conference on Electro Information Technology (EIT, '17)*, pp. 254–259, Lincoln, Neb, USA, 2017.
  - [27] X. D. Yan, Z. Shu, and S. M. Sharkh, "Hybrid modelling and control of single-phase grid-connected NPC inverters," in *Proceedings of the Applied Power Electronics Conference and Exposition (APEC '16)*, pp. 2223–2228, Long Beach, Calif, USA, 2016.
  - [28] X. Yan, Z. Shu, S. M. Sharkh, and T. Chen, "Output-feedback switching control of DC-DC cuk converters using multiple sampling," in *Proceedings of the International Automatic Control Conference (CAC '15)*, pp. 1–6, Yilan, Taiwan, 2015.
  - [29] Y.-C. Chu and M. Z. Q. Chen, "Efficient model predictive algorithms for tracking of periodic signals," *Journal of Control Science and Engineering*, vol. 2012, Article ID 729748, 13 pages, 2012.
  - [30] J. Macias and A. Gomez, "Self-tuning of kalman filters for harmonic computation," *IEEE Transactions on Power Delivery*, vol. 21, no. 1, pp. 501–503, 2006.